Dinàmica no lineal de sistemes làsers: potencials de Lyapunov i diagrames de bifurcacions

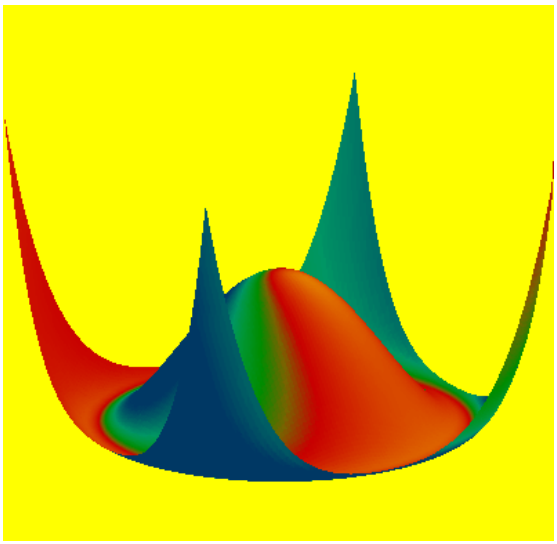

Departament de Física

Universitat de les Illes Balears

Març de 2002

Memòria presentada per Catalina Mayol Serra
per optar al Grau de Doctora en Ciències Físiques
per la Universitat de les Illes Balears.

Raúl Toral Garcés, Catedràtic de la Universitat de les Illes Balears, i Claudio R. Mirasso, Professor Titular de la mateixa Universitat,

CERTIFIQUEN

que la present memòria ha estat realitzada per Catalina Mayol Serra sota la seva direcció en aquest departament i que constitueix la seva Tesi per optar al títol de Doctora en Ciències Físiques.

I, per a què consti, firmen la present en Palma de Mallorca a 23 de gener de 2002.

Raúl Toral Garcés

Claudio R. Mirasso

Als meus pares
Isabel i Mateu,
i a la memòria de
sa meva padrina,
al cel sia.

Agraïments

Amb aquestes línees voldria agrair a totes les persones que m'han ajudat durant els temps que he tardat en l'elaboració dels resultats i redacció d'aquesta memòria.

En primer lloc, tot el suport rebut pels meus dos directors, els professors Raúl Toral i Claudio Mirasso, i tot el que he après durant el temps que he tingut la oportunitat de realitzar investigació amb ells.

Seguidament, al professor Mario Natiello, per la seva hospitalitat i dedicació científica durant les meves dues estades a la Universitat de Lund. De la mateixa manera als professors Luis Pesquera i Sergei I. Turovets, amb els que vaig poder compartir unes setmanes de recerca intensa a la Universidad de Cantabria.

També agrair a tots els professors del Departament de Física de la Universitat de les Illes Balears, la majoria dels quals foren professors meus durant els cursos corresponents a la Llicenciatura; i sobretot als components del Grup de Física No Lineal, amb els quals he compartit cursos de doctorat i molts seminaris.

A continuació, a totes les companyes i companys que he tingut a l'Agència EFE durant aquests anys. N'han passat molts, però amb tots hem disfrutat d'un bon ambient de treball i companyerisme. Així mateix, a totes les persones que he conegut en aquests anys quan he assistit a cursos o congressos, que han fet aquestes estades fora de l'illa molt agradables.

Finalment, als meus pares i germà, per fer–me sempre costat, escoltar–me i donar bons consells.

Contents

Capítol 1

Introducció i estructura de la memòria

En l'estudi de sistemes dinàmics és important calcular els punts fixos de la dinàmica determinista del sistema i determinar la seva estabilitat. Per obtenir aquests resultats es pot fer servir el potencial de Lyapunov, tant en el cas de sistemes mecànics com no mecànics. Aquesta funció dinàmica decreix al llarg de les trajectòries, i és possible calcular els punts fixos com els extrems de la funció de Lyapunov. En alguns casos, l'existència del potencial de Lyapunov permet entendre les trajectòries a l'estat transitori i a l'estacionari. La distribució de probabilitat estacionària en el cas de la dinàmica estocàstica pot, sota determinades condicions, estar també governada pel potencial de Lyapunov. Part del propòsit d'aquest treball és explicar la dinàmica d'alguns sistemes làsers utilitzant aquests potencials.

Físicament, un làser és un dispositiu en què el llum emès s'origina en el procés d'emissió estimulada. Els tres elements bàsics que es requereixen són: un mitjà amb guany, una cavitat òptica i un mecanisme de bombeig. Des del punt de vista dinàmic, els distints tipus de làsers es poden classificar segons el ritme de decaïment de les variables involucrades en les equacions d'evolució: el camp elèctric dins la cavitat, la inversió de població i la polarització material. En els làsers de classe B, la polarització decau cap a l'estat estacionari molt més ràpidament que les altres variables i es pot eliminar adiabàticament. Per als làsers de classe A, una única equació per al camp elèctric és suficient per descriure la dinàmica.

Aquest treball tracta els làsers de classe A i classe B, estudiant la seva dinàmica, en els casos determinista i en presència de renou, fent ús del potencial de Lyapunov.

El control d'un làser a partir de l'aplicació d'un senyal injectat coherent és una àrea important de recerca amb una gran varietat d'aplicacions. Quan als làsers se'ls aplica un senyal injectat, la dinàmica resultant esdevé molt complexa. El comportament del sistema pot ser qualitativament diferent depenent de l'elecció dels paràmetres: estats amb la mateixa freqüència que la d'entrada, polsos, rutes cap al caos, etc. De l'estudi del conjunt invariant d'aquest sistema no lineal, es veu que la bifurcació Hopf–sella–node (HSN) (el camp vectorial linealitzat té un punt fix

degenerat amb dos autovalors imaginaris i un zero) actua com a centre organitzatiu.

La modulació a alta velocitat dels diodes làsers és una àrea en estudi a causa de les seves possibles aplicacions. Els làsers en aquestes circumstàncies poden presentar diversos comportaments no lineals: distorsió harmònica, període doble, biestabilitat, i caos. L'objectiu de part d'aquest treball és el d'obtenir els dominis d'existència de les inestabilitats bàsiques involucrades. Ens restringim a l'estudi de les resonàncies principals: màxima resposta del sistema a una pertorbació externa quan la freqüència de modulació es varia (s'entén com a resposta la intensitat màxima de la potència òptica de sortida).

Aquesta memòria es basa en els següents articles:

[1] C. Mayol, R. Toral i C.R. Mirasso, "Lyapunov–potential description for laser dynamics", Physical Review A **59**, 4690 (1999).

[2] C. Mayol, M.A. Natiello i M. Zimmermann,"Resonance structure in a weakly detuned laser with injected signal". International Journal of Bifurcation and Chaos **11**, 2587 (2001).

[3] C. Mayol, S.I. Turovets, R. Toral, C.R. Mirasso i L. Pesquera, "Main Resonances in Directly Modulated Semiconductor Lasers: Effect of Spontaneous Emission and Gain Saturation". IEE Proc.–Optoelectronics **148**, 41 (2001).

[4] C. Mayol, R. Toral, C.R. Mirasso, S.I. Turovets i L. Pesquera, "Theory of Main Resonances in Directly Modulated Diode Lasers". Acceptat a IEEE Journal of Quantum Electronics, a publicar–se el març de 2002.

[5] C. Mayol, R. Toral, C.R. Mirasso i M.A. Natiello, "Class A lasers with injected signal: bifurcation set and Lyapunov potential function". Enviat a Physical Review E (2002).

A la part I de la memòria es resum els elements bàsics que s'utilitzen a la resta del treball. En el capítol 2, es presenta la relació entre els potencials de Lyapunov i les equacions dinàmiques; en el capítol 3, es fa un resum d'anàlisi de bifurcacions; i en el capítol 4, apareixen les característiques del làser com a sistema dinàmic.

La part II es destina a l'estudi dels làsers de classe A. En el capítol 5, basat en [1], es descriu la dinàmica d'aquests làsers mitjançant el potencial de Lyapunov. En el capítol 6, basat en [5], els làsers de classe A amb senyal injectat s'estudien, obtenint el conjunt de bifurcacions a l'estacionari i estudiant la dinàmica amb el potencial de Lyapunov quan és possible.

La part III tracta de la dinàmica dels làsers de classe B. En el capítol 7, basat en [1], la dinàmica de les equacions de balanç per a aquests làsers s'analitza en termes del potencial, incloent els termes de saturació de guany i d'emissió espontània. El capítol 8, basat en [2], tracta dels làsers de classe B amb senyal injectat. El treball que es presenta completa la sèrie d'estudis anteriors de bifurcacions de làsers amb senyal injectat a prop de la singularitat Hopf–sella–node; s'analitza el rang de paràmetres on el tipus *II* Hopf–sella–node s'espera. En el capítol 9, basat en [3] i [4], s'estudia les resonàncies principals, i l'impacte que els termes de saturació de guany i emissió espontània tenen en ells, en els làsers directament modulats.

Chapter 1

Introduction

In the study of a dynamical system, it is important to obtain its invariant sets, being the fixed points the simplest ones. In some systems, either mechanical or non–mechanical, it is possible to construct a dynamical function (called Lyapunov potential) that decreases along trajectories. The usefulness of Lyapunov functions lies on that they allow an easy calculation of the fixed points of a dynamical (deterministic) system as the extrema of the Lyapunov function as well as determining the stability of these fixed points. In some cases, the existence of a Lyapunov potential gives an intuitive understanding of the transient and stationary trajectories as movements of test particles in the potential landscape. In the case of nondeterministic dynamics, i.e. in the presence of noise terms, and under some general conditions, the stationary probability distribution can also be governed by the Lyapunov potential and averages can be performed with respect to a known probability density function. Part of the aim of this work is to explain the dynamics of some laser systems by using Lyapunov potentials.

1.1 Lasers: Classification

Physically, a laser is a device in which the emitted light is originated in a process of stimulated emission. For obtaining laser action three basic ingredients are necessary: a gain medium (that amplifies the electromagnetic radiation inside the cavity), an optical cavity (that provides the necessary feedback) and a pumping mechanism. Lasers are classified depending on the material which constitutes the gain medium. For example, semiconductor lasers are those for which the gain medium is a semiconductor material. A complete understanding of a laser is based on a fully quantum–mechanical description [Haug, 1969; Sargent *et al.*, 1974]. However, a simpler description can be given in terms of evolution equations for the electric field inside the cavity, the population inversion and the material polarization. Different types of lasers can be classified according to the decay rate of the variables involved in the equations. In class C lasers, the material polarization, the population inversion and the electric field decay within comparable time scales. For

class B lasers, the material polarization decays towards the steady state much faster than the other variables and it can be adiabatically eliminated. Finally, in class A lasers, the population inversion and the material polarization decay much faster than the electric field and only one complex equation is required to describe the dynamics.

In this work we will deal with class A and class B lasers. Both lasers decay to their steady states when their thresholds are crossed. However, this simple dynamics becomes richer when an injected signal is applied or some of the parameters are modulated. During this thesis these effects will be discussed with some detail.

1.2 Laser with injected signal

The control of a laser via an injected coherent signal is an active area of research with a great variety of applications. Experiments and numerical analysis with this special arrangement have been performed leading to different kinds of behaviours (locked lasers, pulses, etc.) [Braza and Erneux, 1990; Gavrielides *et al.*, 1997; Simpson *et al.*, 1997; Nizette and Erneux, 1999]. The behaviour of the system can be qualitatively different depending on the choice of parameters and numerical simulations in three–dimensional models of lasers with injected signal, revealed multistability [Wieczorek *et al.*, 2000b] and different "routes to chaos" for different parameter regions [Tredicce *et al.*, 1985a; Solari and Oppo, 1994; Krauskpof *et al.*, 2000; Wieczorek *et al.*, 2000a; Wieczorek *et al.*, 2000c].

A good theoretical understanding of the underlying mechanisms governing the great variety of possible behaviours was required. An early attempt in this direction, [Solari and Oppo, 1994] aimed to approximate the three–dimensional rate equations for a class B laser in the vicinity of the parameter region, where this system becomes a Hamiltonian system, by a more tractable two–dimensional averaged system [Guckenheimer and Holmes, 1983]. A detailed study of the invariant sets revealed that at the heart of this nonlinear system, the Hopf–saddle–node bifurcation played the role of an organizing center. This local bifurcation arises when the linearization of the vector field has a degenerate fixed point with two purely imaginary and a simple zero eigenvalue. The unfolding of this bifurcation requires two parameters (the amplitude injection rate β and the detuning η of the injected signal to the unperturbed laser operating frequency), and four different variants known as type (*I–IV*) have been studied [Guckenheimer and Holmes, 1983; Wiggins, 1991]. All of these types display curves of saddle–node and Hopf bifurcations of fixed points in parameter space, which are tangent at one point. For increasing cavity detuning $\theta > 0$, Solari and Oppo [Solari and Oppo, 1994] found that type *II*, *I* and *III* may be visited (in that order).

The interest in a physical (and testable) application displaying the above qualitative changes close to the Hopf–saddle–node bifurcation, is not restricted to the determination of the well known invariant sets which result from normal form analysis (saddle–node, primary and secondary Hopf bifurcations). Global behaviour not present in the usual unfolding of Hopf–saddle–node singularity has recently been

studied as a primary source for chaotic behaviour in lasers with injected signal. For example, in the large cavity detuning regime (corresponding to type *III* of Hopf–saddle–node) Zimmermann *et al.* [Zimmermann *et al.*, 1997] showed the occurrence of Sil'nikov homoclinic orbits [Šil'nikov, 1965] to any of the saddle–focus fixed points (locked solutions). Furthermore, as the detuning is decreased the transition from type *III* to type *I* showed that the homoclinic orbits to a fixed point, at the critical θ where the Hopf–saddle–node type changes turns to a homoclinic tangency to the periodic orbit of Hopf–saddle–node [Zimmermann *et al.*, 2001]. This novel behaviour opens the possibility that this physical system may become an ideal test–bench for new global bifurcation scenarios.

In the previous studies on the global bifurcations in laser with injected signal, a combination of the Hopf–saddle–node singularity together with a global reinjection resulted in a proper framework for understanding the laser dynamics. However, in type *II*, which is the interesting case for our work, we find a new possible complication which involves a heteroclinic cycle with the off state.

1.3 Directly modulated lasers

High–speed modulation of laser diodes is an important area of study due to the possible applications of these devices. Diode lasers clearly exhibit in such circumstances various kinds of nonlinear behaviour, i.e., harmonic distortion, multi–pulse response on the time scale of one modulation period, period doubling, amplitude and/or pulse position bistability, and chaos [Kawaguchi, 1994]. Usually, these complicated dynamical phenomena are considered as harmful to the practical application and should be avoided. Nevertheless, there have been some experimental demonstrations of feasibility of using a resonance period doubling regime and pulse position bistability for realizing high speed optical logic elements [Gallagher *et al.*, 1985]. Also, large capacity information transmission and ultrafast optical processing systems [Liu and Ngai, 1993; Mirasso *et al.*, 1993; Breuer and Petermann, 1997] are representative of the possible applications of these systems. Recently, a great deal of interest has been generated by the potential of using lasers running in a chaotic regime as the carriers of information in secure chaotic communication schemes [Mirasso *et al.*, 1996; Goedgebuer *et al.*, 1998; Fisher *et al.*, 2000]. In addition to the optical feedback and saturable absorption effects, chaos in laser diodes induced by modulation in the pump current is another option for building transmitters and receivers for encoded optical communications.

Before Liu and Ngai [Liu and Ngai, 1993] succeeded in observing chaos in a 1.55 μm InGaAsP distributed feedback bulk laser, followed by the report on a similar observation in 1.55 μm multiple quantum well lasers [Matsui *et al.*, 1998], there had been some controversy in earlier theoretical predictions [Tang *et al.*, 1963] and experimental results [Hemery *et al.*, 1990; Kao and Lin, 1993]. Specifically, chaotic and high periodic regimes had not been experimentally observed in contrast to numerical predictions based on the rate equations. It is well known [Agrawal, 1986] that the

gain saturation factor contributes to the damping of relaxation oscillations and it might be the reason for eliminating chaos. The presence of spontaneous emission in the cavity and the Auger recombination factor have also been numerically examined as being one cause of the suppression of chaos [Tang and Wang, 1987]. The importance of noise terms is again under consideration [Lim *et al.*, 2000]. Finally, the gain sharing among multi–longitudinal oscillating modes was identified as an effective gain compression factor and therefore leading to suppression of chaos [Wada *et al.*, 1998]. Now, it is largely accepted that a single mode laser diode with relatively small gain saturation and spontaneous emission parameters might undergo a period doubling route to chaos under current modulation. From the analytical side, such an impact of these parameters was explained in the framework of the small signal analysis showing an increase of the system damping with the increase of the above mentioned parameters [Yoon *et al.*, 1989]. In addition, Hori *et al.* [Hori *et al.*, 1988] suggested that in the large signal modulation regime, the spontaneous emission term, besides contributing to a linear damping of the system, leads to an additional nonlinear damping. This effect would change the representation of the typical Toda oscillator potential topology for the laser and would be also responsible for suppression of chaos. Nevertheless, specific mechanisms of these effects in the large signal regime are not yet fully understood. To the best of our knowledge, a detailed study of the role of spontaneous emission and gain saturation on nonlinear dynamics in the large signal regime is still lacking even in the framework of the simple rate equation model.

Part of this work aims to clarify the parameter domains of the basic instabilities involved. We will restrict ourselves to the study of main resonances to which little attention has been paid in previous works. Defining the response variable as maximum intensity in the optical–power output, a main resonance is understood as the maximum response of the system to the external perturbation when the modulation frequency of the external perturbation is varied. Although main resonances were considered theoretically and numerically [Erneux *et al.*, 1987; Samson and Turovets, 1987; Schwartz, 1988; Samson *et al.*, 1990; Schwartz and Erneux, 1994] and also experimentally [Samson *et al.*, 1992; Chizhevsky and Turovets, 1993; Bennett *et al.*, 1997; Chizhevsky, 2000], for conventional class B lasers the impact of large gain saturation and spontaneous emission terms, which are typical for laser diodes, is not fully understood yet. By using the asymptotic quasi–conservative theory [Katz, 1955; Drozdov, 1955; Erneux *et al.*, 1987; Samson and Turovets, 1987] with an appropriate Lyapunov potential describing the laser dynamics, we compute the domains of existence for the resonance nT periodic responses in arbitrarily large amplitude modulated laser diodes. For this particular kind of nonlinearity, these resonant curves are associated to the so–called primary saddle–node bifurcations and are often confused in experiments with the multiperiodic windows in chaos. When considering gain saturation and spontaneous emission terms on the dynamics we find that, besides increasing the damping of relaxation oscillations, these parameters change the topology of the Lyapunov potential, increasing the thresholds of instabilities in the system. The theory is substantiated by numerical results. The

estimations for primary saddle–node bifurcations in strongly modulated laser diodes create the basis for a systematic search for a priori wanted regimes in simulations or experiment and also naturally explain pulse position multistability [Gallagher *et al.*, 1985; Chizhevsky and Turovets, 1993].

Another way of obtaining nonlinear effects in lasers is by modulating their losses. Cavity loss can be modulated in practise by using a variable reflector or in a two–section laser when modulating periodically the passive section.

1.4 Structure of the work

This manuscript is based on the following papers:

[1] C. Mayol, R. Toral and C.R. Mirasso, "Lyapunov–potential description for laser dynamics", Physical Review A **59** (6), 4690–4698 (1999).

[2] C. Mayol, M.A. Natiello, and M.G. Zimmermann, "Resonance structure in a weakly detuned laser with injected signal". International Journal of Bifurcation and Chaos **11** (10), 2587–2605 (2001).

[3] C. Mayol, S.I. Turovets, R. Toral, C.R. Mirasso, and L. Pesquera, "Main Resonances in Directly Modulated Semiconductor Lasers: Effect of Spontaneous Emission and Gain Saturation". IEE Proc.–Optoelectronics **148** (1), 41–45 (2001).

[4] C. Mayol, R. Toral, C.R. Mirasso, S.I. Turovets, and L. Pesquera, "Theory of Main Resonances in Directly Modulated Diode Lasers". Accepted in IEEE Journal of Quantum Electronics, to appear in March 2002.

[5] C. Mayol, R. Toral, C.R. Mirasso, and M.A. Natiello, "Class *A* lasers with injected signal: bifurcation set and Lyapunov potential function". Submitted to Physical Review E (2002).

and it is structured as follows.

In part I some basic concepts are given:

- In chapter 2, a brief review of the relation between Lyapunov potentials and the dynamical equations and the splitting of the latter into conservative and dissipative parts is given. We also present some results on Fokker–Plank equations and numerical integration of stochastic equations, which are used in the following chapters.
- In chapter 3, a review of bifurcation analysis is done.
- In chapter 4, the main features of the laser as a dynamical system are reviewed.

Part II is devoted to the study of class A lasers:

- In chapter 5, based on [1], the Lyapunov potential gives an intuitive understanding of the dynamics observed in the numerical simulations for class A lasers. In the presence of noise, the probability density function obtained from the potential allows the calculation of stationary mean values of interest as, for example, the mean value of the number of photons. We will show that the mean value of the phase of the electric field in the steady state varies linearly with time only when noise is present, in a phenomenon reminiscent of noise–sustained flows.

- In chapter 6, based on [5], class A lasers with injected signal are studied. The dynamical behaviour in the steady state is more complex than the non–injected signal case due to the introduction of new degrees of freedom. The bifurcation set is obtained in terms of the amplitude and phase of the injected signal by using the tools introduced in chapter 3. Moreover, this complex dynamical system is studied in terms of a Lypunov potential function whenever it is possible. In particular, noise–sustained flows are also obtained and mean values calculated by using the Lyapunov potential in the case of a injected signal without detuning.
  The bifurcation set obtained reveals the complexity of the system and the importance of the parameter choice in experiments. Class A lasers with injected signal are the simplest example one can consider. A more complex situation arises considering class B lasers with injected signal (chapter 8). From the dynamical point of view the main difference between class A and class B lasers is the number of variables that one works with. For class A lasers, two variables suffice and the full bifurcation set can be described. For class B lasers, three variables, a more complex variety of phenomena can appear and the system can also show chaotic behaviour when injecting an external signal. Although part of the bifurcation structure of class B lasers is already present in class A lasers, the overall dynamics of the former becomes extremely complicated.

Part III deals with the dynamics of class B lasers:

- In chapter 7, based on [1], the dynamics of rate equations for class B lasers is presented in terms of the intensity and the carriers number (we will restrict ourselves to the semiconductor laser). In this case we obtain a potential which helps us to analyse the corresponding dynamics in the absence of noise fluctuations. By using the conservative part of the equations, we obtain an expression for the period of the oscillations in the transient regime following the laser switch–on. This expression extends a simpler one that identifies the laser dynamics with a Toda oscillator, by adding in the expression for the period the corresponding modifications due to gain saturation and spontaneous emission noise terms.

- Chapter 8, based on [2], deals with class B lasers with injected signal. The work presented here completes the above series of studies of bifurcations of the laser with injected signal in the neighbourhood of the Hopf–saddle–node singularity, see Sec. 1.2. We analyse a range of parameters where type *II* Hopf–saddle–node is expected by using the tools of chapter 3. The main bifurcation structure consists of a (secondary) Hopf bifurcation on the periodic orbit associated to the Hopf–saddle–node bifurcation. We have analysed in detail the resonance structure which reveals a rich interaction with other bifurcations *not* present in the usual Hopf–saddle–node scenario. We find that the Arnold tongues are truncated by another (secondary) Hopf bifurcations of periodic orbits. These in turn originate in an Andronov global bifurcation at the saddle–node of fixed points (saddle–node infinite period bifurcation) [Kuznetsov, 1997]. Another particular behaviour is that inside the Arnold tongues we also find homoclinic bifurcations to a saddle fixed point corresponding to the off state of the laser. Finally we show how the Arnold tongues of increasing winding number, together with all their associated bifurcations, *accumulate* towards the Hopf–saddle–node bifurcation point.

- In chapter 9, based on [3] and [4], we have undertaken analytical and numerical calculations in the framework of the single mode rate equation model with direct modulation with the aim of clarifying the parameter domains of the basic instabilities involved and relating them to the reported experiments using $1.55\mu m$ InGaAs distributed feedback lasers [Liu and Ngai, 1993]. We study main resonances and the impact that large gain saturation and spontaneous emission terms have on them. By using the asymptotic quasi–conservative theory with an appropriate Lyapunov potential describing the laser dynamics, the one presented in chapter 7, we have computed the domains of existence of resonances in arbitrarily large amplitude modulated laser diodes, and compared them to the numerical results.

In the final chapter, we summarize the main results obtained as well as some possible extensions and other problems.

Part I

Conceptes bàsics

Capítol 2

Resum de sistemes dinàmics

En aquest capítol, es resumeixen alguns resultats bàsics en sistemes dinàmics que seran utilitzats en capítols posteriors. En primer lloc, es revisa la forma de tractar equacions diferencials estocàstiques. Llavors, s'introdueix la definició de potencial de Lyapunov i les diferents maneres que aquest potencial es relaciona amb les equacions dinàmiques per a sistemes determinístics. Per acabar, les relacions entre processos estocàstics i potencials de Lyapunov es presenten en els casos on la funció densitat de probabilitat estacionària per a un procés estocàstic es pot obtenir a partir del potencial de Lyapunov.

Per descriure els sistemes dinàmics, s'utilitzen equacions diferencials que modelitzen el sistema. En el cas de sistemes determinístics, s'empren equacions diferencials ordinàries o equacions diferencials en derivades parcials. El tractament d'aquest tipus d'equacions està ben establert, i es pot fer analíticament o emprant mètodes numèrics.

Alguns sistemes tenen alguna de les seves parts modelada de forma aleatòria, ja que el coneixement d'aquestes parts no és prou detallat o és massa complex per poder ésser tractat de manera determinista. Aquestes parts aleatòries són les que contenen els *processos aleatoris*, o també coneguts com *termes de renou*. Les equacions diferencials que contenen els termes aleatoris són les *equacions diferencials estocàstiques*. Les equacions estocàstiques on els termes aleatoris apareixen linealment s'anomenen *equacions de Langevin*. Segons que la funció que multiplica el terme de renou en l'equació de Langevin sigui constant o no, tendrem, respectivament, renou additiu o multiplicatiu. Dels diferents termes de renou que poden ésser considerats, es restringeix l'estudi al *renou blanc*, que es caracteritza per ser un procés gaussià Markovià de mitja zero i delta–correlacionat (2.2). L'equació diferencial estocàstica de Langevin no està completament definida a menys que es digui quina interpretació s'agafa per realitzar integrals que involucren el procés aleatori, les interpretacions sovint més emprades són la de Itô i la de Stratonovich. La generació numèrica de les trajectòries que defineix l'equació diferencial estocàstica de Langevin ve donada per la generalització dels mètodes utilitzats amb equacions diferencials ordinàries, com el de Runge–Kutta o el de Euler. En aquest cas, les equacions recurrents que

s'obtenen al afegir els termes de renou donen lloc als mètodes de Milshtein i de Heun. Aquests mètodes són els que s'utilitzen per obtenir molts dels resultats que es presenten en les parts II i III de la memòria.

L'evolució d'un sistema dinàmic es pot classificar en diferents categories depenent de la relació del *potencial de Lyapunov* amb les equacions de moviment. El teorema d'estabilitat de Lyapunov diu que si es coneix una funció de les variables del sistema que sigui una funció decreixent en l'evolució temporal, els mínims de l'esmentada funció en termes de les variables són els punts fixos estables de la dinàmica del sistema. L'evolució del sistema és cap al mínims de la funció de Lyapunov, i a més, el sistema queda a prop d'aquests mínims quan hi actuen petites pertorbacions. El potencial de Lyapunov dóna informació de l'estabilitat global del sistema: dels possibles mínims, el més estable és aquell que té el valor del potencial més baix. Els sistemes per als quals existeix un potencial de Lyapunov s'anomenen *sistemes potencials*, mentre que els altres són *sistemes no potencials*. Dins els sistemes potencials es pot fer una subdivisió depenent de com es relacionen les derivades de la funció de Lyapunov amb les equacions del moviment. El tipus més general, i que serà del nostre interès en els capítols posteriors, és l'anomenat *flux potencial no relaxacional* (2.26, 2.28): les trajectòries van cap al mínim del potencial sense necessitat de seguir les línies de màxim pendent, i pot haver–hi una dinàmica residual una vegada que s'ha arribat al mínim. Perquè el potencial que s'obté sigui un bon potencial de Lyapunov, una condició suficient és que verifiqui la *condició d'ortogonalitat* (2.30), que relaciona els termes residuals amb les derivades del potencial.

El potencial de Lyapunov introduït per a sistemes determinístics pot ser també d'utilitat en el cas de considerar sistemes amb renou. Les equacions diferencials estocàstiques es tracten amb la seva funció densitat de probabilitat, que verifica l'equació de Fokker–Planck (2.33). Quan la part determinista de les equacions estocàstiques és un flux potencial, es pot obtenir una expressió per a la funció densitat de probabilitat estacionària en termes del potencial (2.38). Ara bé, algunes restriccions addicionals s'han de satisfer per a la matriu que relaciona el potencial i les equacions del moviment i els termes residuals, com la *condició de fluctuació–dissipació* (2.35) i la condició de divergència nul·la per als termes residuals (2.37). En tot cas, existeix un resultat més general, indicant que es pot obtenir la funció densitat de probabilitat a partir del potencial de Lyapunov sempre i quan la intensitat del renou sigui molt petita. La utilitat de la funció densitat de probabilitat apareix a l'hora de calcular valors mitjos de les variables d'interès (2.39).

Als capítols 5, 6 i 7 s'estudia la dinàmica de làsers de classe A i classe B mitjançant els potencials de Lyapunov.

Chapter 2

Summary of Dynamical Systems

In this chapter, we summarize some results on dynamical systems that will be used subsequently. First, a way of dealing with stochastic differential equations is given. Then, we introduce the definition of Lyapunov potential and the different forms in which the potential is related to the dynamical equations for deterministic systems. Finally, the relationships between stochastic processes and Lyapunov potentials are presented in the cases where the stationary probability distribution function for an stochastic process can be obtained from the Lyapunov potential.

2.1 Brief review on Stochastic Processes

The aim of this section is to give a brief introduction to the basic techniques of stochastic processes that will be used during the rest of this work. We follow closely Ref. [San Miguel and Toral, 1997].

Dynamical systems can be described by a set of differential equations, usually derived after considering certain approximations. Deterministic systems can be well described either by ordinary differential equations or partial differential equations. There is a well established literature to deal with this kind of equations either analytically or numerically, although in some cases the results obtained can be quite complicated due to nonlinear terms appearing in the equations. Furthermore, there are some systems for which certain parts of their behaviour are modelled as random, because the knowledge of these parts is not detailed enough or it is too complex to be treated deterministically. Random parts are those containing a *random process* usually referred to as a *noise term*, $\xi(t)$. The differential equations containing a random process are referred to as *stochastic differential equations*.

Stochastic equations in which the random processes appear linearly are known as *Langevin equations*. For a real variable x, the Langevin equation has the general form

$$\frac{dx}{dt} = q(x,t) + g(x,t)\,\xi(t). \tag{2.1}$$

If the function $g(x,t)$ is a constant, the noise is called *additive*, otherwise, it is a

multiplicative noise.

There are different noise terms that can be considered, all of them defined by their moments and their correlation functions. We will restrict our study to the *white noise*, characterized as a Markovian[1] Gaussian process of mean value and correlations given by

$$\begin{aligned} \langle \xi(t) \rangle &= 0, \\ \langle \xi(t_1)\, \xi(t_2) \rangle &= \delta(t_1 - t_2). \end{aligned} \tag{2.2}$$

The white noise term can be considered as the derivative of the Wiener process, $W(t)$, which has a Gaussian, time dependent, probability density function

$$f(W;t) = \frac{1}{\sqrt{2\,\pi\,t}} \exp\left(-\frac{W^2}{2\,t}\right), \tag{2.3}$$

with one–time moments and two–times correlation function

$$\langle W(t) \rangle = 0, \tag{2.4}$$

$$\langle W(t)^2 \rangle = t, \tag{2.5}$$

$$\langle W(t_1) W(t_2) \rangle = \min(t_1, t_2). \tag{2.6}$$

The derivative of the Wiener process has lack of mathematical rigor and can lead to different possible interpretations [van Kampen, 1981; Gardiner, 1985]. The stochastic integral

$$\int_{t_0}^{t} G(t') dW(t'), \tag{2.7}$$

is interpreted as the limit of partial sums

$$S_n = \sum_{i=1}^{n} G_i [W(t_i) - W(t_{i-1})], \tag{2.8}$$

where t_i corresponds to the partition of the time interval

$$(t_0, t) = (t_0, t_1) \bigcup (t_1, t_2) \bigcup \ldots \bigcup (t_{n-1}, t_n = t). \tag{2.9}$$

The arbitrariness in the definition is related to the problem of which G_i one takes in order to evaluate the integral. Amongst all possible interpretations, the most widely used are those of Itô and Stratonovich. In the Itô interpretation $G_i = G(t_{i-1})$, while for the Stratonovich interpretation $G_i = \frac{1}{2}[G(t_i) + G(t_{i-1})]$.

The Langevin stochastic differential equation is not completely defined unless one chooses one of the previous interpretations. However, there is a simple relationship between the results of these most common interpretations. The rule is that the stochastic differential equation in the Itô sense

$$\frac{dx}{dt} = q(x) + g(x)\, \xi(t), \tag{2.10}$$

[1] In a Markovian process the probability of a future event depends only on the present state of the system and not on the way it reached its present situation.

is equivalent to the stochastic differential equation in the Stratonovich sense

$$\frac{dx}{dt} = q(x) - \frac{1}{2}\, g(x)\, g'(x) + g(x)\, \xi(t). \tag{2.11}$$

In the Itô interpretation $\langle G(t)\xi_w(t)\rangle = 0$, for any non–anticipating function $G(t)$ of $\xi_w(t)$ [Gardiner, 1985]. However, this result is not true in the Stratonovich interpretation, where the Novikov's theorem [Novikov, 1964; Novikov, 1965] should be applied. The Stratonovich interpretation enables the use of the rules of ordinary calculus. However, this is not possible in the Itô interpretation, although it is the most mathematically and technically satisfactory.

Since in most of the cases, it is not possible to integrate the differential equations analytically, one will be interested in obtaining the numerical values for the variables as time evolves. In the next subsection, numerical algorithms for the generation of trajectories are reviewed.

Numerical generation of trajectories

For an ordinary (non–stochastic) differential equation of the form

$$\frac{dx(t)}{dt} = q(t, x), \tag{2.12}$$

the second order Runge–Kutta method gives an approximation to $x(t+h)$ of order $O[h^3]$

$$x(t+h) = x(t) + \frac{h}{2}\,[q(t, x(t)) + q(t+h, x(t) + h\, q(t, x(t)))] + O[h^3]. \tag{2.13}$$

This is an improved algorithm upon the Euler method

$$x(t+h) = x(t) + h\, q(t, x(t)) + O[h^2]. \tag{2.14}$$

In the presence of a Langevin equation as (2.1), one is interested in generating trajectories $x(t)$ for different values of the random process. There are different numerical algorithms to solve this problem [Sancho *et al.*, 1982; Gard, 1987; Greiner *et al.*, 1988; Kloeden and Platen, 1992].

For the stochastic differential equation (2.1), in the Stratonovich sense, we can derive the recurrence relation

$$x(t+h) = x(t) + h^{1/2}\, g(x(t))\, u(t) + h\, \left[q(x(t)) + \frac{1}{2}\, g(x(t))\, g'(x(t))\, u(t)^2\right] + O[h^{3/2}], \tag{2.15}$$

which is known as Milshtein method [Milshtein, 1974; Milshtein, 1978; Sancho *et al.*, 1982]. $u(t)$ are a set of independent Gaussian random variables defined only for the discrete set of recurrence times, $t = 0, h, 2\,h, \ldots$, of zero mean and variance one

$$\begin{aligned} \langle u(t) \rangle &= 0, \\ \langle u(t)^2 \rangle &= 1, \\ \langle u(t)\, u(t') \rangle &= 0,\ t \neq t'. \end{aligned}$$

There are different numerical methods for generating the independent Gaussian random variables, based on random numbers uniformly distributed in the interval $(0, 1)$. We follow here the one developed in [Toral and Chakrabarti, 1993].

A modification of (2.15) is the "Euler algorithm"

$$x(t+h) = x(t) + h^{1/2}\, g(x(t))\, u(t) + h\, \left[q(x(t)) + \frac{1}{2}\, g(x(t)) g'(x(t)) \right] + O[h^{3/2}]. \quad (2.16)$$

This algorithm appears naturally when considering the numerical integration of the equivalent stochastic differential equation (2.10) in the Itô formalism.

The same idea of the Runge–Kutta method applied to ordinary differential equations can be applied to stochastic differential equation. By modifying the Euler method (2.16) one obtains the Heun method [Gard, 1987]

$$\begin{aligned} k &= h\, q(t, x(t)), \\ l &= h^{1/2}\, u(t)\, g(t, x(t)), \\ x(t+h) &= x(t) + \frac{h}{2}\, [q(t, x(t)) + q(t+h, x(t)+k+l)] + \\ &\quad \frac{h^{1/2}\, u(t)}{2}\, [g(t, x(t)) + g(t+h, x(t)+k+l)]\,. \end{aligned} \quad (2.17)$$

In this work, we are interested in the numerical solution of a set of coupled ordinary differential equations with *diagonal noise* of the form

$$\frac{dA_i(t)}{dt} = q_i([A]) + g_i(A_i)\, \xi_i(t), \quad i = 1, \ldots, N. \quad (2.18)$$

In this case, the Milshtein method reads

$$\begin{aligned} A_i(t+h) &= A_i(t) + g_i(A_i(t))\, h^{1/2}\, u_i(t) + \\ &\quad h\, \left[q_i([A(t)]) + \frac{1}{2}\, g_i(A_i(t))\, g_i'(A_i(t))\, u_i(t)^2 \right]. \end{aligned} \quad (2.19)$$

While the Heun method is

$$\begin{aligned} k_i &= h\, q_i([A(t)]), \\ l_i &= h^{1/2}\, u_i(t)\, g_i([A(t)]), \\ A_i(t+h) &= A_i(t) + \frac{h}{2}\, [q_i([A(t)]) + q_i([A(t)+k+l])] + \\ &\quad \frac{h^{1/2}\, u_i(t)}{2}\, [g_i(A_i(t)) + g_i(A_i(t)+k_i+l_i)]\,. \end{aligned} \quad (2.20)$$

2.2 Potentials and Lyapunov Functions

The evolution of a system (dynamical flow) can be classified into different categories according to the relationship of the Lyapunov[2] potential to the actual equations of motion [Montagne *et al.*, 1996; San Miguel *et al.*, 1996].

Classification of Dynamical Systems

Consider a deterministic dynamical flow where the real variables $\mathbf{x} \equiv (x_1, \ldots, x_N)$ satisfy the general evolution equations

$$\frac{dx_i}{dt} = f_i(\mathbf{x}), \qquad i = 1, \ldots, N. \tag{2.21}$$

One is usually interested in finding the fixed points $\bar{\mathbf{x}}$ of the dynamical system, i.e. those having a zero time derivative. The knowledge of the fixed points and their stability is usually the first step in the study of a dynamical system. A fixed point $\bar{\mathbf{x}}$ is said to be stable if for any initial condition sufficiently close to $\bar{\mathbf{x}}$, the system remains in the neighbourhood of $\bar{\mathbf{x}}$ as the time evolves. The fixed point is asymptotically stable if for any initial condition, sufficiently close to $\bar{\mathbf{x}}$, the system tends to $\bar{\mathbf{x}}$ with time.

Lyapunov's stability theorem is useful to determine the stability of a fixed point [Guckenheimer and Holmes, 1983]. The theorem states that if a function $V(\bar{\mathbf{x}}) = V(x_1, ..., x_N)$ exists, such that V is bounded from below and $dV/dt \leq 0$, then the minima $\bar{\mathbf{x}}$ of V are stable fixed points of the dynamics. In this case, V is called a *Lyapunov potential* or, simply, the potential.

The description of the behaviour of a dynamical system is greatly simplified if the Lyapunov potential is known: the system evolves towards the minima of the Lyapunov and once there it stays nearby when small perturbations act upon the system. The Lyapunov potential not only tells us about local stability, but also gives information about global stability. In the case of the comparison between only two fixed points $\bar{\mathbf{x}}^{(1)}$ and $\bar{\mathbf{x}}^{(2)}$ such that $V(\bar{\mathbf{x}}^{(1)}) > V(\bar{\mathbf{x}}^{(2)})$, then we can infer that $\bar{\mathbf{x}}^{(2)}$ is the stable fixed point and that $\bar{\mathbf{x}}^{(1)}$ is a metastable fixed point. This means that a sufficiently strong perturbation might take the system out from $\bar{\mathbf{x}}^{(1)}$ to $\bar{\mathbf{x}}^{(2)}$. Therefore, to understand the asymptotic dynamics it is of great importance to find out whether a Lyapunov potential can be found for the dynamical system under study.

The systems for which a Lyapunov function exists are called in the literature *potential systems* and the name *non–potential systems* is reserved for those systems which do not have a Lyapunov function. According to these definitions, the following classification of dynamical systems can be established.

[2] Some details of the biography of the Russian mathematician Aleksandr Mikhailovich Lyapunov (1857-1918) can be found in [Lyapunov, 1992].

(1) Relaxational gradient potential flow

In this case, there exists a function (the *potential*) $V(\mathbf{x}) = V(x_1, ..., x_N)$ in terms of which the evolution equations are written as

$$\frac{dx_i}{dt} = -\frac{\partial V}{\partial x_i}, \quad i = 1, \ldots, N. \tag{2.22}$$

The fixed points of this dynamical system are the extrema of the potential $V(\mathbf{x})$. The trajectories lead to any of the minimum values of $V(\mathbf{x})$ following the lines of maximum slope (steepest descent). In this case the potential $V(\mathbf{x})$ is a Lyapunov function (with the additional condition that $V(\mathbf{x})$ is bounded from bellow). The proof of this statement is very simple indeed

$$\frac{dV}{dt} = \sum_{i=1}^{N} \frac{\partial V}{\partial x_i}\frac{dx_i}{dt} = -\sum_{i=1}^{N}\left(\frac{\partial V}{\partial x_i}\right)^2 \leq 0. \tag{2.23}$$

(2) Relaxational non–gradient potential flow

There exists again a potential function, $V(\mathbf{x})$, but in this case the dynamics is not governed just by $V(\mathbf{x})$, but is given by

$$\frac{dx_i}{dt} = -\sum_{j=1}^{N} S_{ij}\frac{\partial V}{\partial x_j}, \quad i = 1, \ldots, N, \tag{2.24}$$

where $S_{ij}(\mathbf{x})$ is a real, symmetric and positive definite matrix. The fixed points of the dynamics are still given by the extrema of $V(\mathbf{x})$, however the trajectories lead to the minima of $V(\mathbf{x})$ but not necessarily through the lines of maximum slope but instead they can have an orthogonal component due to the fact that the matrix S is not necessarily diagonal. In this sense, we can say that the transient dynamics is not governed only by the potential. However, $V(\mathbf{x})$ is still a Lyapunov functional

$$\frac{dV}{dt} = \sum_{i=1}^{N} \frac{\partial V}{\partial x_i}\frac{dx_i}{dt} = -\sum_{i,j=1}^{N} S_{ij}\frac{\partial V}{\partial x_i}\frac{\partial V}{\partial x_j} \leq 0, \tag{2.25}$$

since, by definition, $S(\mathbf{x})$ is a positive definite matrix.

(3) Non–relaxational potential flow

In these systems the asymptotic behaviour is not determined simply by the minima of the potential, but there exists a residual dynamics once the minima have been reached. A first category within this class is given by

$$\frac{dx_i}{dt} = -\sum_{j=1}^{N} D_{ij}\frac{\partial V}{\partial x_j}, \quad i = 1, \ldots, N. \tag{2.26}$$

Here, $D_{ij}(\mathbf{x})$ is an arbitrary matrix. When $D_{ij}(\mathbf{x})$ is split into a symmetric and an antisymmetric part $D(\mathbf{x}) = S(\mathbf{x}) + A(\mathbf{x})$, $S(\mathbf{x})$ is a positive definite matrix. Again,

the fixed points of the dynamics are determined by the extrema of the potential $V(\mathbf{x})$. $V(\mathbf{x})$ is a Lyapunov potential, i.e.

$$\frac{dV}{dt} = -\sum_{i,j=1}^{N} S_{ij}\frac{\partial V}{\partial x_i}\frac{\partial V}{\partial x_j} - \sum_{i,j=1}^{N} A_{ij}\frac{\partial V}{\partial x_i}\frac{\partial V}{\partial x_j} \leq 0, \tag{2.27}$$

where the second sum of this expression is zero due to the antisymmetry of the matrix $A(\mathbf{x})$.

The second, and more general, category of non–relaxational potential flow is one in which the dynamical equations can be split into two parts, namely

$$f_i = -\sum_{j=1}^{N} S_{ij}\frac{\partial V}{\partial x_j} + v_i, \quad i = 1, \ldots, N. \tag{2.28}$$

Here $S(\mathbf{x})$ is a symmetric, positive definite matrix and $v_i(\mathbf{x})$ represents the residual dynamics after the relaxational part has acted. Since we demand $V(\mathbf{x})$ to be a Lyapunov potential the residual dynamics must not contribute to its decay

$$\frac{dV}{dt} = -\sum_{i,j=1}^{N} S_{ij}\frac{\partial V}{\partial x_i}\frac{\partial V}{\partial x_j} - \sum_{i=1}^{N} v_i\frac{\partial V}{\partial x_i} \leq 0 \tag{2.29}$$

or, since the first term of the r.h.s. is always negative, a sufficient condition is

$$\sum_{i=1}^{N} v_i\frac{\partial V}{\partial x_i} = 0. \tag{2.30}$$

This is the so–called *orthogonality condition.*

Since the above (sufficient) conditions for a potential flow lead to $dV/dt \leq 0$, one concludes that $V(\mathbf{x})$ (when it satisfies the additional condition of being bounded from below) is a Lyapunov potential for the dynamical system. In this case, one can get an intuitive understanding of the dynamics: the fixed points are given by the extremes of $V(\mathbf{x})$ and the trajectories relax asymptotically towards the surface of minima of $V(\mathbf{x})$. This decay is produced by the only effect of the terms containing the matrix $S(\mathbf{x})$ in Eq. (2.28), since the dynamics induced by $v_i(\mathbf{x})$ conserves the potential, and $v_i(\mathbf{x})$ represents the residual dynamics on this minima surface.

(4) Non–potential flow

For non–potential flows, the splitting (2.28) satisfying (2.30) admits only the trivial solution $V(\mathbf{x}) = 0$, $v_i(\mathbf{x}) = f_i(\mathbf{x})$. Notice that for a system to be classified as non–potential, we have to prove the non–existence of nontrivial solutions of (2.30) which, of course, is different from not being able to find nontrivial solutions of (2.30).

There are different examples in the literature of systems that can be classified as above. We only give here the references in order to show the great variety of fields that can be treated with this formalism. The real Ginzburg–Landau equation

(also known in the theory of critical dynamics as model A in the classification of [Hohenberg and Halperin, 1977]) is a relaxational gradient flow. A typical example of relaxational non–gradient flow is the Cahn–Hilliard model [Cahn and Hilliard, 1958] for spinodal decomposition [Gunton *et al.*, 1983] or model B in the context of critical dynamics [Hohenberg and Halperin, 1977]. As examples of non–relaxational potential flows, the nematodynamics equations commonly used to describe the dynamics of liquid crystals in the nematic phase [San Miguel and Sagues, 1987] and the complex Ginzburg–Landau equation [Descalzi and Graham, 1992; Descalzi and Graham, 1994; Montagne *et al.*, 1996] (the classification given above can also be applied in the case of complex variables, the extension is trivial, and it is presented in [San Miguel *et al.*, 1996]).

Potentials and Stationary Distributions

We now consider dynamical systems where noise is included. We will develop the relationship between stochastic equations and Lyapunov potentials introduced in the previous subsection. Consider the dynamical system described by the stochastic equations (Itô sense) of the form

$$\frac{dx_i}{dt} = f_i(\mathbf{x}) + \sum_{j=1}^{N} g_{ij}(\mathbf{x})\, \xi_j(t), \tag{2.31}$$

where $g_{ij}(\mathbf{x})$ are given functions and $\xi_j(t)$ are white noise sources: Gaussian random processes of zero mean and correlations

$$\langle \xi_i(t)\xi_j(t') \rangle = 2\,\epsilon\,\delta_{ij}\,\delta(t-t'), \tag{2.32}$$

where ϵ is the intensity of the noise.

In this case, it is not adequate to talk about fixed points of the dynamics, but consider instead the maxima of the probability density function $P(\mathbf{x},t)$, which satisfies the multivariate Fokker–Planck equation [Risken, 1989; San Miguel and Toral, 1997]

$$\frac{\partial P(\mathbf{x},t)}{\partial t} = \sum_{i=1}^{N} \frac{\partial}{\partial x_i} \left[-f_i P + \epsilon \sum_{j=1}^{N} \frac{\partial}{\partial x_j}(G_{ij} P) \right], \tag{2.33}$$

where the matrix $G(\mathbf{x})$ is

$$G = g\, g^T, \tag{2.34}$$

and whose general solution is unknown. When the deterministic part of (2.31) is a potential flow, a closed form for the stationary distribution $P_{st}(\mathbf{x})$ can be given in terms of the potential $V(\mathbf{x})$ if the following (sufficient) conditions are satisfied

1. The *fluctuation–dissipation* condition, relating the symmetric matrix $S(\mathbf{x})$ to the noise matrix $g(\mathbf{x})$,

$$S_{ij} = \sum_{k=1}^{N} g_{ik}\, g_{jk}, \qquad S = g \cdot g^T. \tag{2.35}$$

2. S_{ij} satisfies

$$\sum_{j=1}^{N} \frac{\partial S_{ij}}{\partial x_j} = 0, \qquad \forall i. \tag{2.36}$$

This condition is satisfied, for instance, for a constant matrix $S(\mathbf{x})$.

3. $v_i(\mathbf{x})$ is divergence free,

$$\sum_{i=1}^{N} \frac{\partial v_i}{\partial x_i} = 0. \tag{2.37}$$

This third condition is automatically satisfied for potential flows of the form (2.26) with a constant matrix $A(\mathbf{x})$.

Under these circumstances, the stationary probability density function is

$$P_{st}(\mathbf{x}) = Z^{-1} \exp\left(-\frac{V(\mathbf{x})}{\epsilon}\right), \tag{2.38}$$

where Z is a normalization constant, such that $\int P_{st}(\mathbf{x}) d\mathbf{x} = \mathbf{1}$. Conditions (2.35), (2.36) and (2.37) appear naturally when one substitutes expression (2.38) into the Fokker–Planck equation (2.33) and imposes that the derivative with respect to time of $P(\mathbf{x}, t)$ is zero. In some sense, the stationary distribution is still governed by the minima of the potential, since the maxima of this stationary distribution will be centered around these minima. The effect of the noise terms on the asymptotic dynamics is to introduce fluctuations (governed by the Gibbs type distribution (2.38)) in the remaining dynamics which occurs in the attractors identified by the minima of $V(\mathbf{x})$.

A more general result, [Graham, 1987; Graham, 1991], states that if conditions (2.36) and (2.37) are not satisfied, then the above expression (2.38) for $P_{st}(\mathbf{x})$ is still valid in the limit $\epsilon \to 0$.

By using (2.38), the mean value in the steady state of a given function $f(\mathbf{x})$ can be calculated as

$$\langle f(\mathbf{x}) \rangle_{st} = \int f(\mathbf{x})\, P_{st}(\mathbf{x}) d\mathbf{x}. \tag{2.39}$$

This is an useful expression because in the presence of noise terms, one can be more interested in calculating the mean values for different values of the noise terms than in one single realization of the process.

In chapters 5, 6 and 7 we discuss the dynamics of lasers by means of Lyapunov potential functions.

Capítol 3

Bifurcacions

En aquest capítol es fa un resum d'anàlisi de bifurcacions que serà utilitzat en els capítols 6 i 8.

Es considera un sistema dinàmic del tipus $\dot{\mathbf{x}} = \mathbf{f}(\mathbf{x})$, on $\mathbf{x} = (x_1, \ldots, x_n)$ i $\mathbf{f} = (f_1, \ldots, f_n)$. Les seves solucions es poden visualitzar com a *trajectòries* en un espai n–dimensional anomenat *retrat de fases*. L'aparièncía de les trajectòries d'aquest retrat de fases és controlada pels *punts fixos*, $f_i(x_1^*, \ldots, x_n^*) = 0$. És possible analitzar l'estabilitat d'un punt fix a partir de linealitzar les equacions al voltant del punt. Un punt fix es diu *estable* quan tots els autovalors de la matriu linealitzada són negatius; és absolutament *inestable* quan tots els autovalors són positius; i *sella*, quan alguns autovalors són positius i d'altres negatius.

L'estructura qualitativa del flux pot canviar quan es varien el paràmetres del sistema. Aquests canvis qualitatius s'anomenen *bifurcacions*. La representació dels punts o línees on apareixen les bifurcacions en l'espai de paràmetres dóna lloc al *conjunt de bifurcacions*.

Hi ha tipus de bifurcacions que apareixen repetidament en molts problemes. Una possible classificació de les bifurcacions es basa en conceptes que tenen el seu origen en la teoria de transversalitat en topologia diferencial. La *codimensió* d'una bifurcació és la menor dimensió en l'espai de paràmetres que conté la bifurcació.

El *teorema de la varietat central* indica una manera per reduir sistemàticament la dimensió de l'espai d'estats que són necessaris quan s'analitzen bifurcacions d'un cert tipus. Aquest mètode aïlla el comportament asimptòtic més complex a partir de localitzar la varietat invariant tangent al subespai generalitzat d'autovectors amb autovalors imaginaris purs.

Una vegada que s'ha aplicat aquest teorema, s'intenta obtenir transformacions de coordenades addicionals que simplifiquen les expressions analítiques del camp vectorial a la varietat central. Els camps vectorials simplificats són les *formes normals*. La dinàmica a prop d'una bifurcació típicament apareix representada per la seva forma normal.

Algunes bifurcacions de codimensió un són les següents. Una bifurcació *sella–node* és el mecanisme bàsic per el qual dos punts fixos són creats o destruïts, com es veu a la figura 3.1. En una bifurcació *transcrítica*, figura 3.2, dos punts fixos canvien la seva estabilitat en el punt de bifurcació. En una bifurcació tipus *forca*, figura 3.3, dos punts fixos apareixen (destrueixen) simètricament amb l'estabilitat d'un punt fix que existia abans del punt de bifurcació i aquest canvia la seva estabilitat.

A més de punts fixos, poden existir altres conjunts invariants en el sistema dinàmic. Un *cicle límit* és una trajectòria tancada aïllada: les trajectòries properes van cap al cicle límit o es fan enfora d'ell en forma d'espiral.

En una bifurcació de *Hopf*, tal com apareix a la figura 3.6, un punt fix canvia la seva estabilitat i apareix o desapareix un cicle límit amb la mateixa estabilitat que la del punt fix abans del punt de bifurcació. En el punt de bifurcació existeixen un parell d'autovalors imaginaris purs.

Existeixen altres formes amb les quals els cicles límits es poden crear o destruir. En una bifurcació *sella–node de cicles*, dos cicles límits es junten i s'aniquilen. En una bifurcació de *període infinit*, el període d'oscil·lació del cicle límit augmenta fins a fer–se infinit en el punt de bifurcació, i dos punts fixos (un sella i un estable/inestable) hi apareixen. En una bifurcació *homoclínica*, part del cicle límit s'apropa cada vegada més a un punt sella, fins que en el punt de bifurcació el cicle toca el punt sella i es forma una òrbita homoclínica.

A més de les bifurcacions indicades fins ara, és possible obtenir bifurcacions locals de codimensió dos. Un dels l'exemples més típics d'aquest tipus de bifurcació és el cas en què apareixen un parell d'autovalors imaginaris i un autovalor zero (bifurcació Hopf–sella–node). De l'anàlisi de la seva forma normal, es veu que quatre diferents tipus de bifurcacions es poden obtenir depenent del valor dels paràmetres del sistema. A les figures 3.7 a 3.10 apareixen el conjunt de bifurcacions i el retrats de fases per cada un dels tipus que sorgeixen.

Un espai de fases bidimensional important és el *torus*. A damunt aquest torus poden existir òrbites tancades (resonàncies), o la trajectòria pot donar voltes al voltant del torus sense fi, flux *quasiperiòdic*.

Les *projeccions de Poincaré* ens poden servir per a estudiar el flux a prop d'òrbites periòdiques. Si es considera un sistema n–dimensional $\dot{\mathbf{x}} = \mathbf{f}(\mathbf{x})$ i S_n una superfície transversa al flux $n-1$–dimensional. La projecció de Poincaré, $\mathbf{x_{k+1}} = \mathbf{P}(\mathbf{x_k})$, és una relació de S_n amb ella mateixa, obtinguda a partir d'obtenir les interseccions de les trajectòries amb S_n: $\mathbf{x_k} \in S_n$. Es pot establir un criteri en termes dels autovalors λ_j de la projecció de Poincaré linealitzada: L'òrbita tancada serà estable si i només si $|\lambda_j| < 1$ per a tots $j = 1, \ldots, n-1$. Contrariament, si $|\lambda_j| > 1$ per a algun j, les pertorbacions al llarg de la direcció j creixen i l'òrbita és inestable. Un cas límit ocorr quan l'autovalor més gran té magnitud $|\lambda_j| = 1$; això passa en bifurcacions d'òrbites periòdiques i cal un anàlisi nolineal d'estabilitat. Els valors λ_j s'anomenen multiplicadors de *Floquet* de l'òrbita periòdica i generalment només es poden obtenir mitjançant integració numèrica.

Chapter 3

Bifurcations

In this chapter, we summarize some results on bifurcation analysis that will be used in chapters 6 and 8. We follow closely Refs. [Guckenheimer and Holmes, 1983; Hilborn, 1994; Strogatz, 1994; Solari *et al.*, 1996].

Let us consider the general dynamical system

$$\dot{\mathbf{x}} \;=\; \mathbf{f}(\mathbf{x}),$$

where $\mathbf{x} = (x_1, \ldots, x_n)$ and $\mathbf{f} = (f_1, \ldots, f_n)$. Its solutions can be visualized as *trajectories* flowing through an n–dimensional phase space with coordinates $(x_1, \ldots, x_n)$. A picture which shows all the qualitatively different trajectories of the system is called a *phase portrait*. The appearance of the phase portrait is controlled by the *fixed points* $f_i(x_1^*, \ldots, x_n^*) = 0$, for $i = 1, \ldots, n$, which represent equilibrium solutions. An equilibrium point is defined to be *stable* if all sufficiently small perturbations away from it damp out in time. Conversely, in *unstable* fixed points, peturbations grow in time. For a *saddle* fixed point some perturbations grow in time whereas others damp out, depending on the direction chosen near the fixed point. It is possible to perform a quantitative measure of the stability of a fixed point by linearizing about it. The eigenvalues of the linearized matrix give information of the stability of the fixed point: for positive eigenvalues perturbations grow in time, for negative eigenvalues perturbations damp out.

The qualitative structure of the flow can change when parameters of the system are varied. In particular, fixed points can be created or destroyed, or their stability change. These qualitative changes in the dynamics are called *bifurcations*, and the parameter values at which they occur are called *bifurcation points*. The representation of the bifurcation points (or lines) in the parameter space will give rise to the *bifurcation set*.

What is of particular interest is that there are some kinds of bifurcations which appear repeatedly in many problems. It would be interesting to have a classification of bifurcations which produces a specific list of possibilities for each example, starting with only general considerations such as the number of parameters in the problem,

the dimension of the phase space, and any symmetries or other special properties of the system. The classification schemes are based upon concepts of differential topology. The *codimension* of a bifurcation is the smallest dimension of a parameter space which contains the bifurcation, and an *unfolding* of a bifurcation is a set of equations which contains the bifurcation in a persistent way.

The *center manifold theorem* provides a mean for systematically reducing the dimension of the state space which needs to be considered when analysing bifurcations of a given type. This theorem states that it is possible to define manifolds tangent to the eigenspaces associated to the eigenvalues of a flow. The center manifold is defined as a manifold tangent to the center eigenspace. The local dynamical behaviour transverse to the center manifold is relatively simple, since it is controlled by the exponentially contracting (and expanding) flows in the local stable (and unstable) manifolds. Then, the center manifold method isolates the complicated asymptotic behaviour by locating an invariant manifold tangent to the subspace spanned by the (generalized) eigenspace of eigenvalues on the imaginary axis.

Once the center manifold theorem has been applied to a system, it is useful to find additional coordinate transformations which simplify the analytical expression of the vector field on the center manifold. The resulting simplified vector fields are called *normal forms*. The dynamics close to a bifurcation typically look like the one represented by its normal form. Moreover, the analysis of the dynamics of the normal forms yields a qualitative picture of the flows of each bifurcation type.

In real physical systems, the explosive instabilities that can appear when analysing the normal forms are compensated by the stabilization influence of higher–order terms.

In the following we will describe some of the bifurcations that will appear in later chapters.

The *saddle–node* bifurcation is the basic mechanism by which fixed points are created or destroyed. As a parameter is varied, two fixed points move toward each other, collide, and mutually annihilate. The prototypical example of a saddle–node bifurcation is the first–order system (normal form)

$$\dot{x} = -r - x^2,$$

where r is a real parameter. In figure 3.1 one can observe a representation of this bifurcation. When $r < 0$, there are two fixed points, one stable and one unstable. When $r = 0$ (bifurcation point), the fixed points coalesce into a half–stable fixed point at $x^* = 0$. For $r > 0$, there are no fixed points at all.

In a *transcritical* bifurcation, with normal form

$$\dot{x} = rx - x^2,$$

the two fixed points switch their stability at the bifurcation point $r = 0$, see Fig. 3.2.

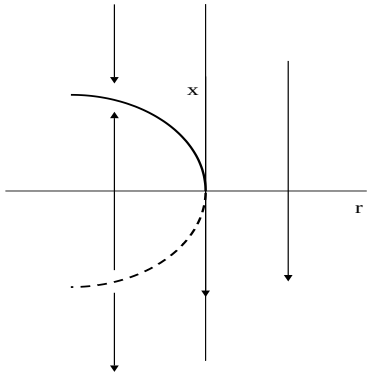

Figure 3.1: Saddle–node bifurcation.

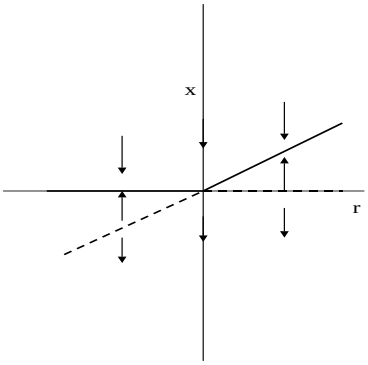

Figure 3.2: Transcritical bifurcation.

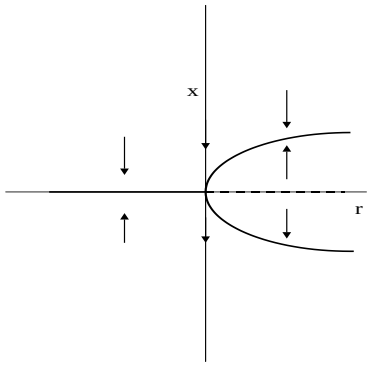

Figure 3.3: Pitchfork bifurcation (supercritical).

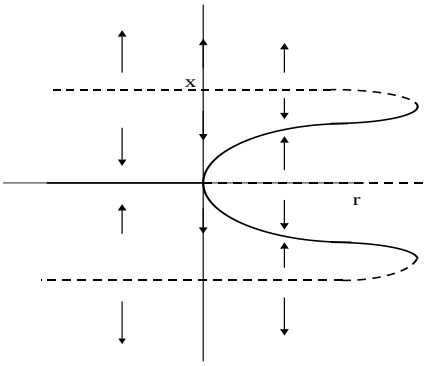

Figure 3.4: Pitchfork bifurcation (supercritical), including a high order term.

The normal form of a *supercritical pitchfork* bifurcation is

$$\dot{x} = rx - x^3.$$

For $r < 0$ the origin is the only fixed point, and it is stable while for $r > 0$, two new stable fixed points appear symmetrically located $x^* = \pm\sqrt{r}$ and the origin becomes unstable, see Fig. 3.3. A more completed form of the supercritical pitchfork bifurcation includes a higher order term

$$\dot{x} = rx - x^3 + x^5,$$

and its representation is the one appearing in Fig. 3.4.

In a *subcritical pitchfork* bifurcation, with normal form

$$\dot{x} = rx + x^3,$$

the nonzero fixed points $x^* = \pm\sqrt{-r}$ are unstable, and exist only below the bifurcation ($r < 0$). The origin is stable for $r < 0$ and unstable for $r > 0$, see Fig. 3.5.

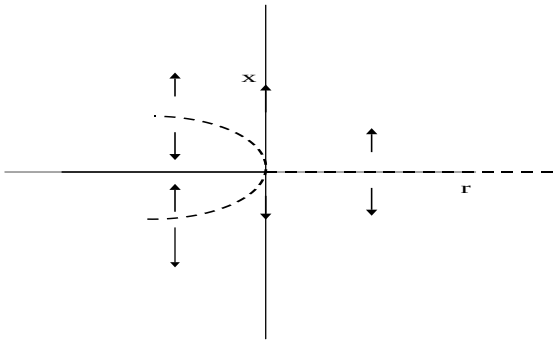

Figure 3.5: Pitchfork bifurcation (subcritical).

Apart from the fixed points, there can appear other invariant sets in the dynamical system. A *limit cycle* is an isolated closed trajectory: neighbouring trajectories are not closed, they spiral toward or away from the limit cycle. If all neighbouring trajectories approach to the limit cycle, the limit cycle is stable or attracting. Otherwise, the limit cycle is unstable, or in exceptional cases, saddle.

In a *Hopf* bifurcation, see Fig. 3.6, a stable (unstable) fixed point changes its stability and an stable (unstable) limit cycle appears or disappears. The normal form is

$$\begin{aligned} \dot{x} &= \mu x - y - (x^2 + y^2)x, \\ \dot{y} &= x + \mu y - (x^2 + y^2)y. \end{aligned}$$

At the bifurcation point, there exist a pair of purely imaginary eigenvalues.

There exist other ways in which limit cycles are created or destroyed. They are harder to detect because they involve large regions of the phase plane than just the neighbourhood of a single fixed point. Hence they are called *global bifurcations*. For each of the bifurcations, there are characteristic *scaling laws* that govern the amplitude and period of the limit cycle as the bifurcation is approached.

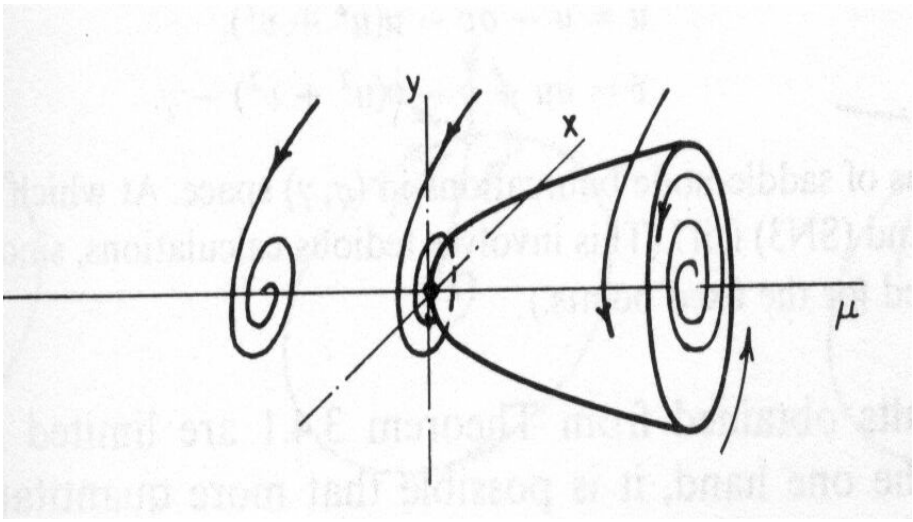

Figure 3.6: Hopf bifurcation.

A bifurcation in which two limit cycles coalesce and annihilate is called a *saddle–node bifurcation of cycles*.

In a *infinite–period bifurcation* (also called Andronov–Leontovich bifurcation), the oscillation period of a limit cycle lengthens and finally becomes infinity, when a fixed point appears on the cycle, at the bifurcation point. Varying the bifurcation parameter, μ, the fixed point splits into a saddle and a node. As the bifurcation is approached, the amplitude of the oscillation stays $O(1)$ but the period of the cycle increases like $O(\mu^{-1/2})$.

The *homoclinic bifurcation* is a kind of infinite–period bifurcation. In this scenario, part of a limit cycle moves closer and closer to a saddle point. At the bifurcation the cycle touches the saddle point and becomes a homoclinic orbit.

Apart from the local codimension–one bifurcation of flows (as saddle–node, pitchfork, transcritical and Hopf bifurcations), it is possible to obtain local codimension–two bifurcations. These will be found in the bifurcation set as intersection of two codimension–one bifurcations.

One of the typical examples of codimension–2 bifurcations is the case in which a pure imaginary pair and a simple zero eigenvalue appear. This is the basis of the analysis of chapter 8, where it is refereed as Hopf–saddle–node bifurcation. The normal form in the reduced planar system is

$$\begin{aligned} \dot{x} &= \mu_1 x + a\, x\, y, \\ \dot{y} &= \mu_2 + b\, x^2 - y^2. \end{aligned} \tag{3.1}$$

The fixed points of the system are given in terms of μ_1, μ_2, a and b. However, the qualitative features (the stability of the invariant sets in different regions) will be different depending on the sign of a and b. Consequently, four types of this bifurcation can be encountered. For a more detailed study of the different types,

the reader can reference to [Guckenheimer and Holmes, 1983] where the parameter region (μ_1, μ_2) is detailed for each part. From that book we have extracted Figs. 3.7 - 3.10, were the bifurcation set and the phase portraits for each case are shown.

An important two–dimensional phase space is the *torus* (this appears when a periodic orbit suffers a Hopf bifurcation changing its stability). We will illustrate some general features of flows on the torus. One could imagine a single point tracing out a trajectory on a torus with coordinates θ_1, θ_2. There are two different cases. The trajectories are closed orbits on the torus, because θ_1 completes p revolutions in the same time than θ_2 completes q revolutions. The resulting curves are called $p : q$ knots (resonances in chapter 8). The second possibility is that every trajectory winds around endlessly on the torus, never intersecting itself and yet never quite close. Each trajectory is dense in the torus and in this case the flow is said to be *quasiperiodic*.

Poincaré maps are useful for studying swirling flows, such as the flow near a periodic orbit. We consider a n–dimensional system $\dot{\mathbf{x}} = \mathbf{f}(\mathbf{x})$ and let S_n be a $n-1$–dimensional surface transverse to the flow. The Poincaré map P is a mapping from S_n to itself, obtained by following trajectories from one intersection with S_n to the next. If $\mathbf{x_k} \in \mathbf{S_n}$ denotes the k intersection, the Poincaré map is $\mathbf{x_{k+1}} = \mathbf{P}(\mathbf{x_k})$. In supposing a fixed point of P, $\mathbf{x}^*$, a trajectory starting at $\mathbf{x}^*$ returns to $\mathbf{x}^*$ after some time T, and it is therefore a closed orbit for the original system. Moreover, by looking at the behaviour of P near this fixed point, we can determine the stability of the closed orbit. The desired stability criterion is expressed in terms of the eigenvalues λ_j of the linearized Poincaré map: The closed orbit will be linearly stable if and only if $|\lambda_j| < 1$ for all $j = 1, \ldots, n-1$. Conversely, if $|\lambda_j| > 1$ for some j, perturbations along the j direction grow and $\mathbf{x}^*$ is unstable. A borderline case occurs when the largest eigenvalue has magnitude $|\lambda_j| = 1$; this occurs at bifurcations of periodic orbits, and a nonlinear stability analysis is required. The λ_j are called the *characteristic* or *Floquet* multipliers of the periodic orbit and they can only be found by numerical integration.

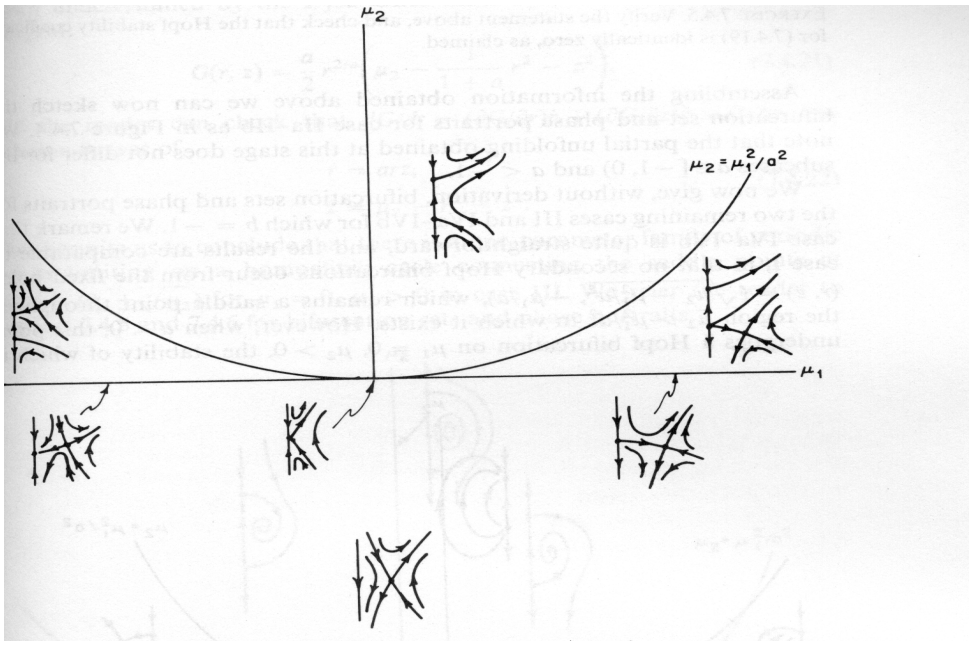

Figure 3.7: Bifurcation set and phase portraits for the unfolding case of a Hopf–saddle–node bifurcation for the type *I* case: $b = +1$, $a > 0$.

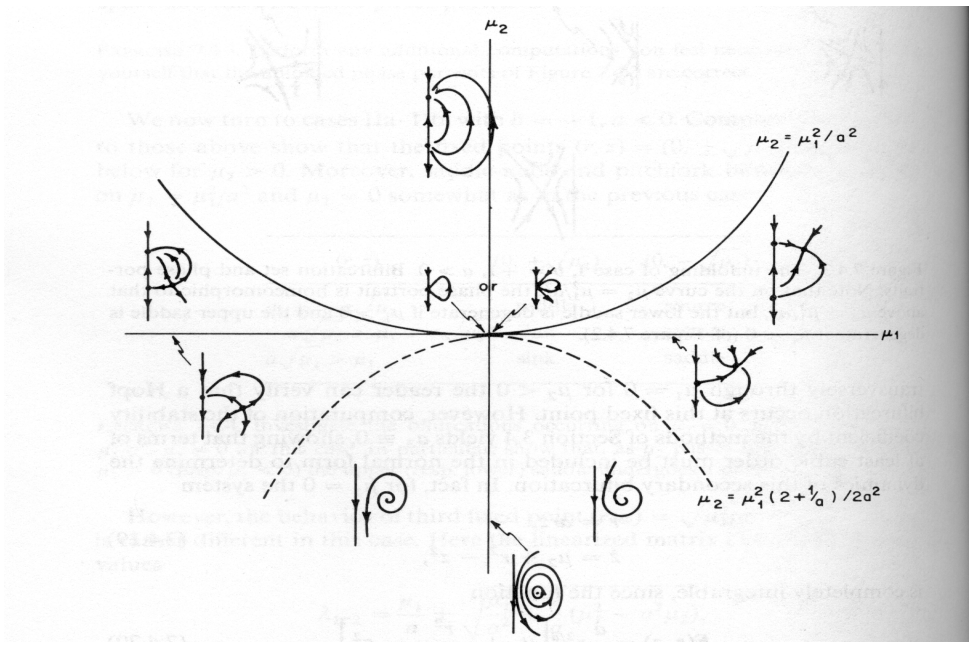

Figure 3.8: Bifurcation set and phase portraits for the unfolding case of a Hopf–saddle–node bifurcation for the type *II* case: $b = +1$, $a < 0$.

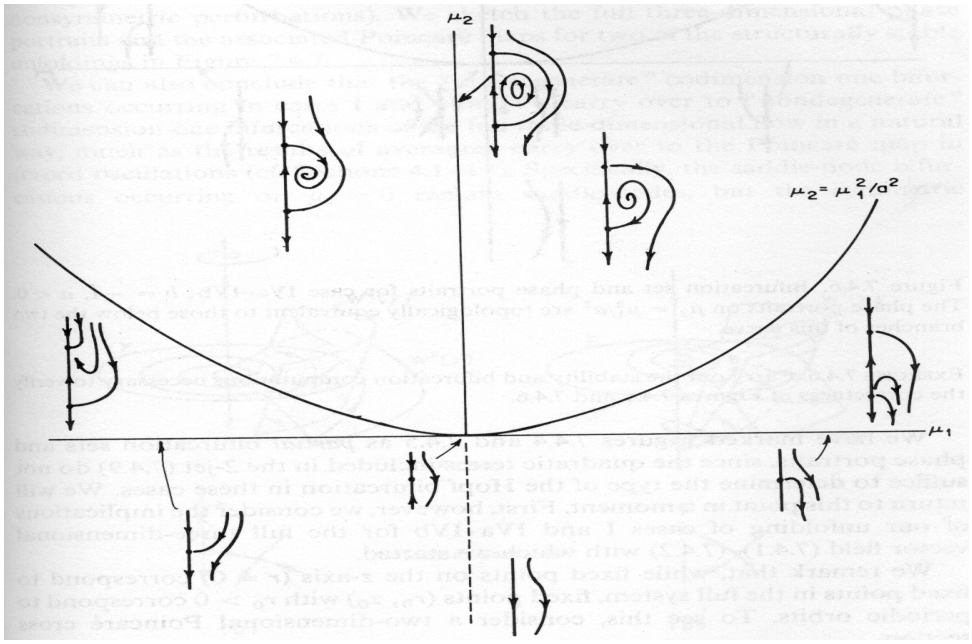

Figure 3.9: Bifurcation set and phase portraits for the unfolding case of a Hopf–saddle–node bifurcation for the type *III* case: $b = -1$, $a > 0$.

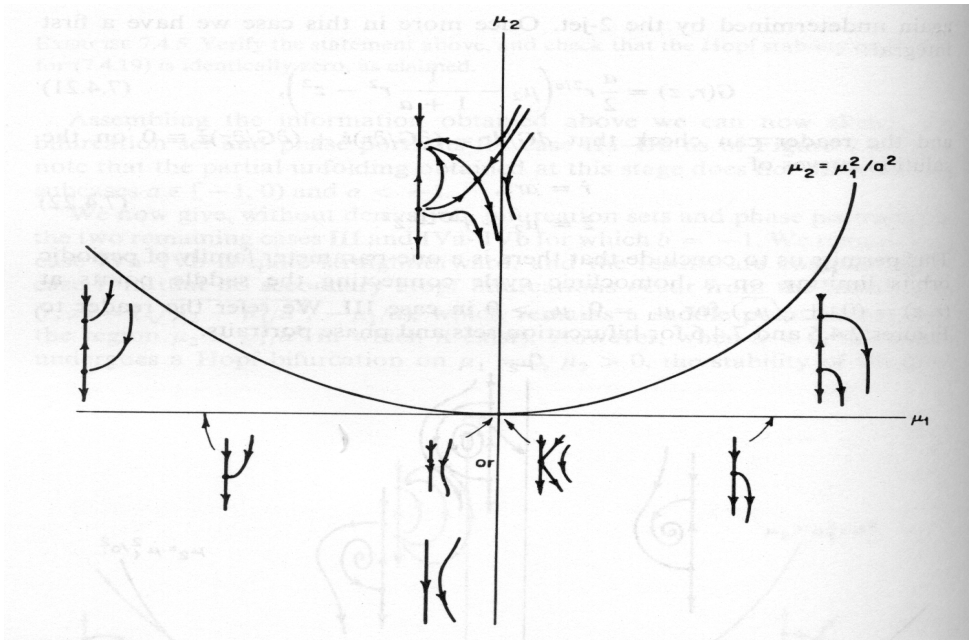

Figure 3.10: Bifurcation set and phase portraits for the unfolding case of a Hopf–saddle–node bifurcation for the type *IV* case: $b = -1$, $a < 0$.

Capítol 4

Làsers: Fenòmens físics i models

En aquest capítol es presenta un breu resum dels fenòmens físics involucrats en els sistemes làser, així com els models que s'utilitzen per descriure el seu comportament.

En un sistema làser una ona electromagnètica interacciona amb el material, i hi poden ocórrer tres processos: emissió espontània, emissió estimulada i absorció. En condicions normals el material es comporta com un absorbent. En condicions de no–equilibri (la població d'un nivell d'energia és major que la població d'un nivell amb energia més baixa), el material actua com un amplificador i la situació és d'*inversió de població*. Un *material actiu* és aquell amb inversió de població.

Per poder convertir l'amplificador en un làser cal a més un terme de realimentació. Aquest efecte es pot obtenir col·locant el material actiu entre dos miralls altament reflectants, de manera que l'ona electromagnètica sigui amplificada a cada viatge dins el material actiu. Per poder haver–hi amplificació es necessita que es verifiqui un cert llindar: l'oscil·lació (inicialitzada pels fotons emesos espontàniament) comença quan el guany del material actiu compensa les pèrdues dins el làser. Per extraure un feix útil del sistema làser es fa un dels dos miralls parcialment transparent.

Així que els tres elements bàsics en un làser són: a) un medi de guany capaç d'amplificar la radiació electromagnètica que es propaga dins la cavitat, b) una cavitat òptica que proporciona la realimentació necessària, i c) un mecanisme de bombeig. Les propietats que caracteritzen els làsers (alta monocromaticitat, coherència temporal i espacial, direccionalitat, ...) han fet que els làsers tinguin un gran ventall d'aplicacions.

La modelització dels sistemes làsers inclou el tractament de processos d'alta complexitat. Una descripció completa de la seva dinàmica es basa en una descripció mecànico–quàntica de la interacció radiació–matèria dins la cavitat làser. No obstant, normalment es fa una descripció en termes de la teoria semiclàssica. Aquesta teoria ignora la naturalesa mecànico–quàntica del camp electromagnètic (perquè el nombre de fotons dins un sistema làser és molt més gran que un) utilitzant les equacions de Maxwell, mentre que el medi amplificador sí que es modela quànticament com una col·lecció d'àtoms de dos nivells a través de les equacions

de Bloch. Les equacions resultants són les de Maxwell–Bloch (4.5 - 4.7), que descriuen les variacions temporals de les variables involucrades en el procés: amplitud complexa lentament variable del camp elèctric que es propaga dins la cavitat, polarització material i inversió de població.

Els làsers es poden classificar segons el ritme de decaïment de les tres variables del sistema. Els làsers de classe C tenen els ritmes de decaïment dels fotons, portadors i polarització material del mateix ordre, i es requereix el conjunt complet de les equacions de Maxwell–Bloch per a la seva descripció. En els làsers de classe B, la polarització material decau cap a l'estacionari molt més ràpidament que les altres dues variables, i es pot realitzar una eliminació adiabàtica d'aquesta variable. D'aquesta manera, els làsers de classe B es descriuen mitjançant dues equacions de balanç, una per a la inversió de població (o nombre de portadors) i una altra per al camp elèctric. Dels distints làsers de classe B existents, es restringeix l'estudi als làsers de semiconductor, on les transicions es produeixen entre bandes d'electrons i forats en comptes d'entre nivells d'energia atòmics o moleculars. Per finalitzar, en els làsers de classe A, tant la inversió de població com la polarització material decauen a l'estacionari molt més ràpidament que el camp elèctric, es pot fer una eliminació adiabàtica d'ambdues variables i, és suficient amb l'equació pel camp elèctric per descriure l'evolució d'aquests làsers.

Una descripció més senzilla de les equacions de Maxwell–Bloch es pot fer promitjant en la direcció de propagació i considerant emissió en un únic mode. Les equacions resultants són les equacions de balanç, que en el cas dels làsers de classe B són les equacions (4.8, 4.9). A l'equació per a la variació de l'amplitud lentament variable del camp elèctric hi ha una competició entre els termes de guany i de pèrdues; a més, s'introdueix el factor d'increment d'amplada de línia o terme de disintonia (α) que considera que en els làsers de semiconductor les transicions ocorren entre bandes d'energia i per tant l'espectre de guany és antisimètric. L'equació per al nombre de portadors consta de tres termes: el bombeig extern, el terme de pèrdues degut a emissió espontània o transicions no radiatives, i el terme d'emissió espontània. L'efecte de l'emissió espontània com una font radiativa es pot incloure en les equacions de balanç amb la inclusió de termes de renou blanc (4.11, 4.12). Quan les equacions s'escriuen en termes de les variables intensitat i fase del camp elèctric (4.14 - 4.16), a l'equació per la intensitat apareix (en la interpretació de Itô) un terme de renou d'emissió espontània promig. El terme de disintonia només apareix en l'equació per la fase del camp elèctric. A partir d'aquestes equacions es poden obtenir les equacions per als làsers de classe A realitzant una eliminació adiabàtica dels portadors.

Els capítols de la part II són dedicats a l'estudi dels làsers de classe A, mentre que els làsers de classe B es tracten al llarg de la part III de la memòria.

Chapter 4

Lasers: Physical phenomena and models

In this chapter we present a brief review of lasers, the physical phenomena involved in these systems and some models used to describe their behaviour. There exist in the literature a huge amount of papers and books related to this subject. Some references that we follow in this section are [Svelto, 1982; Hecht and Zajac, 1986; Petermann, 1988; Homar, 1996].

Laser[1] is the acronym of light amplification by stimulated emission of radiation accounting for the basic mechanism by which a laser works.

Some pioneer works by Einstein in 1917 already described the stimulated emission process. However, it was not until 1954 when Town succeded with the first experiment with the maser (microwave amplification by stimulated emission of radiation). In 1958, Schawlow and Townes predict theoretically the existence of laser systems and in 1960, Theodore H. Maiman announced the first operation of a laser, namely a ruby laser. Since then, a lot of different lasers have been studied, both experimentally and theoretically.

4.1 Physical phenomena in lasers

In a laser system an electromagnetic wave interacts with a material and three processes can occur: a photon can be absorbed by the material or it can be emitted either spontaneously or by stimulated emission. The simplest way to sketch this situation is as follows.

Consider a material whose atoms (or molecules) have two energy levels, 1 and 2, with energies E_1 and E_2 ($E_2 > E_1$). An atom (or molecule) of the given material which is initially in level 2 tends to decay *spontaneously* to level 1 emitting a photon of frequency ν (Planck's law)

$$\nu = \frac{E_2 - E_1}{h}, \tag{4.1}$$

[1] Laser was also a plant with miraculous properties which grew wild over a large area around Cyrene (in present-day Libya) [Svelto, 1982].

where h is the Planck's constant. In this process, the photon is emitted in any direction and with no definite phase relation with that emitted by another atom (or molecule). However, it may happen that an atom initially in level 2 decays to the level 1 forced by an incoming photon. This phenomenon is the basis of the laser operation and it is called *stimulated emission*. Since the process is forced by the incident photon, the emitted photon adds in phase to the incoming one and in the same direction. Finally, an atom in level 1 can undergo a transition from this energy level to level 2 by *absorbing* an incident photon.

Once the basic concepts have been given, we can use them to explain the mechanisms for the operation of a laser. Let us consider two energy levels as above and let N_1 and N_2 be their respective populations. If a plane wave is travelling along the material, the three processes explained before (spontaneous emission, stimulated emission and absorption) can be present. Considering only stimulated emission and absorption processes, the material behaves as an amplifier if $N_2 > N_1$ and it behaves as an absorber if $N_2 < N_1$. Under ordinary conditions the material behaves as an absorber [e.g., in the case of thermal equilibrium for which $N_2/N_1 = \exp\left(-\frac{(E_2-E_1)}{k_B T}\right)$]. If a nonequilibrium condition is reached for which $N_2 > N_1$, the material will act as an amplifier and *population inversion* can be achieved. An *active material* is a material with population inversion.

To turn an amplifier into a laser, a suitable positive feedback has to be introduced. In a laser, the feedback is obtained by placing the active material between two highly reflecting mirrors (e.g., plane–parallel mirrors), such that an electromagnetic wave traveling in a direction orthogonal to the mirrors bounces back and forth between the two mirrors and is amplified on each passage through the active material. By making one of the two mirrors partially transparent, an useful output beam can be extracted. A certain threshold condition must be satisfied: the oscillation (built up from the spontaneous emission) starts when the gain of the active material compensates the losses in the laser. The photons spontaneously emitted along the cavity axis initiate the amplification process.

Summarizing, a laser has three basic ingredients: i) a gain medium capable of amplifying the electromagnetic radiation propagating inside the cavity (typically gas, liquid, solid state or semiconductor materials), ii) an optical cavity that provides the necessary feedback (Fabry–Perot or ring cavities, distributed feedback structures or distributed Bragg reflectors), and iii) a pumping mechanism (electrical discharge, current injection or optical pump). Laser radiation has very useful properties: a high degree of monochromaticity, temporal and spatial coherence, directionality, brightness and it can be produced (using different systems) in a broad range of wavelengths. Likewise, there is a large variety of laser applications. Since its discovery, lasers have been used in metrology, industrial and medical applications, trapping and cooling of atoms, detection of gravitational waves, cutting materials, optical communications, CD players and recorders, printers, etc.

4.2 Modelling lasers

A complete understanding of laser dynamics is based on a fully quantum-mechanical description of matter–radiation interaction within the laser cavity. However, the laser is a system where the number of photons is much larger than one, thus allowing a semiclassical treatment of the electromagnetic field inside the cavity through the Maxwell equations. This fact was introduced in the semiclassical laser theory, developed by Lamb [Lamb, 1964; Sargent *et al.*, 1974] and independently by Haken [Haken and Sauermann, 1963; Haken, 1983; Haken, 1984; Haken, 1985]. The model for the laser dynamics was constructed from the Maxwell–Bloch equations for a single–mode field interacting with a two–level medium. The semiclassical laser theory ignores the quantum–mechanical nature of the electromagnetic field, while the amplifying medium is modelled quantum–mechanically as a collection of two–level atoms through the Bloch equations. The evolution of the wave electric field $\vec{\mathcal{E}}(\vec{x},t)$ can be obtained from the wave equation of the electromagnetic theory

$$\triangle\vec{\mathcal{E}} - \frac{1}{c^2}\ddot{\vec{\mathcal{E}}} - \mu_0\sigma_0\dot{\vec{\mathcal{E}}} = \mu_0\ddot{\vec{\mathcal{P}}} \tag{4.2}$$

where $\triangle$ represents the Laplace operation, c is the velocity of light in vacuum, μ_0 is the vacuum magnetic permeability, σ_0 is the electric conductivity of the medium, and $\vec{\mathcal{P}}(\vec{x},t)$ is the electric polarization of the medium. By assuming a plane–wave structure, $\vec{\mathcal{E}}(\vec{x},t)$ and $\vec{\mathcal{P}}(\vec{x},t)$ can be expressed as

$$\vec{\mathcal{E}}(\vec{x},t) = \frac{1}{2}\left[\vec{e}E(t)e^{i(kz-\Omega_0 t)} + c.c.\right], \tag{4.3}$$

$$\vec{\mathcal{P}}(\vec{x},t) = \frac{1}{2}\left[\vec{e}'P(t)e^{i(kz-\Omega_0 t)} + c.c.\right], \tag{4.4}$$

where k is the resonator wave vector (it has been taken in the z–direction), $\vec{e}$ and $\vec{e}'$ are unit vectors and Ω_0 is the laser frequency.

By using these definitions, the Maxwell–Bloch equations, after appropriate rescaling, are

$$\partial_t E + \frac{c}{\eta_g}\partial_z E = -\frac{\gamma}{2}E + \frac{P}{2}, \tag{4.5}$$

$$\partial_t P = -\gamma_p(1 - i\,\alpha)\,P + \gamma_p\,g_N\,(1+\alpha^2)\,(N - N_o)\,E, \tag{4.6}$$

$$\partial_t N = C - \gamma_N\,N - \frac{1}{2}\,(E\,P^* + E^*\,P). \tag{4.7}$$

E is the slowly–varying complex amplitude of the electric field propagating in the z direction, P is the slowly–varying complex amplitude of the material polarization and N gives the population inversion.

Eq. (4.5) is obtained from the Maxwell's equations by considering an isotropic non–magnetic dielectric medium and a single transversal electrically polarized mode at a given frequency. The other equations are the matter equations that are developed from quantum mechanics. It is assumed two energy levels for the atoms that

participate in the interaction with the laser field. The parameters appearing in the equations are: η_g is the group refractive index of the mode such that c/η_g is the group velocity; γ is the inverse of the photon lifetime or cavity decay rate and it accounts for internal and mirror losses. In (4.6) γ_p is the polarization decay rate, and it accounts for the collision with other atoms or the interaction with lattice vibrations; α is the normalized detuning, which takes into account the difference between the frequency of the transition of the two energy levels and the cavity resonant frequency; g_N is the differential gain at the lasing frequency (in the simplest approximation, g_N is considered to be constant, but a more realistic model includes gain saturation through a nonlinear dependence on the modulus of the electric field, as will be considered later); N_o is the population inversion at transparency (value of the population inversion at which the material is transparent to radiation).

In (4.7), C is the rate at which the carriers, electrons and holes are injected into the active layer due to the external pumping. The second term of this equation, stands for carrier losses due to spontaneous emission or non–radiative transitions. In this work, γ_N (population relaxation parameter due to spontaneous recombinations) is considered as a constant, although a more general form can be also considered [Olshansky *et al.*, 1984]. The third term accounts for the stimulated emission.

Different types of lasers can be classified according to the decay rate of the photons, carriers and material polarization. Arecchi et al. [Arecchi *et al.*, 1984; Tredicce *et al.*, 1985a] were the first to give a classification scheme: class C lasers have all the decay rates of the same order, and therefore the full set of three nonlinear differential equations is required for a satisfactory description of the electric field, the population inversion and the material polarization. For class B lasers, the polarization decays towards the steady state much faster than the other two variables, and it can be adiabatically eliminated. Class B lasers, of which semiconductor lasers [Agrawal and Dutta, 1986] are an example, are then described by two rate equations for the atomic population inversion (or carriers number) and the electric field. Other examples of class B lasers are CO_2 lasers and solid state lasers [Weiss and Vilaseca, 1991]. From now on, when studying class B lasers, we will restrict ourselves to semiconductor lasers. The main characteristic of these lasers is that the transitions occur between electron and hole bands instead of atomic or molecular energy levels [Agrawal and Dutta, 1986; Petermann, 1988; Wilson and Hawkes, 1989; Saleh and Teich, 1991]. Finally, in class A lasers population inversion and material polarization decay much faster than the electric field. Both material variables can be adiabatically eliminated, and the equation for the electric field is enough to describe the dynamical evolution of the system. Some properties of class A lasers, like a dye laser, are studied in [Hernández-García *et al.*, 1990; Ciuchi *et al.*, 1991].

A description simpler than (4.5 - 4.7) can still be obtained when averaging over the z direction and considering single–mode emission (longitudinal, lateral and transversal mode emission). This simple set of equations is called *rate equations* [Statz and deMars, 1960; Tang *et al.*, 1963]. As already pointed out, in semicon-

ductor lasers, and after eliminating the polarization, one ends up with only two equations that describe the slowly varying amplitude of the electric E and the number of carriers N. By taking $\frac{dP}{dt} = 0$ in (4.6) and changing $E \rightarrow E \exp(i\alpha\gamma t/2)$, Eqs. (4.5) and (4.7) become

$$\dot{E} = \frac{(1 + i\,\alpha)}{2}\,[G - \gamma]\,E, \tag{4.8}$$

$$\dot{N} = \frac{J}{e} - \gamma_N\,N - G\,|E|^2, \tag{4.9}$$

where $G = G(N) = g_N\,(N - N_o)$, J accounts for the injection current, and e is the electronic charge ($e = 1.6 \times 10^{-19} C$).

In Eq. (4.8), there is a competition between the gain, G, and the losses, γ, terms. However, the previous expression for G is incomplete since it does not account for some effects as the spectral and spatial hole burning [Agrawal, 1987] or carrier heating [Kressel and Ippen, 1987]. A more general expression for G considering these factors yields [Agrawal and Dutta, 1986]

$$G = G(N, |E|^2) = g_N\,\frac{N - N_o}{1 + s|E|^2}, \tag{4.10}$$

where s is the saturation coefficient and g_N is a constant.

For semiconductor lasers, α is called the linewidth enhancement factor and is defined as the ratio between the derivatives of the real and imaginary parts of the carrier–dependent susceptibility with respect to the carrier density [Henry, 1982]. It considers the fact that, in semiconductor lasers, the lasing transitions occur between energy bands instead of energy levels, giving an asymmetry in the gain spectrum.

In Eqs. (4.8) and (4.9), the effect of spontaneous emission, as a source of radiation, has to be included. This can be treated quantum mechanically, via quantum Langevin equations, or via the density matrix equations. In previous works [Henry, 1982; Henry, 1983] the effect of spontaneous emission was incorporated in the rate equations in the form of noise terms and the resulting equations, interpreted in the Itô sense, are

$$\dot{E} = \frac{(1 + i\,\alpha)}{2}\,[G(N, |E|^2) - \gamma]\,E + \sqrt{2\,\varepsilon\,N}\,\xi_E(t), \tag{4.11}$$

$$\dot{N} = \frac{J}{e} - \gamma_N\,N - G(N, |E|^2)\,|E|^2 - \sqrt{2\,\varepsilon\,N}\,(E^*\,\xi_E(t) + E\,\xi_E^*(t)) + \sqrt{2\,\gamma_N\,N}\,\xi_N(t). \tag{4.12}$$

ε is the spontaneous emission rate. $\xi_E(t)$ is a complex Langevin noise term accounting for the stochastic nature of spontaneous emission and $\xi_N(t)$ describes random non–radiative carrier recombination due to thermal fluctuations. They are considered as Gaussian noise terms of zero mean and correlations

$$\langle \xi_i(t)\,\xi_j(t') \rangle = \delta_{ij}\,\delta(t - t'), \tag{4.13}$$

where ξ_i, ξ_j denote $Re(\xi_E)$, $Im(\xi_E)$ and ξ_N.

Equations (4.11) and (4.12) can be written in terms of the intensity and phase, $E = \sqrt{I}\,\exp(i\phi)$ such that

$$\dot{I} = [G(N,I) - \gamma]\, I + 4\varepsilon\, N + \sqrt{8\,\varepsilon\, N\, I}\,\xi_I(t), \tag{4.14}$$

$$\dot{\phi} = \frac{1}{2}\,\alpha\,[G(N,I) - \gamma] + \sqrt{\frac{2\,\varepsilon\, N}{I}}\,\xi_\phi(t), \tag{4.15}$$

$$\dot{N} = \frac{J}{e} - \gamma_N\, N - G(N,I)\, I - \sqrt{8\,\varepsilon\, N\, I}\,\xi_I(t) + \sqrt{2\gamma_N\, N}\,\xi_N(t), \tag{4.16}$$

where $\xi_I(t)$, $\xi_\phi(t)$ and $\xi_N(t)$ are real gaussian noise terms of zero mean and correlations

$$\langle \xi_i(t)\, \xi_j(t') \rangle = \delta_{ij}\, \delta(t - t'), \tag{4.17}$$

where i, j denote I, ϕ and N. $4\varepsilon N$ represents the mean power spontaneously emitted in the lasing mode.

The equations we have described are for semiconductor lasers (class B lasers). To obtain a set of equations for a class A laser, we can adiabatically eliminate N by setting $\dot{N} = 0$ in (4.9) and obtain N as a function of E. The resulting equation for the electric field after replacing in Eq. (4.8) is

$$\dot{E} = (1 + i\alpha) \left[\frac{g_N (J/e - \gamma_N N_o)/(2\gamma_N)}{1 + (\gamma_N s + g_N)|E|^2/\gamma_N} - \frac{\gamma}{2} \right] E. \tag{4.18}$$

We will devote the chapters of part II to the study of class A lasers. In part III we will study class B lasers.

Part II

Làsers de Classe A

Capítol 5

Làsers de Classe A: Potencial de Lyapunov

En aquest capítol es presenta un exemple d'utilització del potencial de Lyapunov (introduït en el capítol 2) en un sistema dinàmic. El sistema que es considera és el d'un làser de classe A (capítol 4).

La dinàmica del làser de classe A es descriu en termes de l'amplitud complexa lentament variable del camp elèctric, que es pot descompondre en les seves parts real i imaginària. Les equacions resultants són les (5.3) i (5.4), que es tracten en aquest capítol.

En primer lloc es considera el sistema determinista, menyspreant els termes de renou. El resultat de les simulacions es pot veure a les figures 5.1 i 5.2. Començant d'una condició inicial a prop de l'estat apagat, la intensitat es va atracant al seu estat estacionari, mentre que les parts real i imaginària del camp elèctric oscil·len en el temps fins també arribar a un valor constant. En el pla definit per les parts real i imaginària del camp, els sistema realitza una oscil·lació en forma d'espiral. El valor camp elèctric no depèn del paràmetre de disintonia (α), i l'única dependència amb el paràmetre α apareix en la velocitat angular (o equivalentment en la fase del camp elèctric).

Les equacions del làser de classe A constitueixen un flux potencial (5.10), on el paràmetre de disintonia no hi és inclòs. La matriu que relaciona les derivades del potencial amb les equacions de la dinàmica es designa com D, (5.11). Els punts fixos de la dinàmica determinista són els extrems del potencial. Per a un valor del guany fixat de manera que el làser estigui encès, la forma del potencial és del tipus *capell mexicà* (Fig. 5.5), té un màxim central i una corba de mínims que l'envolten. En la dinàmica transitòria, la part simètrica de D és la responsable de dur el sistema cap als mínims del potencial, seguint les línies de màxim pendent. La part antisimètrica (que és proporcional a α) indueix el moviment ortogonal a la direcció de variació màxima del potencial. Aquests dos efectes combinats (corresponents a les parts simètrica i antisimètrica del camp vectorial) produeixen la trajectòria espiral, abans esmentada, en el pla definit per les parts real i imaginària del camp elèctric, amb

una velocitat angular proporcional a α, Fig. 5.6. A partir del camp vectorial dels làsers de classe A, Figs. 5.7 i 5.9, es pot observar que la direcció de rotació (per a un α donat) és diferent entre la part interna i la part externa de les línies de potencial mínim.

La dinàmica de les equacions en presència de renou és tal que les característiques qualitatives de la dinàmica transitòria (a part de petites oscil·lacions degudes al renou) són les mateixes que el cas determinista. Ara bé, les diferències més importants apareixen a prop de la situació estacionària, a causa que l'estat final no té un valor constant per a la fase, sinó que la fase varia amb el temps, Figs. 5.10 i 5.11. En el cas de considerar les equacions amb renou és de gran utilitat considerar valors mitjos. El valor mig de la fase del camp elèctric varia, per a $\alpha \neq 0$, linealment amb el temps en l'estat estacionari, Fig. 5.13, efecte que anomenam *flux sostingut per renou*.

Aquestes característiques de la dinàmica amb renou es poden explicar mitjançant el potencial de Lyapunov, que s'havia obtingut per a la dinàmica determinista. La funció densitat de probabilitat estacionària ve donada a partir del potencial, Eq. (2.38), ja que la matriu D verifica les condicions corresponents. En termes de les variables intensitat i fase del camp elèctric, aquesta funció es pot escriure com a funcions independents de cadascuna de les variables. La funció densitat de probabilitat de la intensitat (5.17), té el seu màxim al valor mínim del potencial, que coincideix amb el valor estacionari de la dinàmica determinista (Fig. 5.14), i és asimètrica al voltant d'aquest màxim, Fig. 5.15. Amb aquesta funció densitat es poden calcular valors mitjos de les variables a l'estacionari. El valor mig de la intensitat a l'estacionari, que no depèn del paràmetre α, es pot calcular analíticament (5.19), el seu valor augmenta així com s'incrementa el valor del paràmetre de renou, Fig. 5.16.

El fet que la fase del camp elèctric fluctuï al voltant d'un valor mig que canvia linealment amb el temps també es pot explicar amb el potencial de Lyapunov. L'origen d'aquest flux sostingut per renou es pot entendre de la següent manera: els termes que indueixen rotació, els proporcionals a α, són zero a la línia de mínims de potencial, i per tant no actuaven a l'estat estacionari determinista. No obstant, les fluctuacions, que ara s'inclouen, permeten que el sistema explori regions de l'espai definit per les parts real i imaginària del camp elèctric on el potencial ja no té el seu valor mínim. La part antisimètrica de D (que conté el paràmetre α) és la responsable de la rotació a l'espai de fases. A causa que el valor mig de la intensitat és més gran que el valor determinístic de l'estat estacionari, el sistema passa més temps, en valor mig, en la part externa del mínim del potencial que en la part interna, i és per aquest motiu que hi ha una contribució distinta de zero al termes rotacionals produint la velocitat de fase observada. El valor mig de la velocitat de rotació es pot calcular a partir de la funció densitat de probabilitat (5.23). La rotació mitja és zero quan el terme de disintonia és zero o en el cas determinista; i a més, aquesta rotació té un sentit oposat al que es tenia en la dinàmica transitòria quan es partia de l'estat apagat. El canvi d'aquest valor mig de la freqüència amb el renou es veu en la figura 5.17.

Chapter 5

Class A Lasers: Lyapunov Potential

In this chapter, a first example of the use of Lyapunov potentials in a dynamical system is presented. The system we consider is a class A laser.

5.1 Model

For class A lasers, such as He-Ne laser, the dynamics of can be described in terms of the slowly varying complex amplitude E of the electric field [Haken, 1984], Eq. (4.18). The noise term is simply additive, as it is usually taken in this kind of lasers. The resulting equation is

$$\dot{E} = (1 + i\,\alpha)\left(\frac{\Gamma}{1 + \vartheta|E|^2} - \kappa\right) E + \zeta(t), \tag{5.1}$$

where α, ϑ, Γ and κ are real parameters. κ is the cavity decay rate; Γ the gain parameter; ϑ the saturation–intensity parameter, and α is the detuning parameter. Their relationship with the variables of class B lasers (4.8) and (4.9) are:

$$\Gamma = g_N\left(\frac{J}{e} - \gamma_N N_o\right)/(2\gamma_N), \quad \kappa = \gamma/2, \quad \vartheta = (g_N + s\gamma_N)/\gamma_N.$$

Another widely used model expands the nonlinear term to give a cubic dependence on the field (third order Lamb theory [Sargent *et al.*, 1974]), but this is not necessary here. Eq. (5.1) is written in a reference frame in which the frequency of the *on* steady state is zero (and the trivial solution has frequency $(\Gamma - \kappa)\alpha$ [Ciuchi *et al.*, 1991]). $\zeta(t)$ is a complex Langevin source term accounting for the stochastic nature of spontaneous emission. It is taken as a Gaussian white noise of zero mean and correlations

$$\langle \zeta(t)\,\zeta^*(t')\rangle = 4\,\Delta\,\delta(t - t'), \tag{5.2}$$

where Δ measures the strength of the noise.

By writing the complex variable E as $E = x_1 + i\,x_2$ and introducing a new dimensionless time such that $t \to \kappa\, t$, the evolution equations become

$$\dot{x}_1 = \left(\frac{a}{b + x_1^2 + x_2^2} - 1\right)\,(x_1 - \alpha\, x_2) + \xi_1(t), \tag{5.3}$$

$$\dot{x}_2 = \left(\frac{a}{b + x_1^2 + x_2^2} - 1\right)\,(\alpha\, x_1 + x_2) + \xi_2(t), \tag{5.4}$$

where $a = \Gamma/(\kappa\vartheta)$ and $b = 1/\vartheta$. $\xi_1(t)$ and $\xi_2(t)$ are white noise terms with zero mean and correlations given by equation (2.32) with $\epsilon = \Delta/\kappa$.

5.2 Class A lasers: Deterministic case

In this section, we consider the reduced equations for a class A laser in the absence of noise, i.e. in the case $\epsilon = 0$,

$$\dot{x}_1 = \left(\frac{a}{b + x_1^2 + x_2^2} - 1\right)\,(x_1 - \alpha\, x_2), \tag{5.5}$$

$$\dot{x}_2 = \left(\frac{a}{b + x_1^2 + x_2^2} - 1\right)\,(\alpha\, x_1 + x_2). \tag{5.6}$$

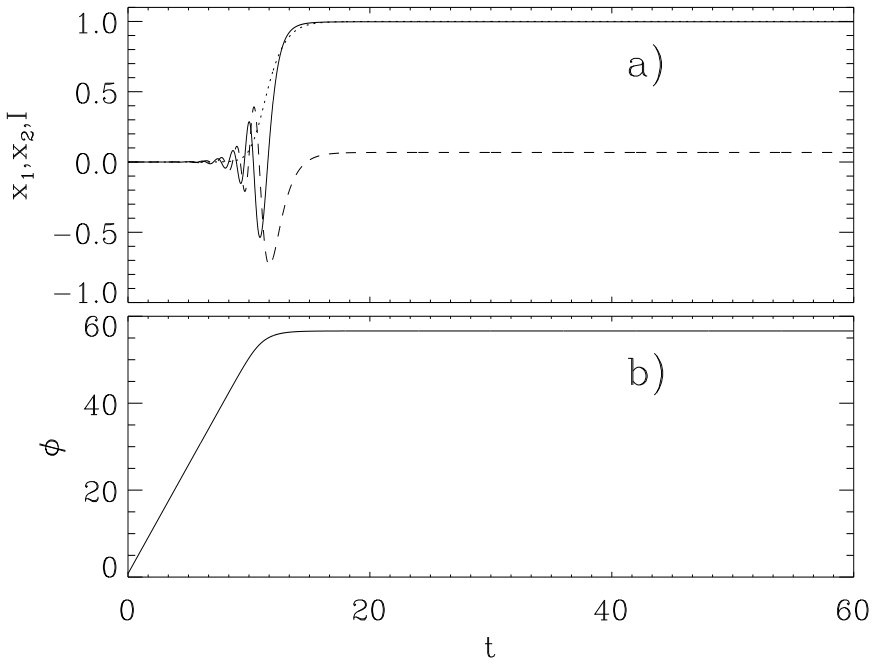

Figure 5.1: Simulation of Eqs. (5.5) and (5.6). (a) Dynamical evolution of x_1 (solid line), x_2 (dashed line) and $x_1^2 + x_2^2$ (dotted line) with time. (b) Phase evolution with time. Parameters: $a = 2$, $b = 1$, $\alpha = 5$. Initial conditions: $x_1 = 10^{-5}$, $x_2 = 10^{-5}$. Dimensionless units.

Performing the change of variables

$$I = x_1^2 + x_2^2 \quad \text{and} \quad \phi = \arctan\left(x_2/x_1\right), \tag{5.7}$$

one obtains a set of equations

$$\dot{I} = 2\left(\frac{a}{b+I} - 1\right) I, \tag{5.8}$$

$$\dot{\phi} = \left(\frac{a}{b+I} - 1\right) \alpha. \tag{5.9}$$

The steady state solutions of (5.8) and (5.9) give rise to two fixed points, one corresponding to the laser *off* ($I = 0$), and the other to the steady state of the system: $I_{st} = a - b$ and $\dot{\phi} = 0$ (fixed intensity and arbitrary phase).

Numerical simulations have been performed using a Runge–Kutta method (explained in chapter 2). When starting with an initial condition close to the *off* state, the intensity I monotonically approaches the steady state value I_{st} while the real and imaginary parts of the electric field (x_1 and x_2) oscillate in time until they reach a constant value, see Fig. 5.1 (a). In Fig. 5.1 (b), it can be seen that the continuous phase (defined between $-\infty$ and ∞) increases until it arrives to a constant value. Fig. 5.2 shows that the imaginary part versus the real part of the field spirals to the fixed point.

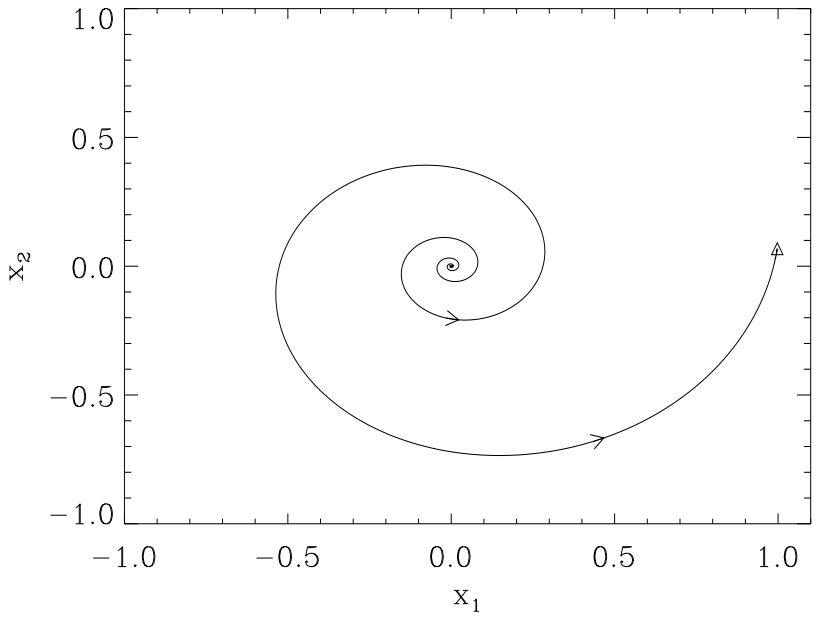

Figure 5.2: x_2 versus x_1 for Eqs. (5.5) and (5.6). Parameters: $a = 2$, $b = 1$, $\alpha = 5$. Initial conditions: $x_1 = 10^{-5}$, $x_2 = 10^{-5}$. Dimensionless units.

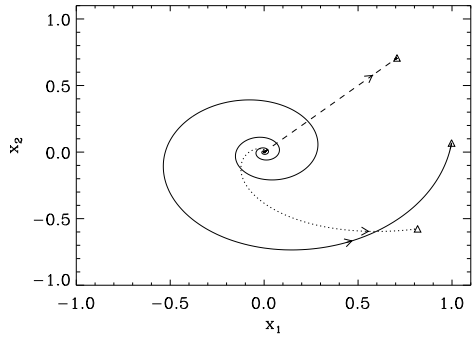

Figure 5.3: x_2 versus x_1 for Eqs. (5.5) and (5.6). Parameters: $a = 2$, $b = 1$. $\alpha = 5$ (solid line), $\alpha = 1$ (dotted line), $\alpha = 0$ (dashed line). Initial conditions: $x_1 = 10^{-5}$, $x_2 = 10^{-5}$. Dimensionless units.

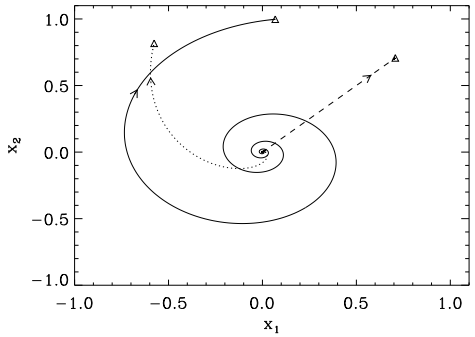

Figure 5.4: x_2 versus x_1 for Eqs. (5.5) and (5.6). Parameters: $a = 2$, $b = 1$. $\alpha = 0$ (dashed line), $\alpha = -1$ (dotted line), $\alpha = -5$ (solid line). Initial conditions: $x_1 = 10^{-5}$, $x_2 = 10^{-5}$. Dimensionless units.

It is worth noting that the final value I_{st} does not depend on α, and the only dependence on α appears in the angular velocity (or equivalently in the phase), as it is shown in Figs. 5.3 and 5.4. In these figures, it can be seen that when α increases the rotation speed increases in the (x_1, x_2) plane, and when the sign of α changes, the rotation sense inverts. Here we have used large values of the parameter α. With these values of α, the influence of this parameter in the dynamical equations can be clearly seen.

Equations (5.5) and (5.6) constitute a potential flow of the form (2.26) where the potential $V(\mathbf{x})$ is given by ([Haken, 1983])

$$V(x_1, x_2) = \frac{1}{2}\left[x_1^2 + x_2^2 - a\,\ln(b + x_1^2 + x_2^2)\right] \tag{5.10}$$

and the matrix $D(\mathbf{x})$ (split into symmetric and antisymmetric parts)

$$D = S + A = \begin{pmatrix} 1 & 0 \\ 0 & 1 \end{pmatrix} + \begin{pmatrix} 0 & -\alpha \\ \alpha & 0 \end{pmatrix}. \tag{5.11}$$

A simpler expression for the potential is given in [Risken, 1989] and [Haken, 1984] valid for the case in which the gain term is expanded in Taylor series.

When writing the potential in terms of I and ϕ, it appears to be independent of the phase (rotational symmetry in the plane (x_1, x_2)),

$$V(I, \phi) = \frac{1}{2}\left[I - a\,\ln(b + I)\right]. \tag{5.12}$$

By using this potential, one can obtain the fixed points of the set of equations and also the transient dynamics.

According to our discussion of chapter 2, the fixed points of the deterministic dynamics are the extrema of the potential $V(\mathbf{x})$: for $a > b$ there is a maximum at

$(x_1, x_2) = 0$ (corresponding to the laser in the *off* state) and a curve of minima given by $x_1^2 + x_2^2 = a - b$ (see Fig. 5.5). The asymptotic stable situation, then, is that the laser switches to the *on* state reaching an intensity $I \equiv |E|^2 = x_1^2 + x_2^2 = a - b$. For $a < b$ the only (stable) fixed point is the *off* state $I = 0$. In this case, the shape of the potential is not the one appearing in Fig. 5.5 but V is paraboloidal.

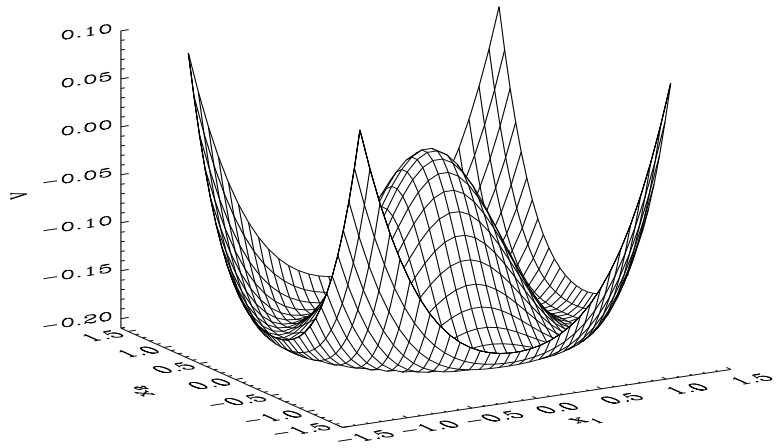

Figure 5.5: Potential for a class A laser, Eq. (5.10) with the parameters: $a = 2$, $b = 1$. Dimensionless units.

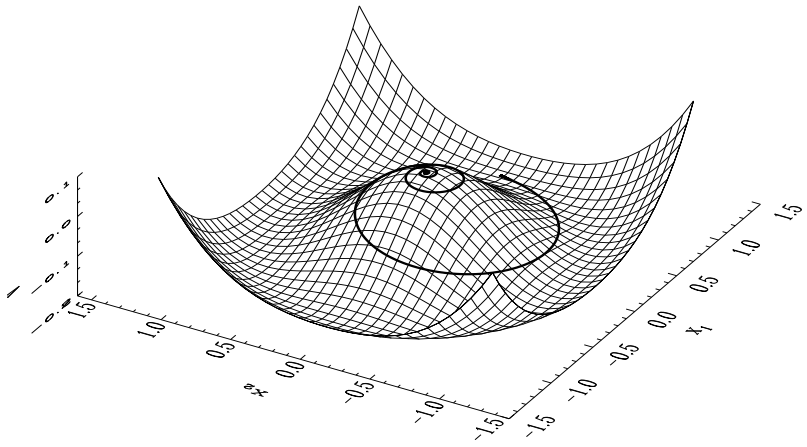

Figure 5.6: Potential for a class A laser, Eq. (5.10) with the parameters: $a = 2$, $b = 1$. Solid line: simulation of Eqs. (5.5) and (5.6) (same as in Figs. 5.1 and 5.2, $\alpha = 5$). Initial conditions: $x_1 = 10^{-5}$, $x_2 = 10^{-5}$. Dimensionless units.

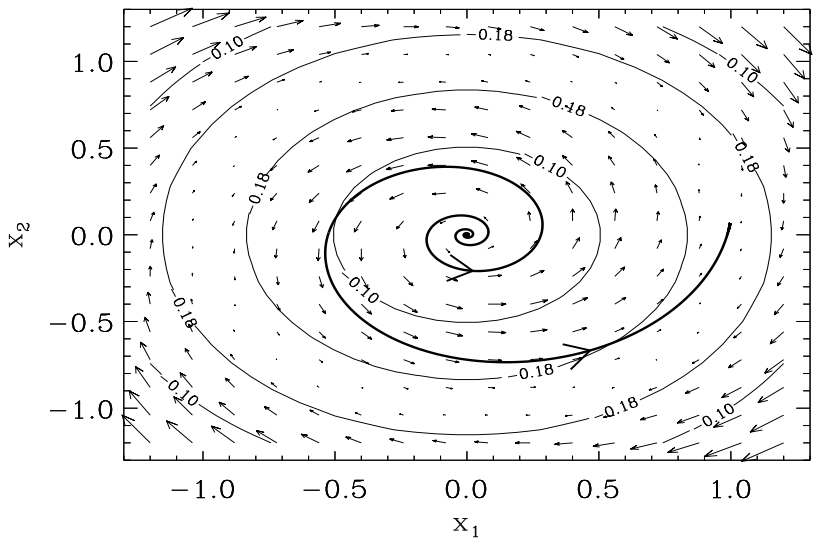

Figure 5.7: Vector field for a class A laser. Thick solid line: simulation of Eqs. (5.5) and (5.6). Thin lines are the equipotential curves of Eq. (5.10) and the arrows indicate the sense of the flow. Parameters: $a = 2$, $b = 1$, $\alpha = 5$. Initial conditions: $x_1 = 10^{-5}$, $x_2 = 10^{-5}$. Dimensionless units.

In the transient dynamics, the symmetric matrix S is responsible for driving the system towards the minima of V following the lines of maximum slope of V. The antisymmetric part A (which is proportional to α) induces a movement orthogonal to the direction of maximum variation of $V(\mathbf{x})$. The combined effects of S and A produce a spiraling trajectory in the (x_1, x_2) plane, with an angular velocity proportional to α, see Figs. 5.6 and 5.7.

Asymptotically, the system tends to one of the minima in the line $I = a - b$, the exact location depending on the initial conditions. The potential decreases in time until it arrives at its minimum value: $V(x_1^2 + x_2^2 = a - b) = \frac{1}{2}[a - b - a\ \ln(a)]$ (see Fig. 5.8).

The different rotation speeds and directions that one could observe in Figs. 5.3 and 5.4 can be explained with the antisymmetric part of the equations. This can be seen by comparing Figs. 5.7 and 5.9 where we have taken different signs of the value of α. In the case of $\alpha = 0$ the antisymmetric part is zero, and there is no rotation in the plane (x_1, x_2) (Fig. 5.12).

Another interesting feature that has to be mentioned here is that the direction of rotation for a given α is different for the internal part of the lines of minimal potential and the external part, see Figs. 5.7 and 5.9. This implies, for $\alpha > 0$, that the trajectories starting near the *off* state will rotate counterclockwise, while those starting with an intensity larger than the equilibrium value, $I > I_{st}$, will rotate clockwise. This difference in the direction of rotation will have an interesting effect in the presence of noise, as discussed in the next section.

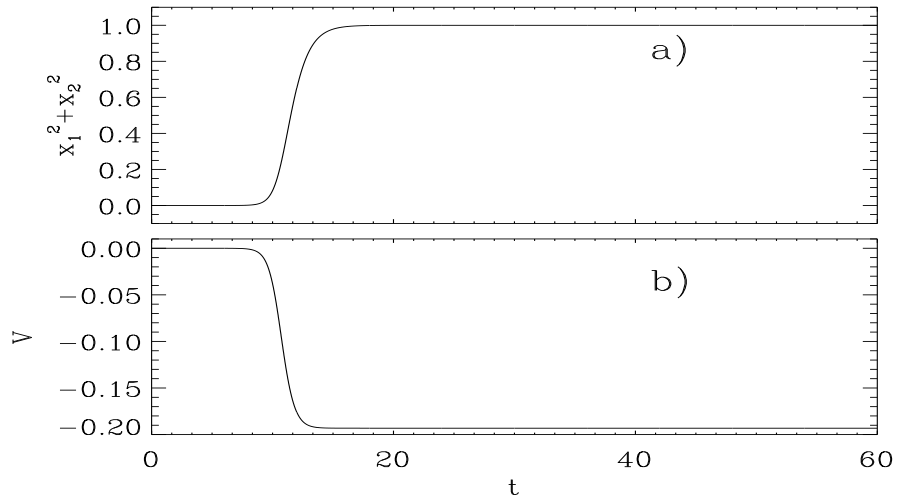

Figure 5.8: Simulation of Eqs. (5.5) and (5.6). (a) Dynamical evolution of the intensity $x_1^2 + x_2^2$ with time. (b) Evolution of the potential given by Eq. (5.10) with time. Parameters: $a = 2$, $b = 1$, $\alpha = 5$. Initial conditions: $x_1 = 10^{-5}$, $x_2 = 10^{-5}$. Dimensionless units.

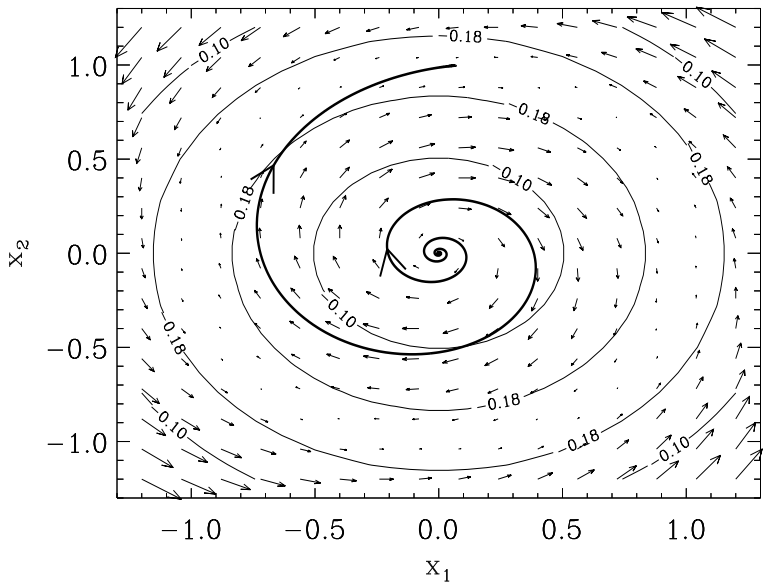

Figure 5.9: Vector field for a class A laser. Thick solid line: simulation of Eqs. (5.5) and (5.6). Thin lines are the equipotential curves of Eq. (5.10) and the arrows indicate the sense of the flow. Parameters: $a = 2$, $b = 1$, $\alpha = -5$. Initial conditions: $x_1 = 10^{-5}$, $x_2 = 10^{-5}$. Dimensionless units.

5.3 Class A lasers with noise

In this section, we consider the set of equations for class A laser in the presence of noise:

$$\dot{x}_1 = \left(\frac{a}{b + x_1^2 + x_2^2} - 1\right)(x_1 - \alpha\, x_2) + \xi_1(t), \tag{5.13}$$

$$\dot{x}_2 = \left(\frac{a}{b + x_1^2 + x_2^2} - 1\right)(\alpha\, x_1 + x_2) + \xi_2(t). \tag{5.14}$$

In the presence of moderate levels of noise, the qualitative features of the transient dynamics remain the same as in the deterministic case. The most important differences appear near the stationary situation.

We have performed simulations of Eqs. (5.13) and (5.14) using the Heun method (2.20) explained in chapter 2. In this case, one can take initial conditions in ($x_1 = 0, x_2 = 0$) and the small fluctuations, induced by noise terms, take the system away from the "off" state. The transient dynamics, see Fig. 5.10, is quite similar to that in the deterministic case (compare with Fig. 5.7). However, the final state does not have a constant phase but it changes in time. The direction in which the phase changes is not constant but varies in time, see Fig. 5.11.

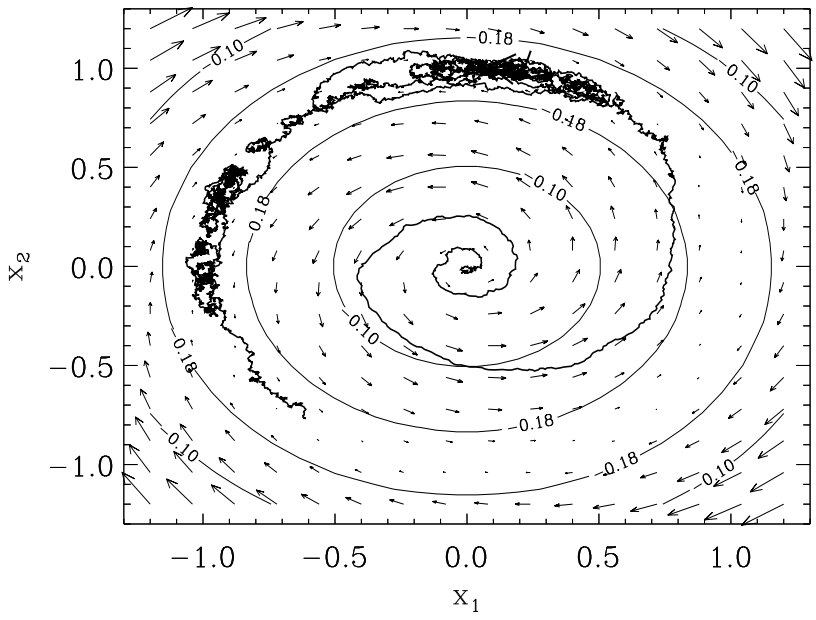

Figure 5.10: Vector field for a class A lasers. Thick solid line: simulation of Eqs. (5.13) and (5.14). Thin lines are the equipotential curves of Eq. (5.10) and the arrows indicate the sense of the flow. Parameters: $a = 2$, $b = 1$, $\alpha = 5$, $\epsilon = 0.001$. Initial conditions: $x_1 = 0$, $x_2 = 0$. Dimensionless units.

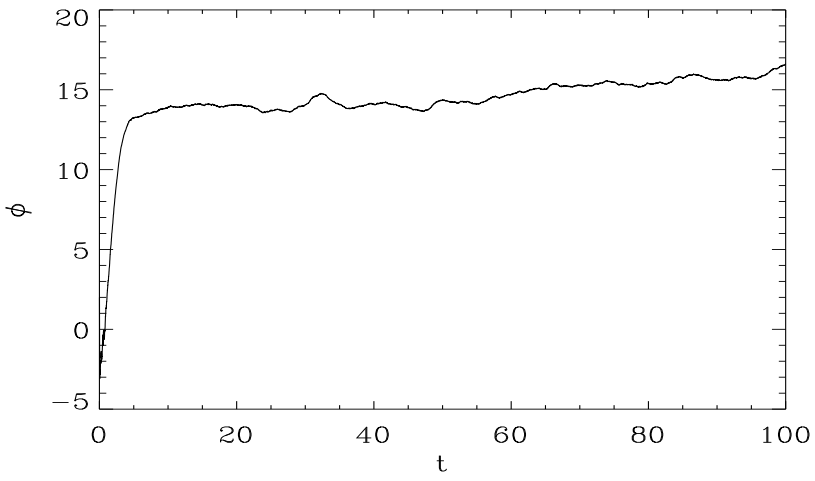

Figure 5.11: Phase evolution with time from the simulation of Eqs. (5.13) and (5.14). Parameters: $a = 2$, $b = 1$, $\alpha = 5$, $\epsilon = 0.001$. Initial conditions: $x_1 = 0$, $x_2 = 0$. Dimensionless units.

Therefore, for $\alpha \neq 0$ the real and imaginary parts of E oscillate not only in the transient dynamics but also in the steady state. The frequency of the oscillations still depends on α (as well as ϵ), while the amplitude of the oscillations depends on the noise strength ϵ.

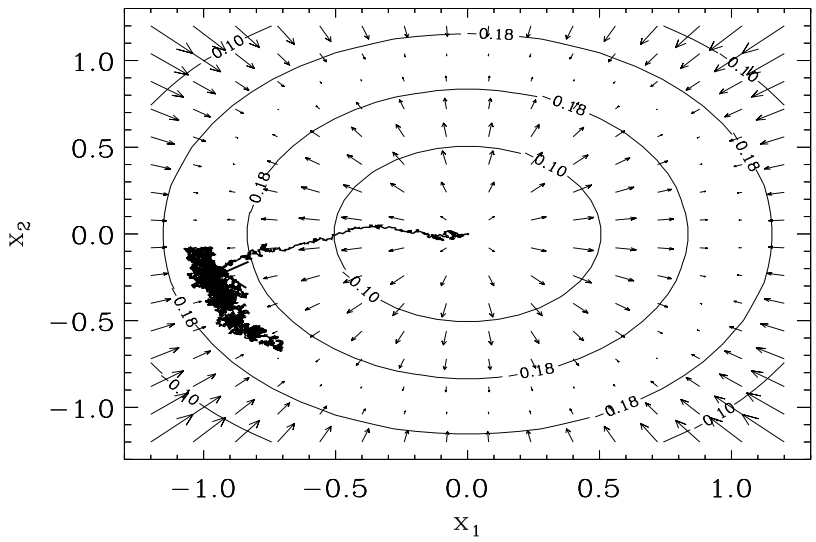

Figure 5.12: Vector field for a class A lasers. Thick solid line: simulation of Eqs. (5.13) and (5.14). Thin lines are the equipotential curves of Eq. (5.10) and the arrows indicate the sense of the flow. Parameters: $a = 2$, $b = 1$, $\alpha = 0$, $\epsilon = 0.001$. Initial conditions: $x_1 = 0$, $x_2 = 0$. Dimensionless units.

For $\alpha = 0$ there is only phase diffusion around the circumference $x_1^2 + x_2^2 = a - b$ that represents the set of all possible deterministic equilibrium states [Ciuchi *et al.*, 1991] (compare Figs. 5.10 and 5.12 which cover the same simulation time).

A small value of the parameter ϵ has been considered in these figures, allowing only a small deviation of the dynamical evolution in the plane (x_1, x_2) around the deterministic steady state (intensity is almost constant). When ϵ increases, the range of values available around the steady state also increases. As the final value of the intensity is approached, and for $\alpha \neq 0$, the phase rotation speed slows down and the mean value of the phase ϕ, of the electric field E, changes linearly with time also in the steady state, see Fig. 5.13.

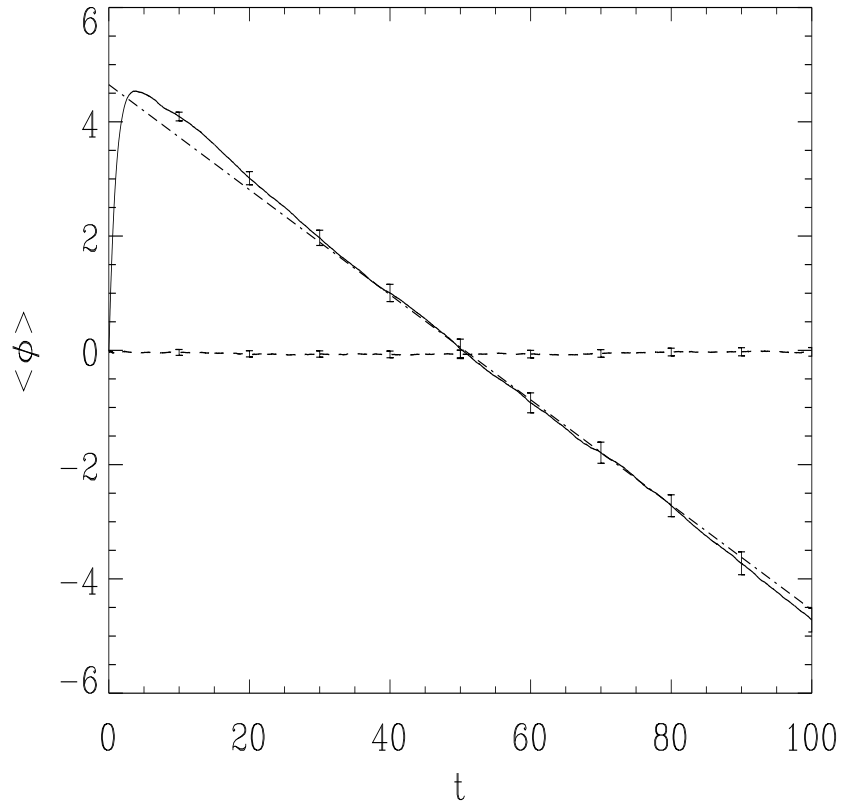

Figure 5.13: Time evolution of the mean value of the phase ϕ in a class A laser, in the case $a = 2$, $b = 1$, $\epsilon = 0.1$. For $\alpha = 0$ (dashed line) there is only phase diffusion and the average value is 0 for all times. When $\alpha = 5$ (solid line) there is a linear variation of the mean value of the phase. Error bars are included for some values. The dot–dashed line has the slope given by the theoretical prediction Eq. (5.23). The initial condition is taken as $x_1 = x_2 = 0$ and the results were averaged over 10000 trajectories with different realizations of the noise. Initial conditions: $x_1 = 0$, $x_2 = 0$. Dimensionless units.

We can understand these aforementioned features of the noisy dynamics using the deterministic Lyapunov potential $V(x_1, x_2)$. Since conditions (2.35), (2.36) and (2.37) are satisfied, the stationary probability distribution is given by (2.38) with $V(x_1, x_2)$ given by (5.10). By changing variables to intensity and phase, we find that the probability density functions for I and ϕ are independent functions (due to the form of the potential (5.12))

$$P_{st}(I, \phi) = P_{st}(I)\, P_{st}(\phi), \tag{5.15}$$

where

$$P_{st}(\phi) = \frac{1}{2\pi} \tag{5.16}$$

is a constant and

$$P_{st}(I) = Z^{-1}\, \mathrm{e}^{-I/(2\,\epsilon)}\, (b + I)^{a/(2\,\epsilon)}, \tag{5.17}$$

where the normalization constant is given by

$$Z = (2\epsilon)^{\frac{a}{2\,\epsilon}+1}\, \mathrm{e}^{\frac{b}{2\,\epsilon}}\, \Gamma\left(\frac{a}{2\,\epsilon} + 1, \frac{b}{2\,\epsilon}\right), \tag{5.18}$$

and $\Gamma(x, y)$ is the incomplete Gamma function. From this expression, we see that, independently of the value of ϵ, $P_{st}(I)$ has its maximum at the deterministic stationary value $I_m = a - b$, and by increasing ϵ the shape of the distribution becomes more asymmetric, see Figs. 5.14 and 5.15.

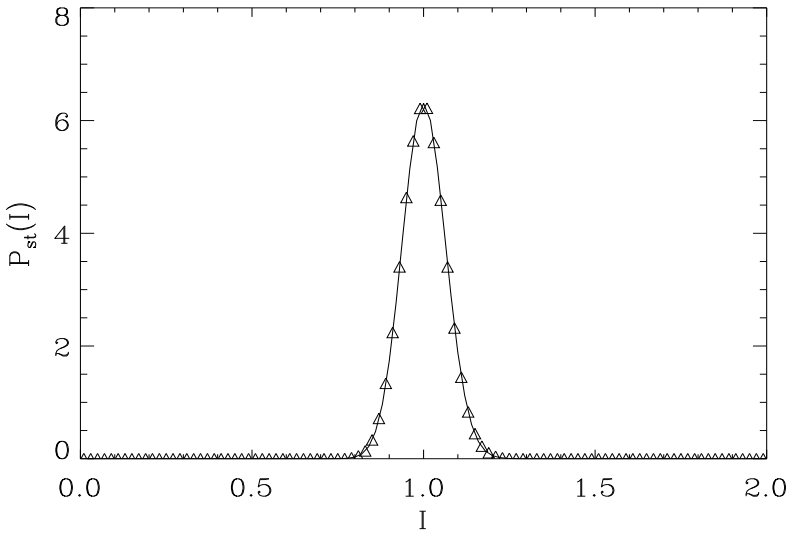

Figure 5.14: Probability distribution function for $I = x_1^2 + x_2^2$ in a class A laser, in the case $a = 2$, $b = 1$, $\epsilon = 0.001$. Dots correspond to the histogram obtained with the simulation of Eqs. (5.13) and (5.14). The solid line correspond to Eq. (5.17). Dimensionless units.

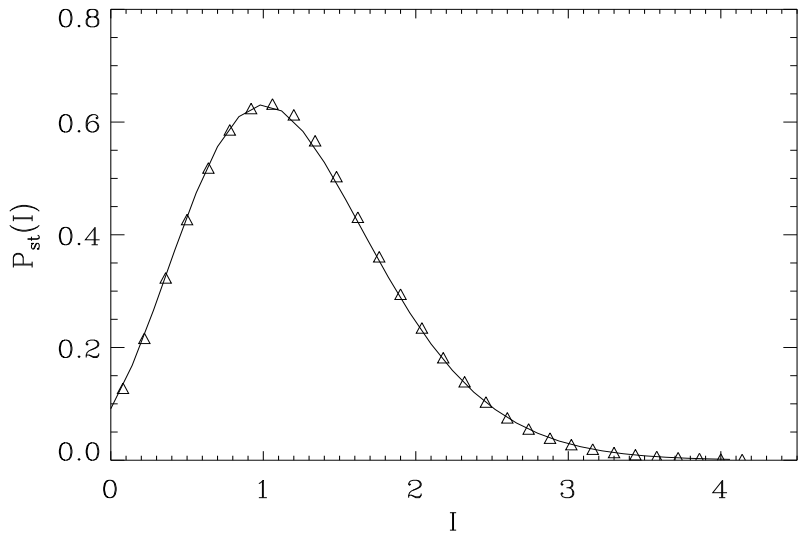

Figure 5.15: Probability distribution function for $I = x_1^2 + x_2^2$ in a class A laser, in the case $a = 2$, $b = 1$, $\epsilon = 0.1$. Dots correspond to the histogram obtained with the simulation of Eqs. (5.13) and (5.14). The solid line correspond to Eq. (5.17). Dimensionless units.

Starting from a given initial condition corresponding, for instance, to the laser in the *off* state, the intensity fluctuates around a mean value that increases monotonically with time. In the stationary state, the intensity fluctuates around the deterministic value $I_m = a - b$ but, since the distribution (5.17) is not symmetric around I_m, the mean value $\langle I \rangle_{st}$ is larger than the deterministic value. By using (5.17) and (2.39) one can easily find that

$$\langle I \rangle_{st} = (a - b) + 2\,\epsilon \left[1 + \frac{\exp(-b/2\,\epsilon)\,(b/2\,\epsilon)^{\frac{a}{2\epsilon}+1}}{\Gamma\left(\frac{a}{2\,\epsilon}+1, \frac{b}{2\,\epsilon}\right)} \right]. \tag{5.19}$$

The evolution of this mean value in terms of the parameter ϵ is plotted in Fig. 5.16. The mean value of I_{st} increases as the noise strength increases. In the deterministic case one obtains the value corresponding to the minimum of the potential.

An expression for the mean value of the intensity in the steady state was also given in [Risken, 1989], valid for the case in which the saturation terms in the dynamical equations are expanded to third order in the field amplitude.

As mentioned before, in the steady state of the stochastic dynamics, the phase ϕ of the electric field fluctuates around a mean value that changes linearly with time. Since any value of ϕ can be mapped into the interval $[0, 2\pi)$, this is consistent with the fact that the stationary distribution for ϕ is uniform, Eq. (5.16). We can easily understand the origin of this *noise sustained flow*: the rotation inducing terms, proportional to α in the equations of motion, are zero at the line of minima of the potential V and, hence, do not act in the deterministic steady state. Fluctuations

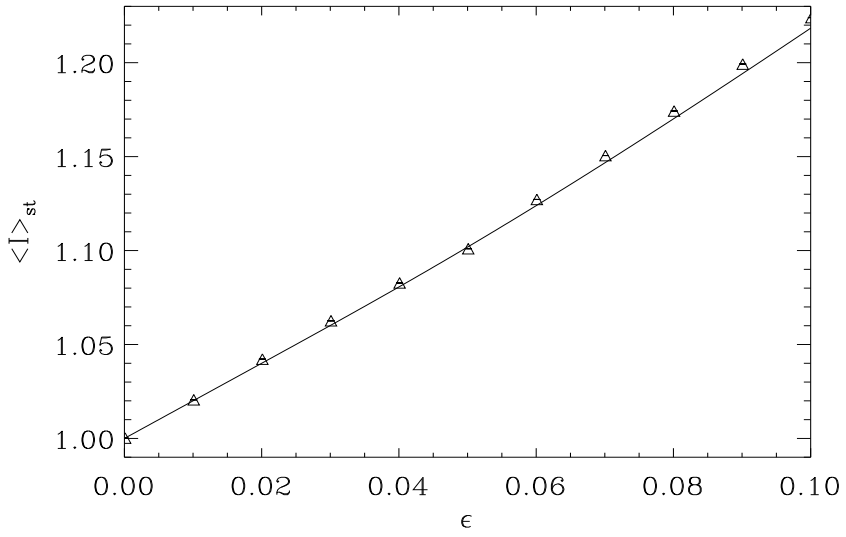

Figure 5.16: Evolution of $< I >_{st}$ with ϵ. Solid line, with Eq. (5.19). Points correspond to the mean values obtained by different simulations of Eqs. (5.13) and (5.14). $a = 2$ and $b = 1$.

allow the system to explore regions of the configuration space (x_1, x_2) where the potential is not at its minimum value. The antisymmetric part of the matrix D (which contains the parameter α) is then the responsible for the rotation in the plane (x_1, x_2). According to Eq. (5.19) the mean value of I is not at the minimum of the potential because there is, on average, a nonzero contribution of the rotational terms producing the observed phase drift.

The rotation speed can be calculated by writing the evolution equation for the phase of the electric field. After a change of variables in Eqs. (5.13 – 5.14) to intensity and phase, $x_1 + ix_2 = \sqrt{I}e^{i\phi}$, the evolution equations become (Itô sense)

$$\dot{I} = \left(\frac{a}{b+I} - 1\right) 2\,I + 4\,\epsilon + 2\sqrt{I}\,\xi(t), \tag{5.20}$$

$$\dot{\phi} = \left(\frac{a}{b+I} - 1\right) \alpha + \frac{1}{\sqrt{I}}\,\xi(t), \tag{5.21}$$

where $\xi(t)$ is a white noise term with zero mean value and correlations given by (2.32). In these equations one can see that apart from the stochastic noise terms, in the first equation it appears an extra term corresponding to the mean number of photons spontaneously emitted. Hence, the steady state is not $\langle I \rangle_{st} = a - b$ but it has a corrective term depending on ϵ as shown in (5.19).

By taking the average value of (5.21) and using the rules of the Itô calculus (the mean value of the last term of that equation is zero), one gets

$$\langle \dot{\phi} \rangle = \alpha \left\langle \frac{a}{b+I} - 1 \right\rangle. \tag{5.22}$$

By using the distribution (5.17) and the expression (2.39), one obtains the stochastic frequency shift

$$\langle \dot{\phi} \rangle_{st} = -\alpha \, \frac{\exp(-b/2\,\epsilon)\,(b/2\,\epsilon)^{\frac{a}{2\epsilon}}}{\Gamma\left(\frac{a}{2\,\epsilon}+1, \frac{b}{2\,\epsilon}\right)}. \tag{5.23}$$

Notice that this average rotation speed is zero in the case of no detuning ($\alpha = 0$) or for the deterministic dynamics ($\epsilon = 0$) and that, due to the minus sign, the rotation speed is opposite to that of the deterministic transient dynamics when starting from the *off* state. These results are in excellent agreement with numerical simulations of the rate equations in the presence of noise (see Fig. 5.13). The evolution of the mean value of the frequency with ϵ is plotted in Fig. 5.17. One can see the phase drift is negligible for a small values of ϵ.

The noise sustained flow we have obtained in this laser system implies that the laser frequency will be shifted with respect to the deterministic one in the presence of noise. It would be interesting to check experimentally the existence of this noise induce phase drift. However, according to our results, the noise intensity required for an observable phase drift is much larger than the typical noise intensity in experiments. Nevertheless, this necessary extra noise could be externally induced.

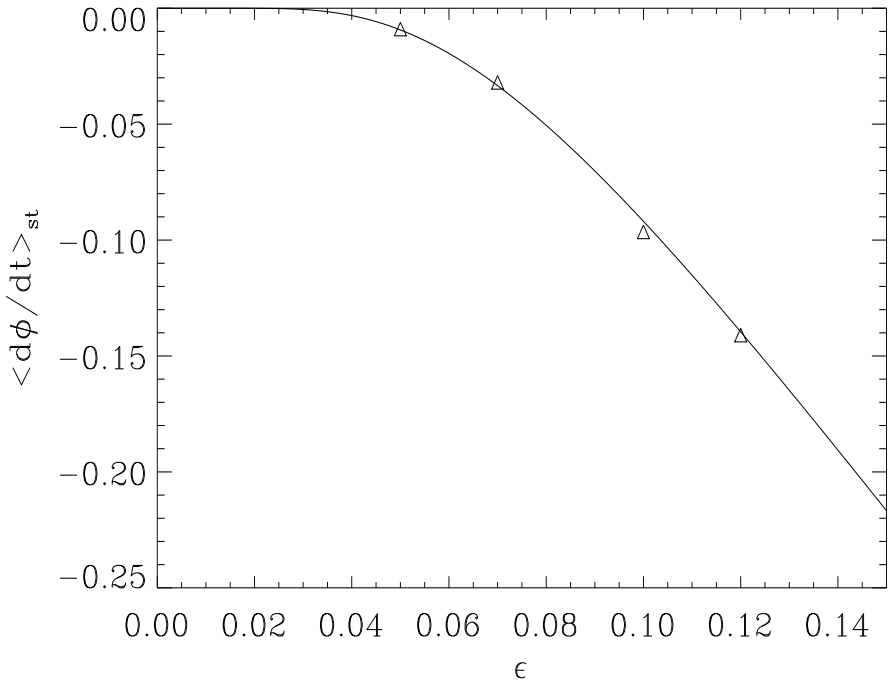

Figure 5.17: $< \dot{\phi} >_{st}$ versus ϵ as given by (5.23). Points correspond to the mean values obtained by simulating Eqs. (5.13) and (5.14). $a = 2$, $b = 1$ and $\alpha = 5$.

Capítol 6

Làsers de Classe A amb senyal injectat: Conjunt de bifurcacions i potencial de Lyapunov

En aquest capítol es descriu el conjunt de bifurcacions (capítol 3) per a un làser de classe A amb senyal injectat, en termes de l'amplitud, ρ, i freqüència, η, del senyal que s'aplica. A més, s'explica el comportament dinàmic d'aquests tipus de làsers, en els casos que es possible, en termes del potencial de Lyapunov (capítol 2).

El sistema que es considera és el d'un làser de classe A (capítol 4) amb un camp òptic monocromàtic aplicat. La dinàmica del sistema ve donada per la variació temporal del camp elèctric, Eq. (6.1). Escrivint les equacions en el sistema de referència que rota amb la freqüència del camp aplicat, les equacions que s'obtenen per a les parts real i imaginària del camp elèctric són les que es tracten en aquest treball, (6.3 – 6.4) (Els punts fixos d'aquestes equacions corresponen, en el sistema de referència inicial (6.1), a una solució per a les variables que oscil·la a la mateixa freqüència del camp aplicat).

La dinàmica del sistema és tal que, per a valors petits de η el sistema oscil·la en el pla definit per les parts real i imaginària del camp elèctric fins arribar a un punt fix. Quan s'augmenta el valor de la freqüència per damunt d'un cert valor, η_L, la intensitat del camp elèctric té un valor aproximadament constant, però la fase evoluciona linealment amb el temps.

Per a valors més grans de η i depenent del valor de ρ, la dinàmica és més complexa i apareixen distints possibles estats estacionaris. En la secció 6.2, es descriu el conjunt de bifurcacions complet, format per les distintes regions de l'espai de paràmetres (ρ, η), amb diferent comportament qualitatiu a l'estat estacionari. El conjunt de bifurcacions obtingut és el que apareix a la figura 6.2, i les distintes regions senyalades tenen punts fixos i òrbites periòdiques amb l'estabilitat que apareix a la Taula 6.1. En la bifurcació sella–node, línea sòlida, dos punts fixos col·lapsen a l'espai de fases i desapareixen (per exemple de la regió 5 a la 1). A la bifurcació de Hopf, línees a trossos curts, un punt fix canvia la seva estabilitat i es crea una

òrbita periòdica (com passant de la regió 2 a la 3). En les òrbites homoclíniques (línees de punts), l'òrbita periòdica va augmentant el seu període fins arribar a infinit en la corba homoclínica i allà desapareix, per exemple acostant–se de la regió 3 cap a la 4. La intersecció entre les bifurcacions sella–node, Hopf i homoclínica és una singularitat Takens–Bogdanov [els dos punts gruixuts de la figura 6.2 (a)]. Les zones de coincidència entre les corbes sella–node i òrbites homoclíniques, corresponen a bifurcacions Andronov–Leontovich: una òrbita periòdica en la regió on no hi ha punts fixos col·lisiona a l'òrbita homoclínica amb el punt fix sella–node. Cal notar que hi existeixen aquest tipus de bifurcacions a cada una de les branques de la bifurcació sella–node. En línies a trossos llargs apareix la bifurcació sella–node d'òrbites periòdiques: passant de la regió 6 a la 7 dues òrbites periòdiques de distinta estabilitat col·lisionen i es destrueixen.

En la secció 6.3, apareix el potencial (6.25) en el cas de considerar un camp real, $\eta = 0$. Té la forma de *capell mexicà* inclinat, Fig. 6.9. La dinàmica transitòria del sistema va cap a l'estacionari seguint una trajectòria espiral, igual que en el cas $\rho = 0$, capítol 5. A causa de la inclinació del potencial, es romp la simetria de fase pel sistema, i l'estat final és fixat per a la intensitat i la fase. La bifurcació sella–node en la línia $\eta = 0$ es pot obtenir partint que el potencial és més inclinat per a valors més grans de ρ, i en aquesta bifurcació els punts fixos sella i inestable desapareixen.

En el cas $\rho = 0$, $\eta \neq 0$, el sistema es pot escriure en termes d'un flux potencial, (2.26). El potencial és el mateix que en el cas sense injecció (5.10), i el terme residual (6.27) conté el terme de la freqüència. El cas determinista es pot entendre com el moviment damunt la superfície del potencial cap al mínim. En el mínim, la part residual actua donant el moviment harmònic de freqüència la d'injecció.

La forma qualitativa del potencial en alguna regió del cas general ($\rho \neq 0$, $\eta \neq 0$) es pot inferir a partir del potencial en els dos casos límits descrits. Per a un valor de $\rho \neq 0$, es va augmentant η partint de $\eta = 0$. Inicialment el potencial té la forma del potencial inclinat en una direcció; quan s'augmenta η, el potencial es deforma de manera que els punts mínim i sella es van apropant, fins a desaparèixer en la bifurcació sella–node. Apareixeria un conjunt de mínims en forma d'el·lipse, on els termes residuals serien els responsables del moviment periòdic en l'estat estacionari. L'el·lipse de mínims es deformaria contínuament en la regió 9 fins arribar a ser, quan es va disminuint ρ, el capell mexica en la línia $\rho = 0$.

En presència de renou, la funció densitat de probabilitat estacionària es pot obtenir a partir del potencial (en el cas $\rho\eta = 0$), (6.33). La intensitat fluctua al voltant del valor determinista, però com la funció densitat de probabilitat no és simètrica, el valor mig de la intensitat és major que el valor determinista, Fig. 6.11. La fase del camp elèctric també fluctua al voltant de un valor mig que canvia linealment en el temps, Fig. 6.12. Les fluctuacions permeten que el sistema explori regions fora del mínim i, després, els termes rotacionals (proporcionals a α) actuen. El valor mig es pot calcular a partir de l'expressió (6.35), i aquest *flux sostingut per renou* depèn del camp aplicat i del valor del renou, Fig. 6.13.

Chapter 6

Class A lasers with injected signal: Bifurcation set and Lyapunov–potential function

In this chapter, we describe the bifurcation set for a class A laser with an injected signal in terms of the amplitude and the frequency of the applied field by using the concepts introduced in chapter 3. We explain the dynamical behaviour of this kind of lasers in terms of a Lyapunov potential (chapter 2) in the case where such a description is possible. In particular, a full description for the deterministic and nondeterministic dynamics can be given by using the Lyapunov potential for some particular values of the external parameters. This represents an extension of the work performed in chapter 5 for class A lasers without injection. Depending also on the value of these parameters, the phase of the electric fields drifts also with time in the stochastic case, as it was found in the non–injected laser (section 5.3).

The chapter is organized as follows. In Sec. 6.1, we present the model equations for a class A laser with injected signal used in remaining sections. In Sec. 6.2, the bifurcation set in terms of the amplitude and frequency of the injected signal is determined. While a portion of the lines presented in this bifurcation set can be analytically calculated, the rest of the bifurcation set has been numerically computed. In Sec. 6.3, we describe the laser dynamics in terms of a potential function, valid for the case of a zero–detuning injected signal, and discuss its relevance both in the deterministic and stochastic dynamics.

6.1 Model

We consider a class A laser [Haken, 1985] whose dynamics can be described in terms of the slowly varying complex amplitude E of the electric field (5.1). The physical electric field is given by $\mathcal{E}(t) = [E(t)e^{i\Omega_0 t} + c.c.]/2$. The laser is injected with a monochromatic optical field $E_x e^{i\Omega t}$ of amplitude E_x and frequency Ω. The

resulting evolution equation is [Haken, 1984; van der Graaf, 1997]

$$\dot{E}(t) = (1+i\alpha)\left(\frac{\Gamma}{1+\vartheta|E|^2} - \kappa\right) E + \sigma E_x e^{-i\bar{\eta}t} + \zeta(t), \tag{6.1}$$

where $\bar{\eta} = \Omega_0 - \Omega$ is the detuning between the external field and the free running laser frequency Ω_0. κ, Γ, ϑ and α are (real) intrinsic parameters defined in Sec. 5.1. σ is the injection coupling, proportional to the inverse of the round–trip time τ_{in}. $\zeta(t)$ is a complex Langevin source term accounting for the stochastic nature of spontaneous emission. It is taken as a Gaussian white noise of zero mean and correlations

$$\langle \zeta(t)\zeta^*(t')\rangle = 4\Delta\delta(t-t'), \tag{6.2}$$

where Δ measures the strength of the noise.

By writing the complex variable E as $E = (x_1 + ix_2)e^{-i\bar{\eta}t}$ (i.e. (x_1, x_2) are the real and imaginary parts of the electric field E in the reference system that rotates with frequency $-\bar{\eta}$), and introducing a new dimensionless time $\kappa t \to t$, the evolution equations become

$$\begin{aligned}
\dot{x}_1 &= \left(\frac{a}{b+x_1^2+x_2^2} - 1\right)(x_1 - \alpha x_2) + \rho - \eta x_2 + \xi_1(t)\cos(\eta t) - \xi_2(t)\sin(\eta t), \\
\dot{x}_2 &= \left(\frac{a}{b+x_1^2+x_2^2} - 1\right)(\alpha x_1 + x_2) + \eta x_1 + \xi_1(t)\sin(\eta t) + \xi_2(t)\cos(\eta t),
\end{aligned}$$

where $a = \Gamma/(\kappa\beta)$, $b = 1/\beta$, $\rho = \sigma E_x/\kappa$ and $\eta = \bar{\eta}/\kappa$, and $\zeta(t) = \xi_1(t) + i\xi_2(t)$ introduces real white noise processes, ξ_1 and ξ_2, with zero mean and correlations given by (2.32) with $\epsilon = \Delta/\kappa$. The statistical properties that follow from this set of equations are contained in the Fokker–Planck equation (2.33) for the time evolution of the probability density function [Risken, 1989]. A simpler, yet equivalent set of equations, in the sense that they give rise to the same Fokker–Planck equation, is [Hernández-García *et al.*, 1990]

$$\dot{x}_1 = \left(\frac{a}{b+x_1^2+x_2^2} - 1\right)(x_1 - \alpha x_2) + \rho - \eta x_2 + \xi_1(t), \tag{6.3}$$

$$\dot{x}_2 = \left(\frac{a}{b+x_1^2+x_2^2} - 1\right)(\alpha x_1 + x_2) + \eta x_1 + \xi_2(t). \tag{6.4}$$

These equations can be written in terms of the intensity I and phase ϕ, by making the change of variables $x_1 = \sqrt{I}\cos(\phi)$ and $x_2 = \sqrt{I}\sin(\phi)$,

$$\frac{dI}{dt} = 2\left[\frac{a}{b+I} - 1\right] I + 2\rho\sqrt{I}\cos(\phi) + 2\sqrt{I}\,\xi_I(t), \tag{6.5}$$

$$\frac{d\phi}{dt} = \alpha\left[\frac{a}{b+I} - 1\right] - \frac{\rho}{\sqrt{I}}\sin(\phi) + \eta + \frac{1}{\sqrt{I}}\,\xi_\phi(t), \tag{6.6}$$

where $\xi_I(t)$ and $\xi_\theta(t)$ are white noise processes of mean zero and correlations (2.32). The multiplicative terms of these equations have to be understood in the Stratonovich sense [Risken, 1989].

In the next sections, the system of equations (6.3 – 6.4) is studied. For convenience, we will switch between the descriptions (6.3 – 6.4) and (6.5 – 6.6) whenever it simplifies the discussion.

6.2 Bifurcation set

We consider throughout this section the deterministic version of Eqs. (6.3) and (6.4), i.e. the case $\epsilon = 0$. It is easy to observe that any trajectory remains bounded in the (x_1, x_2) plane. This comes from the asymptotic form of Eq. (6.5) in the limit $I \to \infty$, namely $\dot{I} = -2I$, which shows that trajectories with a large intensity I are restored towards the origin. Consequently, the only asymptotic behaviour of Eqs. (6.3 – 6.4) can be either a fixed point or a periodic orbit. As Eqs. (6.3 – 6.4) are written in the reference frame that rotates with frequency $-\eta$, a fixed point solution represents a situation in which the frequency of the laser electric field E equals that of the injected field. We are interested in finding the *locking range*, i.e. the set of parameters (ρ, η) for the injected field such that there exist *stable* fixed point solutions, also called *locking* solutions.

6.2.1 The fixed point solutions

The intensity I_s and phase ϕ_s of the fixed points are found by setting $\dot{I} = \dot{\phi} = 0$ in (6.5 – 6.6). The resulting equations can be rewritten as

$$\rho^2 = I_s \left[\frac{a}{b + I_s} - 1\right]^2 (1 + \alpha^2) + 2\alpha\eta I_s \left[\frac{a}{b + I_s} - 1\right] + I_s\eta^2, \tag{6.7}$$

$$\eta = \frac{\rho}{\sqrt{I_s}}\sqrt{1 + \alpha^2}\sin(\phi_s + \arctan(\alpha)). \tag{6.8}$$

We consider henceforth the case $a > b$ (corresponding to the lasing mode of operation $\Gamma > \kappa$). For given (ρ, η), the third degree–polynomial equation (6.7) can have either one or three real (always nonnegative) solutions for the intensity I_s, see Fig. 6.1. Particularly, in the case $\rho = 0$, the two fixed solutions for the intensity suffer a transcritical bifurcation, Fig. 3.2, at $a = b$. By multiplying Eq. (6.7) by $(1 + \alpha^2)$, one gets

$$\frac{\rho^2(1 + \alpha^2)}{I_s} = \left[\left(\frac{a}{b + I_s} - 1\right)(1 + \alpha^2) + \eta\alpha\right]^2 + \eta^2. \tag{6.9}$$

From this equation, it is straightforward to show that for any point of those solutions the condition

$$|\eta| \leq \frac{\rho}{\sqrt{I_s}}\sqrt{1 + \alpha^2} \tag{6.10}$$

is always satisfied, hence ensuring that there will be the corresponding solution for ϕ_s obtained from Eq. (6.8).

The lines separating the one fixed point solution region from the three fixed point solutions region can be found by using standard methods of algebra. These lines form the so–called *saddle–node* curve (solid line in Figs. 6.2 (a), 6.2 (b) and 6.3).

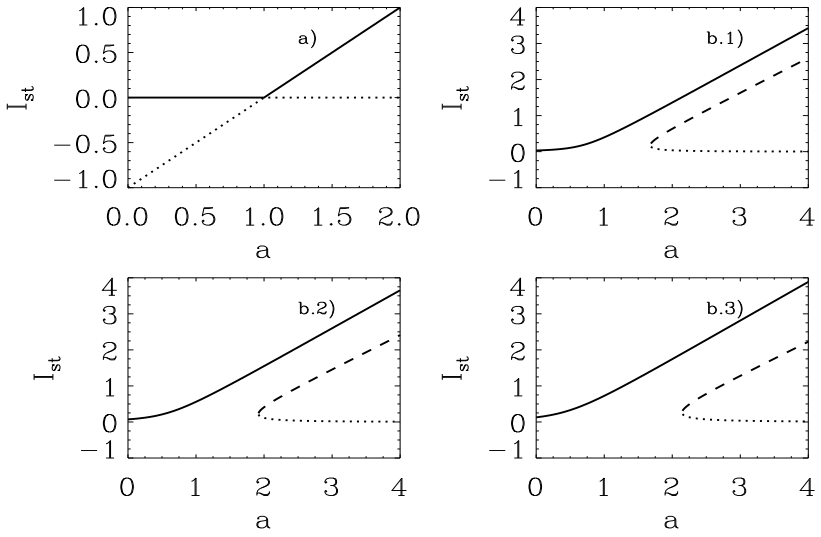

Figure 6.1: Fixed points for the intensity for a class A laser with injected signal, Eq. (6.7), versus a. Solid line: stable fixed point, dashed line: saddle point, dotted line: unstable point. $\alpha = 2$. $b = 1$. (a) $\rho = 0$, (b.1) $\rho = 0.4$, (b.2) $\rho = 0.6$, (b.3) $\rho = 0.8$.

It turns out that the three fixed points region is a connected set enclosing region labelled 2, 3, 4, 5, 8, 10 shown in Fig. 6.2 (a) for a typical case $a = 2$, $b = 1$, $\alpha = 2$. In regions 1, 6, 7, 9 only one fixed point exists. For moderate values of the intensity ρ, there is a range of values for the frequency $\eta \in (\eta_1, \eta_2)$ for which three fixed points exist, whereas for very large intensity, only one fixed point exists for all values of η. A similar scenario occurs for $\alpha = 0$, see Fig. 6.3 where the three fixed points region is labelled as 5, and only one fixed point appears in regions 1, 7, 9.

6.2.2 The periodic orbit solutions

At the saddle–node curve, a saddle point and another fixed point merge and disappear. In some cases this gives rise to a periodic orbit through an Andronov–Leontovich bifurcation. Near the bifurcation, it is possible to obtain approximately the evolution equation for the angle variable $\phi(t)$ by assuming that the intensity of the periodic orbit is constant. This approximation, which can be obtained via perturbation theory on the laser equations to lowest order [Zimmermann *et al.*, 2001], is derived here heuristically by neglecting fluctuations in the intensity, setting $\dot{I} = 0$ in Eq. (6.5), but allowing for a time dependent phase in Eq. (6.6) for ϕ. Setting $I = I_o$ constant in Eq. (6.5) and replacing in Eq. (6.6) we obtain

$$\dot{\phi} = \eta - \frac{\rho\sqrt{1+\alpha^2}}{\sqrt{I_o}} \sin(\phi + \arctan(\alpha)). \tag{6.11}$$

The next approximation is to consider that I_o is the intensity of the field at the nearest point (ρ, η) in the saddle–node curve with the same value of the external field amplitude ρ. Hence, I_o is computed as the double root of Eq. (6.7) taking the adequate value $\eta = \eta_1$ or $\eta = \eta_2$.

Eq. (6.11) is known as Adler's equation [Adler, 1946] and it can be easily analyzed by writing it as

$$\dot{\phi} = -\frac{dU}{d\phi}, \tag{6.12}$$

using the potential function

$$U(\psi) = -\eta_L \cos(\phi + \arctan(\alpha)) - \eta\phi, \tag{6.13}$$

where we have introduced

$$\eta_L = \frac{\rho\sqrt{(1+\alpha^2}}{\sqrt{I_o}}. \tag{6.14}$$

The dynamics of ϕ can be explained in terms of relaxation in the potential U. For $|\eta| < \eta_L$ the potential has local minima and the phase eventually stops in one of them. This is a fixed point solution which has been discussed in the previous subsection. A periodic orbit solution is obtained only in the case $|\eta| \geq \eta_L$ where the phase ϕ varies monotonically with time. The explicit solution is

$$\phi(t) = 2\arctan\left[\frac{\eta_{ef}}{\eta}\tan\left(\frac{\eta_{ef}}{2}t\right) + \frac{\eta_L}{\eta}\right] - \arctan(\alpha) - \eta t, \tag{6.15}$$

where $\eta_{ef} = \sqrt{\eta^2 - \eta_L^2}$.

Therefore, within this approximation, the line separating a fixed point from a periodic orbit solution is given by $|\eta| = \eta_L$. Notice that our derivation of this relation is different from the usual one in which one derives it by demanding that Eq. (6.10) is satisfied. We have shown that Eq. (6.10) is indeed satisfied for all values of η and ρ and that the condition $|\eta| = \eta_L$ determining the locking range is an approximated one. By using Eq. (6.7) this condition can be rewritten as

$$\rho = |\eta|\sqrt{\frac{a}{1+\alpha^2-\alpha\eta} - \frac{b}{1+\alpha^2}}. \tag{6.16}$$

The range of validity of this approximation has to be checked numerically. In Fig. 6.2 (c) we compare the exact result with the approximate one in the typical case $a = 2$, $b = 1$, $\alpha = 2$. It can be seen that the approximation is quite good for small values of ρ but it worsens as the intensity ρ is increased.

When crossing the saddle–node curve, for example crossing from region 9 or 1 to region 5 in Fig. 6.2 (a), the periodic orbit disappears. As a precursor of this disappearance, the period of the periodic orbit, T, grows in regions 1, 9 until it finally diverges at the saddle–node curve. The divergence can be fitted, for a fixed value of η to the law $T \sim (\rho_r - \rho)^{-1/2}$ [Strogatz, 1994], being ρ_r the value of ρ where the bifurcation occurs, see Fig. 6.4.

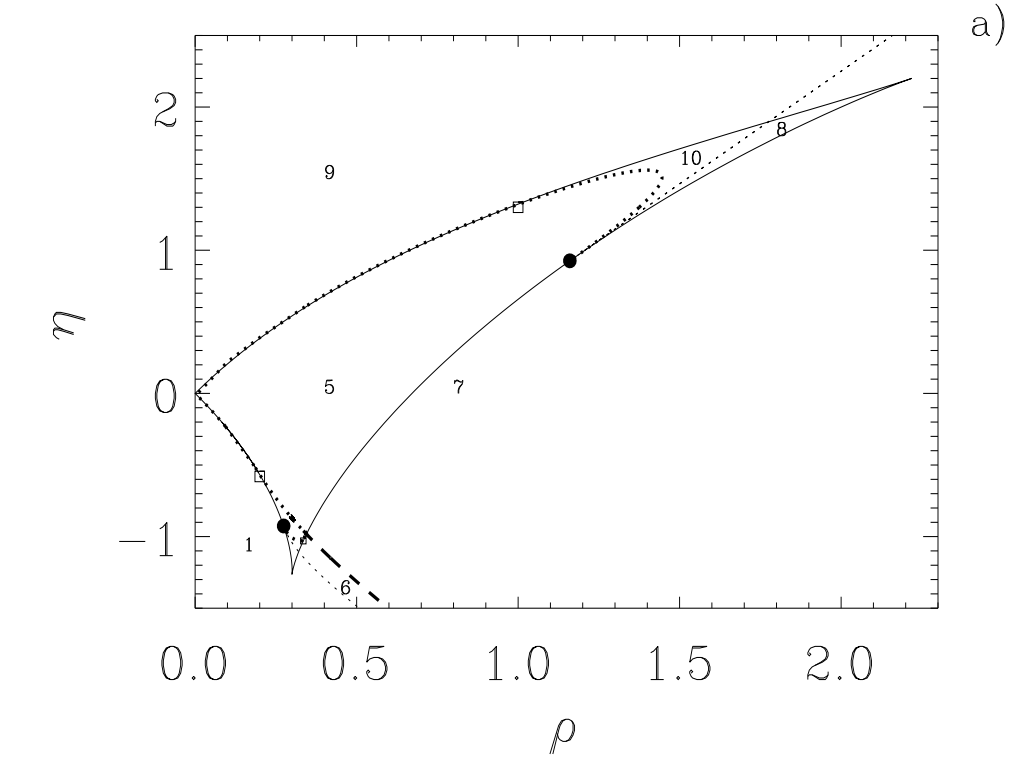
a)
2
1
0
−1
η
9
10
8
5
7
1
6
0.0
0.5
1.0
1.5
2.0
ρ

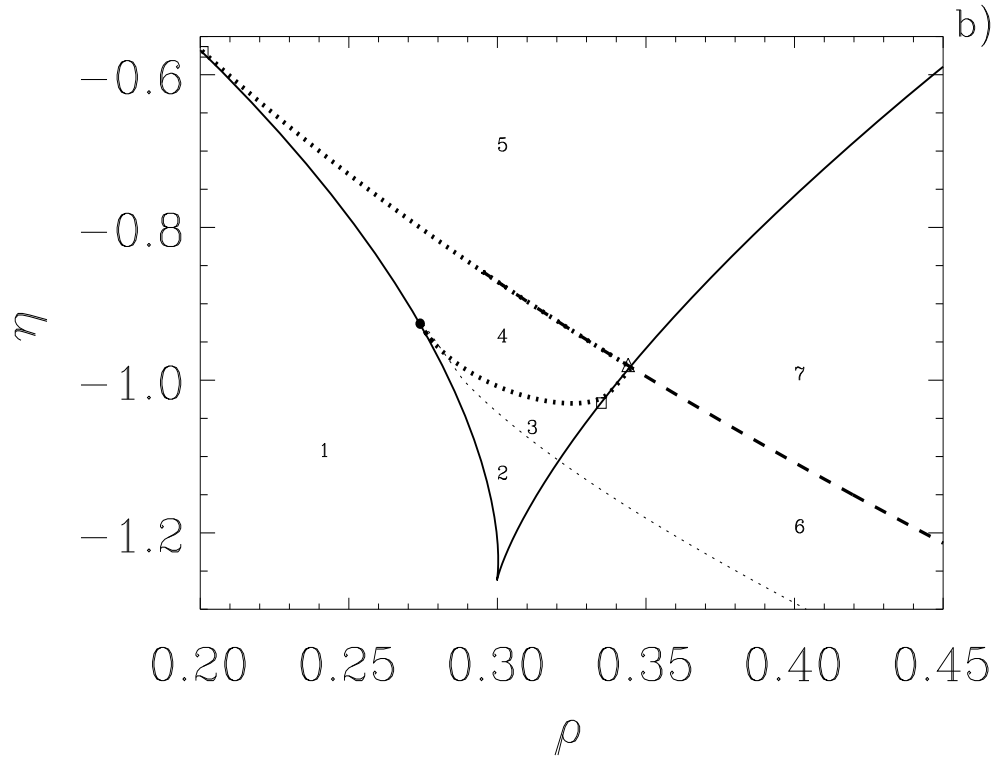
b)
−0.6
−0.8
−1.0
−1.2
η
5
4
7
3
1
2
6
0.20
0.25
0.30
0.35
0.40
0.45
ρ

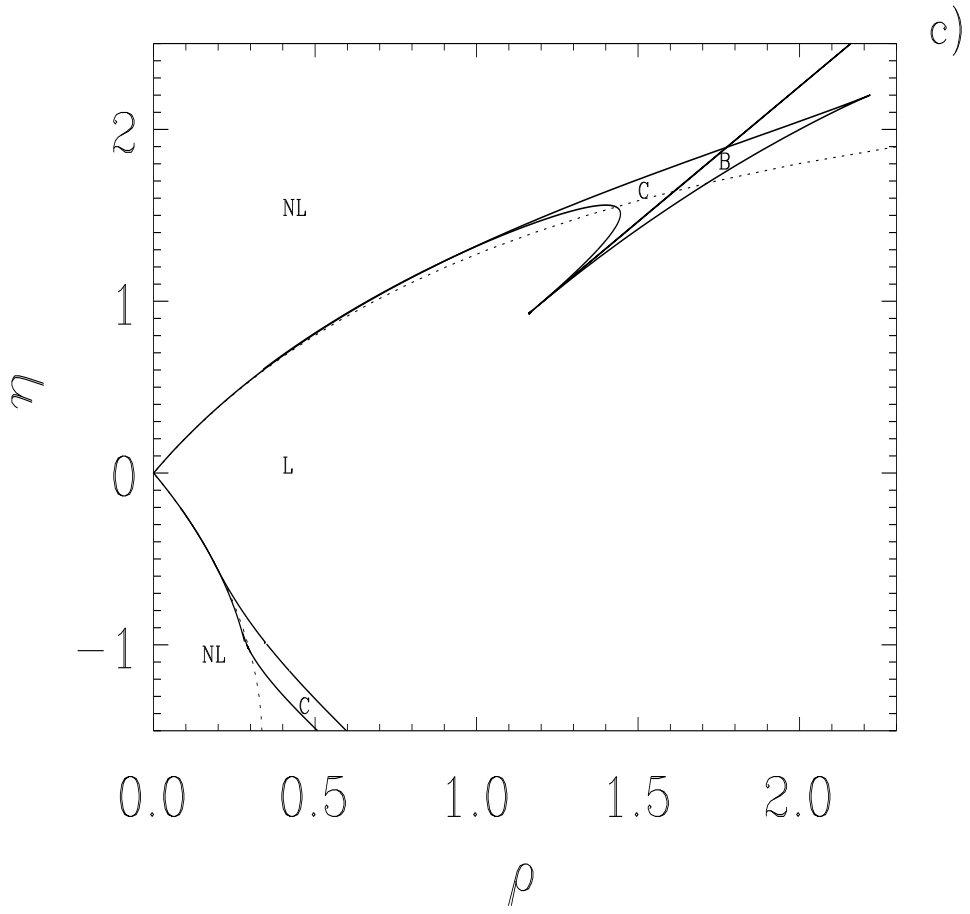

Figure 6.2: Bifurcation set for a class A laser with an injected signal for $a = 2$, $b = 1$ and $\alpha = 2$. In (a) and (b) the solid line is the saddle–node curve separating regions 1, 6, 7, 9 with one fixed point solution from regions 2, 3, 4, 5, 8, 10 with three fixed point solutions; the short–dashed lines separating the pairs of regions $8 - 10$, $2 - 3$, $7 - 9$ and $1 - 6$, are Hopf bifurcation, as given by Eq. (6.20), where a periodic orbit is created; the dotted lines are homoclinic bifurcation where the periodic orbits of regions 4 and 10 disappear when going to region 5, and one periodic orbit in 3 disappears when going to region 4; the coincidence of the curve of homoclinic orbits with the saddle–node curve mark the existence of Andronov–Leontovich bifurcation where the periodic orbit of 9 and 1 disappears when crossing to 5; the long–dashed line is a saddle–node bifurcation of periodic orbits and going from 7 to 6 two periodic orbits of different stability are created; the two big solid dots are Takens–Bogdanov points. There also exist homoclinic saddle–node codimension–2 points, in the intersection between the saddle-node curves and the homoclinic orbits (squares and triangle). In (c) we indicate the different regions of stability: in L, one fixed point is the stable solution; in NL, one periodic orbit is the stable solution; in C there is coexistence of a stable fixed point and a periodic orbit; finally, in B there are two stable fixed points. The dotted line is the approximate locking range given by Eq. (6.16).

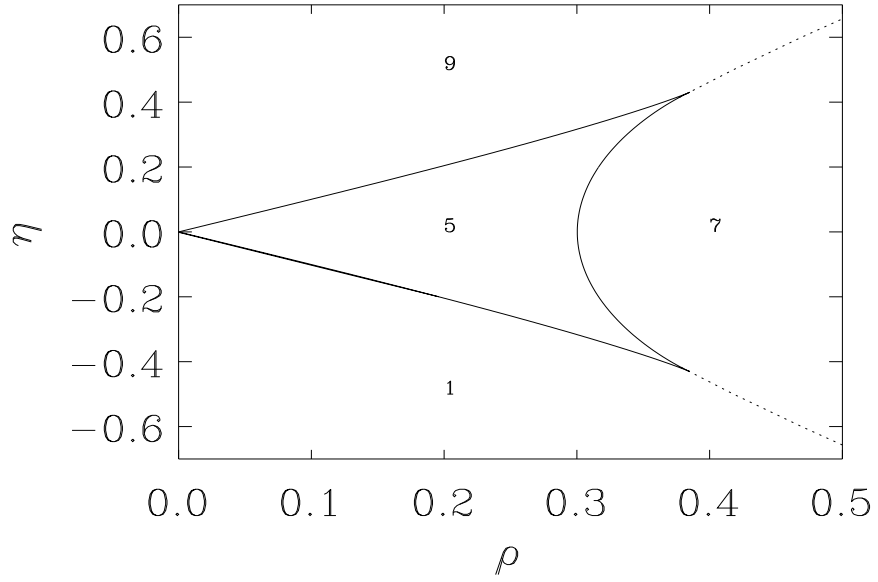

Figure 6.3: Bifurcation set for a class A laser with an injected signal for $a = 2$, $b = 1$ and $\alpha = 0$. The solid line is the saddle–node curve separating regions 1, 7, 9 with one fixed point solution from region 5 with three fixed point solutions. The dotted lines separating the pairs of regions $7-9$ and $7-1$, are Hopf bifurcation, as given by Eq. (6.20), where a periodic orbit is created. The locking range is formed by regions 5, 7 where a single fixed point is the only stable solution. In 1 and 9 the stable solution is a periodic orbit.

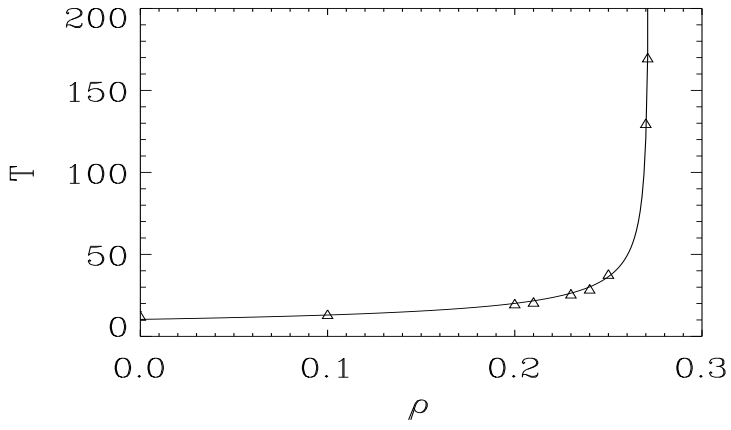

Figure 6.4: Period of the stable periodic orbit of region 9 of diagram of Fig. 6.2 versus ρ. $\eta = 0.5$ (diamonds). Solid line: $5.4/\sqrt{\rho_r - \rho}$, with $\rho_r = 0.272$.

6.2.3 Unfolding the bifurcation set

In the following we will perform the stability analysis of the different fixed points and the periodic orbit solutions. The fixed points for I are given by (6.7) and an equation that can have either one or three real roots depending on ρ and η. The stability of these fixed points defines the different regions of interest. Stability properties can be established in terms of the eigenvalues of the linearization matrix (Jacobian) of Eqs. (6.3 – 6.4) at the fixed points, see chapter 3. The local bifurcation takes place when the real part of some eigenvalue crosses zero.

The results of the stability analysis depend on the value of the parameter α. For $\alpha = 0$, the only possibility is to have regions in which either a stable fixed point or a stable periodic orbit exist, see Fig. 6.3. However, for $\alpha > 0$ a much richer behaviour appears. We summarize the results for the typical case $a = 2$, $b = 1$, $\alpha = 2$ shown in Fig. 6.2: In regions 5, 7 there exists only one locking (stable fixed point) solution. In region 8 there exist two locking solutions with different intensity. In regions 1, 2, 9 there exists one stable periodic orbit solution. Finally, in regions 3, 4, 6 and 10 one locking solution coexists with a stable periodic orbit solution. While some of the lines of this bifurcation set shown in Fig. 6.2 can be evaluated analytically, others have to be obtained numerically. We now give details of the calculations of those lines.

6.2.3.a Saddle–node bifurcation

A saddle–node bifurcation occurs when two fixed points are created/annihilated. The saddle–node curve separates, in this case, a region with one fixed point from another with three fixed points. On the saddle–node curve, two fixed points coincide (or equivalently, one of the eigenvalues of the Jacobian is zero). From another point of view, the saddle–node bifurcation curve can be obtained as the lines in the (ρ, η) plane in which the third degree equation (6.7) has a double root. In this case, the equation for the fixed points can be written in the form

$$\mu(I - I_1)(I - I_2)^2 = 0. \tag{6.17}$$

Comparing this expression with the one for the fixed points (6.7) and equating the different orders of I, a system of equations is obtained

$$\left[\begin{array}{rcl} \mu & = & (1+\alpha^2) - 2\alpha\eta + \eta^2, \\ -\mu(I_1 + 2I_2) & = & -2\alpha\eta b + 2b\eta^2 - 2(1+\alpha^)(a-b) + 2\alpha\eta(a-b) - \rho^2, \\ \mu(I_2^2 + 2I_1I_2) & = & (a-b)^2(1+\alpha^2) + 2\alpha\eta b(a-b) + b^2\eta^2 - 2b\rho^2, \\ \mu I_1 I_2^2 & = & b^2\rho^2. \end{array}\right. \tag{6.18}$$

From this system, the variables μ, I_1 and I_2 can be obtained, and an expression that relates ρ to η can be found. The resulting saddle–node bifurcation curve is indicated by a solid line in Figs. 6.2 (a), 6.2 (b) and 6.3.

6.2.3.b Hopf bifurcation

In a Hopf bifurcation of a two–dimensional system such as ours, a fixed point changes its stability (from stable to unstable, or vice versa) and a periodic orbit with opposite stability to the coexistent fixed point is born/disappears. At the bifurcation point, the eigenvalues of the Jacobian matrix J associated to the deterministic system (6.3) and (6.4) [or equivalently and somewhat easier (6.5) and (6.6)] are complex conjugated and pure imaginary. This condition can be written as $Tr(J) = 0$, $Det(J) > 0$. Hence,

$$(b + I)(a - b - I) - aI = 0. \tag{6.19}$$

This equation combined with the one for the fixed points (6.7) leads to the Hopf bifurcation curve,

$$\eta^2 + 2\alpha\eta\left(\sqrt{\frac{a}{b}} - 1\right) + \left(\sqrt{\frac{a}{b}} - 1\right)^2 (1 + \alpha^2) = \frac{\rho^2}{-b + \sqrt{ba}}, \tag{6.20}$$

also shown in Fig. 6.2 (a), 6.2 (b) (short–dashed line). From regions 8 to 10, 7 to 9, 1 to 6 and from 2 to 3 a periodic orbit is born and a fixed point changes its stability. The disappearance of those periodic orbits will be explained in the following subsections.

6.2.3.c Takens–Bogdanov singularities

At the points (ρ_{Hs}, η_{Hs}) where the Hopf and the saddle–node bifurcation curves intersect the eigenvalues of the Jacobian matrix are strictly equal to zero. This condition gives

$$\eta_{Hs} = \pm\left(\sqrt{\frac{a}{b}} - 1\right)\sqrt{1 + \alpha^2}, \tag{6.21}$$

$$\rho_{Hs} = \sqrt{2b\left(\sqrt{\frac{a}{b}} - 1\right)^3 \sqrt{1 + \alpha^2}(\sqrt{1 + \alpha^2} \pm \alpha)}. \tag{6.22}$$

For the parameters considered in Fig. 6.2 ($a = 2$, $b = 1$ and $\alpha = 2$), it is $(\rho_{Hs}, \eta_{Hs}) = (0.274, -0.926)$ and $(\rho_{Hs}, \eta_{Hs}) = (1.160, 0.926)$. At these intersection points, the Jacobian matrix is different from zero, and its normal form is

$$\begin{pmatrix} 0 & 1 \\ 0 & 0 \end{pmatrix}. \tag{6.23}$$

These points correspond to Takens–Bogdanov singularities [Kuznetsov, 1997]. At these intersection points, indicated in the figure, a homoclinic orbit is also born. These orbits have been found numerically and they are discussed in the next subsection.

6.2.3.d Homoclinic orbits

When (some branch of) the stable and unstable manifolds of a saddle point coincide we are in the presence of a homoclinic orbit. Homoclinic orbits have been obtained numerically using the program AUTO97 [Doedel *et al.*, 1997] as the "infinite-period limit" of periodic orbits. The resulting curves of homoclinic orbits are displayed as dotted lines in Fig. 6.2 (a), 6.2 (b). Their location in parameter space coincides partially with the saddle–node curve.

The intersections of the saddle–node curve and a homoclinic bifurcation occur at codimension–2 points. There exist intersection homoclinic saddle–node codimension–2 points (SH) at each of the saddle–node branches, see Fig. 6.2 and 6.6. The bifurcation structure near to these points was described in [Schecter, 1987]. Note that the location of these codimension–2 points cannot be completely exact due to the fact that the homoclinic orbits are obtained numerically (considering an orbit of large period but not infinite). The bifurcation branch emerging from these points with coincidence of the curve of homoclinic orbits with the saddle–node curve is an Andronov–Leontovich bifurcation.

6.2.3.e Saddle–node of periodic orbits

Besides the bifurcation curves described so far, there exists yet another curve of saddle–node bifurcations of periodic orbits. This is indicated by the the long–dashed curve in Fig. 6.2 (a), 6.2 (b) which has been obtained also numerically. When crossing this curve, the two periodic orbits of region 6 disappear. The point were the saddle–node of periodic orbits, the homoclinic and the neutral saddle curve intersect is a codimension–2 point, labelled as F, in Fig. 6.6. This point is not found exactly at Fig. 6.2 (b) due to numerical evaluation. The presence of this point gives rise to a small region, labelled as 11, where two periodic orbits, and three fixed points exist, see Fig. 6.6 and 6.7. For $\omega \approx -5$ [not shown in the scale of Fig. 6.2 (a)] the Hopf bifurcation and the saddle–node of periodic orbits collide and regions 1 and 7 are directly separated by the Hopf bifurcation.

6.2.3.f Different regions separated by the bifurcation set

We summarize in Table 6.1 the results of the previous subsections concerning the different regions separated by the bifurcation lines. In Fig. 6.5, the phase portrait of different regions is shown, namely regions $3 - 4 - 5 - 6$. In the first line, from left to right the transition from region 4 to 5 is shown. In the first column, one can observe the transition form region 4 to 3 through an homoclinic orbit. The transition from region 3 to 6, as a saddle–node bifurcation, appears in the last line. In the diagonal [Figs. 6.5 (a), 6.5 (e) and 6.5 (i)] one can observe the transition through an Andronov bifurcation. The saddle–node of periodic orbits is reflected in Fig. 6.5 (f). In Fig. 6.7, appears the phase portraits in region 11.

Many of the bifurcation features found in this system are present in other studies, as in the book by Kuznetsov [Kuznetsov, 1997] where a bifurcation diagram

topologically equivalent to ours is displayed in connection with the analysis of a predator–prey model by Bazykin.

These results allow us to identify the stability regions indicated in Fig. 6.2 (c): in **L**, one fixed point is the only stable solution; in **NL**, one periodic orbit is the only stable solution; in **C** there is coexistence of a stable fixed point and a periodic orbit; finally, in **B** there are two stable fixed points.

Table 6.1: Different regions in the bifurcation set for a class A laser with injected signal. We use the notation: f.p. = fixed point, p.o. = periodic orbit, St. = stable and Unst. = unstable.

$1 \rightarrow$	1 f.p. Unst., 1 p.o. St.
$2 \rightarrow$	2 f.p. Unst., 1 f.p. Saddle, 1. p.o. St.
$3 \rightarrow$	1 f.p. Unst., 1 f.p. Saddle, 1 f.p. St., 1 p.o. St., 1 p.o. Unst.
$4 \rightarrow$	1 f.p. Unst., 1 f.p. Saddle, 1 f.p. St., 1 p.o St.
$5 \rightarrow$	1 f.p. Unst., 1 f.p. Saddle, 1 f.p. St.
$6 \rightarrow$	1 f.p. St., 1 p.o. St., 1 p.o. Unst.
$7 \rightarrow$	1 f.p. St.
$8 \rightarrow$	2 f.p. St., 1 f.p. Saddle
$9 \rightarrow$	1 f.p. Unst., 1 p.o. St.
$10 \rightarrow$	1 f.p. Unst., 1 f.p. Saddle, 1 f.p. St., 1 p.o. St.
$11 \rightarrow$	1 f.p. Unst., 1 f.p. Saddle, 1 f.p. St., 1 p.o. St., 1 p.o. Unst.

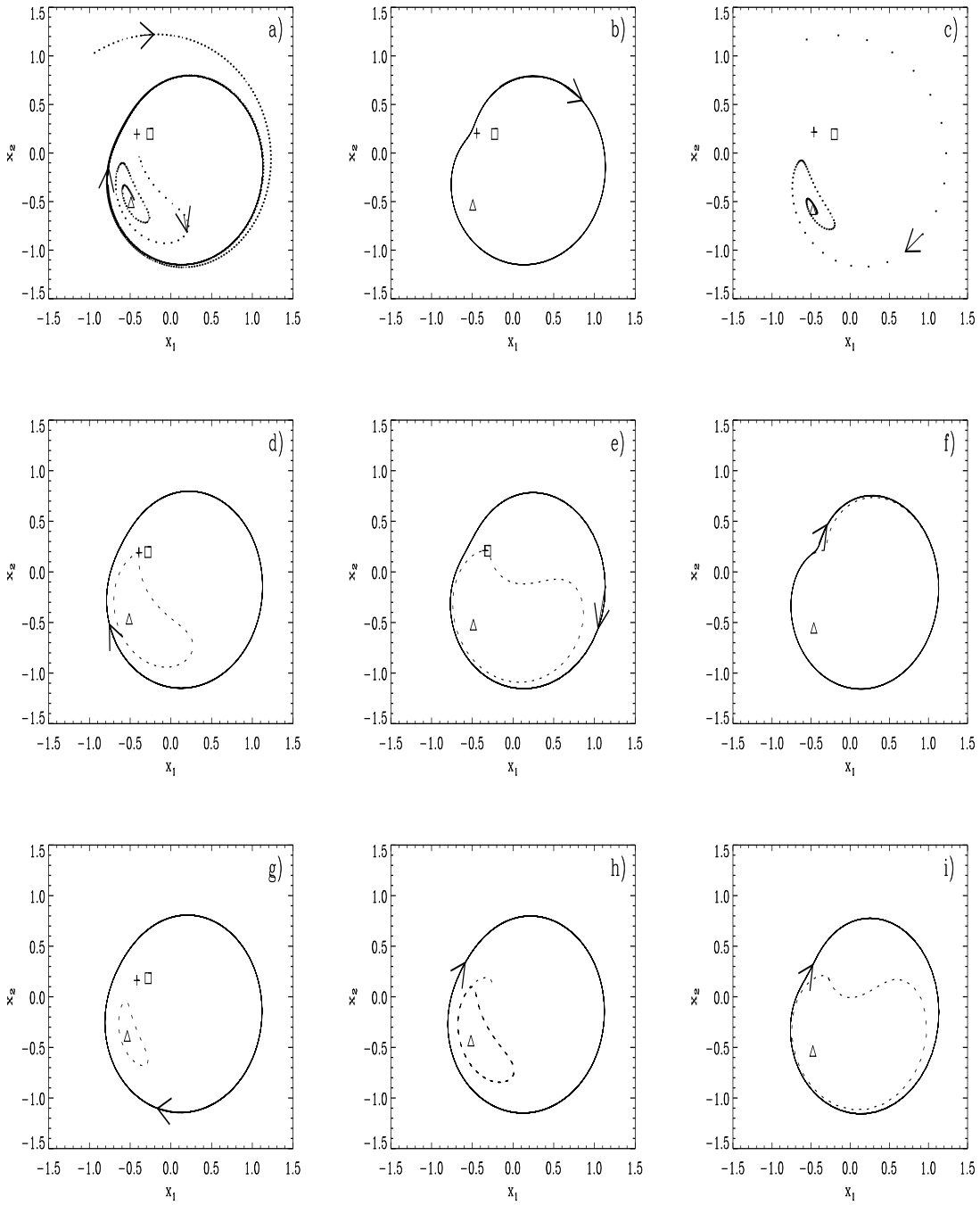

Figure 6.5: Phase portraits in different regions. Triangle: stable fixed point, square: unstable fixed point, cross: saddle point. Solid line: stable orbit, dashed line: unstable orbit. Points: trajectories. (a) Region 4: $(\rho, \eta) = (0.33, -1)$; (b) Near homoclinic $4-5$: $(\rho, \eta) = (0.33, -0.95)$; (c) Region 5: $(\rho, \eta) = (0.33, -0.9)$; (d) Close to homoclinic $3-4$: $(\rho, \eta) = (0.33, -1.03)$; (e) Close to Andronov bifurcation $4-6$: $(\rho, \eta) = (0.34, -1)$; (f) Close to the saddle–node of periodic orbits $6-7$: $(\rho, \eta) = (0.352, -1)$; (g) Region 3: $(\rho, \eta) = (0.33, -1.05)$; (h) Close to the saddle–node $3-6$: $(\rho, \eta) = (0.33, -1.065,)$; (i) Region 6: $(\rho, \eta) = (0.345, -1)$.

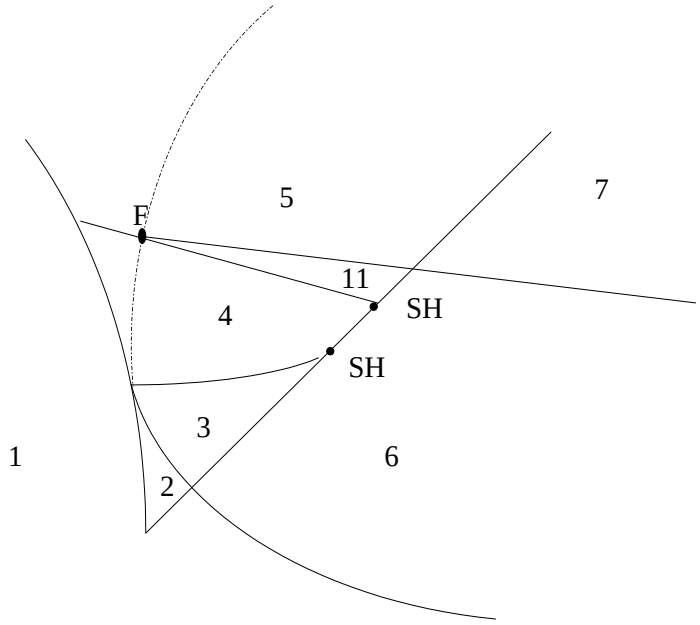

Figure 6.6: Sketch of the partial bifurcation set for a class A laser with injected signal. Different regions and intersection points detailed in Fig. 6.2 and Table 6.1. SH: homoclinic saddle–node codimension–2 points. F: intersection of the saddle–node bifurcation of periodic orbits, the homoclinic orbit and the continuation of the Hopf bifurcation (dotted line, which is not a bifurcation).

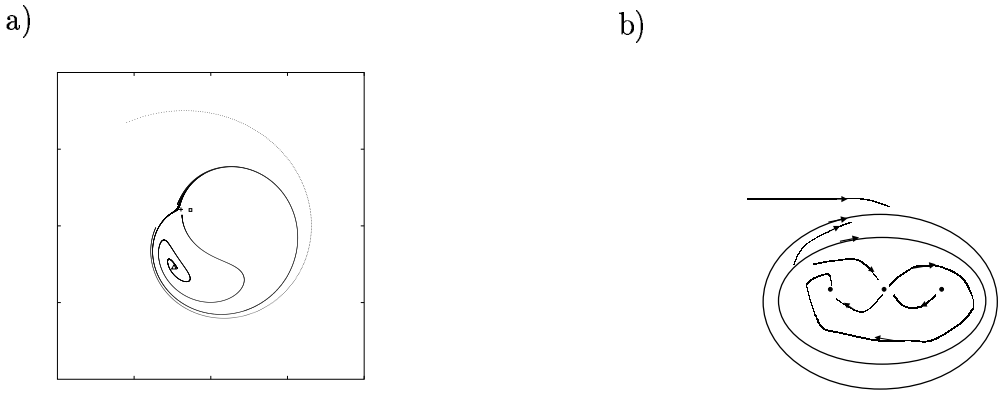

Figure 6.7: Phase portrait at region 11 of the bifurcation set. a) $(\rho, \omega) = (0.34, -0.9713)$, Triangle: stable fixed point, square: unstable fixed point, cross: saddle point. b) Sketch of the phase portrait: arrows indicate the sense of the flow.

6.3 Lyapunov potential

We now look for a description of the dynamical equations in terms of a Lyapunov potential, see Sec. 2.2. Equations (6.3) and (6.4) can be written as

$$\dot{x_i} = -\sum_{j=1}^{2} D_{ij}\frac{\partial V}{\partial x_j} + v_i + \sum_{j=1}^{2} g_{ij}\xi_j, \qquad i = 1,2, \tag{6.24}$$

where the function V is [Haken, 1983]

$$V(x_1,x_2) = \frac{1}{2}\left[x_1^2 + x_2^2 - a\ln(b + x_1^2 + x_2^2)\right] - \frac{\rho}{(1+\alpha^2)}(x_1 - \alpha x_2), \tag{6.25}$$

or, written in terms of intensity and phase,

$$V(I,\phi) = \frac{1}{2}\left[I - a\,\ln(b+I)\right] - \frac{\rho\sqrt{I}}{\sqrt{1+\alpha^2}}\cos\left(\phi + \arctan\alpha\right). \tag{6.26}$$

The matrices D and g, and the vector $\mathbf{v}$ are

$$D = S + A = \begin{pmatrix} 1 & 0 \\ 0 & 1 \end{pmatrix} + \begin{pmatrix} 0 & -\alpha \\ \alpha & 0 \end{pmatrix}, \quad g = \begin{pmatrix} 1 & 0 \\ 0 & 1 \end{pmatrix}, \quad \mathbf{v} = \begin{pmatrix} -\eta x_2 \\ \eta x_1 \end{pmatrix}. \tag{6.27}$$

6.3.1 Deterministic Dynamics

In the deterministic dynamics ($\epsilon = 0$), Eqs. (6.24) show that $V(x_1,x_2)$ is a Lyapunov potential, i.e. a function that monotonically decreases along trajectories, $\dot{V} \leq 0$, provided that the *residual terms* (v_1, v_2) satisfy the *orthogonality condition* (2.30)

$$v_1\frac{\partial V}{\partial x_1} + v_2\frac{\partial V}{\partial x_2} = 0. \tag{6.28}$$

It turns out that this orthogonality condition is satisfied if $\eta\rho = 0$. This means that a Lyapunov function description of the dynamics using (6.25) is valid along the coordinate axis $\eta = 0$ and $\rho = 0$. Notice that the case $\rho = 0$, $\eta \neq 0$ corresponds to a situation in which there is no applied field but the reference system rotates at an arbitrary frequency η.

The equation for the intensity (6.7) can have one or three (positive) real roots depending on the parameters. In Fig. 6.8, the stationary solutions are plotted for a case in which $a > b$. The stability of these solutions follows immediately from the analysis in terms of the potential and it is described in the figure caption. The value at which the saddle and unstable solutions disappear corresponds to the saddle–node bifurcation value for $\eta = 0$ (see Fig. 6.2).

In the transient dynamics towards the stationary states, the combined effects of S and A produce in general a spiral–like trajectory in the (x_1,x_2) plane. The angular velocity of this movement is proportional to α. Finally, the residual term (v_1,v_2) induces a movement which does not decrease the value of the potential and

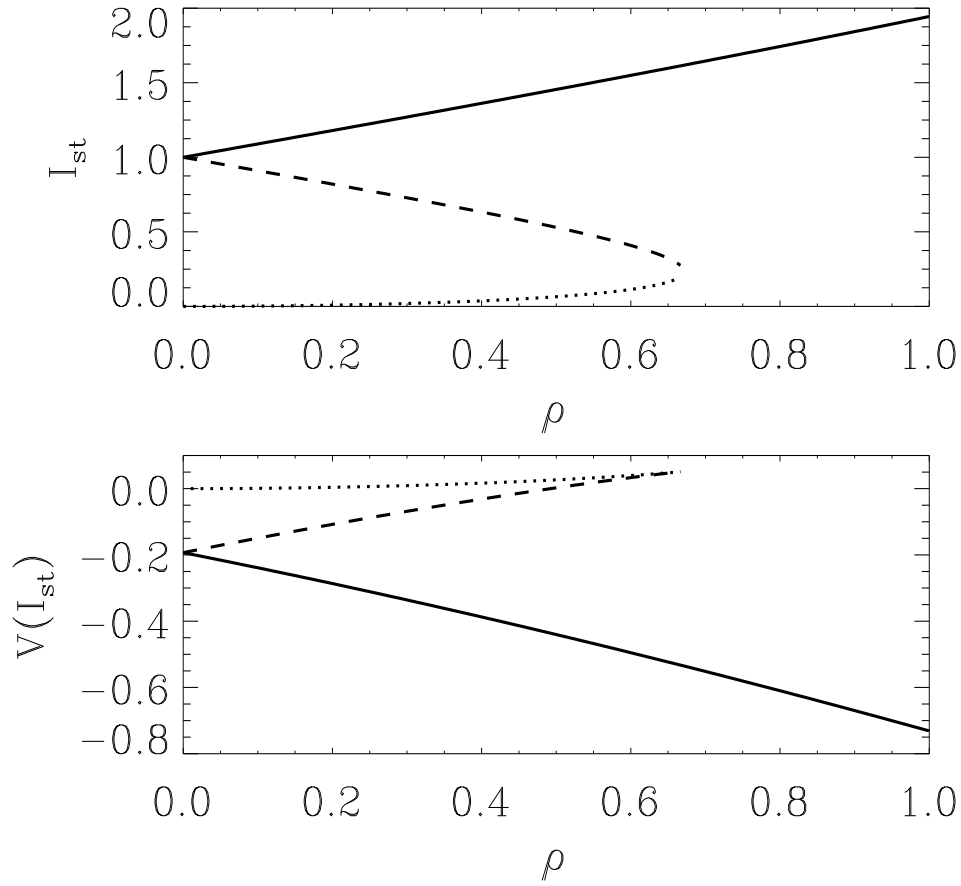

Figure 6.8: Upper figure: Fixed points of Eq. (6.7) versus ρ. Lower figure: Value of the potential, Eq. (6.25), evaluated at the different fixed points versus ρ. $\eta = 0$. $a = 2$, $b = 1$ and $\alpha = 2$. Dimensionless units.

it is responsible for any dynamics after the line of minima of the potential has been reached. We now analyze the different possibilities for the extrema of V.

In the case $\rho = 0$, the potential function was given in chapter 5. The potential does not depend on the phase ϕ of the electric field and it can adopt two qualitatively different shapes:
(i) For $a < b$ the potential has a single minimum at $x_1 = x_2 = 0$ and no maxima. Therefore, the only fixed point is the *off* state $I = 0$, which is stable.
(ii) For $a > b$, the potential has the shape of a *Mexican hat*, see Fig. 6.9 (a). The residual dynamics $\dot{x}_i = v_i$ gives a periodic harmonic movement in the minima of the potential with frequency η. This corresponds to the periodic orbits represented in Fig. 6.2.

In the case of zero–detuning injected signal, i.e. $\rho > 0$, $\eta = 0$, the potential,

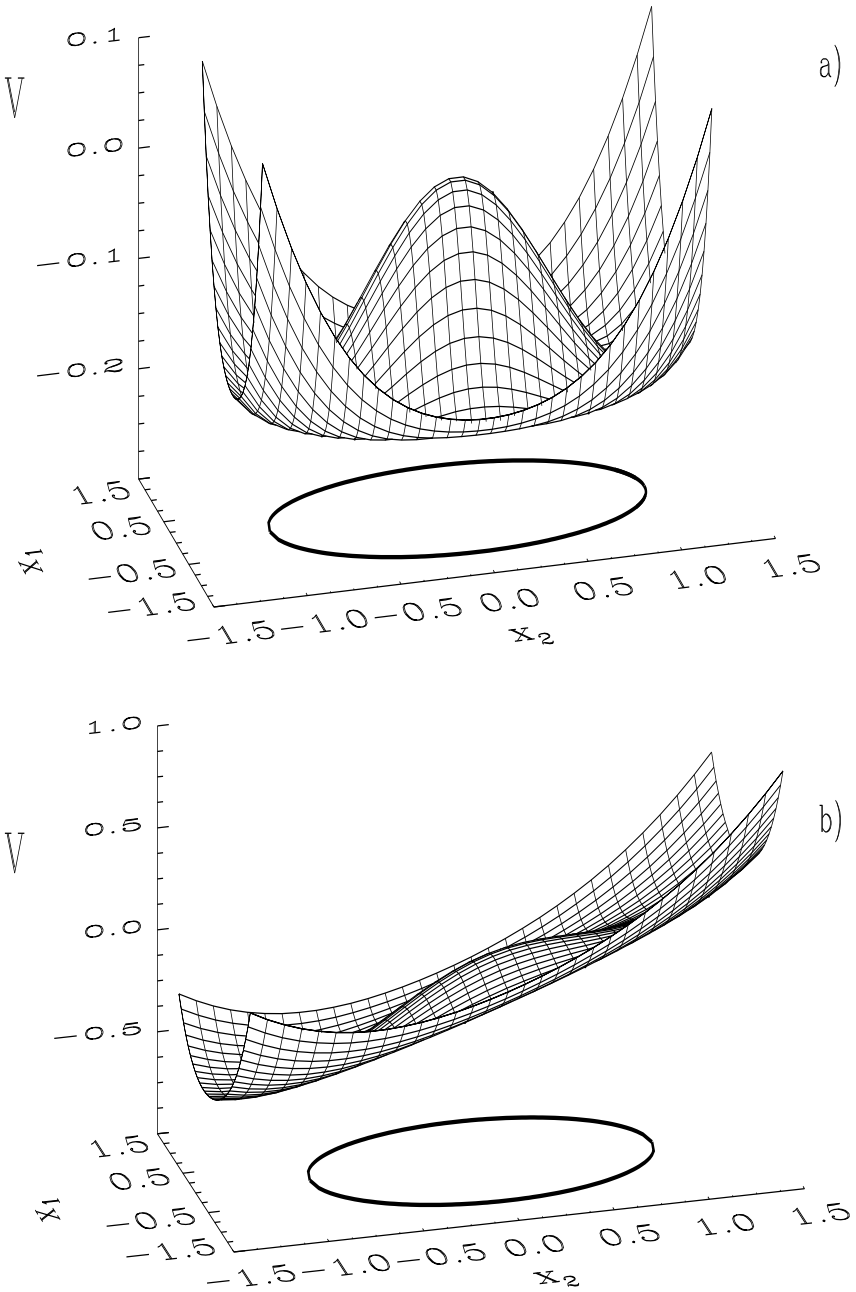

Figure 6.9: Potential for a class A laser with an injected signal with the same frequency of the unperturbed laser, Eq. (6.25), with the parameters $a = 2$, $b = 1$, $\alpha = 2$. Dimensionless units. (a) $\rho = 0$, (b) $\rho = 0.8$. In (a) we also indicate the projection of the line of minima of V and the corresponding line is plotted in (b).

which depends now explicitly on the phase ϕ, is tilted in a preferred direction. In the case $a < b$ the location of the minimum changes and the asymptotic state has a nonzero light intensity, that is proportional to ρ. In the case $a > b$, the Mexican hat is tilted as well in a preferred direction. For small ρ the inclination is small and the effect is that the maximum still remains a maximum, although its location varies slightly. The tilt breaks the symmetry amongst the line of degenerate minima and an absolute minimum is selected. At the same time, one of the previous minima becomes a maximum in the direction orthogonal to the tilt and a saddle point is born. Increasing ρ, the maximum of the Mexican hat and the saddle point disappear (corresponding to the saddle–node curve of figure 6.2) and the potential has only one minimum at a preferred phase direction, see Fig. 6.9 (b). Therefore, the asymptotically stable situation, in this case of $\rho > 0$, $\eta = 0$ and $a > b$ is that the laser switches to an *on* state with a well defined intensity and phase, in agreement with the results shown in Fig. 6.2.

It is an open question the validity of a Lyapunov potential description in the general case, $\rho\eta \neq 0$, and we have not been able to find an analytical expression for the potential V in this general case. However, since we do not expect qualitative changes in the dynamical features near the coordinate axis, we speculate that a Lyapunov potential description continues to be valid, at least for small values of $\eta\rho$.

Assuming the validity of this Lyapunov potential description we can understand the transition from locking to non–locking states. Let us consider a given value of $\rho > 0$ and increase the detuning frequency starting from $\eta = 0$. For $\eta = 0$, the potential is tilted and there are no residual terms, see Fig. 6.9 (b). As η increases, the shape of the potential deforms, the minimum of the potential and the saddle point approach through the deterministic circumference of minima of the system without optical injection, $\rho = 0$ (region 5 of Fig. 6.2). Moreover, the residual terms, proportional to η increase, but they are not big enough to overcome the tilt of the potential and to induce a rotation movement. For a value of η (corresponding to the saddle–node bifurcation) these two points (minimum and saddle) collapse and a periodic motion appear induced by the residual terms (corresponding to region 9 of Fig. 6.2).

Similarly, starting at a point $\eta > 0$ and increasing the intensity of the applied fields, ρ, a similar scenario appears. For $\rho = 0$, the potential has a line of degenerate minima, $I = a - b$, and trajectories are circumferences in the (x_1, x_2) plane induced by the residual terms. Increasing ρ, the line of minima deviate from the circumference due to the change of shape of the potential and it becomes an ellipse, the periodic orbit solution is also induced by the residual terms of the dynamics, which are proportional to η. In fact, it can be shown that the solution in the steady state for very small values of ρ has the form

$$I(t) = \frac{\mathcal{A}}{1 + \rho\sqrt{\mathcal{D}^2 + \mathcal{F}^2}\sin(\phi(t) + \gamma_1)}, \tag{6.29}$$

which represents an ellipse with a time dependent phase. This dependence is of the form

$$\phi(t) = \eta t - \rho\sqrt{\mathcal{B}^2 + \mathcal{C}^2}\sin(\phi(t) + \gamma_2). \tag{6.30}$$

The values of $\mathcal{A}$, $\mathcal{B}$, $\mathcal{C}$, $\mathcal{D}$, $\mathcal{E}$ have been obtained by using equations (6.5) and (6.6) and small values of ρ. The resulting expressions are

$$\begin{aligned}
\mathcal{A} &= a-b, \\
\mathcal{B} &= -\frac{[4(a-b)^2+\eta^2a^2+2\alpha a\eta(a-b)]}{\eta\sqrt{a-b}[4(a-b)^2+\eta^2a^2]}, \\
\mathcal{C} &= -4\frac{\alpha}{\eta}\frac{(a-b)^{3/2}}{[4(a-b)^2+\eta^2a^2]}, \\
\mathcal{D} &= \frac{4a\sqrt{a-b}}{4(a-b)^2+\eta^2a^2}, \\
\mathcal{F} &= \frac{2\sqrt{a-b}a^2\eta}{4(a-b)^3+\eta^2a^2(a-b)}, \\
\gamma_1 &= \arctan(-\mathcal{D}/\mathcal{F}), \\
\gamma_2 &= \arctan(-\mathcal{B}/\mathcal{C}).
\end{aligned} \tag{6.31}$$

Increasing ρ even further, the potential deforms continuously until arriving to the saddle–node bifurcation.

6.3.2 Stochastic effects

In the presence of low–to–moderate levels of noise, $\epsilon > 0$, the qualitative features of the transient dynamics remain the same as in the deterministic case. The most important differences appear near the stationary situation and show up as fluctuations of the intensity and phase of the electric field. While the intensity simply oscillates around its mean value, one can observe in some cases an additional phase drift which shows up as a variation in the frequency of the emitted light. The potential picture developed in the previous section helps us to understand the origin of this noise–induced frequency shift, as well as to compute its magnitude.

Let us look at the potentials depicted in Fig. 6.9. First consider the case $\rho = 0$. The deterministic movement is such that the line of minima (shown as a projection in the (x_1, x_2) plane) is ran at a constant frequency η. On top of that movement there are fluctuations which allow frequent excursions beyond the minima of the potential V. Away from the minima, the antisymmetric part of the dynamics (governed by the matrix A in equation (6.27) and proportional to α) gives a nonzero contribution of the rotation terms producing the observed phase drift. For $\eta = 0$, $\rho \neq 0$, when only one minimum of the potential exists, the fluctuations make the system to explore regions outside this minimum allowing the rotation terms to act again, see Fig. 6.10. Depending on the value of ρ and ϵ the rotation term can be strong enough to produce the phase flow.

After these qualitative arguments, we now turn to a more quantitative calculation. In those cases in which a Lyapunov potential $V(x_1, x_2)$ exists and the matrices D and g of (6.24) satisfy the fluctuation–dissipation relation (2.35), the stationary probability distribution is given by equation (2.38). This relation is exact if the

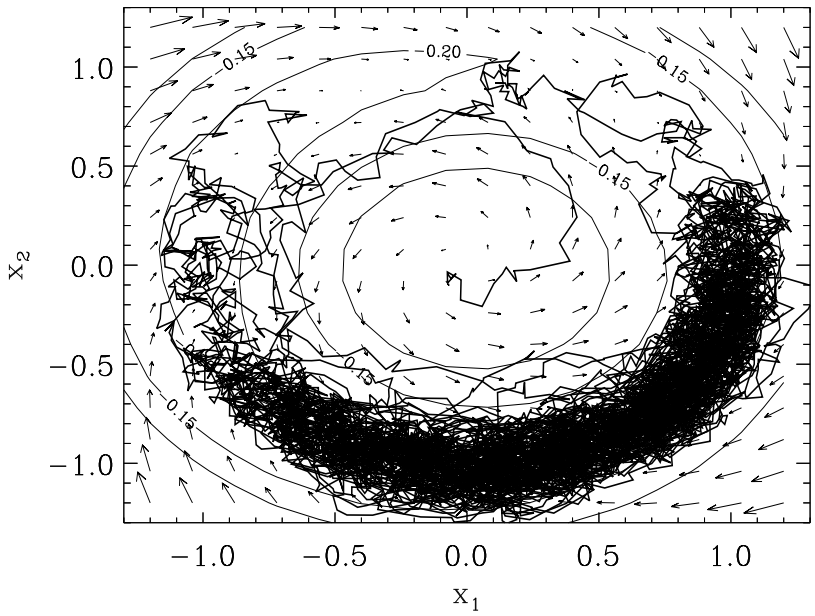

Figure 6.10: Vector field for a class A lasers with injected signal. Thick solid line: simulation of Eqs. (6.3) and (6.4). Thin lines are the equipotential curves of Eq. (6.25) and the arrows indicate the sense of the flow. Parameters: $a = 2$, $b = 1$, $\alpha = 2$, $\eta = 0$, $\rho = 0.05$. $\epsilon = 0.01$. Initial conditions: $x_1 = 0$, $x_2 = 0$. Dimensionless units.

residual terms $\mathbf{v}$ satisfy the orthogonality condition (6.28) and if they are divergence–free (2.37) (as they are in our case). In other cases, it has to be understood as an approximation valid in the limit of small noise $\epsilon \to 0$.

By changing variables to intensity and phase, we find that the probability density function is

$$P_{st}(I,\phi) = Z^{-1}\, e^{-I/2\epsilon}\, (b+I)^{a/2\epsilon}\, \exp\left(\frac{\rho\sqrt{I}}{\epsilon\sqrt{1+\alpha^2}}\cos(\phi+\arctan(\alpha))\right), \qquad (6.32)$$

and the marginal probability density function for I is

$$P_{st}(I) = Z^{-1} e^{-I/2\epsilon} (b+I)^{a/2\epsilon}\, \mathcal{I}_0\left(\frac{\rho\sqrt{I}}{\epsilon\sqrt{1+\alpha^2}}\right), \qquad (6.33)$$

where $\mathcal{I}_0$ is the Bessel function of the first kind and order 0. Expression (6.33) reduces to (5.17) for $\rho = 0$.

The maximum of the probability density function, I_m, is given by

$$b + I_m = a + \frac{(b+I_m)\rho}{\sqrt{I_m}\sqrt{1+\alpha^2}}\frac{\mathcal{I}_1(\bar{\rho})}{\mathcal{I}_0(\bar{\rho})}, \qquad (6.34)$$

where $\bar{\rho} \equiv \rho\sqrt{I_m}/(\epsilon\sqrt{1+\alpha^2})$ and $\mathcal{I}_1$ is the Bessel function of the first kind and order 1. For $\epsilon = 0$, deterministic case, $\mathcal{I}_1(\bar{\rho})/\mathcal{I}_0(\bar{\rho}) = 1$ and the equation is reduced to (6.7) with $\eta = 0$.

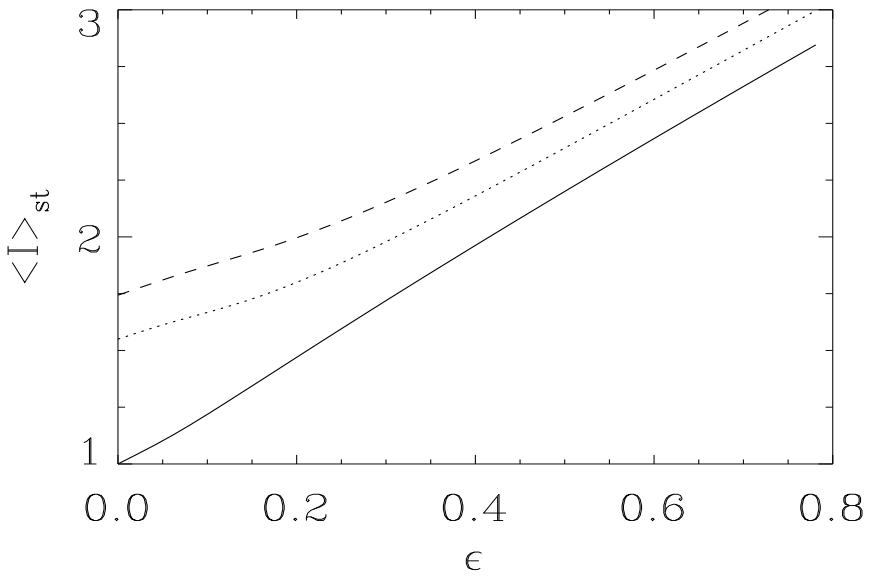

Figure 6.11: Mean value of the intensity in the steady state in a class A laser with zero–detuning ($\eta = 0$) injected signal for $a = 2$, $b = 1$ and $\alpha = 2$. The solid line corresponds to $\rho = 0$ and has been computed using the analytical result Eq. (5.19), the dotted line ($\rho = 0.6$) and the dashed line ($\rho = 0.8$) have been computed numerically using Eq. (6.33).

The steady state average value for the intensity $\langle I \rangle_{st} = \int dI\, I P_{st}(I)$ can be analytically computed in the case $\rho = 0$ with the result (5.19). In the most general case, for $\rho \neq 0$, the mean value can be computed numerically by using (6.33). In Fig. 6.11, this mean value is plotted versus ϵ, for fixed value of ρ. The mean value is always larger than the deterministic ($\epsilon = 0$) case.

As mentioned before, in the steady state of the stochastic dynamics, the phase of the electric field ϕ fluctuates around a mean value that changes linearly with time. This is clearly seen in the numerical simulations (see Fig. 6.12) and it physically corresponds to a change $\Delta\omega$ in the emission frequency of the laser.

This frequency shift can be computed as the average value of the phase derivative $\langle \dot{\phi} \rangle$. In the case that the steady state is a periodic orbit of period T, one needs to subtract from this value the intrinsic frequency $2\pi/T$. By taking the average value of Eq. (6.6) and using the rules of the stochastic calculus, one arrives to

$$\Delta\omega = Z^{-1}\alpha \int_0^\infty e^{-I/2\epsilon}(b+I)^{a/2\epsilon} \left[\frac{(a-b-I)}{b+I} I_o\left(\frac{\rho\sqrt{I}}{\epsilon\sqrt{1+\alpha^2}}\right) + \sqrt{I}\, I_1\left(\frac{\rho\sqrt{I}}{\epsilon\sqrt{1+\alpha^2}}\right)\right] dI. \tag{6.35}$$

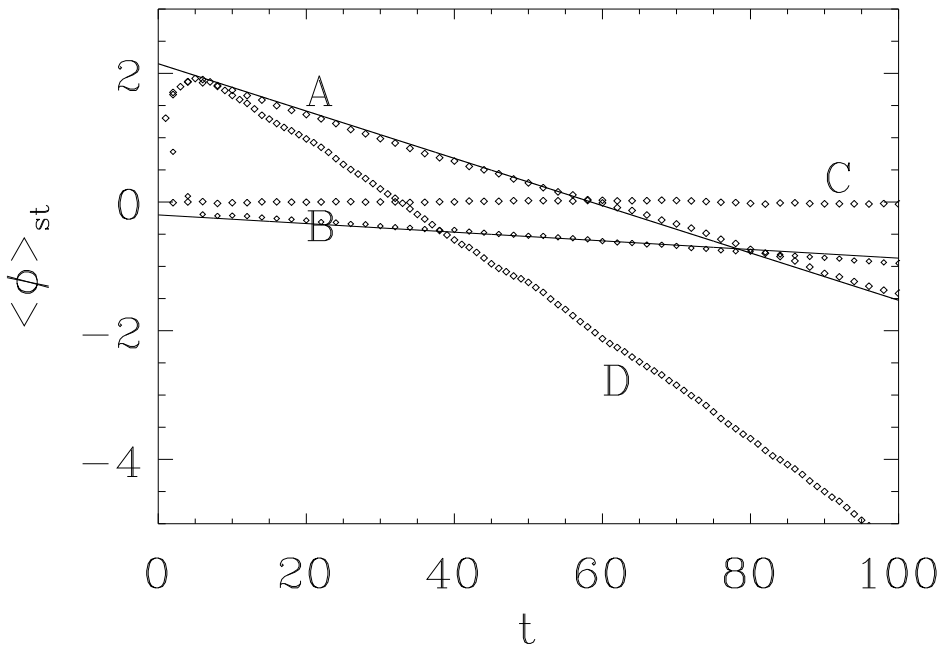

Figure 6.12: Time evolution of the mean value of the phase ϕ in a class A laser without injected signal $\rho = 0$ (line A) and zero–detuning injected signal $\rho = 0.6$, $\eta = 0$ (line B), in the case $\alpha = 2$ there is a linear variation of the mean value of the phase at late times. For $\alpha = 0$ (line C) there is only phase diffusion and the average value is 0 for all times. The solid lines have the slope given by the theoretical prediction Eq. (6.35). Line D: time evolution of $< \phi >_{st} -2\pi t/T$, being T the period of the periodic orbit in the deterministic case, for $\rho = 0.5$, $\eta = 1$. In all the curves: $a = 2$, $b = 1$ and $\epsilon = 0.1$.

Notice that this stochastic frequency shift is zero in the case $\alpha = 0$ or for the deterministic dynamics ($\epsilon = 0$). In the case $\rho = 0$ this expression analytically reduces to (5.23).

For $\rho \neq 0$, one needs to evaluate the expression (6.35) numerically. In all cases, the results are in excellent agreement with numerical simulations of the rate equations in the presence of noise. In Fig. 6.13, we plot the stochastic frequency shift as a function of the noise intensity for several values of ρ. For a fixed value of ρ, $|\Delta\omega|$ increases as ϵ increases, since a larger value of ϵ can induce larger fluctuations and larger excursions in phase space (x_1, x_2) away from the minima of the potential. For fixed ϵ, $|\Delta\omega|$ decreases as ρ increases. This result can be understood by noticing that when ρ is increased, the inclination of the potential increases and the trajectory becomes more confined around a fixed value.

In the case $\rho \neq 0$ and $\eta \neq 0$, the stochastic frequency shift is also present, see Fig. 6.12 (line D), although it is not possible to compute its magnitude because we do not have an explicit expression for the Lyapunov potential.

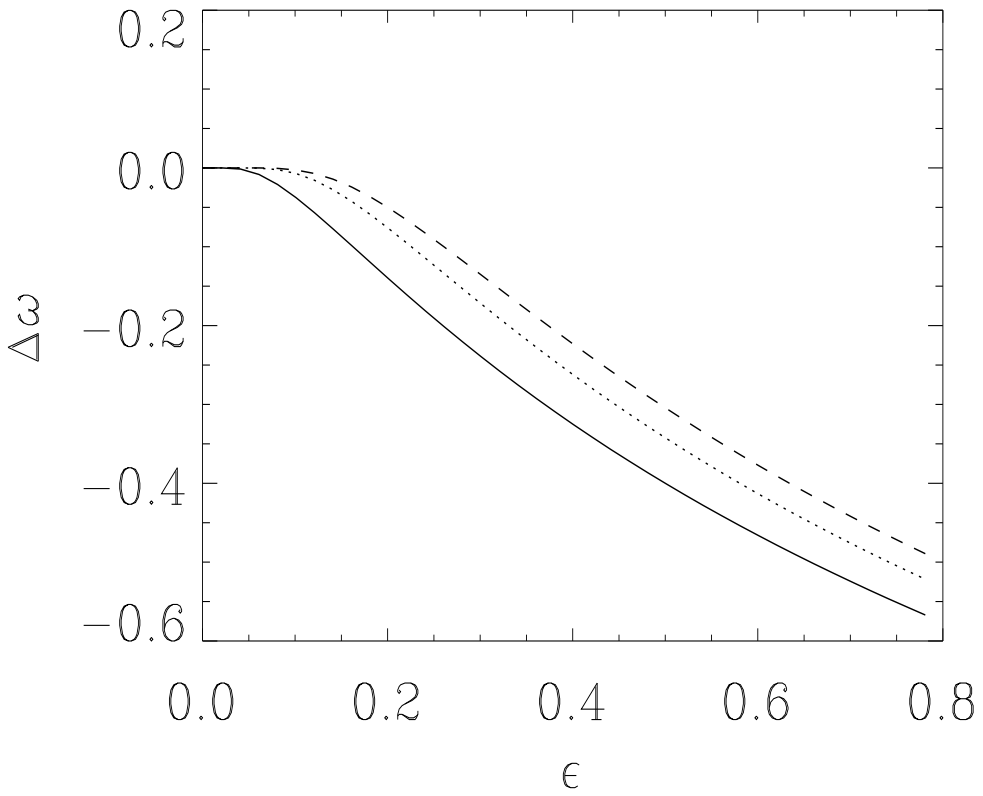

Figure 6.13: Stochastic frequency shift $\Delta\omega \equiv \langle\dot{\phi}\rangle$ in a class A laser for $a = 2$, $b = 1$ and $\alpha = 2$. For $\rho = 0$ (solid line) the explicit result Eq. (5.23) is used, whereas for $\rho = 0.6$ (dotted line) and $\rho = 0.8$ (dashed line) (6.35) has been numerically evaluated.

Part III

Làsers de Classe B

Capítol 7

Làsers de Classe B: Potencial de Lyapunov

En aquest capítol s'estudia la dinàmica del làser de classe B (capítol 4), primer a partir de l'anàlisi numèrica de les equacions i, seguidament aquesta dinàmica s'explica emprant el potencial de Lyapunov (capítol 2) que s'obté.

La dinàmica d'un làser de classe B es descriu mitjançant dues equacions d'evolució, una per a l'amplitud lentament variable del camp elèctric dins la cavitat làser i l'altra per al nombre de portadors. El camp elèctric es pot escriure en termes d'intensitat òptica i fase. En el tractament que es fa en aquest capítol, es menyspreen els termes aleatoris, però es manté el valor mig de l'emissió espontània en l'equació per a la intensitat, Eqs. (7.1 - 7.3). En el cas determinístic, les equacions per a la intensitat del camp elèctric i els portadors no depenen de la variable fase del camp, per tant aquesta variable no es considera en el tractament inicial. L'evolució dinàmica de la intensitat i portadors és tal que ambdues variables arriben a l'estat estacionari realitzant oscil·lacions esmorteïdes amb un període que decreix en el temps, Figs. 7.1, 7.2 i 7.3 .

La dinàmica de la intensitat i portadors es pot explicar mitjançant un potencial de Lyapunov. Un estudi similar s'havia realitzat prèviament [Oppo and Politi, 1985], però sense considerar ni el terme de saturació de guany, ni el valor mig del terme d'emissió espontània. En aquest capítol, s'inclouen aquests dos paràmetres en el potencial (7.14). Observant la seva forma, Fig. 7.4, té un únic mínim, i per tant una única solució estable. El moviment cap a aquest mínim té dues components: una conservativa que produeix trajectòries equipotencials i, una d'esmorteïment que és la responsable de decréixer el valor del potencial. Aquests dos efectes combinats condueixen els sistema cap al mínim seguint un moviment espiral. Els paràmetres de saturació de guany i emissió espontània, inclosos en el tractament potencial, són els responsables d'augmentar els coeficients de la part simètrica de la matriu que associa el potencial i les equacions de moviment, i d'incrementar, com a conseqüència, els termes de dissipació.

La fase del camp elèctric, que oscil·la en el temps fins a arribar a un valor

estacionari, es pot incloure fàcilment en la descripció potencial. Així, el conjunt de les tres variables que descriuen el làser de classe B és de tipus flux potencial no relaxacional (2.26), amb el potencial descrit en el paràgraf anterior (només depenent de la intensitat i el nombre de portadors) i la inclusió de termes addicionals (que contenen el paràmetre α) en la matriu antisimètrica que relaciona el potencial amb les equacions del sistema, (7.23).

Cal indicar que el potencial que s'ha obtingut només és vàlid en el cas determinista, a causa que la matriu que relaciona el gradient del potencial amb les equacions dinàmiques no satisfà la condició fluctuació–dissipació (2.35).

A partir de què el potencial en funció del temps és aproximadament constant entre dos pics de la intensitat, Fig. 7.1, es pot estimar el període de les oscil·lacions de relaxació realitzant un símil mecànic i reduint el problema a un d'energia constant. S'obté una relació entre el període i l'energia del sistema (7.26). Del càlcul numèric d'aquesta expressió, Fig. 7.6, s'observa que el període decreix quan el valor del potencial disminueix. Combinant aquest resultat amb el decreixement temporal del potencial, es pot explicar que el període de les oscil·lacions disminueix en el temps. La comparació dels resultats de l'expressió aproximada i el període real de les simulacions és molt acceptable, Fig. 7.7.

De l'expressió aproximada per al període de les oscil·lacions de relaxació, és possible quantificar la seva discrepància amb el valor exacte a prop de l'estat estacionari. La freqüència exacta de les oscil·lacions de relaxació a prop de l'estacionari és la part imaginària dels autovalors de les equacions d'evolució linealitzades al voltant de la solució estacionària. Els resultats que finalment es comparen són les expressions (7.27) i (7.35).

Per poder entendre completament la variació del període en el temps, caldria avaluar la variació temporal del potencial entre dos pics consecutius d'intensitat. Aquesta variació és deguda al termes dissipatius de les equacions de moviment. Encara que no ha sigut possible obtenir–la exactament, s'ha obtingut una expressió simple a partir d'arguments semi–empírics per a la variació temporal del potencial, Eq. (7.39) i Fig. 7.8. Aquesta expressió es basa en l'evolució de les variables en el temps a prop de l'estacionari. La forma resultant pel potencial, combinat amb què el període és linealment relacionat amb el potencial, suggereix una expressió semi–empírica per a l'evolució temporal del període, Eq. (7.40). L'expressió senzilla resultant, decaïment exponencial del període, ajusta no només a l'estacionari, sinó també en el règim transitori, Figs. 7.7 i 7.9.

Chapter 7

Class B Lasers: Lyapunov Potential

In this chapter, we describe the dynamics of class B lasers in terms of a Lyapunov potential function.

7.1 Model

The dynamics of a typical class B laser, for instance a single mode semiconductor laser, can be described in terms of two evolution equations, one for the slowly varying complex amplitude E of the electric field inside the laser cavity and the other for the carriers number N (or electron-hole pairs), Eqs. (4.11) and (4.12) [Agrawal and Dutta, 1986]. These equations include noise terms accounting for the stochastic nature of spontaneous emission and random non–radiative carrier recombination due to thermal fluctuations. Both noise sources are usually assumed to be white Gaussian noise sources.

The equation for the electric field can be written in terms of the optical intensity I (normalized in such a way that I is equal to the number of photons inside the cavity) and the phase ϕ by defining $E = \sqrt{I}\, e^{\mathrm{i}\phi}$. For simplicity, we neglect the explicit random fluctuations terms and retain, as usual [Agrawal and Dutta, 1986], the mean power of the spontaneous emission. The equations are (4.14 - 4.16) without the explicit fluctuating stochastic terms

$$\frac{dI}{dt} = [G(N,I) - \gamma]\, I + 4\,\varepsilon\, N, \tag{7.1}$$

$$\frac{d\phi}{dt} = \frac{1}{2}\,\alpha\,[G(N,I) - \gamma], \tag{7.2}$$

$$\frac{dN}{dt} = \frac{J}{e} - \gamma_N\, N - G(N,I)\, I. \tag{7.3}$$

$G(N,I)$ is the material gain given by

$$G(N,I) = g_N\, \frac{(N - N_o)}{1 + s\, I}. \tag{7.4}$$

Table 7.1: Definitions and typical values of the parameters for semiconductor lasers.

PARAMETERS		VALUES
J/e	Carriers injected per unit time	$>$ threshold
γ	Cavity decay rate	$0.5\,\mathrm{ps}^{-1}$
γ_N	Carrier decay rate	$0.001\,\mathrm{ps}^{-1}$
N_o	Number of carriers at transparency	1.5×10^8
g_N	Differential gain parameter	$1.5 \times 10^{-8}\,\mathrm{ps}^{-1}$
s	Gain saturation parameter	$10^{-8} - 10^{-7}$
ε	Spontaneous emission rate	$10^{-8}\,\mathrm{ps}^{-1}$
α	Linewidth enhancement factor	$3 - 6$

The definitions and typical values of the parameters for some semiconductor lasers are given in Table 7.1. While the first term of Eq. (7.1) accounts for the stimulated emission, the second one accounts for the mean value of the spontaneous emission in the lasing mode. Eqs. (7.1 - 7.3) are written in the reference frame in which the frequency of the *on* state is zero when spontaneous emission noise is neglected. The threshold condition for lasing is obtained by setting $G(N, I) = \gamma$, $I = 0$ and neglecting spontaneous emission. The number of carriers at threshold is given by $N_{th} = N_o + \frac{\gamma}{g_N}$, and the threshold current is $J_{th} = e\gamma_N N_{th}$, and represents the minimum injection current needed to fully compensate the losses. Eq. (7.2) shows that $\dot{\phi}$ is linear with N and slightly (due to the smallness of the saturation parameter s, see Table 7.1) nonlinear with I.

Since in the deterministic case considered henceforth the evolution equations for I and N do not depend on the phase ϕ, we can concentrate only on the evolution of I and N. One can obtain a set of simpler dimensionless equations by performing the following change of variables

$$y = \frac{2\,g_N}{\gamma}\,I,\; z = \frac{g_N}{\gamma}\,(N - N_o),\; \tau = \frac{\gamma}{2}\,t. \tag{7.5}$$

The equations then become

$$\frac{dy}{d\tau} = 2\left(\frac{z}{1+\bar{s}\,y} - 1\right) y + c\,z + d\,, \tag{7.6}$$

$$\frac{dz}{d\tau} = a - b\,z - \frac{z\,y}{1+\bar{s}\,y}, \tag{7.7}$$

where we have defined

$$a = \frac{2\,g_N}{\gamma^2}\left(\frac{J}{e} - \gamma_N\,N_o\right), \tag{7.8}$$

$$b = \frac{2\,\gamma_N}{\gamma}, \tag{7.9}$$

$$
\begin{aligned}
c &= \frac{16\,\varepsilon}{\gamma}, \\
d &= \frac{16\,\varepsilon\,g_N\,N_o}{\gamma^2}, \\
\bar{s} &= \frac{s\,\gamma}{2\,g_N}.
\end{aligned}
\tag{7.10}
$$

The injected current, J, which is externally controlled, is contained in a. The effect of the spontaneous emission term, ε, appears in c and d. Equations (7.6, 7.7) form the basis of our subsequent analysis. The steady states are

$$
y_{st} = \frac{1}{4\,(1+b\,\bar{s})}[2\,(a-b)+d\,(1+b\,\bar{s})+c\,a\,\bar{s}+\sqrt{v}], \tag{7.11}
$$

$$
z_{st} = \frac{a\,(1+\bar{s}\,y_{st})}{b+y_{st}\,(1+b\,\bar{s})}, \tag{7.12}
$$

where the constant v is given by

$$
\begin{aligned}
v &= 4\,(a-b)^2+4\,d\,(a+b)\,(1+b\,\bar{s})+d^2\,(1+b\,\bar{s})^2 \\
&+ c\,[8\,a+4\,a\,\bar{s}\,(a+b)+2\,d\,a\,\bar{s}\,(1+b\,\bar{s})]+c^2\,a^2\,\bar{s}^2.
\end{aligned}
\tag{7.13}
$$

For a value of the injected current below threshold ($J < J_{th}$ or equivalently to $a-b<0$), y_{st} is very small. This corresponds to the *off* solution in which the only emitted light corresponds to the spontaneous emission.

There is another solution for y_{st} given by Eq. (7.11) with a minus sign in front of $\sqrt{v}$ which, however, does not correspond to any possible physical situation, since it yields $y_{st}<0$.

In the absence of noise, saturation and stimulated emission terms, the steady states are: *off* state, $y_{st}=0$, $z_{st}=a/b$ and *on* state, $y_{st}=a-b$, $z_{st}=1$. Above threshold, stimulated emission occurs and the laser operates in the *on* state with large y_{st}. In what follows, we will concentrate on the evolution following the laser switch–on to the *on* state.

It is known that the dynamical evolution of y and z is such that they both reach the steady state by performing damped oscillations [Agrawal and Dutta, 1986] whose period decreases with time. This fact is different from the usual relaxation oscillations that are calculated near the steady state by linearizing the dynamical equations. The time evolution of y and z is shown in Figs. 7.1 and 7.2, while the corresponding projection in the (y,z) phase–plane is shown in Fig. 7.3.

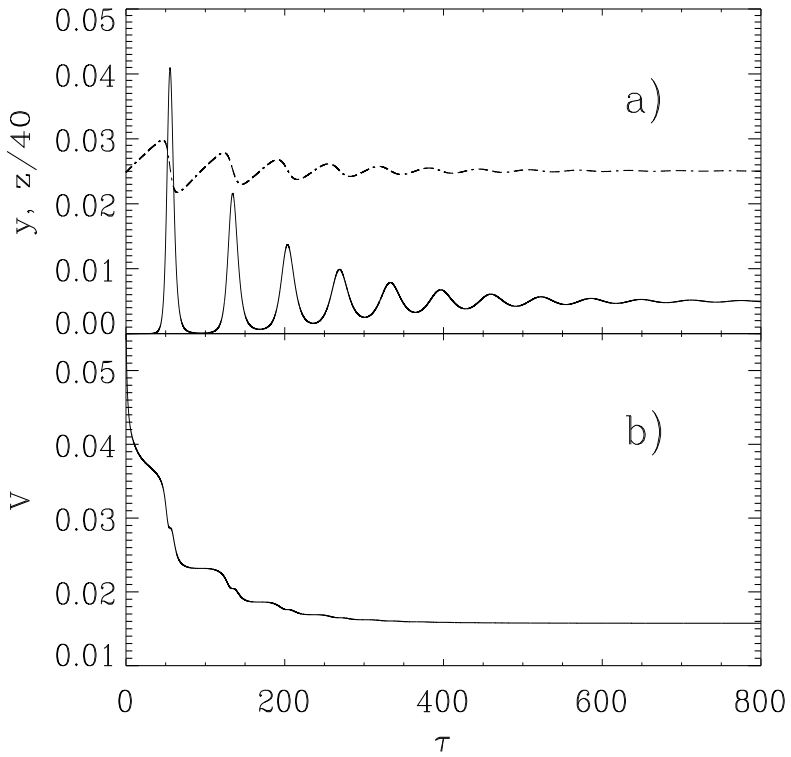

Figure 7.1: a) Normalized intensity, y (solid line) and normalized carriers number, $z/40$ (dot–dashed line) versus time in a class B laser obtained by numerical solution of Eqs. (7.6) and (7.7). b) Plot of the potential (7.14). Parameters: $a = 0.009$, $b = 0.004$, $\bar{s} = 0.5$, $c = 3.2 \times 10^{-9}$, $d = 1.44 \times 10^{-8}$ which correspond to physical parameters in Table 7.1 with $J = 1.2\, J_{th}$. The initial conditions are taken as $y = 5 \times 10^{-8}$ and $z = 0.993$. Dimensionless units.

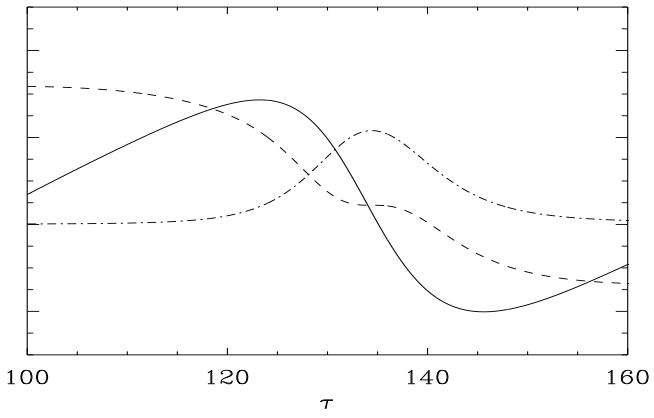

Figure 7.2: Enlargement of Fig. 7.1. z (solid line), y (dot–dashed) line and V (dashed line), (different variables have been rescaled in other to fit the same vertical scale). Same parameters than in Fig. 7.1.

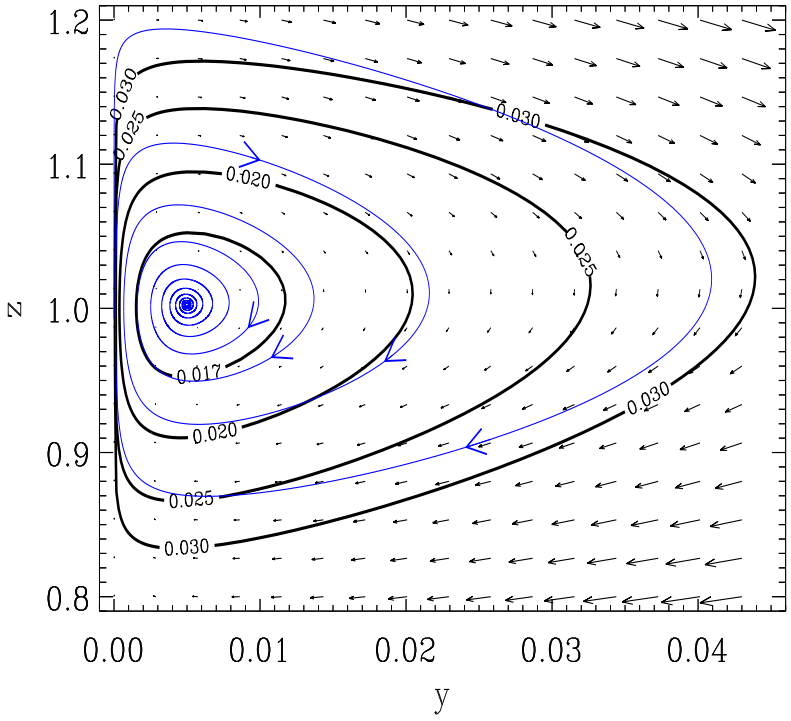

Figure 7.3: Number of carriers versus intensity (scaled variables), blue line. The vector field and contour plot (thick lines) are also represented. Same parameters than in Fig. 7.1. Dimensionless units.

7.2 Potential for class B lasers

We are interested in obtaining a Lyapunov potential that can help us to explain the dynamics observed in the previous section. A similar study was done in Toda potential [Oppo and Politi, 1985] without considering neither the saturation term nor the mean value of the spontaneous emission power, and under those conditions an expression for the period of the transient oscillations was obtained. In our work, we calculate the period of the oscillations by taking into account these two effects. However, the potential is only valid in the deterministic case, since we have not been able to obtain a potential such that the symmetric matrix S, relating the gradient of the potential to the dynamical equations [see Eq. (2.28)] satisfies the fluctuation–dissipation relation (2.35).

The period is obtained in terms of the potential, by assuming that the latter has a constant value during one period. It will be shown that this assumption works reasonably well and gives a good agreement with numerical calculations. Near the steady state, the relaxation oscillations can be also calculated in this form, but the potential is almost constant and consequently is the period.

The evolution equations (7.6, 7.7) can be cast in the form of a non–relaxational potential flow, Eq. (2.26), with the following Lyapunov potential

$$V(y,z) = a_1\, y + a_2\, y^2 + a_3 \ln(y) + \frac{a_4}{y} + \frac{1}{2}\, B^2(y,z), \tag{7.14}$$

where

$$\begin{aligned} a_1 &= \frac{1}{2} - \frac{1}{2}\, a\, \bar{s} + b\, \bar{s} - \frac{1}{4}\, \bar{s}\, d\, (1 + b\, \bar{s}) - \frac{1}{4}\, a\, \bar{s}^2\, c, \\ a_2 &= \frac{\bar{s}}{4}\, (1 + b\, \bar{s}), \qquad (7.15) \\ a_3 &= -\frac{1}{2} \left(a - b + (a\, c + b\, d)\, \bar{s} + \frac{d}{2} \right), \\ a_4 &= \frac{(a\, c + b\, d)}{4}, \\ B(y,z) &= z - 1 - \bar{s}\, y + \frac{(d + c\, z)}{2y}\, (1 + \bar{s}\, y). \qquad (7.16) \end{aligned}$$

The corresponding (nonconstant) matrix D is given by

$$D = \begin{pmatrix} 0 & -D_{12} \\ D_{12} & D_{22} \end{pmatrix}, \tag{7.17}$$

being

$$D_{12} = \frac{4\, y^2}{(1 + \bar{s}\, y)\, [2\, y + c\, (1 + \bar{s}\, y)]}, \tag{7.18}$$

$$D_{22} = \frac{4\, y\, [(1 + 2\, \bar{s} + b\, \bar{s})\, y^2 + b\, y + d + c\, z]}{(1 + \bar{s}\, y)\, [2\, y + c\, (1 + \bar{s}\, y)]^2}. \tag{7.19}$$

According to the general results of section 2.2, it is possible to split the dynamics in purely relaxational part plus a conservative part. The conservative part corresponds to the antisymmetric components of matrix D and, in this case, can be obtained simply by setting $D_{22} = 0$.

The form of the potential appears in Fig. 7.4.

This potential reduces to the one obtained in Ref. [Oppo and Politi, 1985] when setting $c = d = \bar{s} = 0$ (which corresponds to setting the laser parameters $\varepsilon = s = 0$). The potential in this case takes an easier form

$$V(y,z) = \frac{1}{2}[y - (a - b) \ln(y)] + \frac{1}{2}(z - 1)^2, \tag{7.20}$$

with the corresponding matrix

$$D = \begin{pmatrix} 0 & -2y \\ 2y & b + y \end{pmatrix}. \tag{7.21}$$

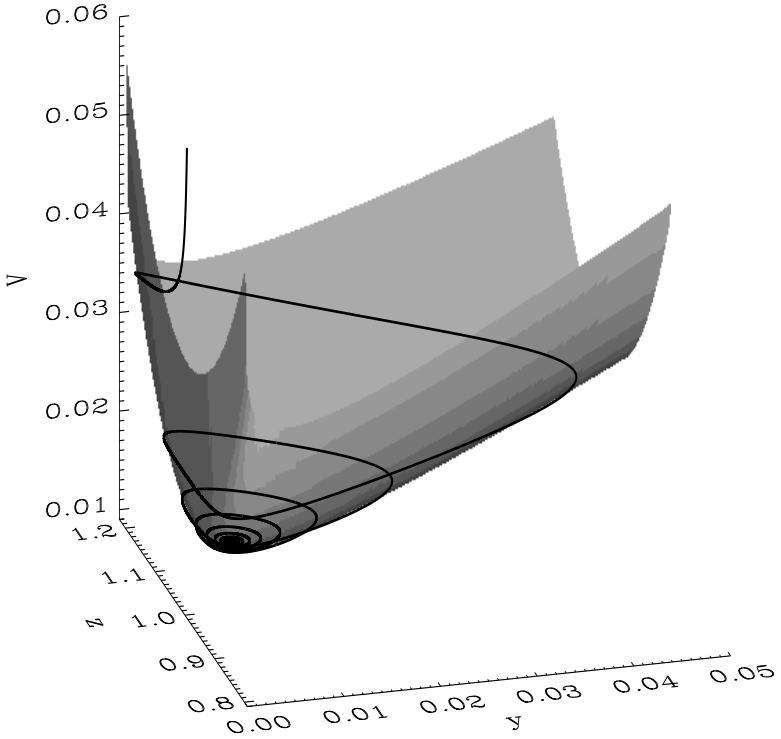

Figure 7.4: Potential for a class B laser. Solid line: simulation of Eqs. (7.6) and (7.7). Same parameters than in Fig. 7.1. Dimensionless units.

As expected, non–vanishing values for the parameters s and ε increase the dissipative part of the potential (D_{22}) associated with the damping term. This is in accordance with the result of Lee and Shin [Lee and Shin, 1989] when linearizing the rate equations around the steady state.

The equipotential lines of (7.14) are also plotted in Fig. 7.3. It is observed that there is only one minimum for V and hence the only stable solution (for this range of parameters) is that the laser switches to the *on* state and relaxes to the minimum of V. The movement towards the minimum of V has two components: a conservative one that produces closed equipotential trajectories and a damping that decreases the value of the potential. The combined effects drives the system to the minimum following a spiral movement, best observed in Figs. 7.3 and 7.4.

In the absence of saturation and noise, $\bar{s} = 0$, $c = 0$, $d = 0$, the maxima and minima of the dynamical variable $y(t)$ occur always at $z = 1$. This is because the equipotential lines of V in the plane (y, z) are symmetric around the line $z = 1$, see Eq. (7.20). However, for other nonzero values of $\bar{s}$, c, d, the potential changes slighty its "orientation" in the plane (y, z) and the maxima of $y(t)$ are not at the previous value of z, but instead satisfy the relationship obtained by cancelling (7.6),

see Fig. 7.3.

Let us consider again the potential (7.14). This potential only depends on the intensity and not on the phase of the electric field. However, the equation for the phase, in the normalized variables,

$$\frac{d\phi}{d\tau} = \left[\frac{z}{(1+\bar{s}\,y)} - 1\right]\alpha, \tag{7.22}$$

can be also deduced from the potential. The full system can be written as

$$\begin{pmatrix} \frac{dy}{d\tau} \\ \frac{d\phi}{d\tau} \\ \frac{dz}{d\tau} \end{pmatrix} = \begin{pmatrix} 0 & 0 & -D_{12} \\ 0 & 0 & -D_{13} \\ D_{12} & D_{13} & D_{22} \end{pmatrix} \begin{pmatrix} \frac{\partial V}{\partial y} \\ \frac{\partial V}{\partial \phi} \\ \frac{\partial V}{\partial z} \end{pmatrix}, \tag{7.23}$$

where

$$D_{13} = -\frac{\left(\frac{d\phi}{d\tau}\right)}{\left(\frac{\partial V}{\partial z}\right)} = -\frac{\left(\frac{z}{(1+\bar{s}y)} - 1\right)}{B(y,z)\left[1 + \frac{c}{2y}(1+\bar{s}y)\right]}\,\alpha, \tag{7.24}$$

and $B(y,z)$ is defined by (7.16). D_{13} it can be introduced as an antisymmetric term in the matrix D because the potential does not depend on ϕ, so the equation for z is not modified. In the case $\bar{s} = c = d = 0$, it is $D_{13} = -\alpha$.

An interesting feature of the phase is that it oscillates until it arrives to a stationary value, see Fig. 7.5. This change in time is due to the extra dependence on the variable z. This behaviour is different from the one of the class A laser in which the phase increases or decreases monotonously, see Fig. 5.1 (b).

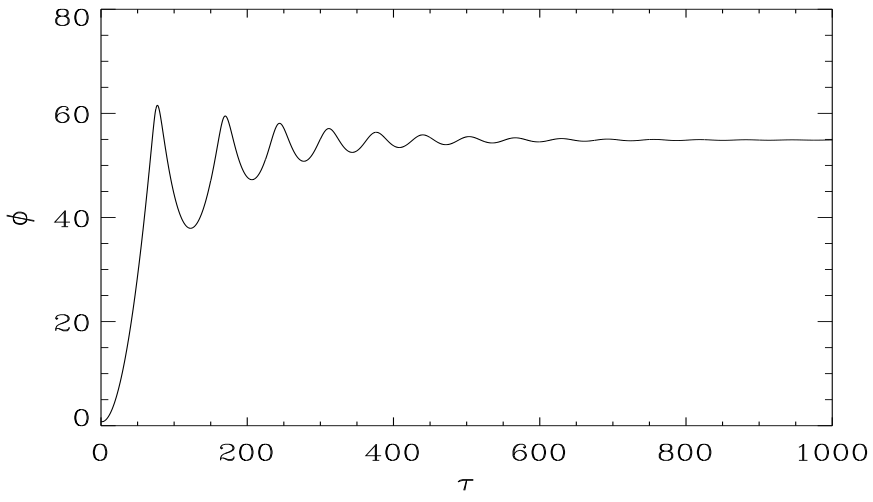

Figure 7.5: Phase of the electric field versus time in a class B laser obtained by numerical solution of Eqs. (7.1 - 7.3). Same parameters than in Fig. 7.1. $\alpha = 5$. Dimensionless units.

7.2.1 Period of the relaxation oscillations

The time evolution of the potential is plotted in Fig. 7.1. In this figure it can be seen that the Lyapunov potential is approximately constant between two consecutive peaks of the relaxation oscillations as it can be also observed with the equipotential lines of Fig. 7.3 (however, in the peak of intensity, the potential decreases steeply, as can be seen in Fig. 7.2). This fact allows us to estimate the relaxation oscillation period by approximating $V(y,z) = E$, constant, during this time interval. When the potential is considered as constant, the period can be evaluated by the standard method of elementary Mechanics: z is replaced by its expression obtained from (7.6) in terms of y and $\dot{y}$ in $V(y,z)$. Using the condition that $V(y,z) = E$, we obtain

$$E = a_1\, y + a_2\, y^2 + a_3\, \ln(y) + a_4 \frac{1}{2} + \frac{1}{2}\left[\frac{\dot{y}}{y}\frac{(1+\bar{s}\, y)}{2}\right]^2 . \tag{7.25}$$

From this equation, we can calculate the relaxation oscillation period T, by using $\dot{y} = \frac{dy}{dt}$ and integrating over a cycle. This leads to the expression

$$T = \int_{y_a}^{y_b} \frac{1+\bar{s}\, y}{y} \frac{dy}{\left[2\left(E - a_1\, y - a_2\, y^2 - a_3\, \ln(y) - a_4\, y^{-1}\right)\right]^{1/2}}, \tag{7.26}$$

where y_a and y_b are the values of y that cancel the denominator. We stress the fact that the only approximation used in the derivation of this expression is that the Lyapunov potential is constant during two maxima of the intensity oscillations. In other words, we have made a mechanical simile and reduced the problem to one with constant energy. A numerical evaluation of this integral yields the dependence of the period, T, with the value of the energy, $E = V$, as plotted in Fig. 7.6.

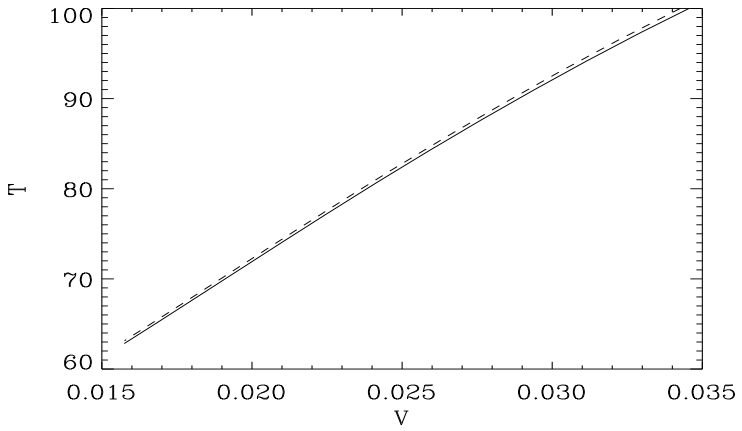

Figure 7.6: Period versus potential for a class B laser obtained with (7.26). Solid line $\bar{s} = 0$, dashed line $\bar{s} = 2$. Other parameters, same than in Fig. 7.1. Dimensionless units.

Equation (7.26) reduces, in the case $c = d = \bar{s} = 0$, to the one previously obtained by using the relation between the laser dynamics and the Toda oscillator derived in [Oppo and Politi, 1985].

According to Fig. 7.6, the period T decreases as the potential V decreases. Since the Lyapunov potential decreases with time, this explains the fact that the period of the oscillations in the transient regime decreases with time. In Fig. 7.7, we compare the results obtained with the expression (7.26) for the period with the ones obtained from numerical simulations of the rate equations (7.6, 7.7). In the simulations we compute the period as the time between two peaks in the evolution of the variable y. As seen in this figure, the above expression for the period, when using the numerical value of the potential V, accurately reproduces the simulation results although it is systematically lower than the numerical result. The discrepancy is less than one percent over the whole range of times.

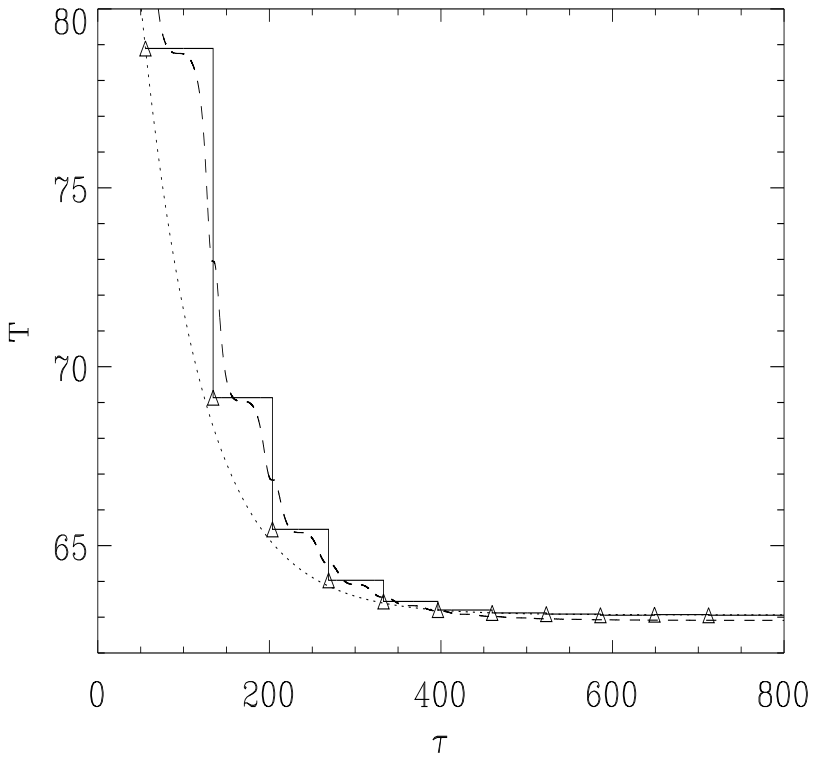

Figure 7.7: Period versus time in a class B laser. Solid line has been calculated as the distance between two peaks of intensity, with triangles plotted at the beginning of each period; dashed line has been calculated using the expression (7.26), with the value of the potential V obtained also from the simulation; dotted line corresponds to the semi-empirical expression (7.40). Same parameters than in Fig. 7.1. We have used $\tau_0 = 55.55$, coinciding with the position of the first intensity peak. Dimensionless units.

It is possible to quantify the difference between the approximate expression (7.26) and the exact values near the stationary state.

By considering (7.26) near the steady state with $y = y_{st} + \delta y$, $E = V_{st} + \delta V$ ($V_{st} = V(y_{st}, z_{st})$) and retaining the lowest terms in δy and δV, one can perform the integral analytically, obtaining an approximation for the period of the steady state

$$T_{st,ap} = \frac{2\,\pi}{D_{12,st}\,\sqrt{K\,F - H^2}}, \tag{7.27}$$

where

$$\begin{aligned} K &= 2\left(a_2 - \frac{1}{2}\,\frac{a_3}{y_{st}^2} + \frac{a_4}{y_{st}^3} + \frac{1}{2}\left[\bar{s} + \frac{(d + c\,z_{st})}{2\,y_{st}^2}\right]^2\right), \\ F &= \left[1 + c\,\frac{(1 + \bar{s}\,y_{st})}{2\,y_{st}}\right]^2, \\ H &= -\left[1 + \frac{c\,(1 + \bar{s}\,y_{st})}{2\,y_{st}}\right]\left[\bar{s} + \frac{(d + c\,z_{st})}{2\,y_{st}^2}\right], \end{aligned} \tag{7.28}$$

and $D_{12,st}$ is the coefficient D_{12} calculated in the steady state.

The result (7.27) could be obtained starting from the linearization of potential (7.25), expanding this expression near the steady state, and then calculate the period from the resulting expression.

The period of the relaxation oscillations near the steady state can also be obtained by the standard procedure of linearizing the evolution equations near the steady state solution. Applying a small perturbation $y = y_{st} + \delta y$ and $z = z_{st} + \delta z$ to Eqs. (7.6) and (7.7), one has after linearization

$$\dot{\delta y} = a_{11}\,\delta y + a_{12}\,\delta z, \tag{7.29}$$

$$\dot{\delta z} = a_{21}\,\delta y + a_{22}\,\delta z, \tag{7.30}$$

where

$$\begin{aligned} a_{11} &= 2\left(\frac{z_{st}}{(1 + \bar{s}\,y_{st})^2} - 1\right), \\ a_{12} &= \left(\frac{2\,y_{st}}{1 + \bar{s}\,y_{st}} + c\right), \\ a_{21} &= -\frac{z_{st}}{(1 + \bar{s}\,y_{st})^2}, \\ a_{22} &= -\left(b + \frac{y_{st}}{1 + \bar{s}\,y_{st}}\right). \end{aligned} \tag{7.31}$$

The eigenvalues of the linearized equations (7.29) and (7.30) are

$$\lambda = -\frac{\varrho}{2} \pm i\,\omega, \tag{7.32}$$

with

$$\varrho = -(a_{11} + a_{22}), \tag{7.33}$$

$$\omega = \frac{1}{2}\sqrt{|(a_{11} - a_{22})^2 + 4\, a_{12}\, a_{21}|}. \tag{7.34}$$

The frequency ω of the relaxation oscillations near the steady state is the imaginary part of the eigenvalues of the linearized equations (7.29) and (7.30). This yields a period $T_{st} = 2\,\pi/\omega$ which can be rewritten in terms of K, F, H, $D_{12,st}$ and $D_{22,st}$ in order to have a better comparison with the approximate period (7.27)

$$T_{st} = \frac{2\,\pi}{D_{12,st}\,\sqrt{K\,F - H^2}}\left[1 - \frac{D_{22,st}^2}{D_{12,st}^2}\frac{F^2}{4\,(K\,F - H^2)}\right]^{-1/2}. \tag{7.35}$$

The difference between (7.27) and (7.35) vanishes with $D_{22,st}$ (i.e. D_{22} in the stationary state). Since $K\,F - H^2$ is always a positive quantity, our approximation will give, at least asymptotically, a smaller value for the period.

In order to have a complete understanding of the variation of the period with time, we need to compute the time variation of the potential $V(\tau)$ between two consecutive intensity peaks. This variation is induced by the dissipative terms in the equations of motion. Although we were not able to derive an expression for the variation of the potential (see [Oppo and Politi, 1985] for an approximate expression in a simpler case), we found that a semi–empirical argument can yield a very simple law which is well reproduced by the simulations. We start by studying the decay to the stationary state in the linearized equations. After expanding around the steady state, the dynamical equations (7.29) and (7.30) show that the variables decay to the steady state as

$$\delta y(\tau), \delta z(\tau) \propto \exp(-\frac{\varrho}{2}\tau), \tag{7.36}$$

where ϱ, (7.33), can be rewritten as

$$\varrho = D_{22,st}\; F. \tag{7.37}$$

In the case of $\bar{s} = 0$, $c = 0$ and $d = 0$ (neither saturation term nor spontaneous emission term are considered) $\varrho = a$.

Expanding $V(y, z)$ around the steady state (y_{st} and z_{st} correspond to extrema of the potential), it is found that

$$V - V_{st} \propto \delta y^2, \delta z^2, \delta y\, \delta z\,. \tag{7.38}$$

Using (7.36) and taking the initial condition at an arbitrary τ_0 we find an expression for the decay of the potential

$$V(\tau) - V_{st} = [V(\tau_0) - V_{st}] \exp\left(-\varrho\,(\tau - \tau_0)\right). \tag{7.39}$$

In Fig. 7.8 we plot $\ln[V(\tau) - V_{st}]$ versus time and compare it with the approximation (7.39). One can see that it fits $\ln[V(\tau) - V_{st}]$ reasonably well not only near the steady state (where it was derived), but also during the transient dynamics. The value of τ_0, being a free parameter, was chosen at the time at which the first peak of the intensity appeared. Although other values of τ_0 might produce a better fit, the one chosen here has the advantage that it can be calculated analytically by following the technique of Ref. [Balle *et al.*, 1991]. It can be derived from Eq. (7.26) that the period T depends linearly on the potential V. This fact, combined with the result of Eq. (7.39), suggests the semi–empirical law for the evolution of the period

$$T(\tau) - T_{st} = [T(\tau_0) - T_{st}] \exp\left(-\varrho\,(\tau - \tau_0)\right). \tag{7.40}$$

This simple expression fits well the calculated period not only near the steady state, but also in the transient regime, see Figs. 7.7 and 7.9. The small differences observed near the steady state are due to the fact that the semi–empirical law, Eq. (7.40), is based on the validity of Eq. (7.26) between the period and the potential. As it was already discussed above, that expansion slightly underestimates the asymptotic (stationary) value of the period. By complementing this study with the procedure given in [Balle *et al.*, 1991] to describe the switch–on process of a laser, and valid until the first intensity peak is reached, we can obtain a complete description of the variation of the oscillations period in the dynamical evolution following the laser switch–on.

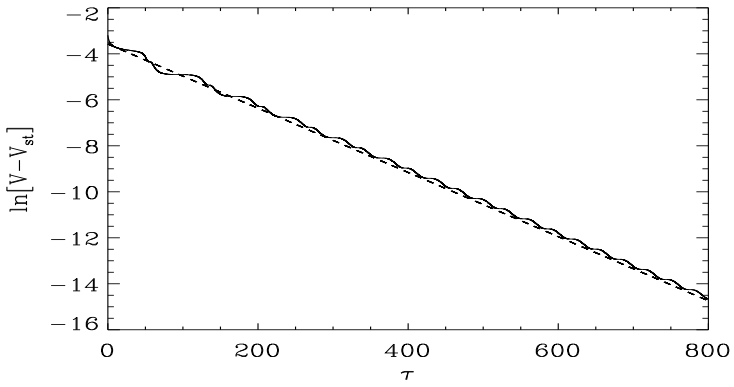

Figure 7.8: Logarithm of the potential difference versus time in a class B laser (solid line), compared with the theoretical expression in the steady state (7.39) (dashed line). Same parameters than in Fig. 7.1 and τ_0 as in Fig. 7.7. Dimensionless units.

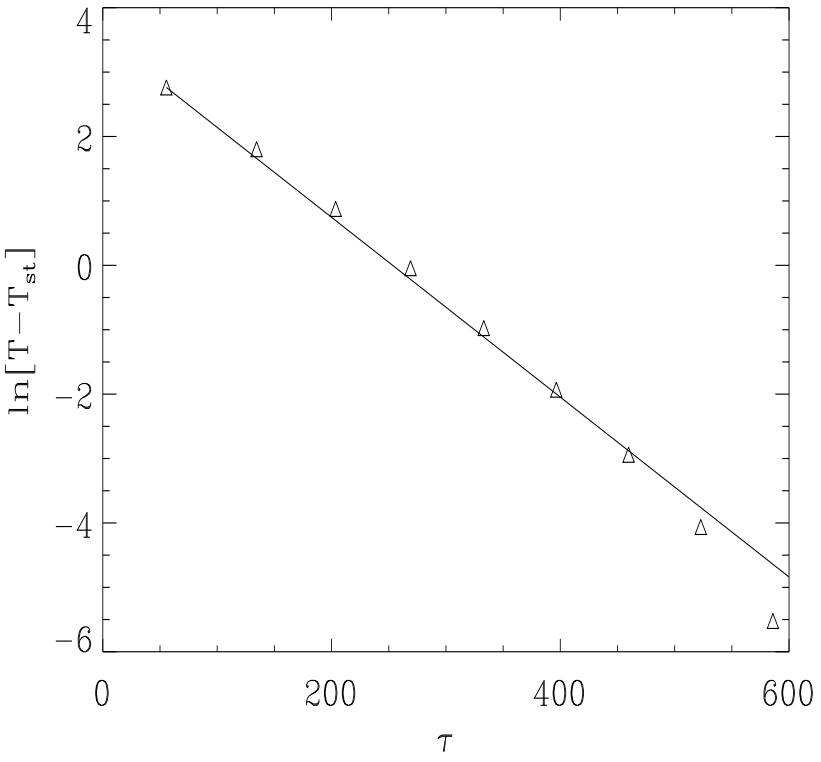

Figure 7.9: Logarithm of the period difference versus time in a class B laser. Triangles correspond to the period calculated from the simulations as the distance between two consecutive intensity peaks, at the same position than in Fig. 7.8. The solid line is the semi–empirical expression Eq. (7.40). Same parameters than in Fig. 7.1 and τ_0 as in Fig. 7.7. Dimensionless units.

Capítol 8

Estructura de resonàncies en un làser de classe B amb senyal injectat

En aquest capítol es descriu la dinàmica qualitativa i el conjunt parcial de bifurcacions (capítol 3) per a un làser de classe B amb senyal injectat amb termes de disintonia petits. El treball d'aquest capítol completa una sèrie d'estudis (veure la secció 1.2) sobre bifurcacions en làsers amb senyal injectat en la proximitat de la singularitat Hopf–sella–node.

Les equacions de balanç (capítol 4) en un sistema de referència que gira a la freqüència del senyal injectat són les (8.1) per al camp elèctric, E, i el nombre de portadors, W. El camp injectat està caracteritzat per l'amplitud β, i la freqüència η. Per al tractament que es fa en aquest capítol s'agafa un valor pel paràmetre de disintonia amb el qual les equacions queden tipus II de la bifurcació Hopf–sella–node.

En les distintes seccions d'aquest capítol es van introduint a poc a poc els distints conjunts invariants del sistema i les seves bifurcacions a causa de la complexitat del conjunt complet de bifurcacions. S'han seleccionat distints colors per a cada tipus de bifurcacions. El conjunt final obtingut és el de la figura 8.22.

La bifurcació sella–node (punts vermells) i la bifurcació de Hopf (punts blaus) dels punts fixos de les equacions, es poden calcular analíticament (8.4 - 8.6). La seva intersecció dóna el punt Hopf–sella–node. Aquestes bifurcacions separen les regions de l'espai de paràmetres (β, η) segons l'estabilitat dels punts fixos A, B i C, Fig. 8.1. A la regió 1, A és estable, B inestable i C sella; un parell d'aquests punts fixos s'aniquilen quan es creua els costats del triangle: cap a la regió 4, B i C col·lapsen; cap a les regions 6, 3 i $3'$, A i B s'aniquilen deixant en aquestes regions el punt C. Un punt fix estable existeix en les regions 1, 4 i 5, que correspon, en termes físics, a tenir una freqüència de sortida sintonitzada amb la d'entrada. El punt fix C correspon a l'estat del làser apagat, i en totes les regions d'interès és un punt sella.

La bifurcació de Hopf (primària) ocorr o bé en el punt fix A ò B, creant una òrbita periòdica transversal, T, al pla $W = 0$. Realitzant un circuit tancat al voltant

del punt Hopf–sella–node: de 1 a 5, el punt B inestable torna sella i es crea l'òrbita T inestable. Aquesta òrbita existeix fins a la regió 3, allà sofreix una bifurcació de Hopf (secundària) quan passa a la regió $3'$, creant un torus transversal inestable, Fig. 8.3. L'òrbita T estable continua existint en la regió 2, i mor en la bifurcació de Hopf (primària) amb el punt fix A. L'òrbita T té un període que divergeix per a valors de β petits (Fig. 8.10), desapareixent a l'òrbita homoclínica a C, Fig. 8.2.

Per completar el conjunt d'invariants en les regions 3 i $3'$, cal incloure una òrbita periòdica longitudinal, L, que és aproximadament coplanar al pla $W = 0$. Aquesta òrbita, estable a 3 però inestable a $3'$, té un període que divergeix a la bifurcació sella–node (bifurcació d'Andronov, Fig. 8.21).

Els punts fixos A i B, juntament amb l'òrbita T corresponen a l'escenari Hopf–sella–node tipus *II*. L'òrbita L és una part integral del conjunt de bifurcacions, i la interacció de les bifurcacions que sofreixen aquestes dues òrbites organitza l'estructura de resonàncies. La bifurcació de Hopf secundària s'interrompeix en una illa de bifurcacions de període doble d'òrbites periòdiques (cercle blau figura 8.2) i acaba en una bifurcació sella–node d'òrbites periòdiques (triangle rosa).

El moviment quasi–periòdic pot sofrir fenòmens de resonància i generar òrbites periòdiques. Aquestes òrbites poden ésser classificades per un nombre p de voltes seguint l'òrbita primària, T, i q que denota el nombre de voltes fetes al voltant l'òrbita primària abans de tancar–se. A la figura 8.7, es veu l'estructura de resonàncies per distints valors de q. Les línies en color rosa corresponen a bifurcacions sella–node d'òrbites periòdiques. Per a $q > 4$ es comporten com l'estructura estàndard de llengües d'Arnold i es van acumulant cap el punt Hopf–sella–node.

L'estructura de les òrbites periòdiques dins cada resonància és bastant similar. Com exemple s'estudia la resonància 3, Fig. 8.9. A la figura 8.10 (a), es veu que per a β a prop de la bifurcació de Hopf secundària de T, una òrbita periòdica inestable i una sella neixen i tornen a col·lapsar en un valor de β més gran a la bifurcació sella–node revers. Per a un valor de η més baix, Fig. 8.10 (b), la branca inestable té un període que divergeix i s'originen dues bifurcacions homoclíniques (cercle verd de la figura 8.9). El tall de la figura 8.10 (c) indica que l'òrbita periòdica resonant es junta amb l'òrbita L. Aquest procés d'unió de les resonàncies transversal en la solució de l'òrbita periòdica s'observa a totes les resonàncies. A prop del procés d'unió s'observa que l'òrbita L també bifurca en una Hopf secundària (línies negres per valors de β grans), que té així mateix té resonàncies 1/2 (cercles color blau corresponents a bifurcacions de període doble).

Les resonàncies fortes ($q \leq 4$) tenen una estructura més complicada que la indicada. En particular, les bifurcacions sella–node de les llengües no ocorr en el torus. El torus pot créixer quan els paràmetres canvien i col·lisionar amb una òrbita resonant. Això corresponen a una bifurcació homoclínica a una òrbita periòdica amb la destrucció final del torus (diamands negres). Els punts d'intersecció d'aquestes homoclíniques, les Hopf secundàries i les resonàncies corresponen a singularitat tipus Takens–Bogdanov, Fig. 8.15.

Entre les resonàncies transversals indicades, s'han obtingut altres resonàncies, Fig. 8.18, encara que una classificació de les mateixes és prou complicada.

Chapter 8

Resonance structure in a class B laser with injected signal

In this chapter, we describe the qualitative dynamics and bifurcation set for a laser with injected signal for small cavity detunings by using the definitions included in chapter 3.

The work presented in this chapter completes the above series of studies of bifurcations of a laser with injected signal in the neighbourhood of the Hopf–saddle–node (HSN) singularity, as it was reviewed in section 1.2. We numerically analyse the weak cavity detuning regime for a fixed value of the detuning parameter $\theta = 0.5$ (in adequate units), where type *II* Hopf–saddle–node is expected. The small–detuning case is particularly relevant for applications, since a natural ambition when constructing laser cavities is to obtain low detunings. Long–time behaviour depending on the amplitude and the frequency shift of the applied signal is studied. The main bifurcation structure consists of a (secondary) Hopf bifurcation on the periodic orbit associated to the Hopf–saddle–node bifurcation. We have analysed in detail the resonance structure which reveals a rich interaction with other bifurcations *not* present in the usual Hopf–saddle–node scenario.

In the next section we review the representative equations for a laser with injected signal, together with the unfolding of the Hopf–saddle–node bifurcation. In Sec. 8.2, the resonance structure is described, while Sec. 8.3 discusses the Andronov global bifurcation occurring in this laser, and its interaction with other bifurcations. Finally, a global outlook and discussion is given in Sec. 8.4.

8.1 Equations for the laser with injected signal

The model for a laser system is given in terms of the Maxwell–Bloch equations, chapter 4. In a great variety of lasers, the decay times associated with the population inversion and the electric field have different time scales, allowing for the adiabatic elimination of the fast decaying polarization variable (class B) [Solari and Oppo, 1994]. The dimensionless rate equations in a reference frame that rotates with the

injected signal may be written as

$$\begin{aligned} \frac{dE}{dt} &= EW + i(\theta W + \eta)E + \beta, \\ \frac{dW}{dt} &= A^2 - \chi W(1 + g|E|^2) - |E|^2, \end{aligned} \tag{8.1}$$

where E is the complex envelope of the electric field and W is proportional to the population inversion. θ represents the detuning between the atomic and the nearest eigenfrequency of the cavity, A is proportional to the amount of pumped atoms, $\chi \geq 0$ is proportional to the inverse of the decay time of the population inversion and g is inversely proportional to $1+\theta^2$. For typical lasers, χ is small. η is the detuning of the perturbation frequency and the unperturbed laser operating frequency and $\beta \geq 0$ is the intensity of the injected signal. The relationship between the parameters used in this model and the parameters in the Maxwell–Bloch equations can be found in [Solari and Oppo, 1994]. The model can be justified for small signal intensity ratio, $\beta/A^2 \ll 1$, although it has been argued that it can be successfully applied beyond this limit [Oppo *et al.*, 1986]. Our present study centers in this limit and in some cases we have explored a region beyond this limit in order to understand the fate of some invariant sets. The set of equations (8.1) can be obtained from Eqs. (4.11) and (4.12), in the absence of noise terms and without injected signal, by performing the suitable change of variables.

Solari and Oppo [1994] performed a reduction of the three–equations model by averaging over the fast relaxation oscillation motion, reducing the dynamics to a two–equations system. In this way, the difficulty of finding analytic expressions for most of the local bifurcations is simplified. A close analysis of the singularities of this model, reveals that the system organizes around the codimension–2 Hopf–saddle–node local bifurcation. One finds that after a suitable change of coordinates one may arrive to its normal form representation (3.1) [Guckenheimer and Holmes, 1983]

$$\begin{aligned} r' &= (\mu + \bar{a}\, v)\, r + \mathcal{O}(3), \\ v' &= \nu + \bar{b}\, r^2 - v^2 + \mathcal{O}(3), \\ \zeta' &= \bar{c} + \bar{a}\, v + \mathcal{O}(2), \end{aligned} \tag{8.2}$$

where $\bar{a}$, $\bar{b}$, $\bar{c} \neq 0$ and μ and ν are the bifurcation parameters, all function of the laser parameters. The signs of $\bar{a}$ and $\bar{b}$ classify different types of flows: type I for ($\bar{a} > 0$, $\bar{b} > 0$), type II for ($\bar{a} < 0$, $\bar{b} > 0$), type III for ($\bar{a} > 0$, $\bar{b} < 0$), type IV for ($\bar{a} < 0$, $\bar{b} < 0$).

One of the main achievements of the Solari and Oppo average model is that they have established that the actual laser with injected signal operation is controlled by the cavity detuning parameter θ in the following way:

type II: $0 < \theta < 1$,
type I: $1 < \theta < \sqrt{3}$,
type III: $\sqrt{3} < \theta$.

We refer the reader to [Zimmermann *et al.*, 2001] for a detailed account of the normal form computations for the three–dimensional laser with injected signal equations (8.1), where the above results are validated up to order $O(\chi^2)$, for

$$\begin{aligned}
\bar{a}(\theta) &= (1+gA^2)\frac{(\theta^2-1)}{4\theta}\chi + O(\chi^2), \\
\bar{b}(\theta) &= -(1+gA^2)\frac{(1+\theta^2)(\theta^2-3)}{8\theta}\chi + O(\chi^2), \\
\bar{c} &= \sqrt{2}A + O(\chi^2), \\
\mu(\beta,\eta) &= \theta\left(\frac{2}{1+\theta^2} - \frac{\chi}{\beta\theta\sqrt{1+\theta^2}}\right), \\
\nu(\beta,\eta) &= 2\left(\frac{\beta\sqrt{1+\theta^2}+\eta}{\beta(1+\theta^2)}\right).
\end{aligned} \tag{8.3}$$

The main characteristics of each type of flow may be summarized as follows. A saddle–node bifurcation occurs for $\nu = \nu_{\rm sn} = 0$, where a pair of saddle–focus fixed points are born at $(r, v) = (\pm\sqrt{\nu}, 0)$. These fixed points may as well bifurcate in a Hopf bifurcation along a parabola in parameter space, $\nu = \nu_{\rm Hopf} = \mu^2/\bar{a}^2$. The periodic orbit will be at $v_{\rm Hopf} = -\mu/\bar{a}$ and its radius is given by $r^2_{\rm Hopf} = (\mu^2/\bar{a}^2 - \nu)/\bar{b}$. The main differences between type *I-III*, lie in the region of existence and stability of the periodic orbit. In type *III* the periodic orbit always co–exists with the fixed points ($\nu > \mu^2/\bar{a}^2 > 0$), while in type *I* the periodic orbit exists before the creation of the fixed points (for $\nu < 0$, $r_{\rm Hopf} > 0$). Type *II* is similar to type *I*, but the stability of the periodic orbit may change. A degenerate (secondary) Hopf bifurcation occurs on the semiaxis $\mu = 0, \nu < 0$, where the periodic orbit becomes a center. Addition of appropriate third order terms to the normal form (8.2) breaks, in general, this degeneracy resulting in a bifurcation to a torus. The fate of the torus will depend on the perturbation applied to (8.2) and results concerning this type are unknown. Kirk [Kirk, 1991] has analysed these kind of perturbations for type *III*, where the secondary Hopf bifurcation occurs in the semiaxis $\mu = 0, \nu > 0$, coexisting with the fixed points. In her analysis she found that the torus breaks–up in Arnold tongues [Arnold, 1983], which in turn ends up as *resonances of another secondary Hopf bifurcation*. Below a similar scenario will be found.

In this work we investigate the small detuning regime $0 < \theta < 1$ corresponding to type *II*, a case not studied in complete detail in previous works. In terms of bifurcations and periodic orbit organization, the most prominent feature is the (secondary) Hopf bifurcation of periodic orbits associated to the Hopf–saddle–node singularity. This will be one of our main objects of study, where we will discuss the interaction of its resonances with other bifurcations not present in the (local) normal form analysis.

8.2 Bifurcation set for small detuning

We have integrated numerically equations (8.1) with fixed parameters $A = 1$, $\chi = 0.3$ and $g = 0$[1]. Most computations were done with the AUTO97 [Doedel *et al.*, 1997] continuation package, in the parameters (β, η) and $0 < \theta = 0.5 < 1$. In general, the locus in parameter space of a particular bifurcation will be presented as points, representing the actual computation performed. To guide the reader we have selected different colours for each type of bifurcation.

Given the complexity of the full bifurcation set found, we will introduce in steps the different invariant sets and their bifurcations. Readers not interested in the technical details of the calculation may refer to Fig. 8.22 for the full bifurcation set discussed in this chapter.

8.2.1 Invariant sets close to the Hopf–saddle–node bifurcation

We begin our numeric exploration with the locus of the saddle–node, Hopf and Hopf–saddle–node bifurcations of fixed points. These may be explicitly computed, with the relevant equations being:

1. The fixed point equation may be reduced to,

$$\begin{aligned}(1+\theta^2)Y^3 &- 2[A^2(1+\theta^2)+\chi\eta\theta]Y^2 \\ &+ [A^4(1+\theta^2)+2A^2\chi\eta\theta+\chi^2\eta^2]Y-\chi^2\beta^2=0,\end{aligned} \tag{8.4}$$

   a cubic polynomial in $Y = |E|^2$.

2. The saddle–node condition, i.e., when one of the eigenvalues of the Jacobian is zero,

$$3(1+\theta^2)Y^2-4[A^2(1+\theta^2)+\chi\eta\theta]Y+A^4(1+\theta^2)+2A^2\chi\eta\theta+\chi^2\eta^2=0. \tag{8.5}$$

3. The Hopf condition (i.e., when two (complex conjugated) eigenvalues of the Jacobian are pure imaginary) reads

$$\begin{aligned}&(1+\theta^2)Y^3-[3A^2(1+\theta^2)+\chi^2(\theta^2-3)+2\eta\chi\theta]Y^2 \\ +\;&[3A^4(1+\theta^2)+A^2[(\theta^2-5)\chi^2+4\eta\chi\theta]+2\chi^4+\theta\chi^3\eta+\eta^2\chi^2]\,Y \\ -\;&[(1+\theta^2)A^6+2A^4(\eta\chi\theta-\chi^2)+A^2(\eta^2\chi^2+\chi^4)]=0.\end{aligned} \tag{8.6}$$

The fixed point equation reveals that there are regions of one or three fixed points, separated by saddle–node bifurcations. The simultaneous solution of (8.4) and (8.5) (the fixed point equation will then have a double root) gives the locus of

[1] In real lasers $g \in [0, 1]$. However, the qualitative features of the bifurcations around the Hopf–saddle–node bifurcation will not change if g is kept small. In [Zimmermann *et al.*, 2001] it is found to slightly modify the second–order coefficients in the Hopf–saddle–node normal form.

the saddle–node curve, while solution of (8.4) with (8.6) gives the locus of the Hopf curve. When all three equations are simultaneously satisfied there is a tangency point where the Hopf–saddle–node occurs [Zimmermann *et al.*, 2001],

$$\begin{aligned} \eta_{\rm hsn}(\theta) &= -\frac{(1+\theta^2)}{2\theta}\left(1-\frac{1}{4\,\theta^2 A^2}\,\chi^2\right)\,\chi+\mathcal{O}(\chi)^4, \\ \beta_{\rm hsn}(\theta) &= \frac{A\,\sqrt{1+\theta^2}}{2\theta}\left(1-\frac{(1+\theta^2)}{4\,\theta^2 A^2}\,\chi^2\right)\,\chi+\mathcal{O}(\chi)^4. \end{aligned} \tag{8.7}$$

A typical bifurcation set displaying these bifurcations is shown in Fig. 8.1. Inside the "triangle" shaped region, three fixed points exist, while outside this region only one fixed point remains. Let us label the fixed points in region 1 as: A stable, B unstable and C saddle. A pair of the above fixed points are annihilated crossing the sides of the triangle: moving into region 4, B and C collide, while entering region 6 or (3, 3′), A and B annihilates leaving in these regions only the fixed point C.[2] In physical terms, *locking* behaviour (output frequency tuned to that of the injected signal) occurs whenever the laser is operated in any of the regions (1, 4, 5), where a stable fixed point exists. On the other hand, fixed point C exists in all regions except 4 in Fig. 8.1 and is approximately situated in $(|E|, W) \approx (0, A^2/\chi)$ for $\beta \ll 1$, which corresponds to the laser–off state. In all regions of interest it is a saddle fixed point.

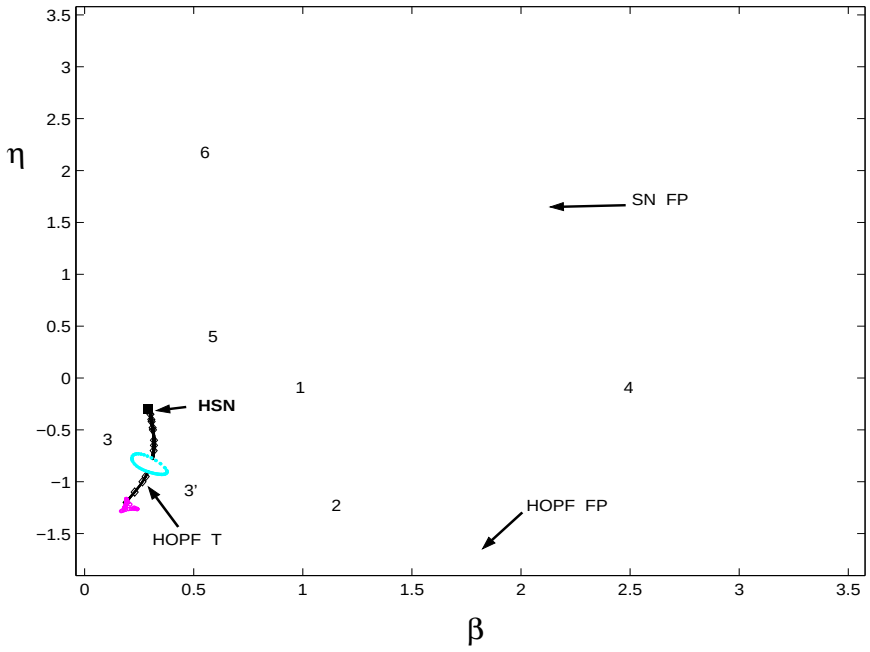

Figure 8.1: Numerical bifurcation set in parameters (β, η) for type *II*. Red line: saddle–node of fixed points (SN FP). Blue line: Hopf bifurcation of fixed points (HOPF FP). The secondary Hopf bifurcation of transversal periodic orbits (HOPF T) separates region 3 and 3'.

[2]Notice that choosing a path far out from the "triangle" shaped region, we have to identify fixed point C in regions (6, 3, 3′) with fixed point A in region 4.

The (primary) Hopf bifurcation occurs on either fixed point A or B, creating a periodic orbit *transversal* to the $W = 0$ plane, which will be referred to as T in what follows. This orbit corresponds to the undamped relaxation oscillation [van Tartwijk and Lenstra, 1995], whose main characteristic is that the phase of the electric field remains bounded. A close inspection in parameter space around the Hopf–saddle–node point reveals that moving from region 1 to region 5, the unstable node B becomes a saddle and creates an unstable T orbit. This orbit exists up to region 3, where it suffers a (secondary) Hopf bifurcation when crossing to region $3'$, creating an unstable transversal torus. The remaining stable T periodic orbit continues to exist up to region 2, when it dies in a (primary) Hopf bifurcation with fixed point A.

To complete the main invariant sets present in region 3 and $3'$, we have to include another periodic orbit. For sufficiently small β we find from (8.1) that for $W \approx 0$, $|E| \approx A$ and the phase $\arg(E(t)) = \eta\ t$, which corresponds to the *cw* (continuous-wave) laser solution [van Tartwijk and Lenstra, 1995] with an unbounded electric field phase. As this orbit lies approximately coplanar to the $W = 0$ plane, it will be referred to as L, the *longitudinal* orbit. For sufficiently small (η, β), this orbit can be easily shown to be stable. However we find that the period of L diverges at the saddle–node bifurcation of fixed point, where the orbit disappears. This global bifurcation is known as Andronov or saddle–node infinite–period bifurcation [Kuznetsov, 1997], and will be addressed in more detail in Sec. 8.3. We remark that the stability of L close to the Andronov bifurcation depends on the stability of the saddle–node fixed point, thus on which side of the Hopf–saddle–node point one is located: in region $3'$ the orbit is unstable, while in region 3 it is stable. From this, it is clear that at least a local bifurcation to L is required. Below we will show that a new secondary Hopf bifurcation on L occurs inside region $3'$.

In summary, we find that fixed points A and B together with the transversal periodic orbit T correspond to the type *II* Hopf–saddle–node scenario proposed by the normal form analysis in the previous section. The periodic orbit L is also an integral part of the bifurcation set of a laser with injected signal, and we will show in the next section how the interaction of bifurcations between these two periodic orbits organize the resonance structure.

8.2.2 Bifurcations of transversal periodic orbits

We begin with a general observation for the existence boundary of transversal T orbit born at the the Hopf bifurcation of fixed points. For a fixed value of η, we find for the continuation of this orbit for decreasing β, its period diverges at a critical $\beta \approx 0.05$, for an interval of η close to 0, where a homoclinic orbit to fixed point C occurs. Figure 8.2 shows the locus of this global bifurcation in parameter space, while Figs. 8.10 and 8.11 show the typical period versus β behaviour. This bifurcation is found not to depend on θ, and was found up to type *III* regime. We leave for Sec. 8.3 the discussion of how this bifurcation is related to the Andronov bifurcation producing L.

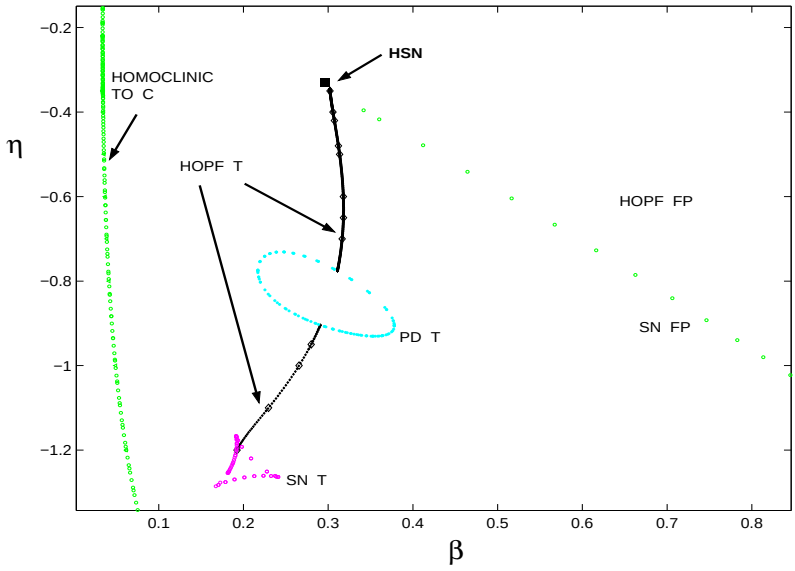

Figure 8.2: Partial numerical bifurcation set showing the homoclinic to C fixed point and the first resonances of the transversal secondary Hopf bifurcation. Saddle–node bifurcation of transversal periodic orbits (SN T) and period doubling bifurcation of transversal periodic orbits (PD T) are indicated.

In Fig. 8.3 (a) we display the main invariant sets for the parameter region bounded by the homoclinic to C and the secondary Hopf bifurcation. We have the stable longitudinal orbit L (which lies approximately on $|E| \approx A = 1, W \approx 0$), together with the unstable transversal orbit T. This orbit has a large variation in the population inversion W, and a bounded electric field phase (the phase does not make a complete turn as L does). Crossing the secondary Hopf bifurcation T and entering region $3'$, we find that T becomes stable and an unstable invariant torus is created. Figure 8.3 (b) shows the invariant sets, where only the intersections of the quasiperiodic orbit with the $W = 0$ plane are shown. A time series of the intensity $|E|^2$ on this solution is shown in Fig. 8.4.

It is well known that in generic systems quasiperiodic motion may suffer resonance phenomena. Local analysis [Arnold, 1983] around the Hopf bifurcation reveals that whenever the ratio of the two competing frequencies is rational, the quasiperiodic motion may disappear and periodic orbits arise. These orbits may be classified by an integer number of p turns following the primary or bifurcating orbit (T in this case), and another integer number q which denotes the number of turns made around the primary orbit, before closing on itself. Precisely on the (secondary) Hopf bifurcation the nontrivial Floquet multipliers are on the unit circle at $e^{\pm i2\pi p/q}$. A general result shows that in the *weak resonances* case $q > 4$ these periodic orbits are born in saddle–node pairs, and in a two–parameter space they trace a 'tongue' (known as Arnold tongue) with the tip lying on the (secondary) Hopf bifurcation. In phase space the periodic orbits are *phase locked* solution on the torus. On the other hand the case $q \leq 4$ are known as *strong resonances* and do not correspond to 'strict' Arnold tongues. The details of each strong resonance in a general study may be found in [Kuznetsov, 1997].

7.2.1 Period of the relaxation oscillations

The time evolution of the potential is plotted in Fig. 7.1. In this figure it can be seen that the Lyapunov potential is approximately constant between two consecutive peaks of the relaxation oscillations as it can be also observed with the equipotential lines of Fig. 7.3 (however, in the peak of intensity, the potential decreases steeply, as can be seen in Fig. 7.2). This fact allows us to estimate the relaxation oscillation period by approximating $V(y,z) = E$, constant, during this time interval. When the potential is considered as constant, the period can be evaluated by the standard method of elementary Mechanics: z is replaced by its expression obtained from (7.6) in terms of y and $\dot{y}$ in $V(y,z)$. Using the condition that $V(y,z) = E$, we obtain

$$E = a_1\, y + a_2\, y^2 + a_3\, \ln(y) + a_4 \frac{1}{2} + \frac{1}{2}\left[\frac{\dot{y}}{y}\frac{(1+\bar{s}\, y)}{2}\right]^2 . \tag{7.25}$$

From this equation, we can calculate the relaxation oscillation period T, by using $\dot{y} = \frac{dy}{dt}$ and integrating over a cycle. This leads to the expression

$$T = \int_{y_a}^{y_b} \frac{1+\bar{s}\, y}{y} \frac{dy}{\left[2\left(E - a_1\, y - a_2\, y^2 - a_3\, \ln(y) - a_4\, y^{-1}\right)\right]^{1/2}}, \tag{7.26}$$

where y_a and y_b are the values of y that cancel the denominator. We stress the fact that the only approximation used in the derivation of this expression is that the Lyapunov potential is constant during two maxima of the intensity oscillations. In other words, we have made a mechanical simile and reduced the problem to one with constant energy. A numerical evaluation of this integral yields the dependence of the period, T, with the value of the energy, $E = V$, as plotted in Fig. 7.6.

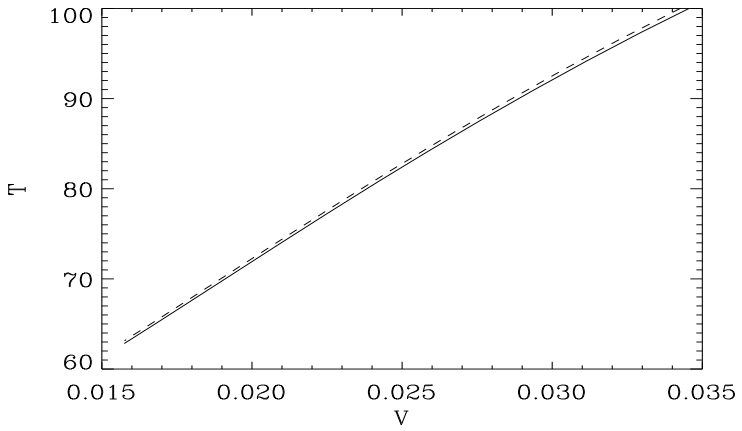

Figure 7.6: Period versus potential for a class B laser obtained with (7.26). Solid line $\bar{s} = 0$, dashed line $\bar{s} = 2$. Other parameters, same than in Fig. 7.1. Dimensionless units.

Equation (7.26) reduces, in the case $c = d = \bar{s} = 0$, to the one previously obtained by using the relation between the laser dynamics and the Toda oscillator derived in [Oppo and Politi, 1985].

According to Fig. 7.6, the period T decreases as the potential V decreases. Since the Lyapunov potential decreases with time, this explains the fact that the period of the oscillations in the transient regime decreases with time. In Fig. 7.7, we compare the results obtained with the expression (7.26) for the period with the ones obtained from numerical simulations of the rate equations (7.6, 7.7). In the simulations we compute the period as the time between two peaks in the evolution of the variable y. As seen in this figure, the above expression for the period, when using the numerical value of the potential V, accurately reproduces the simulation results although it is systematically lower than the numerical result. The discrepancy is less than one percent over the whole range of times.

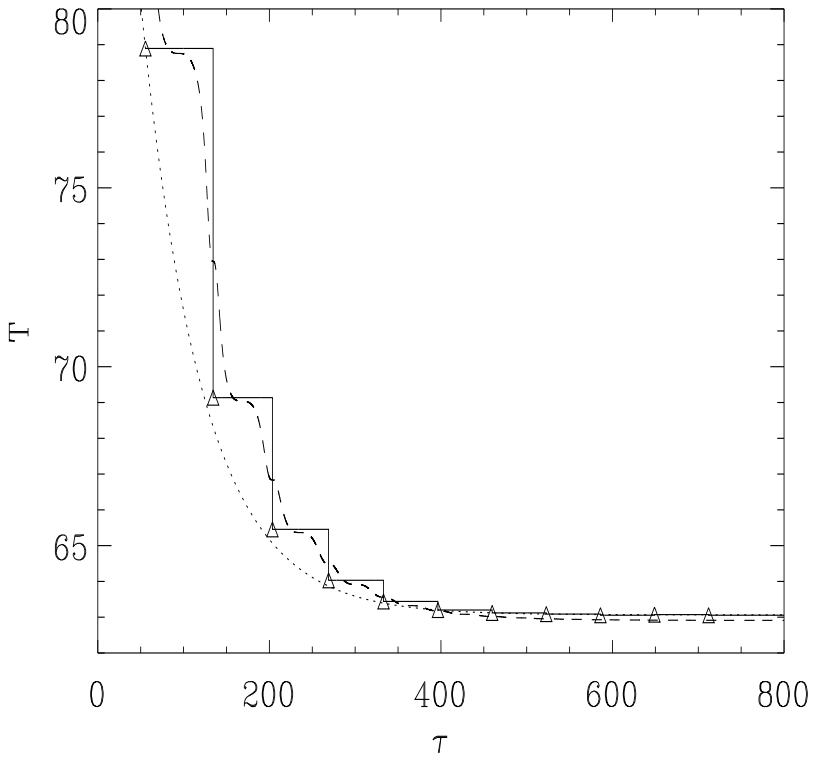

Figure 7.7: Period versus time in a class B laser. Solid line has been calculated as the distance between two peaks of intensity, with triangles plotted at the beginning of each period; dashed line has been calculated using the expression (7.26), with the value of the potential V obtained also from the simulation; dotted line corresponds to the semi-empirical expression (7.40). Same parameters than in Fig. 7.1. We have used $\tau_0 = 55.55$, coinciding with the position of the first intensity peak. Dimensionless units.

It is possible to quantify the difference between the approximate expression (7.26) and the exact values near the stationary state.

By considering (7.26) near the steady state with $y = y_{st} + \delta y$, $E = V_{st} + \delta V$ ($V_{st} = V(y_{st}, z_{st})$) and retaining the lowest terms in δy and δV, one can perform the integral analytically, obtaining an approximation for the period of the steady state

$$T_{st,ap} = \frac{2\,\pi}{D_{12,st}\,\sqrt{K\,F - H^2}}, \tag{7.27}$$

where

$$\begin{aligned} K &= 2\left(a_2 - \frac{1}{2}\,\frac{a_3}{y_{st}^2} + \frac{a_4}{y_{st}^3} + \frac{1}{2}\left[\bar{s} + \frac{(d + c\,z_{st})}{2\,y_{st}^2}\right]^2\right), \\ F &= \left[1 + c\,\frac{(1 + \bar{s}\,y_{st})}{2\,y_{st}}\right]^2, \\ H &= -\left[1 + \frac{c\,(1 + \bar{s}\,y_{st})}{2\,y_{st}}\right]\left[\bar{s} + \frac{(d + c\,z_{st})}{2\,y_{st}^2}\right], \end{aligned} \tag{7.28}$$

and $D_{12,st}$ is the coefficient D_{12} calculated in the steady state.

The result (7.27) could be obtained starting from the linearization of potential (7.25), expanding this expression near the steady state, and then calculate the period from the resulting expression.

The period of the relaxation oscillations near the steady state can also be obtained by the standard procedure of linearizing the evolution equations near the steady state solution. Applying a small perturbation $y = y_{st} + \delta y$ and $z = z_{st} + \delta z$ to Eqs. (7.6) and (7.7), one has after linearization

$$\dot{\delta y} = a_{11}\,\delta y + a_{12}\,\delta z, \tag{7.29}$$

$$\dot{\delta z} = a_{21}\,\delta y + a_{22}\,\delta z, \tag{7.30}$$

where

$$\begin{aligned} a_{11} &= 2\left(\frac{z_{st}}{(1 + \bar{s}\,y_{st})^2} - 1\right), \\ a_{12} &= \left(\frac{2\,y_{st}}{1 + \bar{s}\,y_{st}} + c\right), \\ a_{21} &= -\frac{z_{st}}{(1 + \bar{s}\,y_{st})^2}, \\ a_{22} &= -\left(b + \frac{y_{st}}{1 + \bar{s}\,y_{st}}\right). \end{aligned} \tag{7.31}$$

The eigenvalues of the linearized equations (7.29) and (7.30) are

$$\lambda = -\frac{\varrho}{2} \pm i\,\omega, \tag{7.32}$$

with

$$\varrho = -(a_{11} + a_{22}), \tag{7.33}$$

$$\omega = \frac{1}{2}\sqrt{|(a_{11} - a_{22})^2 + 4\, a_{12}\, a_{21}|}. \tag{7.34}$$

The frequency ω of the relaxation oscillations near the steady state is the imaginary part of the eigenvalues of the linearized equations (7.29) and (7.30). This yields a period $T_{st} = 2\,\pi/\omega$ which can be rewritten in terms of K, F, H, $D_{12,st}$ and $D_{22,st}$ in order to have a better comparison with the approximate period (7.27)

$$T_{st} = \frac{2\,\pi}{D_{12,st}\,\sqrt{K\,F - H^2}}\left[1 - \frac{D_{22,st}^2}{D_{12,st}^2}\frac{F^2}{4\,(K\,F - H^2)}\right]^{-1/2}. \tag{7.35}$$

The difference between (7.27) and (7.35) vanishes with $D_{22,st}$ (i.e. D_{22} in the stationary state). Since $K\,F - H^2$ is always a positive quantity, our approximation will give, at least asymptotically, a smaller value for the period.

In order to have a complete understanding of the variation of the period with time, we need to compute the time variation of the potential $V(\tau)$ between two consecutive intensity peaks. This variation is induced by the dissipative terms in the equations of motion. Although we were not able to derive an expression for the variation of the potential (see [Oppo and Politi, 1985] for an approximate expression in a simpler case), we found that a semi–empirical argument can yield a very simple law which is well reproduced by the simulations. We start by studying the decay to the stationary state in the linearized equations. After expanding around the steady state, the dynamical equations (7.29) and (7.30) show that the variables decay to the steady state as

$$\delta y(\tau), \delta z(\tau) \propto \exp(-\frac{\varrho}{2}\tau), \tag{7.36}$$

where ϱ, (7.33), can be rewritten as

$$\varrho = D_{22,st}\; F. \tag{7.37}$$

In the case of $\bar{s} = 0$, $c = 0$ and $d = 0$ (neither saturation term nor spontaneous emission term are considered) $\varrho = a$.

Expanding $V(y, z)$ around the steady state (y_{st} and z_{st} correspond to extrema of the potential), it is found that

$$V - V_{st} \propto \delta y^2, \delta z^2, \delta y\, \delta z\,. \tag{7.38}$$

Using (7.36) and taking the initial condition at an arbitrary τ_0 we find an expression for the decay of the potential

$$V(\tau) - V_{st} = [V(\tau_0) - V_{st}] \exp\left(-\varrho\,(\tau - \tau_0)\right). \tag{7.39}$$

In Fig. 7.8 we plot $\ln[V(\tau) - V_{st}]$ versus time and compare it with the approximation (7.39). One can see that it fits $\ln[V(\tau) - V_{st}]$ reasonably well not only near the steady state (where it was derived), but also during the transient dynamics. The value of τ_0, being a free parameter, was chosen at the time at which the first peak of the intensity appeared. Although other values of τ_0 might produce a better fit, the one chosen here has the advantage that it can be calculated analytically by following the technique of Ref. [Balle *et al.*, 1991]. It can be derived from Eq. (7.26) that the period T depends linearly on the potential V. This fact, combined with the result of Eq. (7.39), suggests the semi–empirical law for the evolution of the period

$$T(\tau) - T_{st} = [T(\tau_0) - T_{st}] \exp\left(-\varrho\,(\tau - \tau_0)\right). \tag{7.40}$$

This simple expression fits well the calculated period not only near the steady state, but also in the transient regime, see Figs. 7.7 and 7.9. The small differences observed near the steady state are due to the fact that the semi–empirical law, Eq. (7.40), is based on the validity of Eq. (7.26) between the period and the potential. As it was already discussed above, that expansion slightly underestimates the asymptotic (stationary) value of the period. By complementing this study with the procedure given in [Balle *et al.*, 1991] to describe the switch–on process of a laser, and valid until the first intensity peak is reached, we can obtain a complete description of the variation of the oscillations period in the dynamical evolution following the laser switch–on.

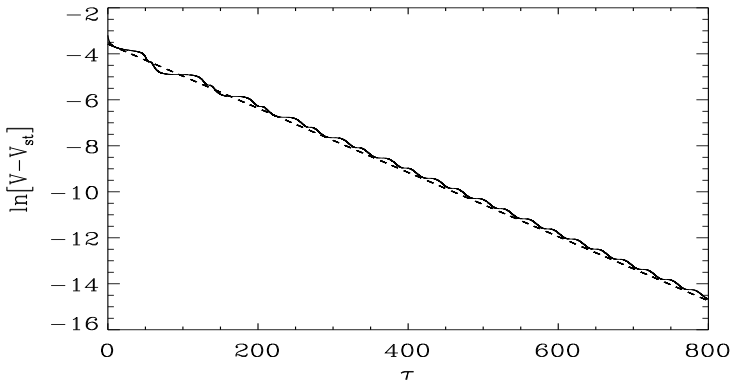

Figure 7.8: Logarithm of the potential difference versus time in a class B laser (solid line), compared with the theoretical expression in the steady state (7.39) (dashed line). Same parameters than in Fig. 7.1 and τ_0 as in Fig. 7.7. Dimensionless units.

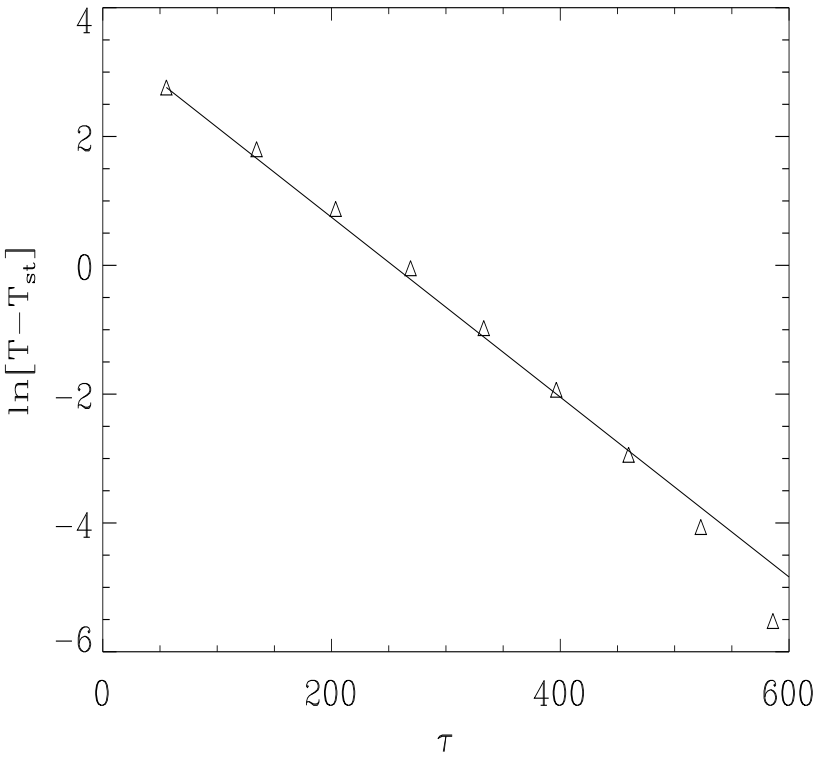

Figure 7.9: Logarithm of the period difference versus time in a class B laser. Triangles correspond to the period calculated from the simulations as the distance between two consecutive intensity peaks, at the same position than in Fig. 7.8. The solid line is the semi–empirical expression Eq. (7.40). Same parameters than in Fig. 7.1 and τ_0 as in Fig. 7.7. Dimensionless units.

Capítol 8

Estructura de resonàncies en un làser de classe B amb senyal injectat

En aquest capítol es descriu la dinàmica qualitativa i el conjunt parcial de bifurcacions (capítol 3) per a un làser de classe B amb senyal injectat amb termes de disintonia petits. El treball d'aquest capítol completa una sèrie d'estudis (veure la secció 1.2) sobre bifurcacions en làsers amb senyal injectat en la proximitat de la singularitat Hopf–sella–node.

Les equacions de balanç (capítol 4) en un sistema de referència que gira a la freqüència del senyal injectat són les (8.1) per al camp elèctric, E, i el nombre de portadors, W. El camp injectat està caracteritzat per l'amplitud β, i la freqüència η. Per al tractament que es fa en aquest capítol s'agafa un valor pel paràmetre de disintonia amb el qual les equacions queden tipus II de la bifurcació Hopf–sella–node.

En les distintes seccions d'aquest capítol es van introduint a poc a poc els distints conjunts invariants del sistema i les seves bifurcacions a causa de la complexitat del conjunt complet de bifurcacions. S'han seleccionat distints colors per a cada tipus de bifurcacions. El conjunt final obtingut és el de la figura 8.22.

La bifurcació sella–node (punts vermells) i la bifurcació de Hopf (punts blaus) dels punts fixos de les equacions, es poden calcular analíticament (8.4 - 8.6). La seva intersecció dóna el punt Hopf–sella–node. Aquestes bifurcacions separen les regions de l'espai de paràmetres (β, η) segons l'estabilitat dels punts fixos A, B i C, Fig. 8.1. A la regió 1, A és estable, B inestable i C sella; un parell d'aquests punts fixos s'aniquilen quan es creua els costats del triangle: cap a la regió 4, B i C col·lapsen; cap a les regions 6, 3 i $3'$, A i B s'aniquilen deixant en aquestes regions el punt C. Un punt fix estable existeix en les regions 1, 4 i 5, que correspon, en termes físics, a tenir una freqüència de sortida sintonitzada amb la d'entrada. El punt fix C correspon a l'estat del làser apagat, i en totes les regions d'interès és un punt sella.

La bifurcació de Hopf (primària) ocorr o bé en el punt fix A ò B, creant una òrbita periòdica transversal, T, al pla $W = 0$. Realitzant un circuit tancat al voltant

del punt Hopf–sella–node: de 1 a 5, el punt B inestable torna sella i es crea l'òrbita T inestable. Aquesta òrbita existeix fins a la regió 3, allà sofreix una bifurcació de Hopf (secundària) quan passa a la regió $3'$, creant un torus transversal inestable, Fig. 8.3. L'òrbita T estable continua existint en la regió 2, i mor en la bifurcació de Hopf (primària) amb el punt fix A. L'òrbita T té un període que divergeix per a valors de β petits (Fig. 8.10), desapareixent a l'òrbita homoclínica a C, Fig. 8.2.

Per completar el conjunt d'invariants en les regions 3 i $3'$, cal incloure una òrbita periòdica longitudinal, L, que és aproximadament coplanar al pla $W = 0$. Aquesta òrbita, estable a 3 però inestable a $3'$, té un període que divergeix a la bifurcació sella–node (bifurcació d'Andronov, Fig. 8.21).

Els punts fixos A i B, juntament amb l'òrbita T corresponen a l'escenari Hopf–sella–node tipus *II*. L'òrbita L és una part integral del conjunt de bifurcacions, i la interacció de les bifurcacions que sofreixen aquestes dues òrbites organitza l'estructura de resonàncies. La bifurcació de Hopf secundària s'interrompeix en una illa de bifurcacions de període doble d'òrbites periòdiques (cercle blau figura 8.2) i acaba en una bifurcació sella–node d'òrbites periòdiques (triangle rosa).

El moviment quasi–periòdic pot sofrir fenòmens de resonància i generar òrbites periòdiques. Aquestes òrbites poden ésser classificades per un nombre p de voltes seguint l'òrbita primària, T, i q que denota el nombre de voltes fetes al voltant l'òrbita primària abans de tancar–se. A la figura 8.7, es veu l'estructura de resonàncies per distints valors de q. Les línies en color rosa corresponen a bifurcacions sella–node d'òrbites periòdiques. Per a $q > 4$ es comporten com l'estructura estàndard de llengües d'Arnold i es van acumulant cap el punt Hopf–sella–node.

L'estructura de les òrbites periòdiques dins cada resonància és bastant similar. Com exemple s'estudia la resonància 3, Fig. 8.9. A la figura 8.10 (a), es veu que per a β a prop de la bifurcació de Hopf secundària de T, una òrbita periòdica inestable i una sella neixen i tornen a col·lapsar en un valor de β més gran a la bifurcació sella–node revers. Per a un valor de η més baix, Fig. 8.10 (b), la branca inestable té un període que divergeix i s'originen dues bifurcacions homoclíniques (cercle verd de la figura 8.9). El tall de la figura 8.10 (c) indica que l'òrbita periòdica resonant es junta amb l'òrbita L. Aquest procés d'unió de les resonàncies transversal en la solució de l'òrbita periòdica s'observa a totes les resonàncies. A prop del procés d'unió s'observa que l'òrbita L també bifurca en una Hopf secundària (línies negres per valors de β grans), que té així mateix té resonàncies 1/2 (cercles color blau corresponents a bifurcacions de període doble).

Les resonàncies fortes ($q \leq 4$) tenen una estructura més complicada que la indicada. En particular, les bifurcacions sella–node de les llengües no ocorr en el torus. El torus pot créixer quan els paràmetres canvien i col·lisionar amb una òrbita resonant. Això corresponen a una bifurcació homoclínica a una òrbita periòdica amb la destrucció final del torus (diamands negres). Els punts d'intersecció d'aquestes homoclíniques, les Hopf secundàries i les resonàncies corresponen a singularitat tipus Takens–Bogdanov, Fig. 8.15.

Entre les resonàncies transversals indicades, s'han obtingut altres resonàncies, Fig. 8.18, encara que una classificació de les mateixes és prou complicada.

Chapter 8

Resonance structure in a class B laser with injected signal

In this chapter, we describe the qualitative dynamics and bifurcation set for a laser with injected signal for small cavity detunings by using the definitions included in chapter 3.

The work presented in this chapter completes the above series of studies of bifurcations of a laser with injected signal in the neighbourhood of the Hopf–saddle–node (HSN) singularity, as it was reviewed in section 1.2. We numerically analyse the weak cavity detuning regime for a fixed value of the detuning parameter $\theta = 0.5$ (in adequate units), where type *II* Hopf–saddle–node is expected. The small–detuning case is particularly relevant for applications, since a natural ambition when constructing laser cavities is to obtain low detunings. Long–time behaviour depending on the amplitude and the frequency shift of the applied signal is studied. The main bifurcation structure consists of a (secondary) Hopf bifurcation on the periodic orbit associated to the Hopf–saddle–node bifurcation. We have analysed in detail the resonance structure which reveals a rich interaction with other bifurcations *not* present in the usual Hopf–saddle–node scenario.

In the next section we review the representative equations for a laser with injected signal, together with the unfolding of the Hopf–saddle–node bifurcation. In Sec. 8.2, the resonance structure is described, while Sec. 8.3 discusses the Andronov global bifurcation occurring in this laser, and its interaction with other bifurcations. Finally, a global outlook and discussion is given in Sec. 8.4.

8.1 Equations for the laser with injected signal

The model for a laser system is given in terms of the Maxwell–Bloch equations, chapter 4. In a great variety of lasers, the decay times associated with the population inversion and the electric field have different time scales, allowing for the adiabatic elimination of the fast decaying polarization variable (class B) [Solari and Oppo, 1994]. The dimensionless rate equations in a reference frame that rotates with the

injected signal may be written as

$$\begin{aligned} \frac{dE}{dt} &= EW + i(\theta W + \eta)E + \beta, \\ \frac{dW}{dt} &= A^2 - \chi W(1 + g|E|^2) - |E|^2, \end{aligned} \tag{8.1}$$

where E is the complex envelope of the electric field and W is proportional to the population inversion. θ represents the detuning between the atomic and the nearest eigenfrequency of the cavity, A is proportional to the amount of pumped atoms, $\chi \geq 0$ is proportional to the inverse of the decay time of the population inversion and g is inversely proportional to $1+\theta^2$. For typical lasers, χ is small. η is the detuning of the perturbation frequency and the unperturbed laser operating frequency and $\beta \geq 0$ is the intensity of the injected signal. The relationship between the parameters used in this model and the parameters in the Maxwell–Bloch equations can be found in [Solari and Oppo, 1994]. The model can be justified for small signal intensity ratio, $\beta/A^2 \ll 1$, although it has been argued that it can be successfully applied beyond this limit [Oppo *et al.*, 1986]. Our present study centers in this limit and in some cases we have explored a region beyond this limit in order to understand the fate of some invariant sets. The set of equations (8.1) can be obtained from Eqs. (4.11) and (4.12), in the absence of noise terms and without injected signal, by performing the suitable change of variables.

Solari and Oppo [1994] performed a reduction of the three–equations model by averaging over the fast relaxation oscillation motion, reducing the dynamics to a two–equations system. In this way, the difficulty of finding analytic expressions for most of the local bifurcations is simplified. A close analysis of the singularities of this model, reveals that the system organizes around the codimension–2 Hopf–saddle–node local bifurcation. One finds that after a suitable change of coordinates one may arrive to its normal form representation (3.1) [Guckenheimer and Holmes, 1983]

$$\begin{aligned} r' &= (\mu + \bar{a}\, v)\, r + \mathcal{O}(3), \\ v' &= \nu + \bar{b}\, r^2 - v^2 + \mathcal{O}(3), \\ \zeta' &= \bar{c} + \bar{a}\, v + \mathcal{O}(2), \end{aligned} \tag{8.2}$$

where $\bar{a}$, $\bar{b}$, $\bar{c} \neq 0$ and μ and ν are the bifurcation parameters, all function of the laser parameters. The signs of $\bar{a}$ and $\bar{b}$ classify different types of flows: type I for ($\bar{a} > 0$, $\bar{b} > 0$), type II for ($\bar{a} < 0$, $\bar{b} > 0$), type III for ($\bar{a} > 0$, $\bar{b} < 0$), type IV for ($\bar{a} < 0$, $\bar{b} < 0$).

One of the main achievements of the Solari and Oppo average model is that they have established that the actual laser with injected signal operation is controlled by the cavity detuning parameter θ in the following way:

type II: $0 < \theta < 1$,
type I: $1 < \theta < \sqrt{3}$,
type III: $\sqrt{3} < \theta$.

We refer the reader to [Zimmermann *et al.*, 2001] for a detailed account of the normal form computations for the three–dimensional laser with injected signal equations (8.1), where the above results are validated up to order $O(\chi^2)$, for

$$\begin{aligned}
\bar{a}(\theta) &= (1+gA^2)\frac{(\theta^2-1)}{4\theta}\chi + O(\chi^2), \\
\bar{b}(\theta) &= -(1+gA^2)\frac{(1+\theta^2)(\theta^2-3)}{8\theta}\chi + O(\chi^2), \\
\bar{c} &= \sqrt{2}A + O(\chi^2), \\
\mu(\beta,\eta) &= \theta\left(\frac{2}{1+\theta^2} - \frac{\chi}{\beta\theta\sqrt{1+\theta^2}}\right), \\
\nu(\beta,\eta) &= 2\left(\frac{\beta\sqrt{1+\theta^2}+\eta}{\beta(1+\theta^2)}\right).
\end{aligned} \tag{8.3}$$

The main characteristics of each type of flow may be summarized as follows. A saddle–node bifurcation occurs for $\nu = \nu_{\rm sn} = 0$, where a pair of saddle–focus fixed points are born at $(r, v) = (\pm\sqrt{\nu}, 0)$. These fixed points may as well bifurcate in a Hopf bifurcation along a parabola in parameter space, $\nu = \nu_{\rm Hopf} = \mu^2/\bar{a}^2$. The periodic orbit will be at $v_{\rm Hopf} = -\mu/\bar{a}$ and its radius is given by $r^2_{\rm Hopf} = (\mu^2/\bar{a}^2 - \nu)/\bar{b}$. The main differences between type *I-III*, lie in the region of existence and stability of the periodic orbit. In type *III* the periodic orbit always co–exists with the fixed points ($\nu > \mu^2/\bar{a}^2 > 0$), while in type *I* the periodic orbit exists before the creation of the fixed points (for $\nu < 0$, $r_{\rm Hopf} > 0$). Type *II* is similar to type *I*, but the stability of the periodic orbit may change. A degenerate (secondary) Hopf bifurcation occurs on the semiaxis $\mu = 0, \nu < 0$, where the periodic orbit becomes a center. Addition of appropriate third order terms to the normal form (8.2) breaks, in general, this degeneracy resulting in a bifurcation to a torus. The fate of the torus will depend on the perturbation applied to (8.2) and results concerning this type are unknown. Kirk [Kirk, 1991] has analysed these kind of perturbations for type *III*, where the secondary Hopf bifurcation occurs in the semiaxis $\mu = 0, \nu > 0$, coexisting with the fixed points. In her analysis she found that the torus breaks–up in Arnold tongues [Arnold, 1983], which in turn ends up as *resonances of another secondary Hopf bifurcation*. Below a similar scenario will be found.

In this work we investigate the small detuning regime $0 < \theta < 1$ corresponding to type *II*, a case not studied in complete detail in previous works. In terms of bifurcations and periodic orbit organization, the most prominent feature is the (secondary) Hopf bifurcation of periodic orbits associated to the Hopf–saddle–node singularity. This will be one of our main objects of study, where we will discuss the interaction of its resonances with other bifurcations not present in the (local) normal form analysis.

8.2 Bifurcation set for small detuning

We have integrated numerically equations (8.1) with fixed parameters $A = 1$, $\chi = 0.3$ and $g = 0$[1]. Most computations were done with the AUTO97 [Doedel *et al.*, 1997] continuation package, in the parameters (β, η) and $0 < \theta = 0.5 < 1$. In general, the locus in parameter space of a particular bifurcation will be presented as points, representing the actual computation performed. To guide the reader we have selected different colours for each type of bifurcation.

Given the complexity of the full bifurcation set found, we will introduce in steps the different invariant sets and their bifurcations. Readers not interested in the technical details of the calculation may refer to Fig. 8.22 for the full bifurcation set discussed in this chapter.

8.2.1 Invariant sets close to the Hopf–saddle–node bifurcation

We begin our numeric exploration with the locus of the saddle–node, Hopf and Hopf–saddle–node bifurcations of fixed points. These may be explicitly computed, with the relevant equations being:

1. The fixed point equation may be reduced to,

$$\begin{aligned}(1+\theta^2)Y^3 &- 2[A^2(1+\theta^2)+\chi\eta\theta]Y^2 \\ &+ [A^4(1+\theta^2)+2A^2\chi\eta\theta+\chi^2\eta^2]Y-\chi^2\beta^2=0,\end{aligned} \tag{8.4}$$

   a cubic polynomial in $Y = |E|^2$.

2. The saddle–node condition, i.e., when one of the eigenvalues of the Jacobian is zero,

$$3(1+\theta^2)Y^2-4[A^2(1+\theta^2)+\chi\eta\theta]Y+A^4(1+\theta^2)+2A^2\chi\eta\theta+\chi^2\eta^2=0. \tag{8.5}$$

3. The Hopf condition (i.e., when two (complex conjugated) eigenvalues of the Jacobian are pure imaginary) reads

$$\begin{aligned}&(1+\theta^2)Y^3-[3A^2(1+\theta^2)+\chi^2(\theta^2-3)+2\eta\chi\theta]Y^2 \\ +\;&[3A^4(1+\theta^2)+A^2[(\theta^2-5)\chi^2+4\eta\chi\theta]+2\chi^4+\theta\chi^3\eta+\eta^2\chi^2]\,Y \\ -\;&[(1+\theta^2)A^6+2A^4(\eta\chi\theta-\chi^2)+A^2(\eta^2\chi^2+\chi^4)]=0.\end{aligned} \tag{8.6}$$

The fixed point equation reveals that there are regions of one or three fixed points, separated by saddle–node bifurcations. The simultaneous solution of (8.4) and (8.5) (the fixed point equation will then have a double root) gives the locus of

[1] In real lasers $g \in [0, 1]$. However, the qualitative features of the bifurcations around the Hopf–saddle–node bifurcation will not change if g is kept small. In [Zimmermann *et al.*, 2001] it is found to slightly modify the second–order coefficients in the Hopf–saddle–node normal form.

the saddle–node curve, while solution of (8.4) with (8.6) gives the locus of the Hopf curve. When all three equations are simultaneously satisfied there is a tangency point where the Hopf–saddle–node occurs [Zimmermann *et al.*, 2001],

$$\begin{aligned} \eta_{\rm hsn}(\theta) &= -\frac{(1+\theta^2)}{2\theta}\left(1-\frac{1}{4\,\theta^2 A^2}\,\chi^2\right)\,\chi+\mathcal{O}(\chi)^4, \\ \beta_{\rm hsn}(\theta) &= \frac{A\,\sqrt{1+\theta^2}}{2\theta}\left(1-\frac{(1+\theta^2)}{4\,\theta^2 A^2}\,\chi^2\right)\,\chi+\mathcal{O}(\chi)^4. \end{aligned} \tag{8.7}$$

A typical bifurcation set displaying these bifurcations is shown in Fig. 8.1. Inside the "triangle" shaped region, three fixed points exist, while outside this region only one fixed point remains. Let us label the fixed points in region 1 as: A stable, B unstable and C saddle. A pair of the above fixed points are annihilated crossing the sides of the triangle: moving into region 4, B and C collide, while entering region 6 or (3, 3′), A and B annihilates leaving in these regions only the fixed point C.[2] In physical terms, *locking* behaviour (output frequency tuned to that of the injected signal) occurs whenever the laser is operated in any of the regions (1, 4, 5), where a stable fixed point exists. On the other hand, fixed point C exists in all regions except 4 in Fig. 8.1 and is approximately situated in $(|E|, W) \approx (0, A^2/\chi)$ for $\beta \ll 1$, which corresponds to the laser–off state. In all regions of interest it is a saddle fixed point.

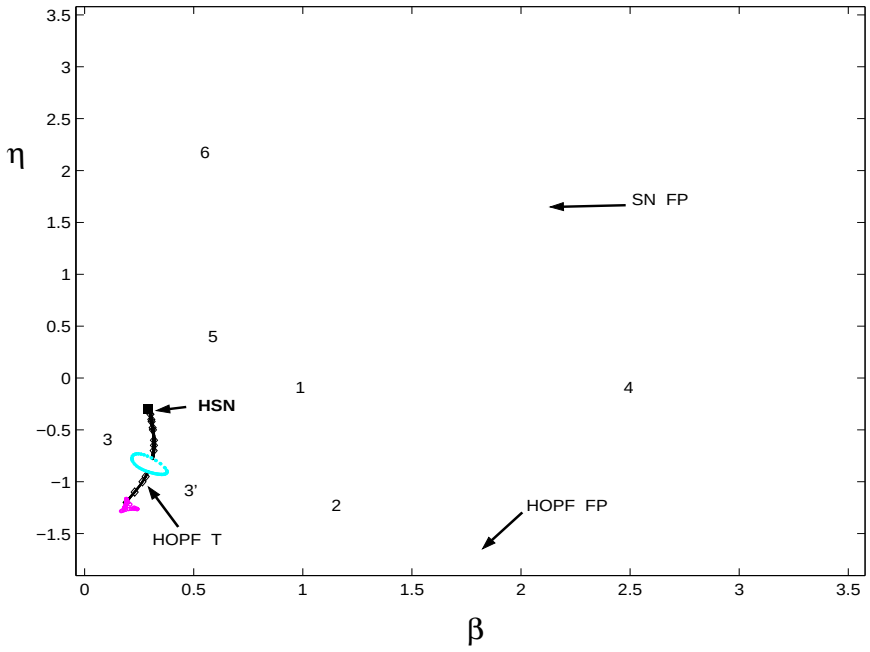

Figure 8.1: Numerical bifurcation set in parameters (β, η) for type *II*. Red line: saddle–node of fixed points (SN FP). Blue line: Hopf bifurcation of fixed points (HOPF FP). The secondary Hopf bifurcation of transversal periodic orbits (HOPF T) separates region 3 and 3'.

[2]Notice that choosing a path far out from the "triangle" shaped region, we have to identify fixed point C in regions (6, 3, 3′) with fixed point A in region 4.

The (primary) Hopf bifurcation occurs on either fixed point A or B, creating a periodic orbit *transversal* to the $W = 0$ plane, which will be referred to as T in what follows. This orbit corresponds to the undamped relaxation oscillation [van Tartwijk and Lenstra, 1995], whose main characteristic is that the phase of the electric field remains bounded. A close inspection in parameter space around the Hopf–saddle–node point reveals that moving from region 1 to region 5, the unstable node B becomes a saddle and creates an unstable T orbit. This orbit exists up to region 3, where it suffers a (secondary) Hopf bifurcation when crossing to region $3'$, creating an unstable transversal torus. The remaining stable T periodic orbit continues to exist up to region 2, when it dies in a (primary) Hopf bifurcation with fixed point A.

To complete the main invariant sets present in region 3 and $3'$, we have to include another periodic orbit. For sufficiently small β we find from (8.1) that for $W \approx 0$, $|E| \approx A$ and the phase $\arg(E(t)) = \eta\ t$, which corresponds to the *cw* (continuous-wave) laser solution [van Tartwijk and Lenstra, 1995] with an unbounded electric field phase. As this orbit lies approximately coplanar to the $W = 0$ plane, it will be referred to as L, the *longitudinal* orbit. For sufficiently small (η, β), this orbit can be easily shown to be stable. However we find that the period of L diverges at the saddle–node bifurcation of fixed point, where the orbit disappears. This global bifurcation is known as Andronov or saddle–node infinite–period bifurcation [Kuznetsov, 1997], and will be addressed in more detail in Sec. 8.3. We remark that the stability of L close to the Andronov bifurcation depends on the stability of the saddle–node fixed point, thus on which side of the Hopf–saddle–node point one is located: in region $3'$ the orbit is unstable, while in region 3 it is stable. From this, it is clear that at least a local bifurcation to L is required. Below we will show that a new secondary Hopf bifurcation on L occurs inside region $3'$.

In summary, we find that fixed points A and B together with the transversal periodic orbit T correspond to the type *II* Hopf–saddle–node scenario proposed by the normal form analysis in the previous section. The periodic orbit L is also an integral part of the bifurcation set of a laser with injected signal, and we will show in the next section how the interaction of bifurcations between these two periodic orbits organize the resonance structure.

8.2.2 Bifurcations of transversal periodic orbits

We begin with a general observation for the existence boundary of transversal T orbit born at the the Hopf bifurcation of fixed points. For a fixed value of η, we find for the continuation of this orbit for decreasing β, its period diverges at a critical $\beta \approx 0.05$, for an interval of η close to 0, where a homoclinic orbit to fixed point C occurs. Figure 8.2 shows the locus of this global bifurcation in parameter space, while Figs. 8.10 and 8.11 show the typical period versus β behaviour. This bifurcation is found not to depend on θ, and was found up to type *III* regime. We leave for Sec. 8.3 the discussion of how this bifurcation is related to the Andronov bifurcation producing L.

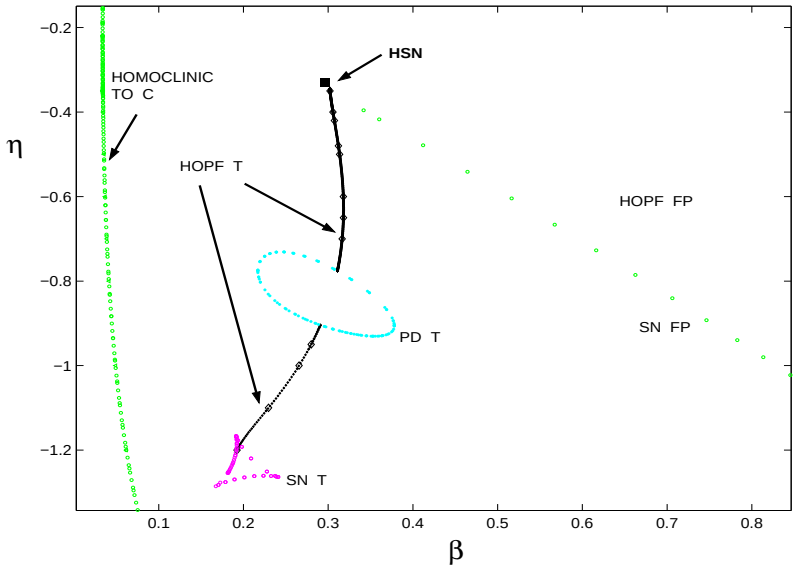

Figure 8.2: Partial numerical bifurcation set showing the homoclinic to C fixed point and the first resonances of the transversal secondary Hopf bifurcation. Saddle–node bifurcation of transversal periodic orbits (SN T) and period doubling bifurcation of transversal periodic orbits (PD T) are indicated.

In Fig. 8.3 (a) we display the main invariant sets for the parameter region bounded by the homoclinic to C and the secondary Hopf bifurcation. We have the stable longitudinal orbit L (which lies approximately on $|E| \approx A = 1, W \approx 0$), together with the unstable transversal orbit T. This orbit has a large variation in the population inversion W, and a bounded electric field phase (the phase does not make a complete turn as L does). Crossing the secondary Hopf bifurcation T and entering region $3'$, we find that T becomes stable and an unstable invariant torus is created. Figure 8.3 (b) shows the invariant sets, where only the intersections of the quasiperiodic orbit with the $W = 0$ plane are shown. A time series of the intensity $|E|^2$ on this solution is shown in Fig. 8.4.

It is well known that in generic systems quasiperiodic motion may suffer resonance phenomena. Local analysis [Arnold, 1983] around the Hopf bifurcation reveals that whenever the ratio of the two competing frequencies is rational, the quasiperiodic motion may disappear and periodic orbits arise. These orbits may be classified by an integer number of p turns following the primary or bifurcating orbit (T in this case), and another integer number q which denotes the number of turns made around the primary orbit, before closing on itself. Precisely on the (secondary) Hopf bifurcation the nontrivial Floquet multipliers are on the unit circle at $e^{\pm i2\pi p/q}$. A general result shows that in the *weak resonances* case $q > 4$ these periodic orbits are born in saddle–node pairs, and in a two–parameter space they trace a 'tongue' (known as Arnold tongue) with the tip lying on the (secondary) Hopf bifurcation. In phase space the periodic orbits are *phase locked* solution on the torus. On the other hand the case $q \leq 4$ are known as *strong resonances* and do not correspond to 'strict' Arnold tongues. The details of each strong resonance in a general study may be found in [Kuznetsov, 1997].

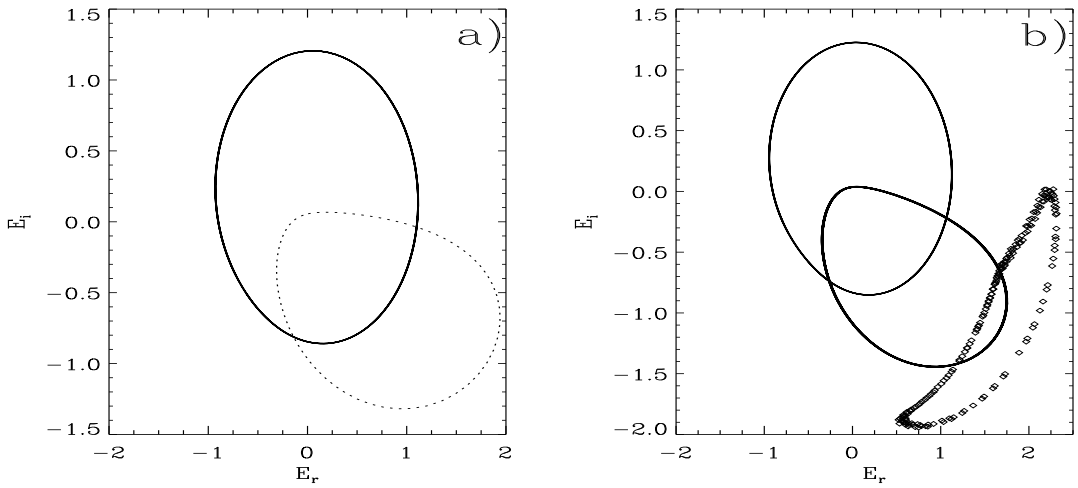

Figure 8.3: Phase portrait in $(E_r = Re(E), E_i = Im(E))$ of periodic orbits in the neighbourhood of the (secondary) Hopf bifurcation of T. Solid lines: stable orbits, dot lines: unstable trajectories. $\eta = -1$. (a) $\beta = 0.24$, (b) $\beta = 0.28$. The torus created is an unstable one.

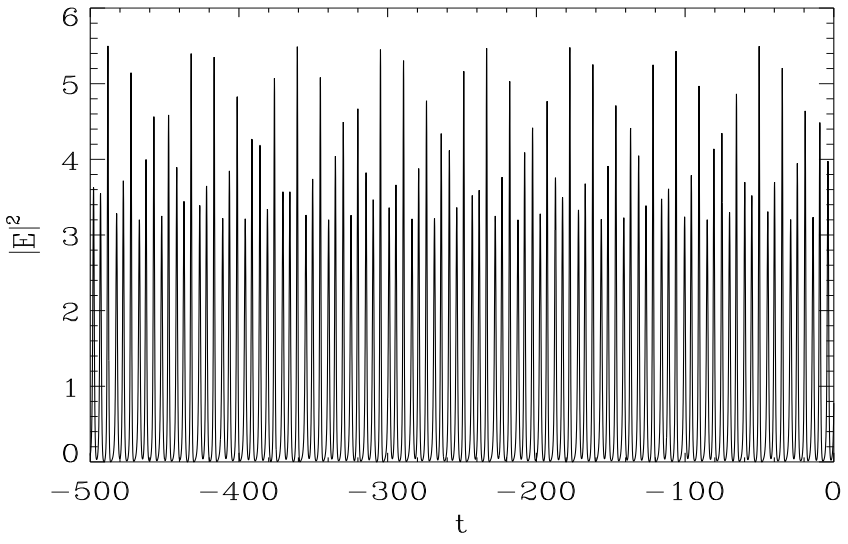

Figure 8.4: Intensity ($|E|^2$) versus time for the unstable transversal torus created in the Hopf bifurcation of T periodic orbits. $\eta = -1$, $\beta = 0.28$.

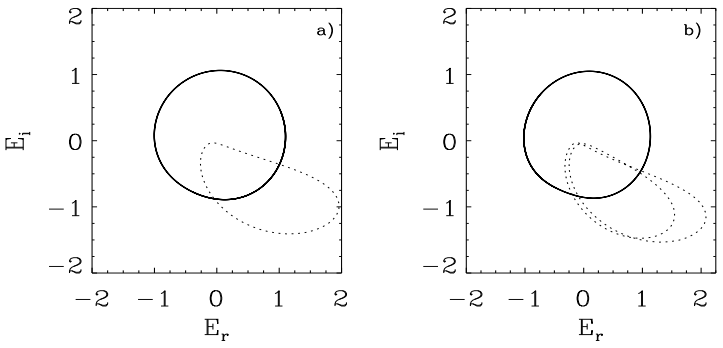

Figure 8.5: Projections in the plane (E_r, E_i) of the orbits that exist in each side of the period doubling bifurcation. Solid lines: stable orbits, dot lines: unstable trajectories. Saddle orbits are not represented. $\eta = -0.8$. (a) $\beta = 0.2$, (b) $\beta = 0.23$.

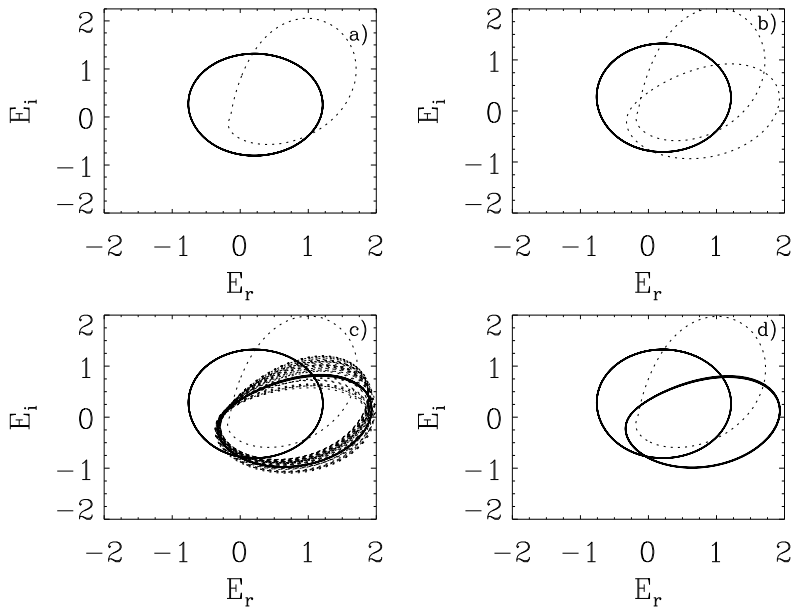

Figure 8.6: Projections in the plane (E_r, E_i) of the orbits that exist in different regions of Fig. 8.15. Solid lines: stable orbits, dot lines: unstable trajectories. Saddle orbits are not represented. $\eta = -1.2$. (a) Region B, $\beta = 0.19$, (b) Region F, $\beta = 0.192$, (c) Region G, $\beta = 0.1939$, (d) Region H, $\beta = 0.1942$. The bifurcations between the different regions are: from B to F a saddle–node bifurcation, from F to G a Hopf bifurcation of periodic orbits, and from G to H a homoclinic of periodic orbits.

In Fig. 8.7 we display the resonance structure for $1/q, q = 1, .., 12$, where the saddle–node of the resonant periodic orbits have been continued in parameter space. Of course in general one expects a countable number of tongues, one for each rational p/q. We will show below the location of other resonances with $p \neq 1$. We find that the tongues corresponding to $q > 4$ behave like standard Arnold tongues, while $q = 1, 2, 3, 4$ behave in a different way as expected. Resonance $q = 4$ is well known not to finish in a cusp singularity (compare with [Kirk, 1991]), while resonance $q = 3$ does not even finish in a cusp bifurcation (see below for a detailed description of this resonance). For lower η, resonance $q = 2$ arises whenever the nontrivial Floquet multipliers of the primary periodic orbit (T) collide in a doubly degenerate -1 eigenvalue. In this case, we find in parameter space the Hopf bifurcation is interrupted by an "isola" of period doubling bifurcations (PD T in Fig. 8.7), see Fig. 8.5. For even lower η we find that the Hopf bifurcation is finally interrupted when the two nontrivial Floquet multipliers become degenerate at $+1$. In this case a saddle–node bifurcation of periodic orbits occurs (SN T in Fig. 8.7), see Fig. 8.6, and in fact a Takens–Bogdanov [Kuznetsov, 1997] singularity takes place. In Sec. 8.2.4 we discuss this with more detail.

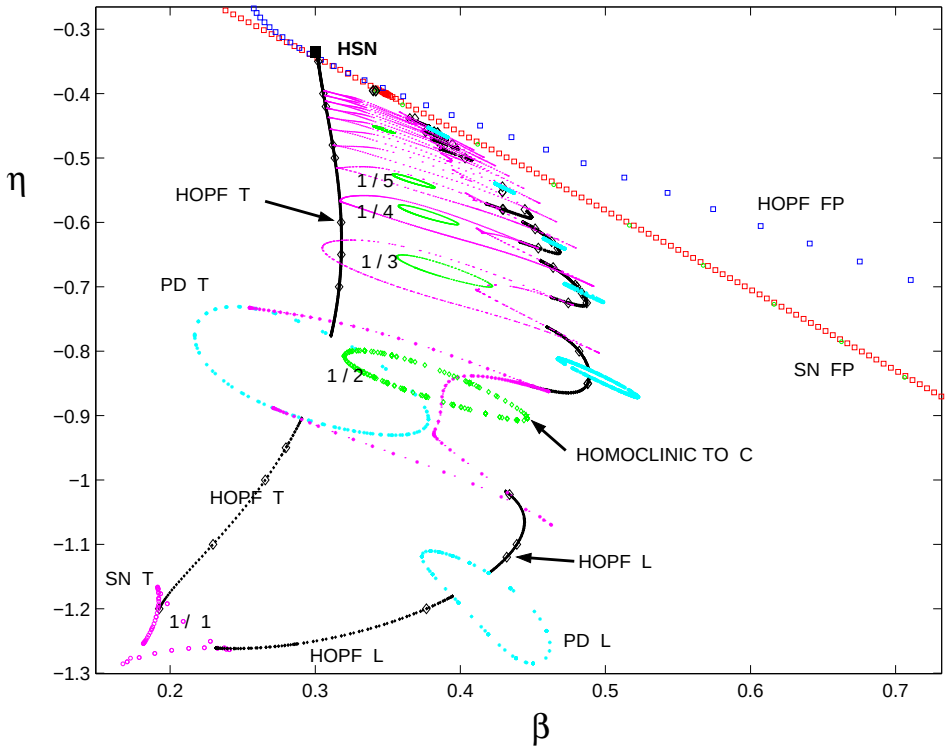

Figure 8.7: Resonance structure for the transversal and longitudinal Hopf bifurcations, together with the homoclinic bifurcation to fixed point C. Period doubling bifurcations of longitudinal orbits (PD L) and Hopf bifurcations of longitudinal orbits (HOPF L) are displayed.

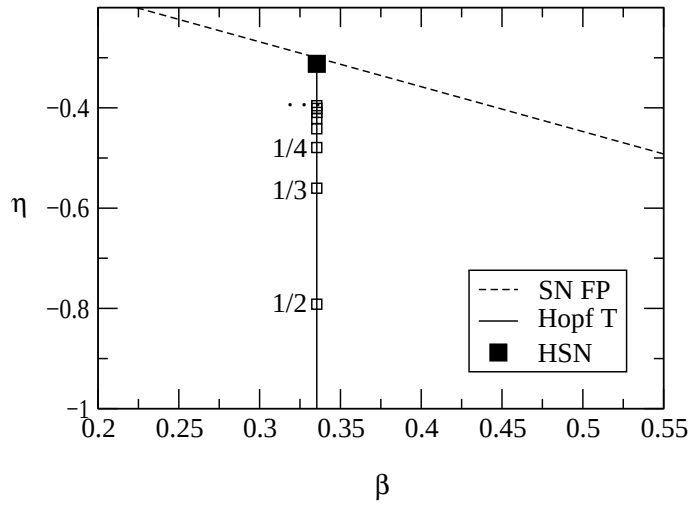

Figure 8.8: Secondary Hopf bifurcation and its resonances $p/q = \{1/2, 1/3, 1/4, ..\}$ from an estimation of the Hopf–saddle–node normal form (8.2) using the laser with injected signal parameters (β, η). The dashed line is the saddle–node of fixed points while the vertical line is the secondary Hopf bifurcation. Compare with Fig. 8.7. ($A = 1$, $\theta = 0.5$, $\chi = 0.3$).

The organization of the tongues in parameter space shows that for increasing q, the resonances appear to accumulate *towards* the Hopf–saddle–node singularity. This may be easily understood by a simple analysis from the Hopf–saddle–node normal form. Truncating the normal form (8.2), the eigenvalues of the Hopf periodic orbit (corresponding to T) at the (degenerate) secondary Hopf bifurcation $\mu = 0, \nu < 0$ are $\lambda_{1,2} = \pm i\ \omega_1 = \pm i\sqrt{2\bar{a}\nu}$. Using the expression of $\bar{a}(\theta)$ and c in (8.3) we may estimate the position of the resonances in parameter space solving

$$p\bar{c} = q\omega_1(\nu), \tag{8.8}$$

for each pair of p, q. It is clear that moving on the secondary Hopf and approaching the Hopf–saddle–node singularity ($\nu \to 0$), the typical secondary frequency ω_1 goes to zero, so a larger q is required to satisfy the resonance condition. Figure 8.8 shows the result of this estimation of the resonance condition using the approximate reparametrization of the laser with injected signal (β, η) parameters in terms of Hopf–saddle–node parameters (8.3):

$$\eta(\mu,\nu) = \frac{(1+\theta^2)(\nu-2)\chi}{2(-2\theta+\mu(1+\theta^2)}, \qquad \beta(\mu,\nu) = \frac{\sqrt{1+\theta^2}\chi}{-2\theta+\mu(1+\theta^2)}. \tag{8.9}$$

The resonance structure is very similar to the one identified by Kirk [Kirk, 1991], but for type *III* Hopf–saddle–node. The main difference is that in this type the invariant torus coexists with the two fixed point solutions, and the possible homoclinic/heteroclinic between them. Her main result was that the Arnold tongues accumulated for increasing winding number towards this homoclinic/heteroclinic bifurcation present for this particular type. In our case we observe that the accumulation of the tongues saddle–nodes is onto the Andronov global bifurcation, occurring at the saddle–node of fixed points.

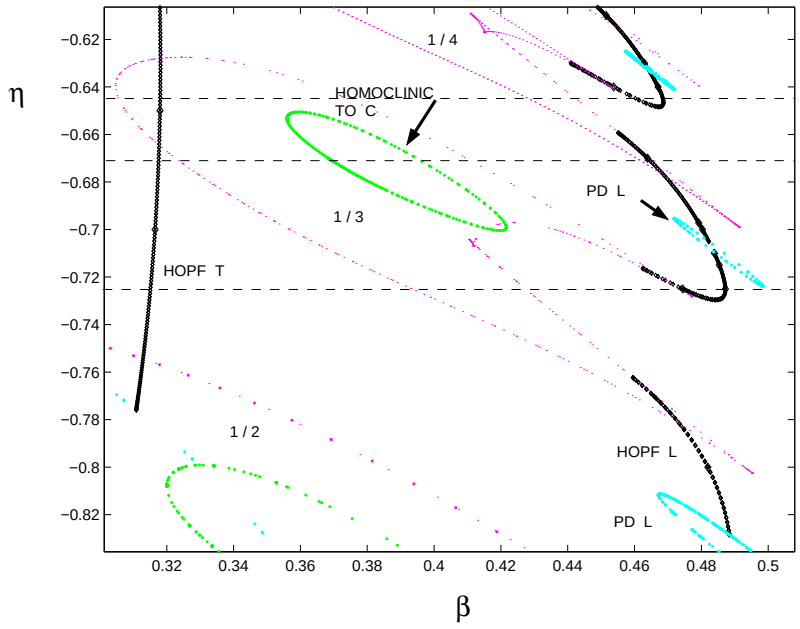

Figure 8.9: Partial numerical bifurcation set around the 1/3 resonance. The horizontal lines are constant–η parameter cuts shown in Fig. 8.10.

8.2.3 Structure and truncation of Arnold tongues

A closer look at how the periodic orbits are organized inside each resonance $q > 2$ is very interesting. To fix ideas we take resonance $q = 3$ shown in Fig. 8.9. We have performed three constant–η parameter cuts displayed in Fig. 8.10, where the period of the orbits as a function of β is shown. In each panel the unstable T periodic orbit is seen to born at $\beta \approx 0.05$ (with diverging period) in a homoclinic bifurcation to C, becoming stable at $\beta \approx 0.30$ in the (secondary) Hopf bifurcation. Also for low β we observe the stable L orbit which suffers a number of saddle–node and Hopf bifurcations as β increases, and finally its period diverge as it approaches at $\beta \approx 0.60$ the saddle–node infinite–period (Andronov) bifurcation.

In Fig. 8.10 (a), close to the Hopf bifurcation of T, a saddle and unstable periodic orbit are born in a saddle–node bifurcation and collide at a higher β in a reverse saddle–node bifurcation. Both bifurcations corresponds to the resonance boundaries shown in Fig. 8.9. For a slightly lower constant–η cut [Fig. 8.10 (b)], we find that the periof of the unstable branch of the resonant periodic orbits "explotes" and two homoclinic bifurcations to C originate. These global bifurcations correspond to the isola of homoclinics to C observed in Fig. 8.9. Finally, in a cut further away from the $q = 3$ resonances of the Hopf of T [Fig. 8.10 (c)], the homoclinics to C disappear and with the aid of another saddle–node bifurcation, the resonant periodic orbits "merge" with the L periodic orbit. Notice in Fig. 8.10 (a) that resonance $q = 4$ already merged to L. The above merging process of transversal resonances into the longitudinal periodic solution is observed for all resonances $1/q$, $q > 2$.

The $q = 2$ resonance reveals a more complex structure due to the fact that it interacts with the period doubling bifurcation of periodic orbits. In Fig. 8.11, the period of the orbits as a function of β for different values of η in this resonance is shown.

One may wonder if there is a topological restriction for the merging process, as the transversal orbit (and its associated resonances) are *linked* in phase space to the longitudinal orbit L, as shown in Fig. 8.3. For this, in Fig. 8.12 (a)–(c) we illustrate a continuation of L, T and a resonant orbit in order to show how the link of a transversal orbit remains as it merges to a longitudinal orbit.

In fact, close to the merging process, the longitudinal orbits L also bifurcates in a secondary Hopf bifurcation. Figure 8.13 (a) illustrates the unstable L longitudinal orbit born at the Andronov bifurcation, bifurcating in a secondary Hopf bifurcation and creating a new unstable longitudinal torus around L [Fig. 8.13 (b)]. Notice also that the electric field intensity time series Fig. 8.14 is also quite different of that of Fig. 8.4.

The remarkable feature is the organization in parameter space of the above bifurcations. We have found that all $1/q$ transversal resonances, end up in a cusp bifurcation with another saddle–node bifurcation. The latter bifurcation is the responsable for the merging described above, and on this branch a $1/q' = 1/1$ secondary Hopf bifurcation occurs on L. Continuation of the new Hopf bifurcation reveals that it suffers a $1/2$ resonance (with a period doubling isola), before it ends at another $1/q' = 1/1$ resonance, corresponding to a transversal tongue $1/(q-1)$. This sequence of bifurcations is seen to occur for all the transversal $1/q$ resonances found.

The complete structure of the phase diagram of Fig. 8.7 has now been described and reveals a high organization which repeats as we approach to the Hopf–saddle–node point. Several bifurcations not present in the local description of Hopf–saddle–node take part of the dynamics: (a) we have the Arnold tongues which for increasing q accumulate to the Andronov bifurcation, (b) the secondary longitudinal Hopf bifurcation connecting subsequent transversal resonances, and (c) the homoclinic bifurcations to C (the off state). The latter global bifurcations have a winding number in correspondence with the resonance to which it belongs. Thus in the limit close to Hopf–saddle–node one expects an accumulation of homoclinic orbits to C of diverging winding number. Furthermore, most turns would follow the smaller loop T, as we approach Hopf–saddle–node. This argument points to the possibility that another global connection between the Hopf–saddle–node fixed point and the laser off state C exists. This has not been explored in detail and deserves further study (see Sec. 8.3 below).

8.2.4 Homoclinics to periodic orbits

As mentioned above, all strong resonances are known to posses more bifurcation structures than those that we have pointed out. In particular, it is well known that unlike what happens in weak resonances, the saddle–node bifurcations of the tongues

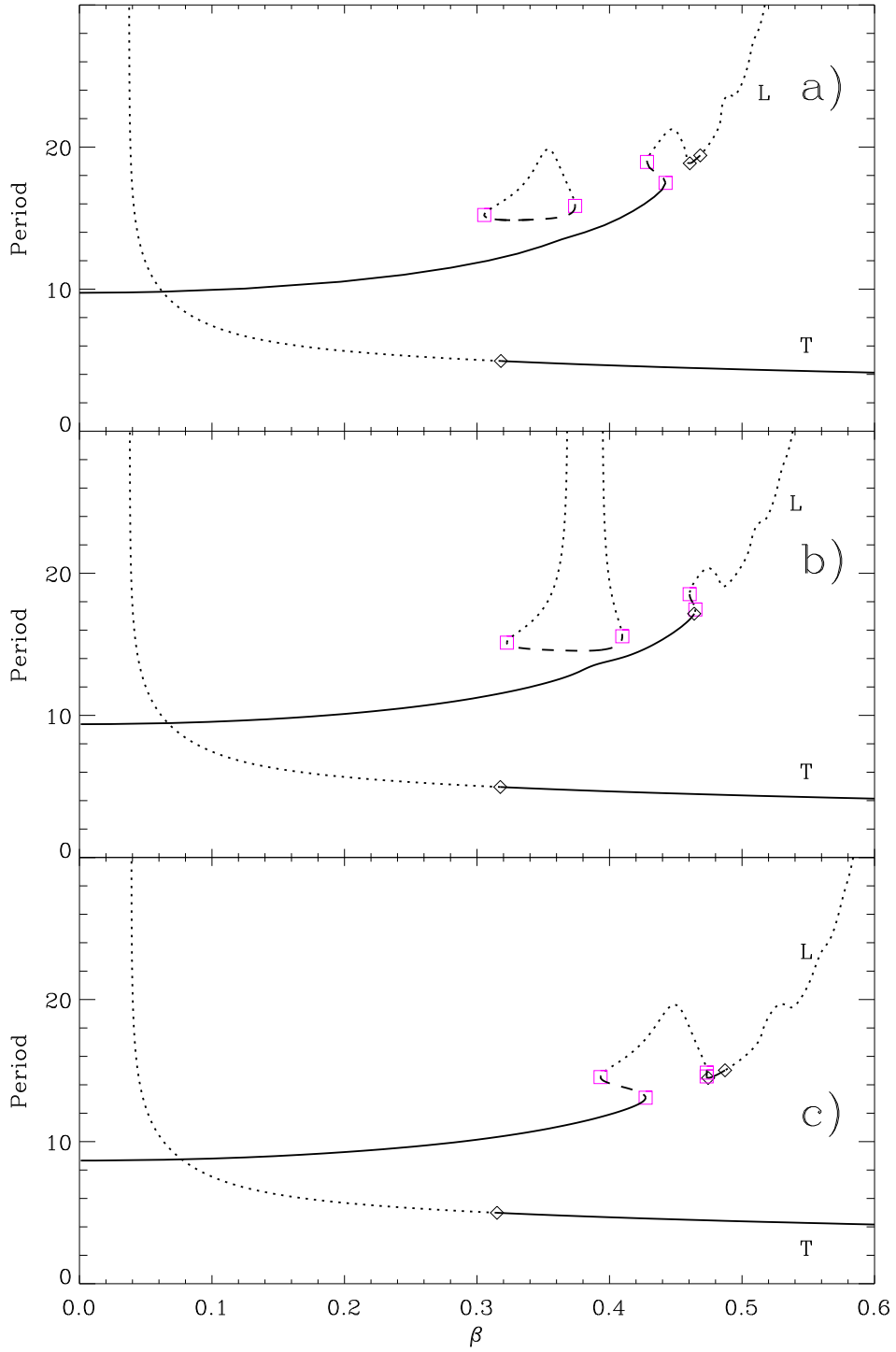

Figure 8.10: Period versus β of periodic orbits inside the resonance $q = 3$. (a) $\eta = -0.645$: the two saddle–node bifurcations forms an "isola" for the resonant periodic orbits close to the HOPF T bifurcation. (b) $\eta = -0.670$: the saddle branch of the isola "explodes" in period, creating two homoclinic bifurcations to C. (c) $\eta = -0.725$: the resonant branch of $q = 3$ periodic orbits merges with the L branch. Merging of the $q = 4$ resonance is also observed in (a). Solid line: stable orbit, dotted line: unstable orbit, dashed line: saddle orbit, squares: saddle–node bifurcations of periodic orbits, diamonds: Hopf bifurcations of periodic orbits.

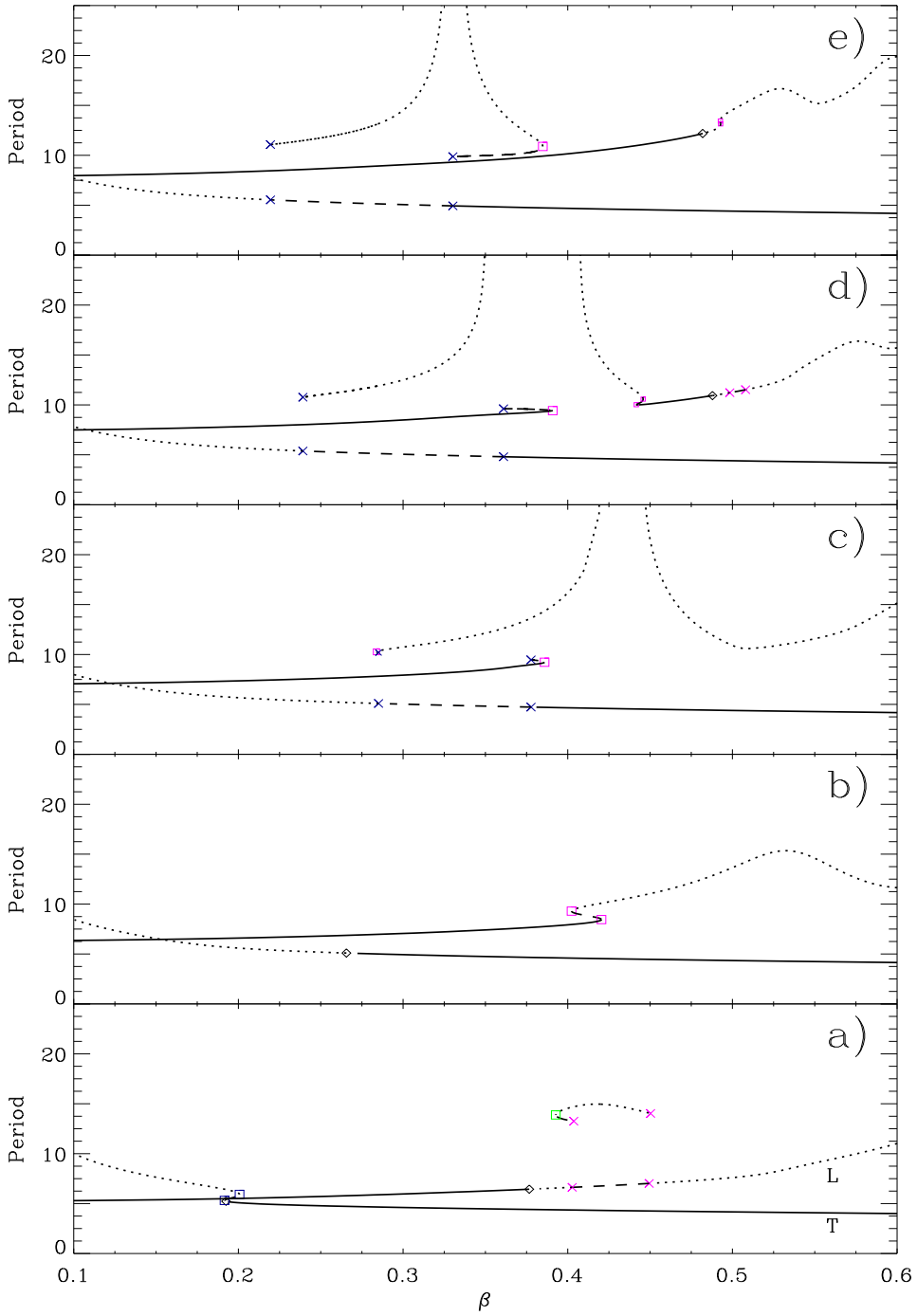

Figure 8.11: Period of the orbits versus β for different values of η: (a) $\eta = -1.2$, (b) $\eta = -1$, (c) $\eta = -0.9$, (d) $\eta = -0.85$, (e) $\eta = -0.8$. Solid line: stable orbit, dotted line: unstable orbit, dashed line: saddle orbit, squares: saddle–node bifurcations of periodic orbits, diamonds: hopf bifurcations of periodic orbits, crosses: period doubling bifurcations of periodic orbits.

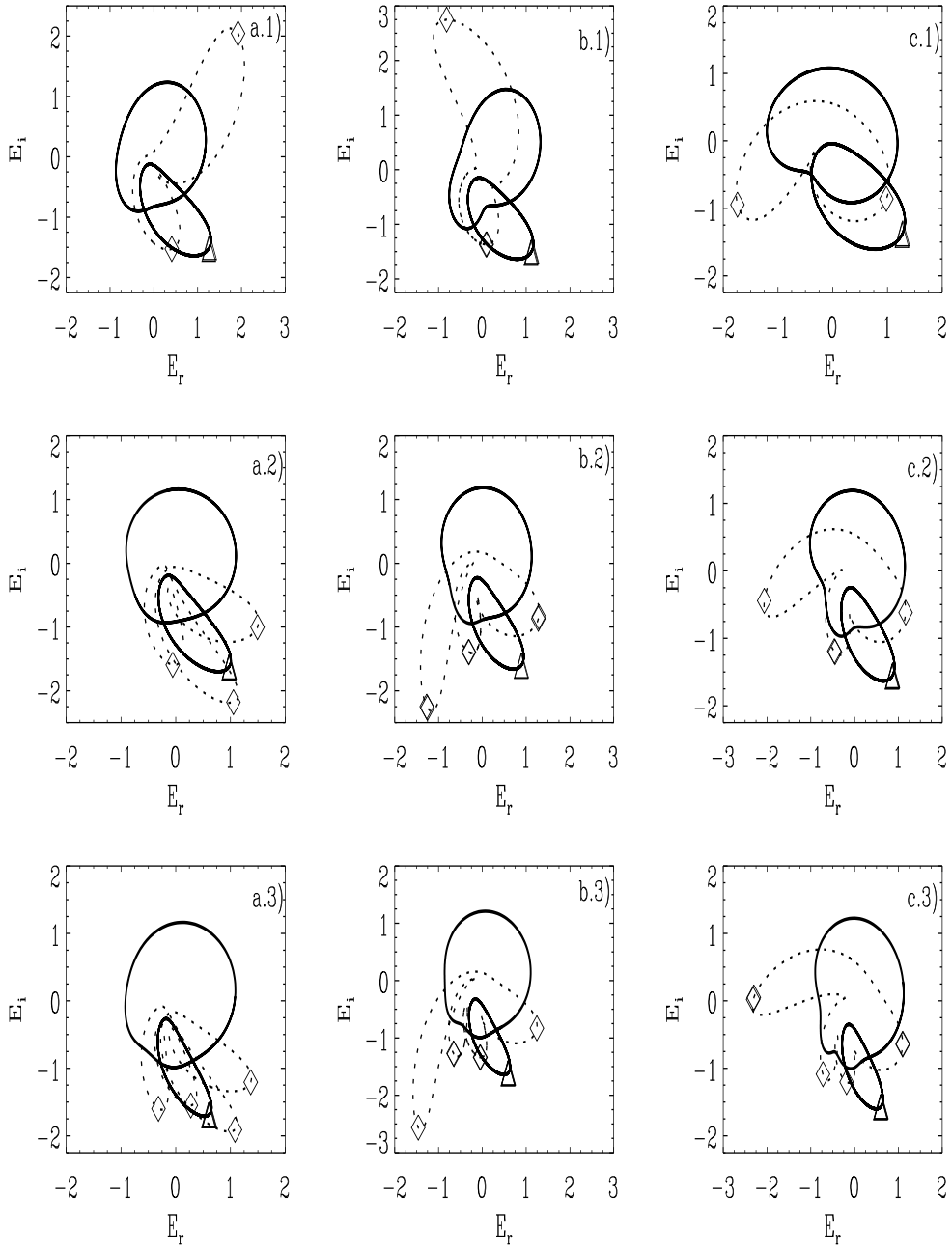

Figure 8.12: Phase portraits of resonance orbits, together with T and L. Each row shows a continuation of a transversal $1/q$ resonance on the right column, ending in a longitudinal $1/q'$ orbit on the right column. For a clear visualization only the first row displays the whole resonance orbit, while only its intersections with $W = 0$ are shown in the subsequent rows. Resonance 1/2 (η, β): (a1) $(-0.77, 0.32)$, (b1) $(-0.83, 0.40)$, (c1) $(-1, 0.41)$. Resonance 1/3: (a2) $(-0.66, 0.32)$, (b2) $(-0.70, 0.38)$, (c2) $(-0.75, 0.44)$. Resonance 1/4: (a3) $(-0.565, 0.32)$, (b3) $(-0.60, 0.38)$, (c3) $(4, -0.64, 0.43)$. Solid lines: stable orbits, dot lines: unstable trajectories. Saddle orbits are not represented.

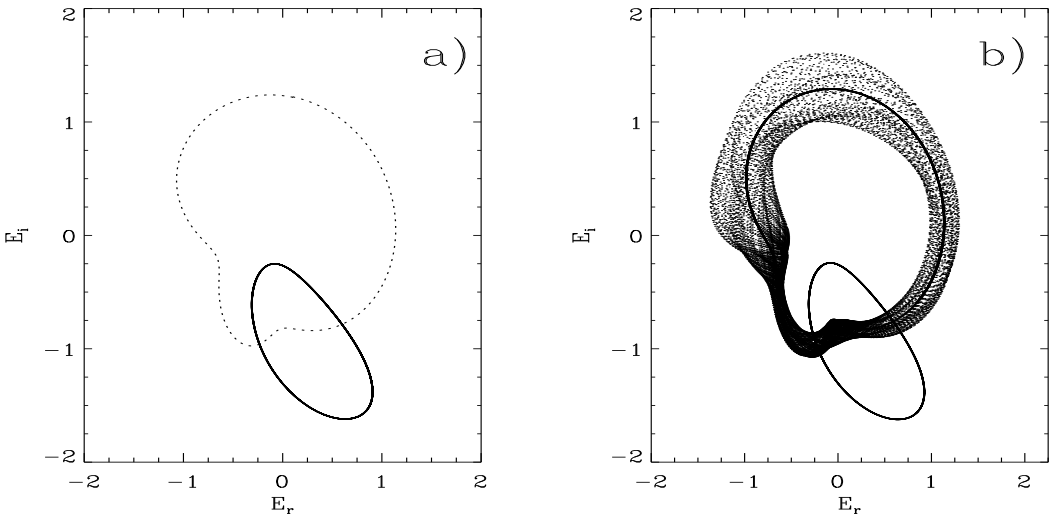

Figure 8.13: Projections in the plane (E_r, E_i) of the orbits that exist in each side of the Hopf bifurcation of L periodic orbits. Solid lines: stable orbits, dot lines: unstable trajectories. $\eta = -0.8$. (a) $\beta = 0.485$, (b) $\beta = 0.477$. The torus created is unstable.

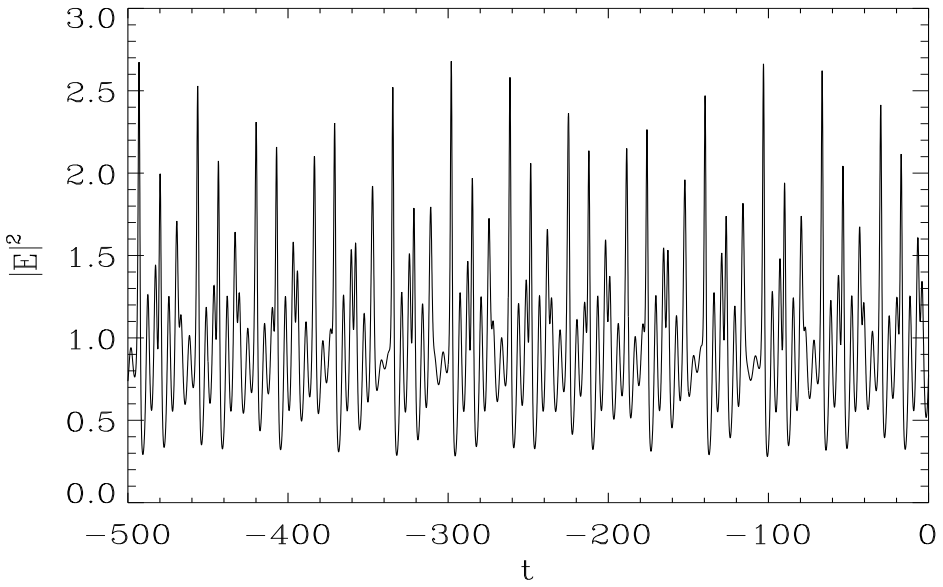

Figure 8.14: Intensity versus time for the torus created at the Hopf bifurcation of L periodic orbits. $\eta = -0.8$, $\beta = 0.477$.

do not occur on the torus. Instead the invariant torus may grow as parameters change and eventually collide with one of the resonant periodic orbits. This would correspond to a *homoclinic bifurcation* to a periodic orbit, with the final destruction of the torus.

One example may be found in the intersection point of all 1/1 resonance points with the saddle–node bifurcation of periodic orbits. At this point one may expect a Takens–Bogdanov singularity [Kuznetsov, 1997] which is well known to have such a global bifurcation. Figure 8.15 shows an enlargement of the 1/1 resonance of the transversal T and longitudinal L orbits, where the diamonds indicate the approximate values where a homoclinic tangency was observed by direct numeric computation.

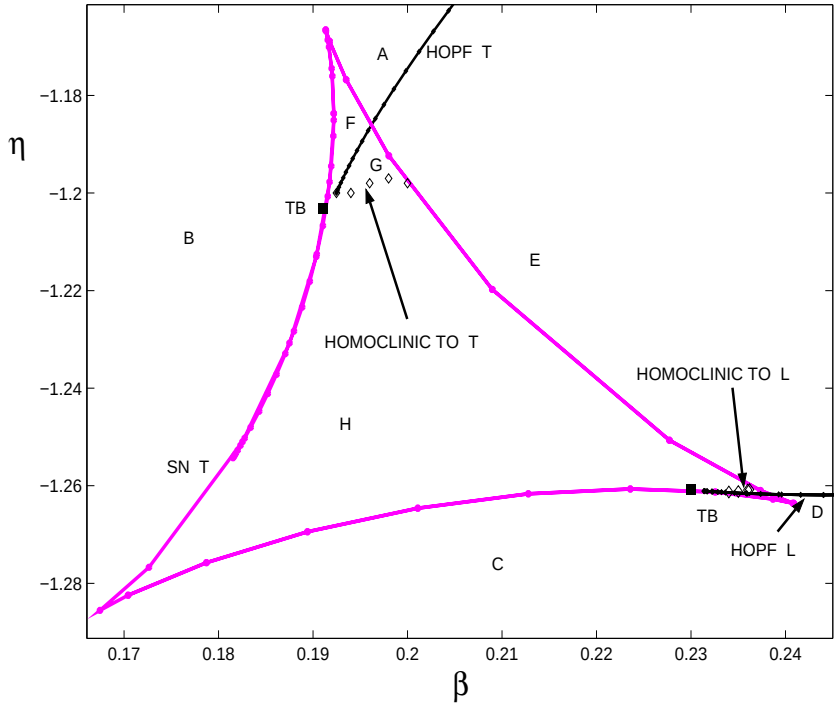

Figure 8.15: Blowup of 1/1 resonance of transversal T and longitudinal L orbits. Diamonds show the locus of homoclinic tangencies to T and L orbits.

A close loop around the Takens–Bogdanov point in Fig. 8.15 describes the main features, see Fig. 8.6 for the orbits in the parameter space. Moving from region B to F two periodic orbits are created, one saddle and one unstable. From F to G the secondary Hopf bifurcation creates an unstable torus, and the unstable periodic orbit becomes stable. In region G the radius of the torus grows as one approaches region H, and finally collides in a homoclinic bifurcation to the saddle periodic orbit. In Fig. 8.16 we illustrate a numeric computation of the stable and unstable manifold of the periodic orbit T, showing clearly a homoclinic bifurcation. Notice that one expects homoclinic tangencies as one departs from the Takens–Bogdanov point. Finally, moving from H to B, the remaining periodic orbits disappear in a saddle–node bifurcation.

An analogous scenario holds for the Takens–Bogdanov point on the longitudinal orbits seen in Fig. 8.15, denoted homoclinic to L. In general, we also find Takens–Bogdanov bifurcation points in all $1/q' = 1/1$ resonances of L described above. We emphasize that this is only an approximate view since at the Takens–Bogdanov point many other bifurcations originate (see [Hirschberg and Laing, 1995]).

A different homoclinic bifurcation to a periodic orbit is the one encountered inside the $1/3$ resonance, see Fig. 8.17. This is a well established result from the normal form analysis of this bifurcation [Arnold, 1983; Kuznetsov, 1997]. The torus is found between the secondary Hopf and the homoclinic tangency. In this case, the torus grows and collides to a saddle period $q = 3$ orbit, which exists in an neighbourhood of the T resonance point.

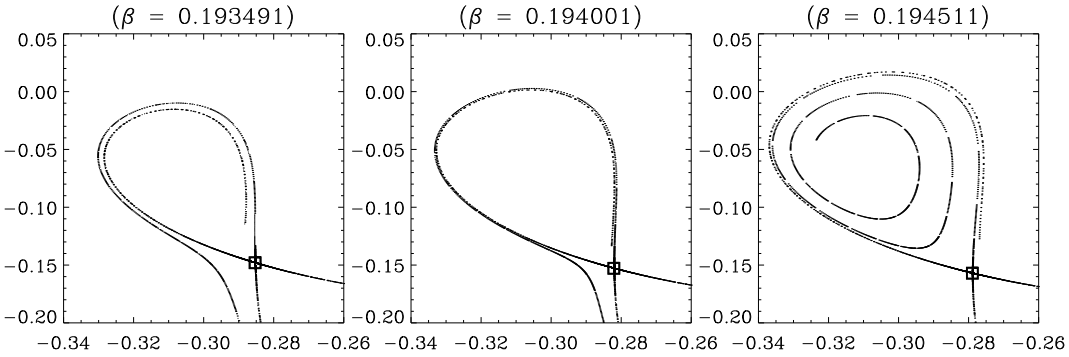

Figure 8.16: Phase portraits of the Poincaré section $W = 0$ for the homoclinic bifurcation of the $1/1$ transversal resonance, in the neighbourhood of the homoclinic tangency. The saddle periodic orbit is at the square, and next we computed the stable and unstable manifolds. ($\eta = -1.20$)

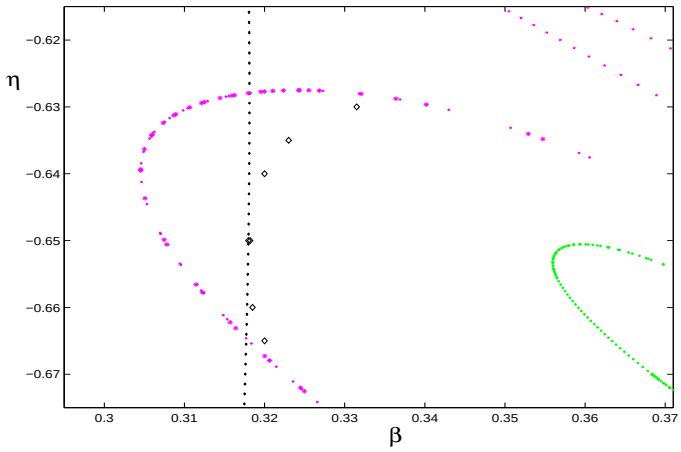

Figure 8.17: Homoclinic bifurcation in $1/3$ resonance. Diamonds account for the homoclinic to the saddle T periodic orbit.

8.2.5 Full resonance structure

In general one expects a countable number of resonances for the breakup of quasiperiodic motion, one for each rational p/q. These may be organized following the Farey sequence [Aronson *et al.*, 1982], where between resonances p/q and p'/q' one always finds resonance $(p+p')/(q+q')$. A full classification of all these resonances is quite complicated so we show the locus of two resonances with $p > 1$. In Fig. 8.18 we display two resonances in between the strong 1/1 and 1/2 of the transversal torus. They show basically the same structure, including the isola of homoclinic bifurcations to C and homoclinic bifurcations to the T. One of them, the transversal 5/8 resonance, becomes a weak resonance in the neighbourhood of the L torus. The other, a transversal 2/3 resonance becomes a strong 1/2 resonance in the neighbourhood of the L torus. Notice also the homoclinic bifurcations to L and T periodic orbits found in this resonance.

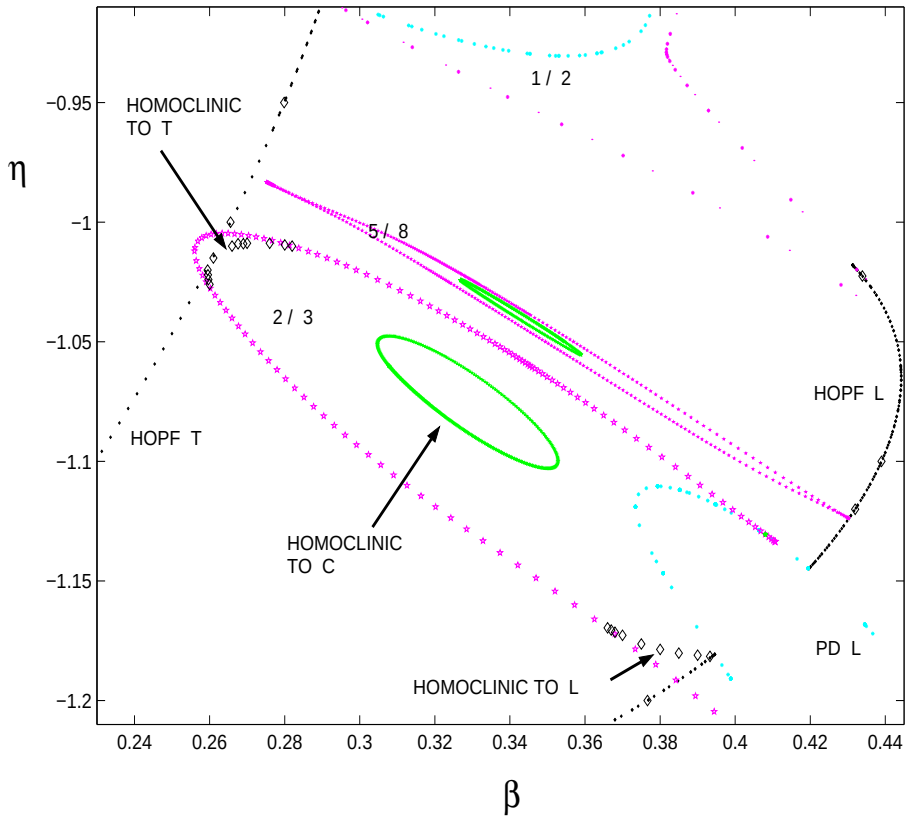

Figure 8.18: Higher order resonance structure between 1/2 and 1/3 transversal resonance. Transversal resonance 2/3 becomes 1/2 resonant to orbit L, while transversal 5/8 resonance becomes a weak resonance to L.

8.3 Andronov bifurcation

We now describe with some more detail the Andronov bifurcation found in the laser with injected signal. In Fig. 8.19 we illustrate the phase portraits of the unfolding of this bifurcation in a one parameter cut. They correspond to the Andronov–Leontovich[3] [Kuznetsov, 1997] bifurcation: a periodic orbit in the region of no fixed point collides in a homoclinic orbit with the saddle–node (SN) fixed point. At the bifurcation point, there exists an orbit leaving the central manifold, and returning after some finite time through the other central manifold of the saddle–node fixed point.

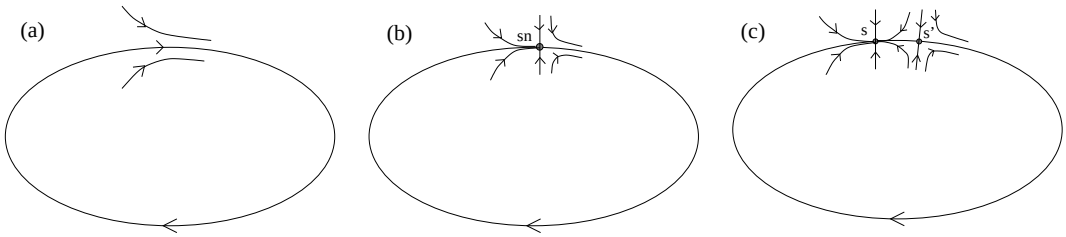

Figure 8.19: One–parameter unfolding of Andronov bifurcation. Note that the stable manifold of the fixed points in (b) and (c) are two–dimensional in a laser with injected signal.

This bifurcation is quite representative in a laser with injected signal and has been confirmed in several parameters regimes. The standard Adlers equation [van Tartwijk and Lenstra, 1995] is a one–dimensional example displaying this bifurcation. Also the two–dimensional averaged model of [Solari and Oppo, 1994], displays this bifurcation at the SN bifurcation of fixed points. This in fact motivated previous studies in global bifurcations, for in generic three–dimensional systems one expects that the global connection connecting the saddle–node to itself should break.

Results for type *III* in [Zimmermann *et al.*, 1997] show that the Andronov global bifurcation exists for sufficiently small (β, η), but become degenerate at a point close to the Hopf–saddle–node singularity, where a new codimension–2 bifurcation known as Shilnikov–saddle–node, occurs. At the bifurcation, the homoclinic orbit leaves through the central manifold the neighbourhood of the saddle–node fixed point, but now returns through the *stable* manifold of the degenerate fixed point. Results for type *I* $(1 < \theta < \sqrt{3})$ show that the Andronov bifurcation exists for the whole interval between $(\beta, \eta) = (0, 0)$ up to the Hopf–saddle–node point. However on the other side of the codimension–2 point, homoclinic tangencies to T occur near the SN bifurcation of fixed points [Zimmermann *et al.*, 2001].

For type *II* we display in Fig. 8.21 a continuation in parameter space of the Andronov bifurcation, approximated by continuation of a very high period L orbit. The locus of this global bifurcation starts at $(\beta, \eta) = (0, 0)$ and extends past the Hopf–saddle–node point. The stability of the periodic orbit depends on the stable

[3]In fact this bifurcation was studied by Andronov in 2–dimensions, while the n–dimensional case was solved by [Šil'nikov, 1966]. However we keep the term Andronov bifurcation to the generic case.

or unstable direction of the degenerate fixed point at the SN bifurcation. Therefore for $|\eta|$ small the stability of L is stable (region 3 in Fig. 8.1), while for values on the other side of the Hopf–saddle–node point, L becomes unstable (region 3′ in Fig. 8.1). In phase space, orbits born at this global bifurcation display a number of transversal oscillation ("bumps") in the region of phase space where the saddle–node fixed point (SN) disappeared. The number of these oscillations diverge as we approach from below the Hopf–saddle–node bifurcation point, for in the neighbourhood of this singular point there are *two* directions with extremely slow dynamics. Moving away from the saddle–node bifurcation, the transversal oscillations are observed to grow in phase space. We have shown in Sec. 8.2.3 how this periodic orbit is found in general to suffer saddle–node bifurcations corresponding to the resonance boundaries of the Arnold tongues, or a secondary Hopf bifurcation. This clarifies the integral role of the Andronov bifurcation in the complete bifurcation structure close to the Hopf–saddle–node bifurcation point.

A new global bifurcation was found involving the Andronov bifurcation. For sufficiently negative η, the homoclinic orbit makes a global excursion which approaches the C fixed point. In parameter space, we find that the Andronov bifurcation collides at a point with the branch of homoclinic bifurcations to C. At the collision point a heteroclinic cycle between the saddle–node (SN) and C fixed point was found. That is, there is a heteroclinic connection leaving through the central manifold of SN and enters C through the stable one–dimensional manifold, and another connection which leaves through the two–dimensional unstable manifold of C, and enters back to SN through its two–dimensional stable(–center) manifold (see Fig. 8.20). This cycle is reminiscent to the T–point bifurcations found for two *non–degenerate* fixed points [Glendinning and Sparrow, 1986; Bykov, 1993; Zimmermann and Natiello, 1998]. So far, this degenerate heteroclinic system has not been studied in detail.

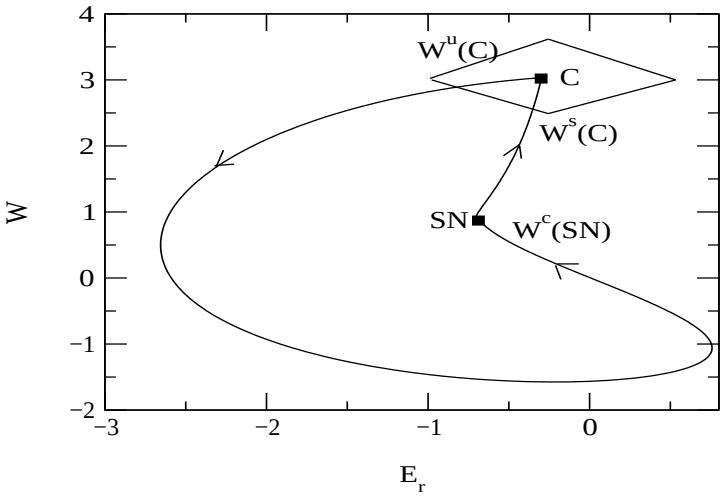

Figure 8.20: T–point bifurcation: phase portrait of heteroclinic cycle between fixed point C and saddle–node fixed point (SN) at $(\beta, \eta) = (-1.117, 0.91595)$. The stable manifold $W^s(C)$ is one–dimensional while the unstable manifold $W^u(C)$ is two–dimensional. W^c (SN) denotes the central manifold of the SN fixed point.

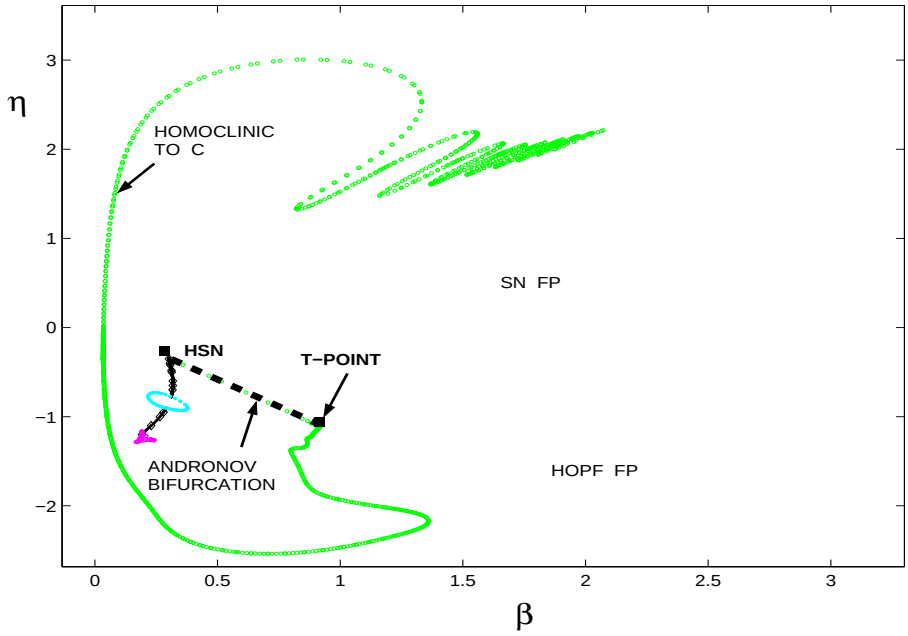

Figure 8.21: Locus of homoclinic bifurcation to C fixed point, T–point, and Andronov bifurcation at the saddle–node of fixed points.

8.4 Discussion

In this work a study of the partial bifurcation set around the type *II* regime of the Hopf–saddle–node singularity in a laser with an injected signal has been performed in order to contribute to the study of this system. It has been performed a careful analysis for one of the regimes not considered before in so detail. Secondary Hopf bifurcations to a transversal and longitudinal (to the $W = 0$ plane) periodic orbits dominate the periodic motion in a region of parameter space where non–locking solutions exists. The former periodic orbit is well described by the unfolding of the Hopf–saddle–node bifurcation, and corresponds to undamped relaxation oscillations, while the latter arises as a saddle–node infinite–period (Andronov) global bifurcation. Our results show how the Arnold tongues arising from the transversal torus are "truncated" in parameter space by resonances of the longitudinal torus. Thus in phase space the periodic orbits are observed to deform continuously from transversal into longitudinal orbits. A partial bifurcation set displaying our main result is shown in Fig. 8.22.

In chapter 6, it was described the bifurcation set for a class A laser with injected signal. The main difference between class A and class B lasers from the dynamical point of view is the number of variables that one works with. For class A lasers two variables suffice and the full bifurcation set can be described. For class B lasers, a three–dimensional system, a more complex variety of phenomena has been described. However, it has to be noticed that part of the bifurcation structure of class B lasers is already present in class A lasers. Hopf–Saddle–node and Takens–

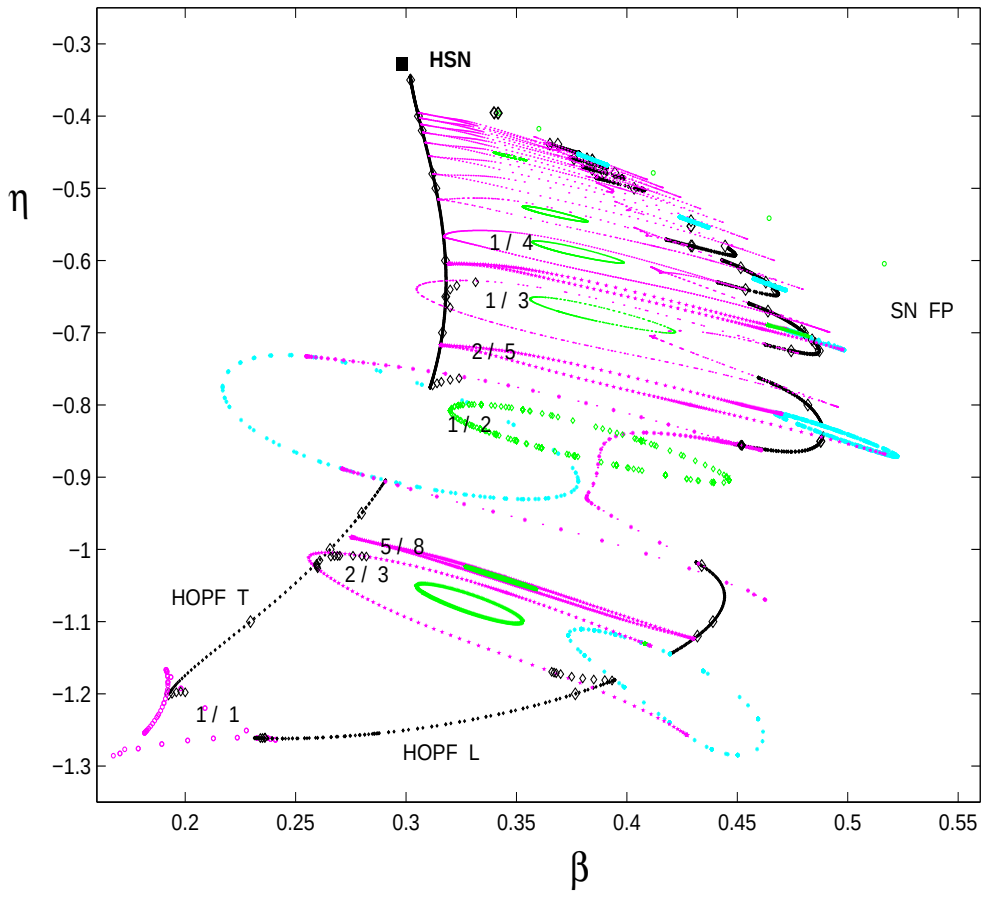

Figure 8.22: Partial numerical bifurcation set for type *II* Hopf–saddle–node in laser with injected signal.

Bogdanov singularities and Andronov global bifurcation were also present in the class *A* case.

Our work also extends [Solari and Oppo, 1994] results on the averaged laser with injected signal equations. The averaged system displays: (a) an Andronov bifurcation creating a longitudinal orbit, (b) a secondary longitudinal Hopf bifurcation on this orbit, which originates from the Hopf–saddle–node point in parameter space, and (c) the characteristic transversal secondary Hopf bifurcation of the type *II* Hopf–saddle–node singularity. However, Solari and Oppo observed as well singular behaviour (orbits going to infinity) when continuing the resulting tori in parameter space. The reason for this is the topological restriction to the deformation of transversal into longitudinal tori in a two–dimensional phase space.

In the three–dimensional setting of laser with injected signal equations we have found instead a family of homoclinic orbits to the off state fixed point, arranged in isolas in parameter space *inside each Arnold tongue* of the corresponding transversal torus. The off state fixed point appears to be at infinity in the averaged equations (due to the change of coordinates), and hence we can conjecture that the singular behaviour observed in the average model results from "bifurcations with infinity"

[Sparrow and Swinnerton-Dyer, 1995], as we move between both tori. A more detailed study of the averaged equations would be desirable to test this conjecture.

Our present work is also related to a recent work on solid–state lasers with optical injection [Yeung and Strogatz, 1998], where a complicated bifurcation diagram close to the saddle–node bifurcation was found. The rate equations studied may be shown to be rescaled to laser with injected signal equations (8.1) with $\theta = 0$ (provided that $g \neq 0$). This particular detuning was shown by Solari and Oppo to be somewhat more delicate, but type *II* Hopf–saddle–node was preserved. Yeung and Strogatz studied the attractors in a parameter cut with constant detuning η, and increasing β approaching the saddle–node bifurcation. Their diagrams showed periodic windows, interspeded by orbits with a large intensity, reminiscent of the homoclinic orbit to the off state found in our work. The most remarkable difference, is that the self–similar structure of periodic windows is reported to accumulate at the saddle–node of fixed points. Instead our work shows that (at least for $\theta = 0.5 > 0$), a *finite* number of resonances are crossed by constant–η cuts in the bifurcation diagram while approaching the saddle–node bifurcation. Nevertheless, it appears that the number of crossed resonances diverges as η approaches the codimension–2 value. Further work should confirm how the secondary Hopf bifurcation we found moves in parameter space as $\theta \to 0$.

Despite the complicated bifurcation set presented, we emphasize that most of this structure remains out of the hand of standard experimental setups due to noise terms that appear in experiments. Nevertheless we would like to point out that a partial confirmation of this bifurcation set should be possible, by following the stable *cw* solution in parameter space, and looking for stable undamped relaxation oscillations. The region of existence of these two stable invariant sets is bounded by the secondary Hopf bifurcation, and by locating the locking region, this may validate the basic features of the type *II* Hopf–saddle–node scenario.

Finally, we would like to emphasize the possible implications of the homoclinic bifurcations to the laser off state found above. The sequence of homoclinics bifurcations for each of the infinite number of resonances *accumulating* towards the Hopf–saddle–node singularity is a remarkable result which needs further detailed study. This phenomenon suggests that the Hopf–saddle–node singularity may have, on top of the saddle–node infinite–period global bifurcation, another pair of heteroclinic orbits to the Hopf–saddle–node fixed point, forming a cycle. So far, we are no longer surprised by the bizarre global bifurcations found in this laser, which provide stimulating motivation for further research.

Capítol 9

Resonàncies principals en làsers de semiconductor modulats

En aquest capítol es calculen els dominis d'existència de les resonàncies principals en làsers de semiconductor directament modulats, veure Sec. 1.3. Els resultats que s'obtenen numèricament al integrar directament les equacions es comparen amb els resultats d'aplicar la teoria quasi–conservativa. En el model es consideren explícitament els termes de saturació de guany i d'emissió espontània.

Les equacions per al làser de semiconductor (9.1) i (9.2) es tracten amb termes de modulació. Primerament es consideren modulacions en el terme de bombeig de tipus sinusoidal (9.3) amb amplitud relativa J_m i freqüència ω_m. La dinàmica de les equacions amb aquesta dimensió addicional esdevé molt més complexa que en el cas de bombeig constant (capítol 7). Per caracteritzar la resposta del sistema es mira el valor màxim de la intensitat òptica I, (I_{max}), quan es modula el làser. Per a valors petits de J_m i ω_m, el sistema es comporta de manera similar a un oscil·lador lineal amb termes d'esmorteïment: oscil·la periòdicament amb la freqüència d'entrada ω_m, i la resposta I_{max} té un màxim a la freqüència de les oscil·lacions de relaxació ω_0. Per a valors grans d'amplitud, apareixen efectes no lineals importants. El màxim de I_{max} ja es no troba a ω_0 sinó que desplaçat cap a una freqüència menor, Fig. 9.1. A més d'aquesta resposta amb la mateixa freqüència de modulació $1T$, també poden aparèixer altres respostes amb altres freqüències. Això dóna lloc a un comportament molt complex amb regions amb multiestabilitat. Les possibles respostes es poden classificar com n/l, on n i l són nombres sensers sense factors comuns, de manera que la resposta té una freqüència $l\,\omega_m/n$. Les respostes $n/1$ també s'anomenen nT atès que el període del senyal resultant és n vegades el període del senyal de modulació. L'existència d'aquestes respostes es veu a la Fig. 9.1, on s'ha dibuixat I_{max} de les respostes estables en funció de ω_m. Anant augmentant el valor de J_m, es veu com van apareixen les distintes respostes nT. A la figura 9.2 apareixen les evolucions temporals per a distints valors de ω_m per a les respostes $1T$ i $2T$. A més d'aquesta estructura bàsica, cadascuna de les respostes poden, així mateix sofrir bifurcacions de període doble, Fig. 9.1 (d), i en qualque cas

donar lloc a comportament caòtic. Cada resposta n/l té un màxim, en ω_m, per a un valor fixat de J_m: aquest màxim és la *resonància* n/l. En aquest treball ens centram en les resonàncies nT, que s'anomenen *resonàncies principals* o resonàncies primeres sella–node ja que coincideixen amb les bifurcacions sella–node on l'òrbita estable esdevé inestable (Fig. 9.1). Les corbes al pla $(\omega_m/\omega_0, J_m)$ que uneixen els punts de les resonàncies nT s'anomenen corbes "esquelet" per a la resonància nT. L'objectiu d'aquest treball és obtenir les corbes esquelet per a les resonàncies nT, Fig. 9.3. Aquesta descripció és d'interès per a treballs experimentals perquè permet determinar la freqüència en la qual es té una resposta màxima per a una amplitud d'injecció fixada. Els resultats obtinguts han ajustat amb els resultats indicats en treballs experimentals [Liu and Ngai, 1993]. El terme de saturació de guany no canvia el comportament dinàmic ni la localització de les corbes esquelet de manera qualitativa, Fig. 9.4. Per a un valor fixat de ω_m, cal un valor més gran de J_m per obtenir la resposta òptima, compatible amb què aquest terme augmenta la dissipació. El terme d'emissió espontània canvia dràsticament el comportament de la dinàmica del sistema per a valors de ω_m petits, Figs. 9.5 i 9.6. Aquest efecte pot ser causa d'un fons de fotons que evita que la intensitat del camp elèctric disminueixi per davall d'un cert valor, donant lloc a una resposta independent de la freqüència.

Els resultats obtinguts numèricament es poden explicar mitjançant la teoria quasi–conservativa. Aquesta teoria, que utilitza la forma potencial per al sistema obtinguda en el capítol 7, assumeix que les òrbites periòdiques es poden aproximar, a prop de la resonància, per òrbites conservatives amb un valor del potencial. Els resultats de la figura 9.7 indiquen que la teoria reprodueix els resultats numèrics en el cas de tenir un terme d'emissió espontània nul. En presència de termes d'emissió espontània, la predicció teòrica reprodueix qualitativament els resultats numèrics, Figs. 9.8 i 9.9. No obstant, la teoria prediu un augment molt més acusat per a l'amplitud òptima de modulació que l'obtinguda numèricament, a causa de la forma del període de les solucions conservatives en funció de l'energia per a valors grans de l'energia.

El cas de modulació al terme de pèrdues també s'estudia. Els resultats de la teoria quasi–conservativa ajusten bastant bé amb els resultats numèrics, Figs. 9.10, 9.11 i 9.12.

Finalment, s'obté en una relació entre l'efecte produït per la modulació al bombeig i la modulació al terme de pèrdues, (9.29). La validesa d'aquesta equivalència apareix en les figures 9.13 i 9.14. Aquesta relació indica que la modulació al terme de pèrdues és més eficient a l'hora de tenir bifurcacions i comportament caòtic que la modulació al bombeig (cal un valor de l'amplitud de modulació, en el cas de les pèrdues, molt menor que en el cas de la modulació al bombeig, per obtenir els mateixos efectes).

Chapter 9

Main resonances in directly modulated semiconductor lasers

In this chapter, we undertake numerical and analytical calculations in the framework of the single mode rate equation model (chapter 4) including a modulation term for the injection current with the aim of determining the parameter domains of the basic instabilities involved. The work presented in this chapter completes the above series of studies of directly modulated semiconductor lasers, as it was reviewed in section 1.3.

Domains of existence of the main resonances in directly modulated semiconductor lasers are obtained by application of the quasi–conservative theory. The predictions are compared with numerical results coming from a direct integration of the model equations and with experimental observations reported by other groups. In both cases we find a good qualitative agreement. We consider a model that contains explicitly the gain saturation and spontaneous emission terms and we focus mainly on the effect that these terms have in the regime of large amplitude of modulation.

The chapter is organized as follows. In section 9.1, we describe qualitatively the response obtained for a diode laser, as described by a single–mode rate equation model, in the presence of pump modulation. In Sec. 9.2, the quasi–conservative theory is used to obtain relations that allow the calculation of the primary saddle–node bifurcations, both for the case of modulation in the pump or in the losses. In Sec. 9.3, the theoretical estimations are compared with numerical results coming from a direct integration of the model equations. The effects of gain saturation and spontaneous emission terms in these bifurcations are explored in detail. In Sec. 9.4, we compare our results to previous experimental works reported by other groups. Finally, in Sec. 9.5, we discuss the main obtained results.

9.1 Dynamical behaviour

The dynamics of a single mode semiconductor laser was discussed in detail in chapter 7. As the evolution equations for I and N do not depend on the phase ϕ, we can concentrate only in the evolution of the former variables. The equations that

give the corresponding dynamics are equations (7.1) and (7.3):

$$\frac{dI}{dt} = \left[g_N \frac{(N - N_o)}{1 + s\,I} - \gamma \right] I + 4\,\varepsilon\,N, \tag{9.1}$$

$$\frac{dN}{dt} = \frac{J}{e} - \gamma_N\,N - g_N \frac{(N - N_o)}{1 + s\,I}\,I. \tag{9.2}$$

Typical values of the parameters involved in the equations were presented in Table 7.1. The dynamics of the equations for constant $J > J_{th}$ is such that both I and N relax to their steady states by performing damped oscillations. The frequency ω_0 of these oscillations close to the steady state can be calculated linearizing the equations of motion (7.35), for the simplest case $s = \varepsilon = 0$, $\omega_0 \approx \sqrt{g_N(J - J_{th})/e} = 25\text{ns}^{-1}$ for parameter values of Table 7.1 and $J = 1.23 J_{th}$.

The purpose of this work is to study the dynamics of Eqs. (9.1) and (9.2) under modulation. In particular, we will consider modulations mainly in the pump current J and also in the losses γ, which would be an option in distributed Bragg reflection or multisection lasers. In order to be more specific, we describe now the qualitative features of the behaviour when the pump is modulated at a given frequency ω_m. More explicitly, we consider

$$J(t) = J_b[1 + J_m \cos(\omega_m t)], \tag{9.3}$$

where J_b is a fixed value of the current (bias current), such that $J_b > J_{th}$. In our simulations we choose $J_b = 1.23 J_{th}$ and values for the relative amplitude of the modulation $J_m < 1$ (to satisfy the physical constraint that the total current has to be positive). When J becomes time dependent, the dynamics are more complex than in the case of constant J, and a very rich dynamical structure can appear depending on the values of J_m and ω_m.

For small values of J_m and for ω_m smaller than $-3dB$ modulation bandwidth frequency, the system behaves almost as a forced linear oscillator with damping terms; the optical intensity I oscillates periodically with the same frequency ω_m of the input current. To characterize the response of the system we look at the maximum value of I (I_{max}) when we modulate the laser. It is well known that, under small signal modulation, the optical response I_{max} has a maximum at the relaxation oscillation frequency ω_0 [dotted line of Fig. 9.1 (a)]. This is an example of the well known phenomenon of linear resonance [Agrawal and Dutta, 1986; Jackson, 1989].

In contrast to the small signal response just described, large amplitude modulation, i.e. large values of J_m, give rise to strong nonlinear behaviours, since the nonlinear terms become relevant in the dynamics of the system. The maximum response (maximum value of I_{max}) is not located anymore at the relaxation oscillation frequency ω_0 but it is shifted to a smaller frequency (*soft* spring oscillator)[1]. This fact can be seen in Fig. 9.1 where the response of the system, for different values of J_m, is shown. In this case we have taken $s = 0$ and $\varepsilon = 0$ in Eqs. (9.1) and (9.2). In

[1]The nonlinear terms of *hard* spring oscillators make the maximum response to be shifted to a bigger frequency than ω_0.

this nonlinear regime, in addition to a response at the same frequency of modulation ω_m, other frequencies can be excited for sufficiently high modulation amplitudes J_m. This fact gives rise to a more complex diagram for the response of the system, leading even to the phenomenon of multistability (several stable responses for the same value of the input parameters). The different possible responses of the system can be classified as n/l where n and l are integer numbers with no common factors, such that the response frequency is $l\omega_m/n$ [Jackson, 1989].

In this work, we will be mainly interested in primary resonances of the type $n/1$. Our interest in these responses is based on the fact that they usually yield the maximum output power. These $n/1$ resonances are also called nT–periodic responses because the period of the resulting signal is n times larger that T_m, where $T_m = 2\pi/\omega_m$ is the period of the external modulation. Different types of stable n/l responses (amplitude I_{max} versus the modulation frequency ω_m) are shown in Fig. 9.1 for different values of the modulation amplitude J_m; while in Fig. 9.2, the time evolution for the intensity is plotted for different values of the frequency ω_m and the common value $J_m = 0.2$. The qualitative picture described is now detailed:

- For small modulation amplitude, see Fig. 9.1 (a) ($J_m = 0.01$, dotted line), the linear approximation applies and there are only single main resonances whose maximum lies approximately at the relaxation frequency.

- For larger modulation amplitudes, Fig. 9.1 (b), the stable $1T$ resonances destabilize themselves via a saddle–node type instability. This allows a hysteresis cycle with discontinuous transitions between the different $1T$ responses. This saddle–node instability is interesting since we have observed that the maximum response appears just before the solution becomes unstable. (We will come back to this point later). When multistability is possible, and for those moderate levels of the amplitude of the modulation, the larger output intensity I_{max} always corresponds to the $1T$ response. Other n/l responses, with $l \neq 1$ can be generated for small frequencies but they have a much smaller output power and they will not be considered in this work.

- After a further increase of J_m (Fig. 9.1 (c), corresponding to $J_m = 0.2$) the $2T$ response appears continuously, when decreasing ω_m (starting, in our example, from $\omega_m/\omega_0 = 3.0$), as a period doubling bifurcation of the $1T$ response (see Fig. 9.2 for temporal trajectories). When ω_m is decreased even further, there appears a range of values of ω_m for which the $1T$ and $2T$ responses are both stable, hence allowing a hysteresis cycle in this bistable region as well as a discontinuous transition between the $1T$ and the $2T$ responses. The $1T$ response, solid line, gives a smaller output that the $2T$ response for the whole frequency range of existence of the $2T$ response, namely for $\omega_m/\omega_0 \in [0.968, 2.118]$. The $1T$ response does not exist (is unstable) in the frequency interval $[1.761, 2.118]$. For even smaller ω_m the $2T$ response finally disappears through a saddle–node instability. The $2T$ response around $\omega_m/\omega_0 \approx 2.0$ is the first subharmonic resonance (parametric resonance [Jackson, 1989]).

- For larger values of J_m [Fig. 9.1(d)] other nT responses with $n > 2$ appear. Each of these nT responses exist for a given range of values of ω_m and are unconnected to the previous $1T$ and $2T$ responses. At both ends of its frequency range, they disappear through saddle–node bifurcations.

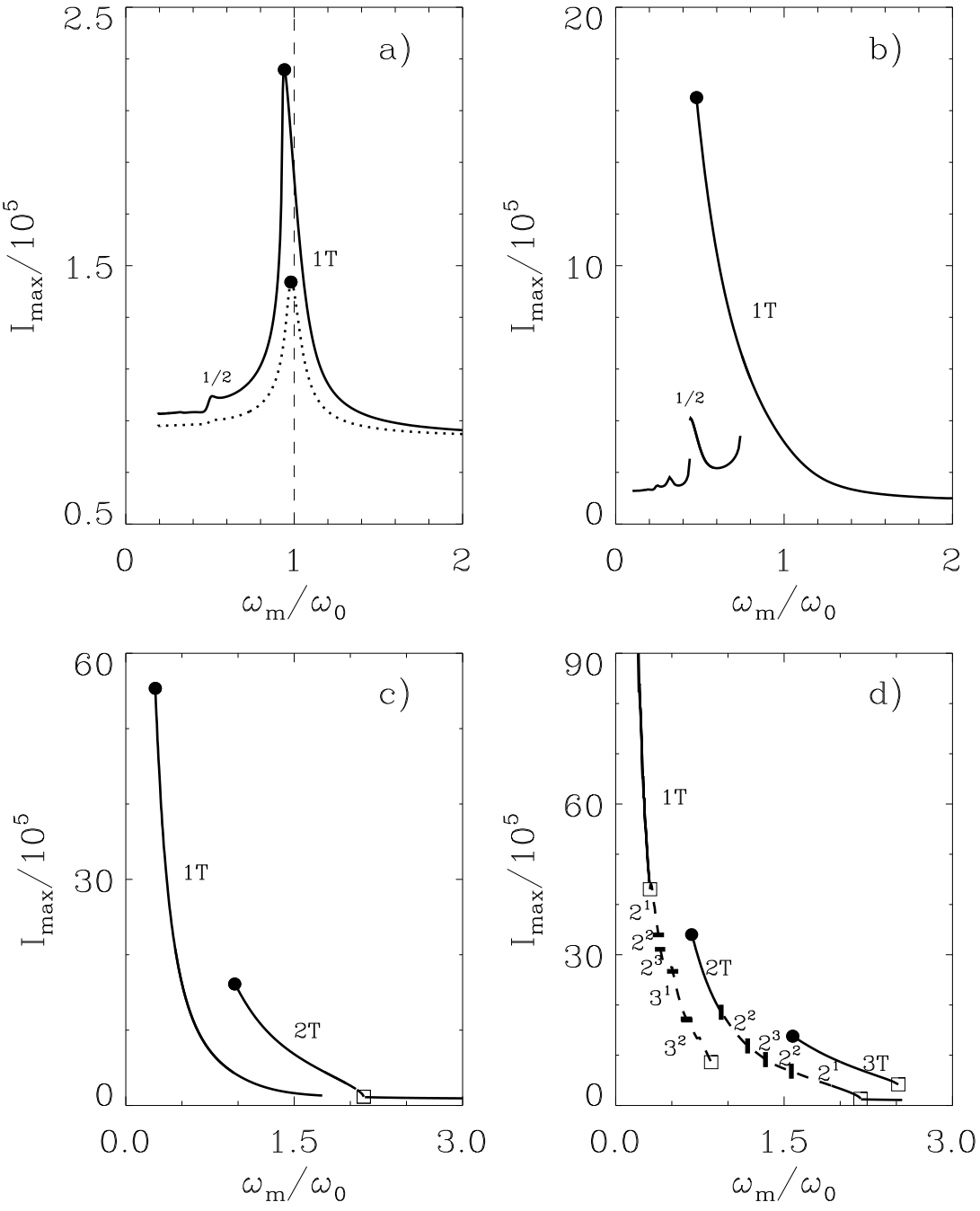

Figure 9.1: Responses, I_{max}, versus the normalized external frequency ω_m/ω_0 for different values of the modulation pump amplitude in the case $J_b = 1.23J_{th}$, $s = 0$, $\varepsilon = 0$. Other parameters as indicated in the text. (a) dotted line: $J_m = 0.01$, solid line: $J_m = 0.02$, (b) $J_m = 0.1$, (c) $J_m = 0.2$ and d) $J_m = 0.3$. The 2^k and 3^k responses correspond to further period doubling bifurcations.

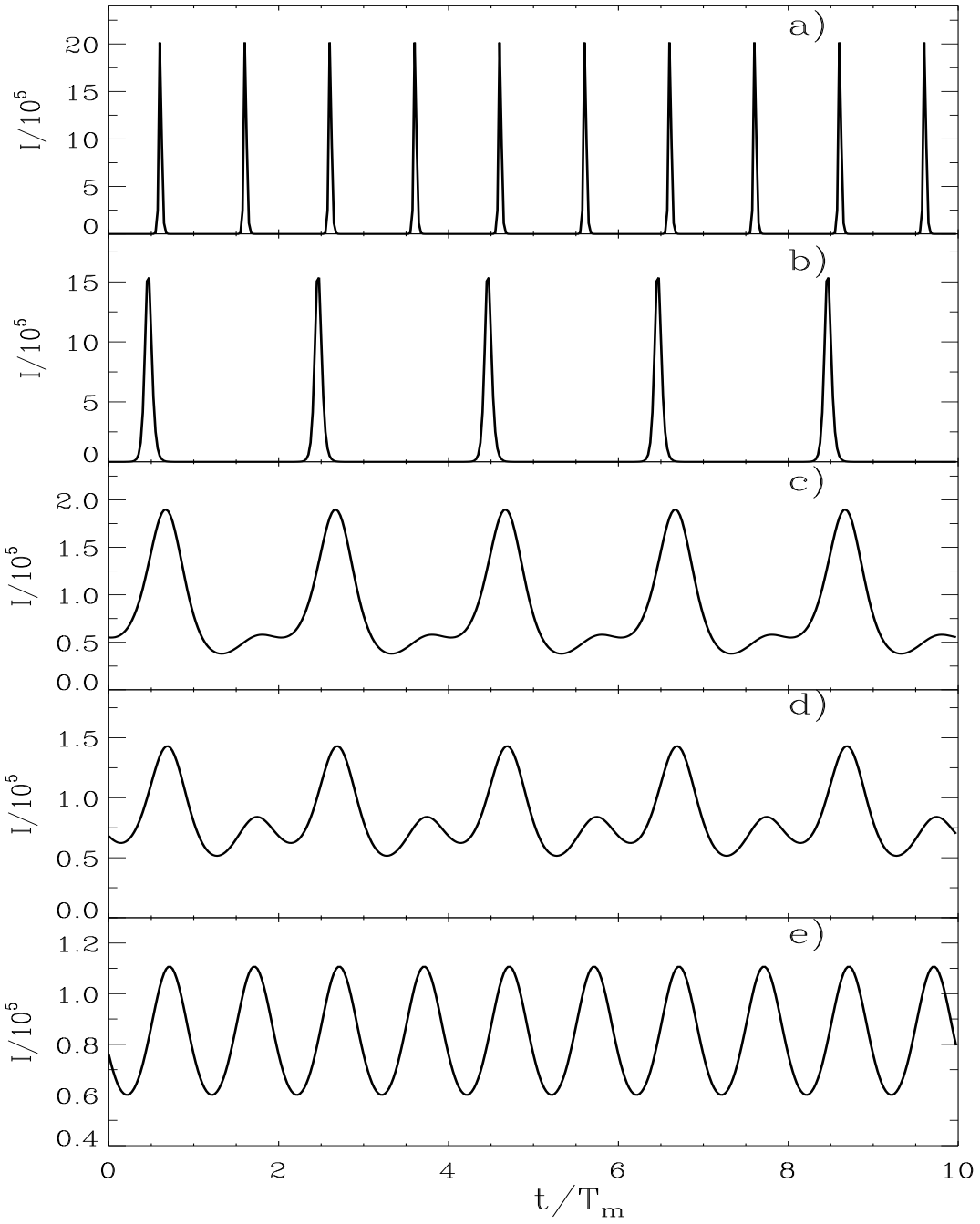

Figure 9.2: Intensity versus time for different values of ω_m/ω_0 for $J_m = 0.2$ corresponding to some points of the curve of Fig. 9.1 (c). (a) $\omega_m/\omega_0 = 0.43$, (b) $\omega_m/\omega_0 = 0.97$, (c) $\omega_m/\omega_0 = 2.08$, (d) $\omega_m/\omega_0 = 2.11$, (e) $\omega_m/\omega_0 = 2.12$. Same parameters as in Fig. 9.1. $T_m = 2\pi/\omega_m$.

Besides this general framework, all the existing nT responses can, at a given value of the modulation amplitude, suffer different types of period doubling bifurcation, period four, etc, or even chaos, following the Feigenbaum route to chaos [Jackson, 1989] or the route period doubling followed by period four, eight, period tripling, etc., as in references [Lamela *et al.*, 1998b; Lamela *et al.*, 1998a]. These are indicated with dashed lines in the corresponding diagram [Fig. 9.1 (d)] and are denoted as 2^k responses, being k an indication of the number of period doubling bifurcation that the orbit has suffered. The same meaning applies for the 3^k responses.

In Fig. 9.2 we plot, for a fixed value of the modulation amplitude [$J_m = 0.2$, corresponding to the diagram in Fig. 9.1 (c)], time evolutions for the intensity $I(t)$ for several values of the frequency ω_m/ω_0. Case (a) corresponds to $\omega_m/\omega_0 = 0.43$ where, according to Fig. 9.1 (c), the $1T$ type solution with maximum intensity appears. Case (b) corresponds to a frequency $\omega_m/\omega_0 = 0.97$ where the $2T$ solution begins to exist. We note that at this frequency, the $2T$ signal has a maximum spectral component in the first harmonic, allowing for a clean time trace of the optical intensity, with no additional peaks, as shown in Fig. 9.2 (b). As the frequency increases, Figs. 9.2 (c) and 9.2 (d), the $2T$ response deteriorates in the sense that the maximum intensity decreases and extra peaks develop in the time series. Finally, for $\omega_m/\omega_0 = 2.12$ the $1T$ response is recovered. However, and in accordance with Fig. 9.1 (c), the maximum intensity is now much smaller that the one of the optimal $1T$ response shown in Fig. 9.2 (a).

For fixed modulation amplitude J_m, each n/l response has its maximum at a given value of the modulation frequency. This maximum is called the n/l resonance. In this work, we are mainly interested in the $n/1$ resonances (or nT resonances) because they usually yield the maximum output power. In the literature, they are also known as *main resonances*. These resonances are indicated by solid dot symbols in Fig. 9.1. The curves in the $(\omega_m/\omega_0, J_m)$ plane joining the points at which nT resonances occur are called the *skeleton* curves for the nT resonances. Our main effort will be directed to finding the skeleton lines for each main resonance of the nT type. This description can be of interest to the experimentalists since it allows determination of the resonance frequency at which the maximum response is obtained for a given external amplitude of the injection current.

With this aim in mind, we have performed intensive numerical simulations to obtain the maximum responses of the system for different J_m and ω_m/ω_0. In principle, for a given J_m, one should find the value of ω_m/ω_0 that maximizes the response at each nT resonance. However, this is a very lengthy procedure that can be avoided by finding, instead, the value of ω_m/ω_0 where a saddle–node bifurcation is born, since, as we have already said, we have observed that the maximum response appears just before the solution becomes unstable. Due to this fact the main resonances are also called *primary saddle–node resonances*. This allows us to identify the position of the maximum response in the $(\omega_m/\omega_0, J_m)$ plane with the position of the bifurcation. The procedure of finding such bifurcation is easier to implement using nonlinear dynamical tools than to perform whole simulations of the rate equations [Doedel *et al.*, 1997].

In Fig. 9.3 the primary saddle–node bifurcation are shown (thick solid lines) in the case $s = 0$ and $\varepsilon = 0$ for the $1T$, $2T$ and $3T$ resonances. We show in some cases that the location of the saddle–node bifurcation coincides, with great accuracy, with that of the maximum I_{max}. The latter have been obtained by numerical simulations of the laser equations and are indicated by symbols in the figure. Notice, however, that the line of the saddle–node bifurcation do not reach the linear limit $\omega_m/\omega_0 = 1$ corresponding to very low amplitude of the modulation, because for small values of modulation amplitude there is no saddle–node bifurcation. We also plot in the same figure some additional lines that correspond to domains of existence of the above mentioned nT resonances. Within these domains, besides the "pure" nT solutions, there exist a rich variety of bifurcated solutions (period doubling, period 4, and so on, indicating the route to chaos described previously). The $1T$ solution only exists below the thin solid line of Fig. 9.3. The $2T$ solution is limited to the region below the thick solid line of $2T$ and the dashed line and it only exists within this limit. Finally, the $3T$ solution is limited to the region below the thick solid line of $3T$ and the dot–dashed line of the figure. In what follows, we will restrict ourselves to the thick lines denoting the maximum of each resonance.

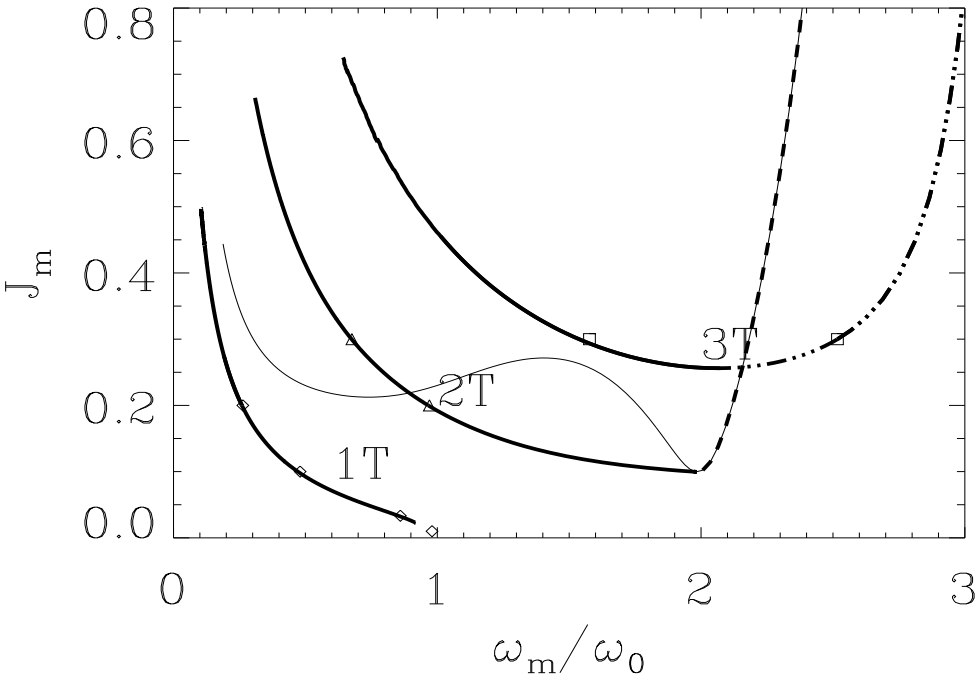

Figure 9.3: Maxima of main resonances in the plane $(\omega_m/\omega_0, J_m)$, solid thick lines. Thin solid line: Period doubling bifurcation of the $1T$ resonance to 2^1 (coincides with the limit of existence of resonance $1T$), dashed line: lowest limit for the existence of the $2T$ resonance, dot–dashed line: lowest limit for the existence of the $3T$ resonance.

We now describe the effect of the gain saturation term. We plot in Fig. 9.4, the changes on the line of main resonances (given in Fig. 9.3 for $s = \varepsilon = 0$) in the case $s \neq 0$ (but still $\varepsilon = 0$). It can be seen clearly that the saturation term does not change qualitatively, neither the location of the lines nor the overall dynamical behaviour of the system. The only difference is that, for a fixed frequency, a larger value of J_m is needed to obtain the optimal periodic response. This is clearly compatible with the fact that the main effect of the saturation term is to increase the dissipation.

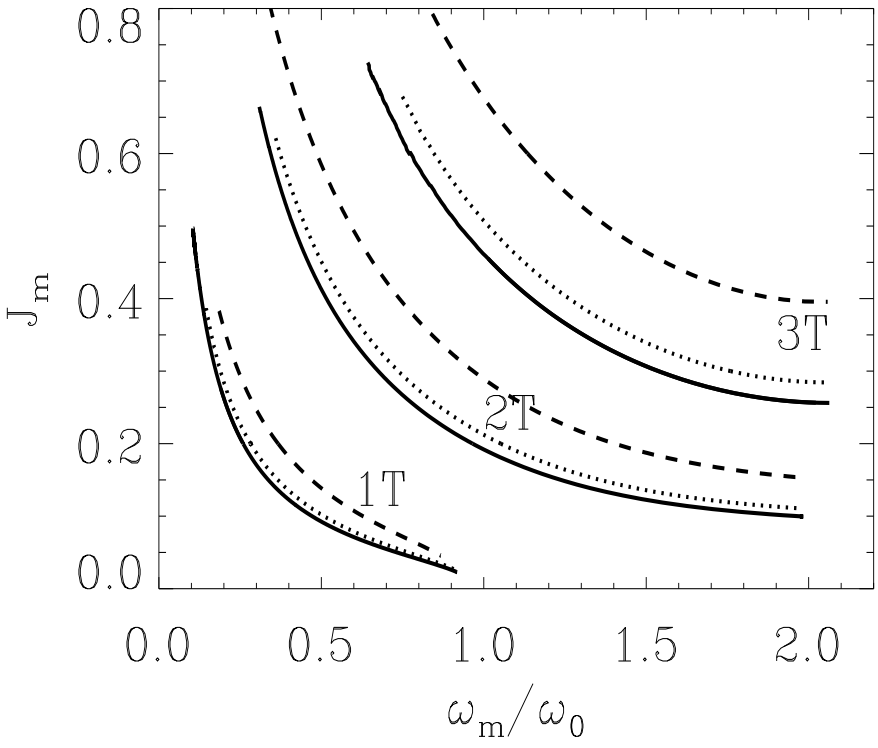

Figure 9.4: Maxima of main resonances in the plane $(\omega_m/\omega_0, J_m)$. Solid line: $s = 0$, dotted line: $s = 6 \times 10^{-9}$, dashed line: $s = 3 \times 10^{-8}$. $\varepsilon = 0$. Other parameters as in Fig. 9.1.

On the contrary, the effect of the spontaneous emission term strongly changes the response of the system. In Fig. 9.5, the lines of I_{max} in the $(\omega_m/\omega_0, J_m)$ plane are shown for the case $\varepsilon \neq 0$ and $s = 0$. One can observe the dramatic change in the behaviour of the response of the system for small frequencies with respect to that observed for $\varepsilon = 0$ (solid line). When increasing the modulation amplitude we find a steep response that indicates that the frequency ω_m for the optimal response I_{max} is less sensitive to the amplitude of the external modulation, J_m. We speculate that this effect might be due to that for $\varepsilon \neq 0$ there is a background of photons preventing the intensity decreasing below a certain value, so yielding a frequency–independent response. For the case $s \neq 0$ and $\varepsilon \neq 0$ we observe combined the same qualitative results as those shown in Fig. 9.4 and Fig. 9.5. It is important to point out that values of s and ε different from zero yield chaos suppression, a fact that has been already pointed out both numerically and experimentally [Tang and Wang, 1987]. Naively, one could expect that the gain saturation parameter plays a more important part in the dynamics. However, we observe that in some situations the main resonances can be affected more strongly by the spontaneous emission factor than by the gain saturation factor.

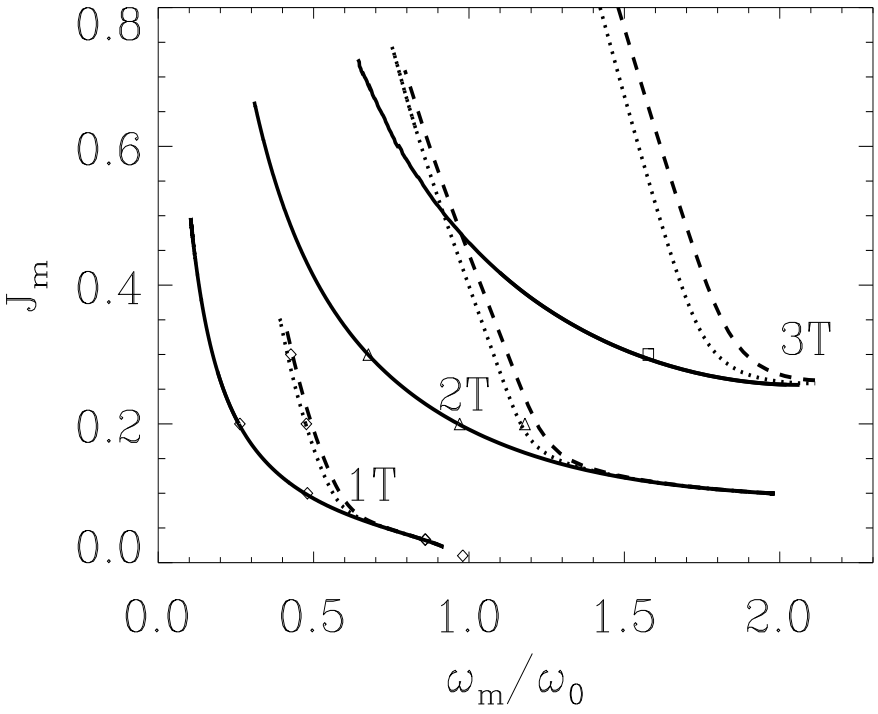

Figure 9.5: Maxima of main resonances in the plane $(\omega_m/\omega_0, J_m)$. Solid line: $\varepsilon = 0$, dotted line: $\varepsilon = 6.2 \times 10^{-11} ps^{-1}$, $\varepsilon = 2.3 \times 10^{-10} ps^{-1}$.

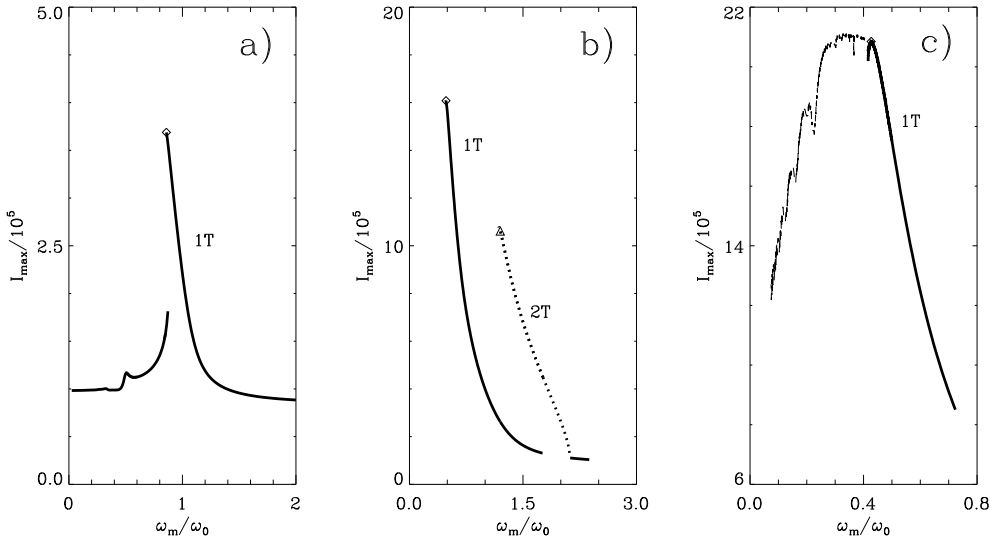

Figure 9.6: Responses, I_{max}, versus the normalized external frequency ω_m/ω_0 for different values of the modulation amplitude. $J_b = 1.23 J_{th}$. $s = 0$, $\varepsilon = 6.2 \times 10^{-11} ps^{-1}$. Other parameters as indicated in the text. (a) $J_m = 0.033$, (b) $J_m = 0.2$ and (c) $J_m = 0.3$.

In the absence of spontaneous emission, $\varepsilon = 0$, the tendency to decrease the main resonance frequency with increasing amplitude of modulation can be explained using a Toda–like potential function (7.14). Physically, it means that a maximum number of photons in the cavity is available for modulation and this number is not limited from below. However, in the presence of spontaneous emission terms, this is not true anymore and the Toda potential as a function of the intensity changes, becoming more symmetric and steeper for very low intensities. A spontaneous emission background is created and during the modulation period the number of photons can not be smaller than this value and, consequently, the response is maintained basically unchanged at any smaller frequency. As soon as the intensity of the laser reaches this background level, the dynamics changes and at low frequencies a non–resonant regime of gain switching (with no dependence on frequency in some modulation frequency interval observed) dominates. In Fig. 9.6, we plot the maxima intensity responses I_{max} against frequency ω_m for different values of J_m, in the case $\varepsilon \neq 0$. Compared with Fig. 9.1, we notice that at small modulation amplitude [$J_m = 0.033$, Fig. 9.6 (a)] the response for small value of ω_m does not change qualitatively and very little quantitative with respect to that of Fig. 9.1 (a). However, for large values of J_m, the effect of ε becomes more evident. At $J_m = 0.2$ [Fig. 9.6 (b)] the

maximum response for the resonance $1T$ is now at a larger frequency than in Fig. 9.1 (c) and, moreover, the corresponding value of I_{max} is much smaller. Increasing J_m even further [$J_m = 0.3$ in Fig. 9.6 (c)], we find that the maximum response for the resonance $1T$ (thick line) is much smaller than in the case of Fig. 9.1 (d), and corresponds to a much larger frequency. It has to be mentioned that in this case, the value of ω_m/ω_0 that maximizes the $1T$ response presents larger differences with the location of the saddle–node than in previous cases [Notice the difference between the maximum and the end of the solid line in Fig. 9.6 (c)]. In Fig. 9.6 (c) we also plot other responses for smallest values of ω_m. These responses, while having a larger output than the $1T$ responses, can either have a period larger than $1T$ or, while still being $1T$, have extra peaks in the time series. They include responses of period $1T$, $2T$, ..., being an example of the structure also reported in [Tang and Wang, 1986]. We also point out that there exists an almost flat response for some range of values of ω_m/ω_0.

9.2 Quasi–conservative theory

Equations (7.1, 7.3) [or equivalently Eqs. (9.1, 9.2)] were reduced to a set of dimensionless equations in chapter 7. These evolution equations can be cast in the form of a *potential* function (7.14) with the relating matrix D (7.17) to the equations of motion (2.26). The decrease of the Lyapunov potential is due to the function $D_{22}(y,z)$ (7.19) appearing in the evolution equation. Therefore, in the dynamical equations we can identify the conservative terms (those proportional to D_{12}) and the dissipative terms (those proportional to D_{22}). If the dissipative terms were not present, i.e. if $D_{22} = 0$, the potential would take a constant value $E = V(y,z)$ and we would have a conservative system with periodic orbits. The frequency $\omega = 2\pi/T$ (T is the corresponding period) of such an orbit of the conservative system is a function of the potential, i.e. $\omega = \omega(E)$, that can be obtained, using standard methods of Mechanics (7.26). Notice that the periodic orbits, that we write as $[y_0(\tau - \tau_0, E), z_0(\tau - \tau_0, E)]$, depend on an initial time τ_0 and on the value of the Lyapunov potential E.

9.2.1 Pump Modulation

We now include the modulation terms. We first consider the case of modulation in the pump as given in (9.3). In terms of the rescaled variables, y and z [related to the initial variables by (7.5)], the equations become

$$\frac{dy}{d\tau} = D_{12}\frac{\partial V}{\partial z}, \tag{9.4}$$

$$\frac{dz}{d\tau} = -D_{12}\frac{\partial V}{\partial y} - D_{22}\frac{\partial V}{\partial z} + A_m \cos(\bar{\omega}_m \tau), \tag{9.5}$$

with

$$A_m = \frac{2J_b J_m g_N}{e\gamma^2}, \quad \bar{\omega}_m = \frac{2}{\gamma}\omega_m. \tag{9.6}$$

We look for nT responses, i.e. periodic solutions $[y^{(n)}(\tau), z^{(n)}(\tau)]$ of equations (9.4) and (9.5) with a frequency $\omega_n = \bar{\omega}_m/n$, or, equivalently, with a period $T_n = n\bar{T}_m = n2\pi/\bar{\omega}_m$. In this case, the potential function $V(y,z)$ is no longer a constant of motion. However, for a periodic orbit, it is still true that the integral of

$$dV = \left[\frac{\partial V}{\partial y}\dot{y} + \frac{\partial V}{\partial z}\dot{z}\right] d\tau \tag{9.7}$$

over a period is equal to zero. By using this property and after replacing in the previous expression $\dot{y}$ and $\dot{z}$ coming from (9.4, 9.5), we obtain that the periodic solutions must satisfy the condition

$$\begin{aligned} A_m \int_0^{T_n} d\tau\, V_z(y^{(n)}(\tau), z^{(n)}(\tau)) \cos(\bar{\omega}_m \tau) = \\ \int_0^{T_n} d\tau\, D_{22}(y^{(n)}(\tau), z^{(n)}(\tau))[V_z(y^{(n)}(\tau), z^{(n)}(\tau))]^2, \end{aligned} \tag{9.8}$$

where V_z stands for $\partial V/\partial z$. The quasi–conservative theory assumes that the periodic orbits $[y^{(n)}(\tau), z^{(n)}(\tau)]$ can be approximated, near the resonance, by conservative orbits $[y_0(\tau - \tau_0, E_n),\, z_0(\tau - \tau_0, E_n)]$, corresponding to the value of the potential E_n that yields the desired frequency, $\omega_n = \omega(E_n)$. Substitution of this ansatz in the above equation leads to

$$\begin{aligned} A_m \int_0^{T_n} d\tau\, V_z(y_0(\tau, E_n), z_0(\tau, E_n)) \cos(\bar{\omega}_m(\tau + \tau_0)) = \\ \int_0^{T_n} d\tau\, D_{22}(y_0(\tau, E_n), z_0(\tau, E_n))[V_z(y_0(\tau, E_n), z_0(\tau, E_n))]^2. \end{aligned} \tag{9.9}$$

By defining R_n, S_n, θ_n by

$$\begin{aligned} R_n &= \int_0^{T_n} d\tau\, D_{22}(y_0(\tau, E_n), z_0(\tau, E_n))\, [V_z(y_0(\tau, E_n), z_0(\tau, E_n))]^2\,, \\ S_n \sin(\theta_n) &= \int_0^{T_n} d\tau\, V_z(y_0(\tau, E_n), z_0(\tau, E_n)) \sin(\bar{\omega}_m \tau), \\ S_n \cos(\theta_n) &= \int_0^{T_n} d\tau\, V_z(y_0(\tau, E_n), z_0(\tau, E_n)) \cos(\bar{\omega}_m \tau), \end{aligned} \tag{9.10}$$

we arrive at

$$A_m \cos(\bar{\omega}_m \tau_0 + \theta_n) = \frac{R_n}{S_n}. \tag{9.11}$$

According to this equation, for given A_m and $\bar{\omega}_m$ there exist at most $2n$ different orbits of period $n\bar{T}_m$. They correspond to the functions $[y_0(\tau - \tau_0, E_n),\, z_0(\tau - \tau_0, E_n)]$ for the $2n$ values of $\tau_0 = (\alpha_n + k\pi)/\bar{\omega}_m$, $k = 0, \ldots, 2n-1$ and $\alpha_n = \arccos(R_n/(S_n A_m)) - \theta_n$. It turns out that n of these solutions are unstable, while the remaining stable ones correspond in fact to trivial translations by a time amount $\bar{T}_m$ of the same basic solution (pulse position multistability [Gallagher *et al.*, 1985; Chizhevsky and Turovets, 1993]). Therefore, for a given value of A_m and $\bar{\omega}_m$ there is just one corresponding stable orbit of the conservative system.

Alternatively, we can look at the previous equation as a condition for the own existence of periodic orbits. For given modulation frequency $\bar{\omega}_m$ there will exist periodic orbits of period $n\bar{T}_m$ if the amplitude of the modulation verifies $A_m \geq R_n/S_n$. Since resonances almost coincide in this case with the limit of existence of periodic orbits (see Fig. 9.1 and the discussion of the previous section), this criterion implies that the skeleton curves for the nT resonance are

$$A_m = \frac{R_n}{S_n}. \tag{9.12}$$

In practice, it is difficult to find solutions of the conservative motion $[y_0(\tau, E), z_0(\tau, E)]$ analytically and one performs a numerical integration of the conservative system (putting by hand $D_{22} = 0$) in order to find the quantities R_n, S_n. However, in the simple case of $s = 0$ and $\varepsilon = 0$, Eq. (9.9) can be simplified by replacing $V_z = \dot{y}_0/(2y_0)$ with help of (9.4) and (7.21), yielding

$$A_m \int_0^{T_n} d\tau \dot{x}_0(\tau, E_n) \cos(\bar{\omega}_m(\tau + \tau_0)) = \int_0^{T_n} d\tau \left[b + y_{st} \exp(x_0(\tau, E_n))\right] \frac{\dot{x}_0(\tau, E_n)^2}{2}, \tag{9.13}$$

where $x_0 \equiv \ln(y_0/y_{st})$, $y_{st} = a - b$ is the steady state value of y in the absence of modulation, and x_0 is a periodic function of frequency w_n, that can be written as a Fourier series in the form

$$x_0(\tau, E_n) = \frac{Q_0}{2} + \sum_{k=1}^{\infty} Q_k \cos[k w_n(\tau + \mu_k)]. \tag{9.14}$$

Using this expression, and after a simple algebra, the integrals of (9.13) can be performed, giving rise to

$$A_m \sin[n\omega_n(\mu_n - \tau_0)] = \frac{a}{2}\omega_n \frac{\sum_{k=1}^{\infty} Q_k^2 k^2}{nQ_n}. \tag{9.15}$$

As discussed earlier, the nT resonances are obtained for $\sin[n\omega_n(\mu_n - \tau_0)] = 1$, i.e.

$$A_m = \frac{a}{2}\omega_n \frac{\sum_{k=1}^{\infty} Q_k^2 k^2}{nQ_n}. \tag{9.16}$$

This expression has the advantage that the contribution of each coefficient in the Fourier series of x_0 appears explicitly. In particular, it shows that the nT resonance may be excited by a finite amplitude of the external modulation only if the $n - th$ harmonic of the conservative solution is different from zero. Therefore, this effect can be considered as harmonic locking of the fundamental relaxation oscillation by an external modulation.

In the case $s \neq 0$ and $\varepsilon \neq 0$ it is also possible to use a series expansion for the variable x_0. However, the resulting expression is so complicated, in the sense that in the denominator different coefficients of the Fourier expansion contribute, that we find simpler instead to use (9.12) to obtain the theoretical skeleton curve.

9.2.2 Loss modulation

Let us turn now to loss modulation. We consider Eqs. (9.1) and (9.2) with a fixed value of the current J but modulated loss term

$$\gamma \to \gamma\,[1 + \gamma_m \cos(w_m t)]. \tag{9.17}$$

The reduced equations for y and z can be written as

$$\begin{aligned} \frac{dy}{d\tau} &= D_{12}\frac{\partial V}{\partial z} - 2y\gamma_m \cos(\bar{\omega}_m \tau), \\ \frac{dz}{d\tau} &= -D_{12}\frac{\partial V}{\partial y} - D_{22}\frac{\partial V}{\partial z}. \end{aligned} \tag{9.18}$$

It is straightforward now to extend the quasi–conservative theory to this case. Proceeding as in the case of pump modulation we arrive at

$$\gamma_m \cos(\bar{\omega}_m t_0 + \theta_n') = \frac{R_n}{S_n'}, \tag{9.19}$$

where (V_y stands for $\partial V/\partial y$), and

$$\begin{aligned} R_n &= \int_0^{T_n} d\tau\, D_{22}(y_0(\tau, E_n), z_0(\tau, E_n))\,[V_z(y_0(\tau, E_n), z_0(\tau, E_n))]^2, \\ S_n' \sin(\theta_n') &= -2\int_0^{T_n} d\tau\, V_y(y_0(\tau, E_n), z_0(\tau, E_n)) \sin(\bar{\omega}_m \tau) y_0(\tau, E_n), \\ S_n' \cos(\theta_n') &= -2\int_0^{T_n} d\tau\, V_y(y_0(\tau, E_n), z_0(\tau, E_n)) \cos(\bar{\omega}_m \tau) y_0(\tau, E_n). \end{aligned} \tag{9.20}$$

The skeleton curves are then given by

$$\gamma_m = \frac{R_n}{S_n'}. \tag{9.21}$$

In the case $s = 0$ and $\varepsilon = 0$, an expression in terms of Fourier series, similar to (9.16) can be derived,

$$\gamma_m = \frac{a}{2}\frac{\sum_{k=1}^{\infty} Q_k^2 k^2}{n^2 Q_n}. \tag{9.22}$$

This expression is equivalent to the one obtained in [Samson and Turovets, 1987] where a laser with periodic modulation of losses, but neglecting the spontaneous emission and gain saturation terms, is studied in detail. Again for s and ε different from zero we need to solve Eq. (9.21) numerically.

9.3 Numerical results

9.3.1 Pump modulation

We compare in figures 9.7 and 9.8 the predictions of the quasi–conservative theory, as given by (9.12) with the numerical simulations of Sec. 9.1. In order to perform this comparison, the skeleton curves have been plotted in terms of the original variables J_m and ω_m by using (7.8) and (9.6). Figure 9.7 gives evidence that the theoretical predictions coincide with the numerical results with a great degree of accuracy in the case $s = 0$ and $\varepsilon = 0$. This figure also shows that a similar agreement between the theory and simulations can be observed for the case of $s \neq 0$ but still $\varepsilon = 0$. In this case, the role of the gain saturation parameter s is such that, for a fixed value of the frequency ω_m, a larger value of modulation amplitude J_m is needed to obtain the optimal periodic response for each main resonance. The effect is quantitatively more important for higher order resonances, $n > 1$.

More dramatic is the effect of the spontaneous emission term ε. In figure 9.8 we can see that very small values of the noise rate ε strongly modify the skeleton curves for modulation frequencies ω_m smaller than a cut–off value ω_c (marked with an arrow in in the figure), whereas they remain basically unchanged for $\omega_m > \omega_c$. For small ω_m the effect of ε is such that much larger values of the modulation amplitude J_m are needed in order to find the optimal response for a given value of ω_m.

The theoretical prediction behaves qualitatively in the same way and predicts correctly the cut–off frequency ω_c. However, it predicts a much sharper increase of the optimal modulation amplitude. This could be explained as follows: while the period of the conservative solutions always increases when the energy increases in the absence of spontaneous emission terms, as it can be seen from Eq. (7.26), the presence of the spontaneous emission noise terms introduces a maximum in the resulting expression of the period as function of the energy. This fact forbids the conservative orbits with a frequency smaller than the cut–off frequency. This means that the conservative orbit we are using can be very different from the orbit followed by the modulated system. For smaller values of ε the boundary approaches to the one for the case $\varepsilon = 0$, as expected. Finally, in Fig. 9.9, the combined effect of s and ε is shown. The same qualitative effect that was already explained also appears for other values of the bias current J_b. For $J_b > 1.23 J_{th}$, the same boundaries appear but for larger values of J_m. This effect was already reported in [Liu and Ngai, 1993] where it is indicated that higher order bifurcations are more likely to occur for smaller dc bias levels than for higher ones.

9.3.2 Loss Modulation

For the case of loss modulation the analytical and numerical results coincide for $s = 0$ and $\varepsilon = 0$, and for the case $s \neq 0$ and $\varepsilon = 0$, analogously to that of the pump modulation case (see Fig. 9.10). However, when the spontaneous emission term is introduced, the boundaries obtained numerically also depart from the analytical predictions, see Figs. 9.11 and 9.12.

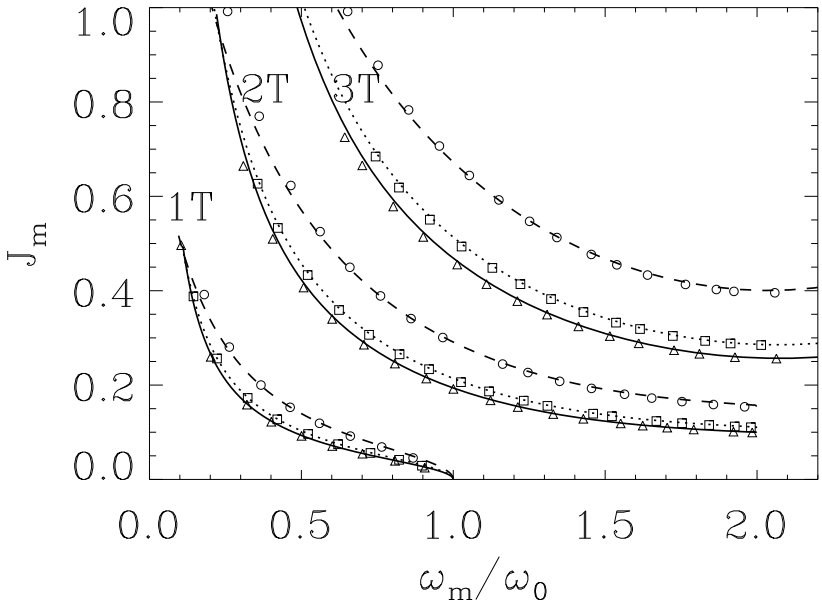

Figure 9.7: Maxima of main resonances in the plane $(\omega_m/\omega_0, J_m)$ for pump modulation. Effect of s. Analytical results (9.12): $s = 0$ (solid line), $s = 6 \times 10^{-9}$ (dotted line), $s = 3 \times 10^{-8}$ (dashed line). Numerical results: $s = 0$ (triangles), $s = 6 \times 10^{-9}$ (squares), $s = 3 \times 10^{-8}$ (circles). $\varepsilon = 0$. Other parameters as in Fig. 9.1.

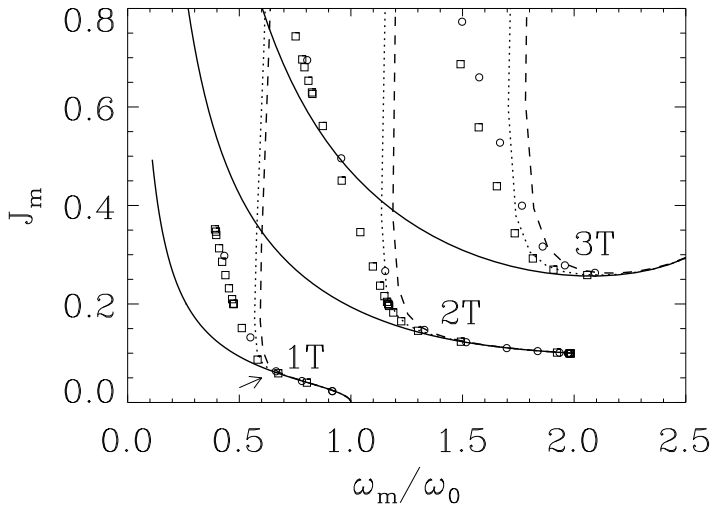

Figure 9.8: Maxima of main resonances in the plane $(\omega_m/\omega_0, J_m)$ for pump modulation. Effect of ε. Analytical results (9.12): $\varepsilon = 0$ (solid line), $\varepsilon = 6.2{\times}10^{-11} ps^{-1}$ (dotted line), $\varepsilon = 2.2{\times}10^{-10} ps^{-1}$ (dashed line). Numerical results: $\varepsilon = 6.2 \times 10^{-11} ps^{-1}$ (squares), $\varepsilon = 2.2 \times 10^{-10} ps^{-1}$ (circles). $s = 0$. Other parameters as in Fig. 9.1. Marked with an arrow the cut-off value ω_c.

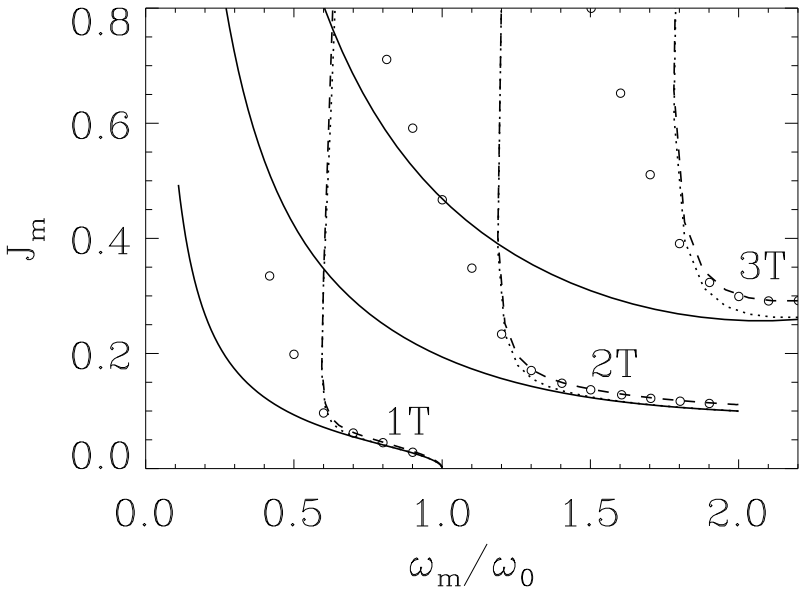

Figure 9.9: Maxima of main resonances in the plane $(\omega_m/\omega_0, J_m)$ for pump modulation. Combined effect of ε and s. Analytical results (9.12): $\varepsilon = 0$, $s = 0$ (solid line), $\varepsilon = 6.2 \times 10^{-11} ps^{-1}$, $s = 0$ (dotted line), $\varepsilon = 6.2 \times 10^{-11} ps^{-1}$, $s = 6 \times 10^{-9}$ (dashed line). Numerical results: $\varepsilon = 6.2 \times 10^{-11} ps^{-1}$, $s = 6 \times 10^{-9}$ (circles). Other parameters as in Fig. 9.1.

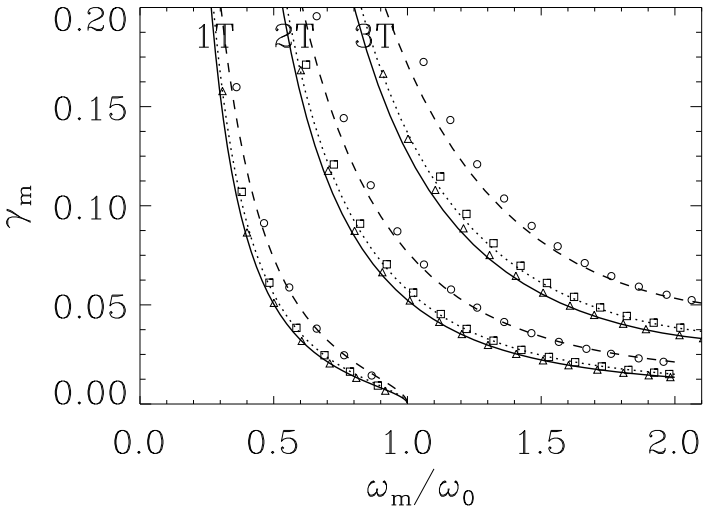

Figure 9.10: Maxima of main resonances in the plane $(\omega_m/\omega_0, J_m)$ for loss modulation. Effect of s. Analytical results (9.21): $s = 0$ (solid line), $s = 6 \times 10^{-9}$ (dotted line), $s = 3 \times 10^{-8}$ (dashed line). Numerical results: $s = 0$ (triangles), $s = 6 \times 10^{-9}$ (squares), $s = 3 \times 10^{-8}$ (circles). $\varepsilon = 0$. Other parameters as in Fig. 9.1.

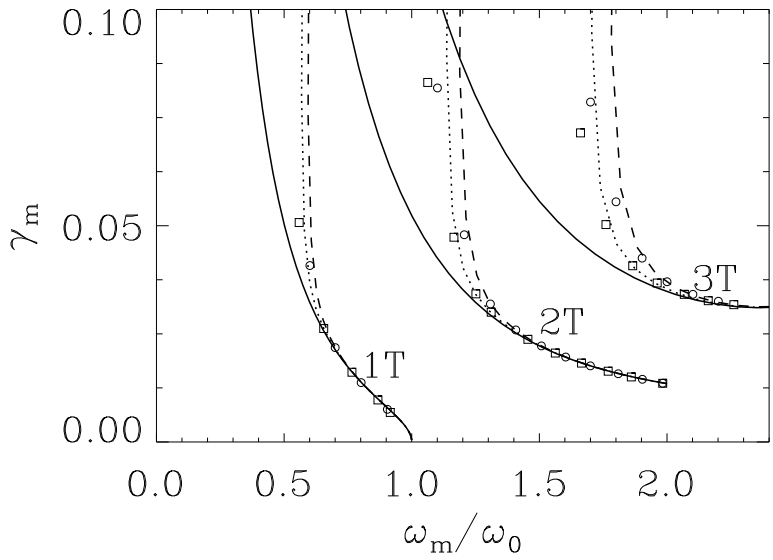

Figure 9.11: Maxima of main resonances in the plane $(\omega_m/\omega_0, J_m)$ for loss modulation. Effect of ε. Analytical results (9.21): $\varepsilon = 0$ (solid line), $\varepsilon = 6.2\times10^{-11}ps^{-1}$ (dotted line), $\varepsilon = 2.2\times10^{-10}ps^{-1}$ (dashed line). Numerical results: $\varepsilon = 6.2 \times 10^{-11}ps^{-1}$ (squares), $\varepsilon = 2.2 \times 10^{-10}ps^{-1}$ (circles). $s = 0$. Other parameters as in Fig. 9.1.

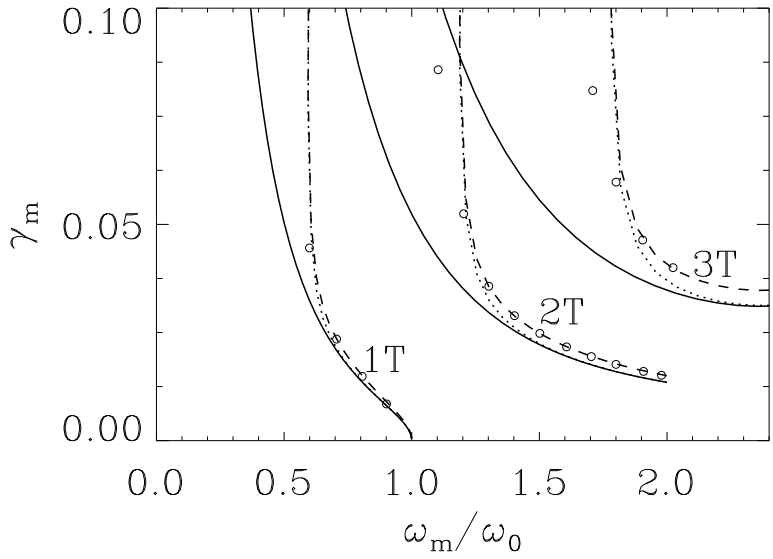

Figure 9.12: Maxima of main resonances in the plane $(\omega_m/\omega_0, J_m)$ for loss modulation. Combined effect of ε and s. Analytical results (9.21): $\varepsilon = 0$, $s = 0$ (solid line), $\varepsilon = 6.2 \times 10^{-11}ps^{-1}$, $s = 0$ (dotted line), $\varepsilon = 6.2 \times 10^{-11}ps^{-1}$, $s = 6 \times 10^{-9}$ (dashed line). Numerical results: $\varepsilon = 6.2 \times 10^{-11}ps^{-1}$, $s = 6 \times 10^{-9}$ (circles). Other parameters as in Fig. 9.1.

It is possible to obtain an interesting relation between the effect produced by loss modulation and pump modulation. The relation can be obtained more clearly if we write the evolution equation for the variable $x = \ln(y/y_{st})$, defined in terms of the stationary value y_{st} of the variable y in the absence of modulation. For small ε, s, it is $y_{st} \approx a - b$. It turns out that the resulting equations in the case of modulation in the pump or in the losses take basically the same form, namely

$$\ddot{x} + \dot{x}^2 G_1(x) + \dot{x} G_2(x) + G_3(x) = F_{P,L}(x, \tau), \tag{9.23}$$

$G_1(x)$, $G_2(x)$, and $G_3(x)$ are given functions of x whose detailed expressions are not needed here. The only difference is in the right hand side of this equation which for the case of modulation in the pump is

$$\begin{aligned} F_P(x,\tau) &= A_m \cos(\bar{\omega}_m \tau)\, F_1(x), \\ F_1(x) &= \frac{2}{1 + \bar{s} y_{st} \exp(x)} + \frac{c}{y_{st} \mathrm{e}^x}, \end{aligned} \tag{9.24}$$

while in the case of modulation in the losses it is:

$$F_L(x, \dot{x}, \tau) = 2\gamma_m \bar{\omega}_m \sin(\bar{\omega}_m \tau) - 2\gamma_m \cos(\bar{\omega}_m \tau) F_2(x, \dot{x}), \tag{9.25}$$

$$F_2(x, \dot{x}) = b + \frac{y_{st} \exp(x)}{1 + \bar{s} y_{st} \exp(x)} + \dot{x} \left[\frac{2\bar{s} y_{st}^2 \mathrm{e}^{2x} + c(1 + \bar{s} y_{st} \mathrm{e}^x)^2}{(1 + \bar{s} y_{st} \mathrm{e}^x)[2 y_{st} \mathrm{e}^x + c \mathrm{e}^{2x}(1 + \bar{s} y_{st} \mathrm{e}^x)]} \right]. \tag{9.26}$$

It is easy to see that the term containing F_2 is negligible compared to the first contribution to $F_L(x, \dot{x}, \tau)$. In fact, if we consider the value of F_2 in the steady state in the absence of modulation, $x = \dot{x} = 0$, we obtain $F_2 \approx a$. A typical value is $a \approx 0.01$ while the product $\gamma_m \bar{\omega}_m$ is of order 1 for $\omega_m \sim \omega_0$. If we replace now $F_1(x)$ by its steady state value $F_1(0)$, approximate the term $1 + \bar{s} y_{st} \approx 1$ and neglect the term proportional to c , we arrive at

$$F_P \approx 2A_m \cos(\bar{\omega}_m \tau), \tag{9.27}$$

$$F_L \approx 2\gamma_m \bar{\omega}_m \sin(\bar{\omega}_m \tau). \tag{9.28}$$

Therefore, we conclude that the role of the modulation in the pump is equivalent to the modulation in the losses, besides a trivial phase shift, if $A_m = \gamma_m \bar{\omega}_m$. In terms of the physical parameters, this is equivalent to

$$J_m = \gamma_m \omega_m \frac{\gamma e}{g_N J_b}. \tag{9.29}$$

This result shows that modulation in the pump or in the losses produce equivalent results if the respective modulation amplitudes are conveniently rescaled. It is possible to arrive at this result directly, in the case $s = \varepsilon = 0$, by comparing the expressions in terms of Fourier coefficients (9.16) and (9.22). The validity of this equivalence of modulation in the pump and in the losses is shown in Figs. 9.13 and 9.14, where we compare, for typical values of s and ε, the skeleton lines in the case of pump and loss modulation after the latter have been rescaled according to (9.29).

It is clear from these figures that the proposed equivalence after parameter rescaling works well in the cases that have been shown. A similar agreement is observed for other boundaries and values of the parameters.

Since relation (9.29) implies, for typical values of the parameters, that $J_m > \gamma_m$ we recover the known results that loss modulation is more efficient to get bifurcations and chaos. This relation can be applied in the large modulation signal regime (nonlinear regime), and hence it can be considered as an extension of previous analytical results in the case of the linear regime [Tredicce *et al.*, 1985b].

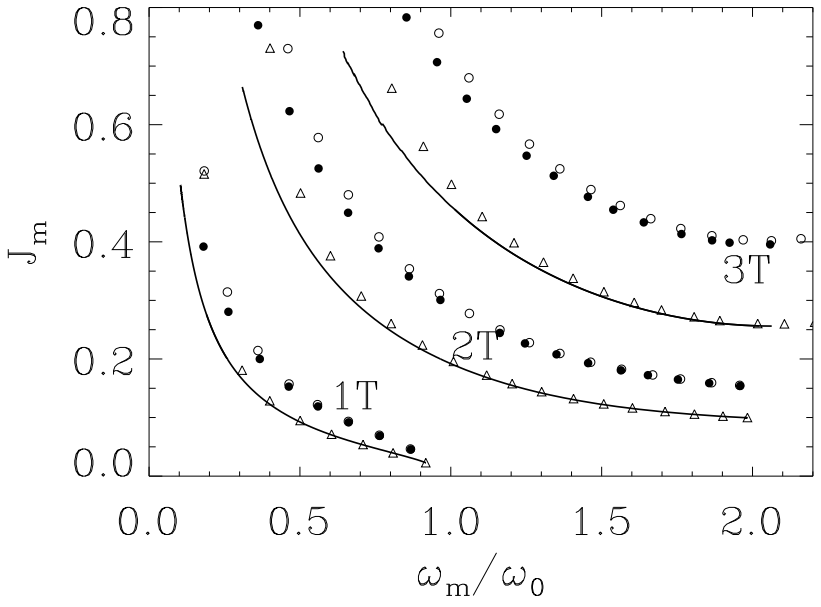

Figure 9.13: Maxima of main resonances in the plane $(\omega_m/\omega_0, J_m)$. Numerical results. Pump modulation: $s = 0$ (solid line) (equivalent to theoretical results), $s = 3 \times 10^{-8}$ (filled circles). Loss modulation multiplied by factor of Eq. (9.29): $s = 0$ (triangles), $s = 3 \times 10^{-8}$ (circles). $\varepsilon = 0$, $J_b = 1.23 J_{th}$.

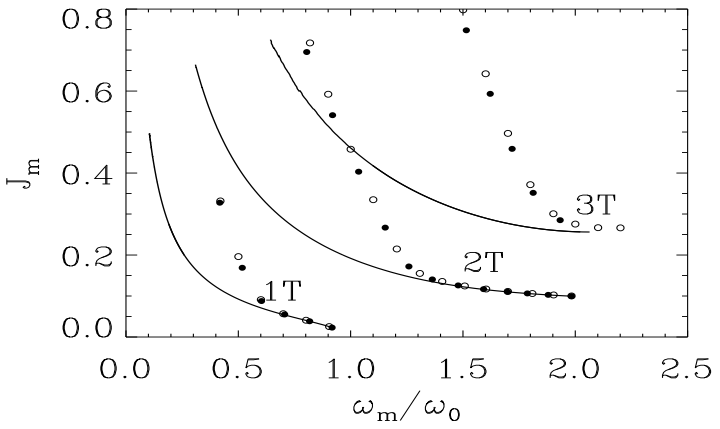

Figure 9.14: Maxima of main resonances in the plane $(\omega_m/\omega_0, J_m)$. Numerical results. Pump modulation: $\varepsilon = 0$ (solid line), $\varepsilon = 2.2 \times 10^{-10} ps^{-1}$ (filled circles). Loss modulation multiplied by factor of Eq. (9.29): $\varepsilon = 2.2 \times 10^{-10} ps^{-1}$ (circles). $s = 0$, $J_b = 1.23 J_{th}$.

9.4 Comparison to experiments

The fingerprints of nT resonance regimes, which discern from non–resonance nT periodic windows in chaos, is a dominant ω_m/n component in microwave spectra. In particular, $\omega_m/2$ component in microwave spectra was dominating in the observations of Refs. [Liu and Ngai, 1993; Bennett *et al.*, 1997; Matsui *et al.*, 1998; Wada *et al.*, 1998], pointing out the resonance $2T$ regime, that in time domain leads to sharp spikes like the ones presented in Fig. 9.2 (b) (no intermediate spikes at interval $2T_m$). A direct example of resonant $2T$ regime observation and possible applications to all-optical clock division can be found in [Yang and Liu, 2001].

According to our predictions, resonant regimes with $n > 2$ also exist in the system. However, they are dynamical isolas that cannot be observed with smooth sweeping of modulation parameters, besides the special cases of pulse excitation [Samson *et al.*, 1990; Chizhevsky and Turovets, 1993; Chizhevsky, 2000] or chaotic crisis on the basic $1T$ periodic branch leading to switching to a $3T$ branch as it was observed in [Liu and Ngai, 1993] and explained in [Lamela *et al.*, 1998a; Lamela *et al.*, 1998b]. Particularly relevant to our work is the paper by Liu and Ngai [Liu and Ngai, 1993] where the response of a single mode distributed feedback laser subjected to current modulation is considered experimentally. We summarize the observations they obtain when changing the modulation frequency and amplitude of the radio frequency signal and compare them to our results:

a) For small modulation frequency there is only a $1T$ period response for any signal amplitude. This behaviour also appears in our system, as it was visualized in Fig. 9.7 for $\omega_m/\omega_0 < 0.2$, for $J_m < 1$.

b) For intermediate modulation frequency there is a transition from $1T$ to $2T$

responses when increasing the modulation amplitude. This fact could be seen in Fig. 9.7 in the region $0.2 < \omega_m/\omega_0 < 2.$, for the corresponding values of J_m. A further transition from $2T$ back to $1T$ is experimentally, but nor numerically, observed.

c) $3T$ and $4T$ solutions appear for large enough modulation frequency and amplitude. We find these solutions also in the case of large enough values of the modulation frequency and amplitude, see Figs. 9.7, 9.8 and 9.9. The $4T$ solution would appear for larger values of the amplitude not plotted in the figure. We have checked that for $s = 0$ and $\varepsilon = 0$ the corresponding $4T$ boundary for pump modulation would have its minimum value at $\omega_m/\omega_0 \sim 2.3$ and $J_m \sim 0.4$. However, identification of the $3T$ branch observed in [Liu and Ngai, 1993; Bennett *et al.*, 1997] is still hard to make as resonant due to the fact that the microwave spectra gives a dominate modulation component at ω_m, but not at the subharmonic $\omega_m/3$ as it might be expected for a purely resonant regime.

9.5 Discussion

We have undertaken a numerical and analytical study to identify the optimal responses of a semiconductor laser subjected to an external periodic modulation in the pump of relative amplitude J_m and frequency ω_m. We have computed the lines in the $(\omega_m/\omega_0, J_m)$ plane that give a maximum response for each type of nT resonance (skeleton lines) and compared them to the numerical results. The influence of saturation and spontaneous emission terms on the dynamics has also been examined. We have found that these specific laser diode parameters increase the thresholds of instabilities in the system, a fact that can be interpreted as an effect of the increase in the damping of relaxation oscillations. A qualitative comparison with experiments has also been performed, our results qualitatively agree in part with the experimental observations with $1.55\mu m$ InGaAs distributed lasers [Liu and Ngai, 1993]. The analytical results we have obtained by an application of the quasi–conservative theory allow us to explain satisfactorily the effect of the saturation term. The role of the gain saturation parameter is such that, for a fixed value of the frequency ω_m, a larger value of modulation amplitude J_m is needed to obtain the optimal periodic response for each main resonance. This effect is more important for higher order resonances. However, the effect of the spontaneous emission term in the skeleton lines has not been completely explained by the analytical results and the discrepancy between the numerical and analytical results is due to the form of the conservative solution.

Loss modulation has also been considered and analytical and numerical results are in reasonable agreement. Furthermore, we have obtained a relation that shows the equivalence between pump and loss modulation. This equivalence relation, having a large validity for the numerical boundaries, allows to compute the boundary limits for pump (or loss) modulation if the loss (pump) boundaries are known. We have explain the experimental results that loss modulation is more efficient to get bifurcation and chaos than pump modulation.

Conclusions

Conclusions i possibles extensions

En aquest treball s'ha estudiat la dinàmica dels làsers de classe A i de classe B en termes del potencial de Lyapunov. En el cas que s'injecti un senyal al làser o es modulin alguns dels paràmetres, apareix un comportament molt més complex i s'estudia el conjunt de bifurcacions.

1) Als làsers de classe A, la dinàmica determinista s'ha interpretat com el moviment damunt el potencial de Lyapunov, i s'han identificat els termes relaxacionals i conservatius en les equacions de la dinàmica. L'efecte combinat d'aquests dos termes produeix una trajectòria espiral en el pla definit per les parts real i imaginària del camp elèctric, amb una velocitat angular proporcional al terme de disintonia.

En la dinàmica estocàstica (quan termes de renou additiu s'inclouen en les equacions) s'obté un *flux sostingut per renou* per a la fase del camp elèctric, que prové de la interacció dels termes conservatius i els termes de renou. Aquest flux en la fase es manifesta com un corriment de la freqüència intrínseca d'emissió de la llum làser. Una expressió analítica permet calcular l'evolució de la fase. Encara que seria interessant comprovar experimentalment l'existència d'aquest corriment de freqüència induït per renou, cal recalcar que d'acord amb els nostres resultats, la intensitat del renou que es requereix per obtenir un corriment de freqüència observable és molt més gran que la intensitat de renou típica en els experiments. No obstant, aquest renou extra necessari podria ésser induït externament. A més, el corriment de freqüència, obtingut en els làsers de classe A, apareix en altres tipus de làsers, com en els làsers de classe B, encara que en aquest cas s'hauria de desenvolupar una teoria apropiada. Caldria resaltar la importància d'aquest flux induït per renou. Aquest podria aparèixer en altres sistemes, i seria en particular interessant considerar un símil mecànic del potencial de Lyapunov que s'ha obtingut.

2) Per als làsers de classe A amb senyal injectat, s'ha descrit el conjunt de bifurcacions complet (de forma analítica i numèrica) i s'ha determinat el conjunt d'amplituds (ρ) i freqüències (η) en el qual el làser respon ajustant la seva freqüència a la del camp extern. Aquest resultat apareix resumit a la Fig. 6.2 (c) on s'ha identificat regions on la resposta no és a la mateixa freqüència de la d'injecció (indicades amb NL a aquella figura). A dins les regions on el làser respon a la mateixa freqüència que la d'injecció es pot distingir entre una regió on hi ha una única resposta estable (L), regions de coexistència de la solució a la mateixa freqüència de la

d'injecció amb una a distinta freqüència (C), i finalment un a regió on hi coexisteixen dues solucions a la mateixa freqüència que la freqüència d'injecció però amb distinta intensitat (B). S'han descrit qualitativament les característiques observades en la dinàmica determinista en termes del potencial de Lyapunov, identificant els termes relaxacionals, conservatius i els residuals en les equacions dinàmiques. Encara que aquesta descripció és estrictament vàlida només en el cas de senyal injectat amb freqüència zero, les característiques qualitatives no canvien quan el producte $\rho\eta$ és petit.

A la dinàmica estocàstica (quan el renou additiu que prové de l'emissió espontània es considera explícitament en les equacions), s'ha utilitzat la imatge del potencial de Lyapunov per explicar la presència del *corriment de freqüència estocàstic* del llum làser igual com s'havia fet en els làsers de classe A sense injecció. El mateix potencial permet realitzar un càlcul quantitatiu d'aquest efecte. Els resultats s'ajusten a les simulacions numèriques de les equacions model i esperam que serveixin de guia per a futurs experiments en l'observació en sistemes làsers reals, tot i que s'hauran de tenir en compte les limitacions experimentals i termes de renou a l'hora de fer comparacions.

3) En el cas dels làsers de class B, s'ha obtingut un potencial de Lyapunov només vàlid en el cas determinista, quan les fluctuacions de renou es menyspreen. La dinàmica és del tipus no relaxacional amb una matriu D no constant. El punt fix corresponent a que el làser es troba a l'estat d'encès s'ha interpretat com el mínim del potencial. La relaxació cap a aquest mínim es realitza a través d'oscil·lacions esmorteïdes. A partir de l'observació que el valor del potencial és quasi bé constant entre dos pics consecutius d'intensitat, durant el procés transitori de relaxació cap a l'estat estacionari, s'ha pogut obtenir una expressió aproximada per al període d'aquestes oscil·lacions. A més, l'expressió que relaciona el període de les oscil·lacions al valor del potencial ens ha permès obtenir una relació semiempírica que ajusta (sense cap paràmetre ajustable i amb gran exactitud) el període de les oscil·lacions des del règim no lineal fins a les oscil·lacions de relaxació a prop de l'estat estacionari.

4) Hem realitzat un estudi del conjunt de bifurcacions parcial al voltant del règim tipus II de la singularitat Hopf–sella–node en un làser de classe B amb senyal injectat, a causa de què existia una falta d'estudi detallat al voltant d'aquest tipus en la literatura existent. Els paràmetres de bifurcació que s'han considerat són la intensitat del senyal injectat i la disintonia entre la freqüència de la pertorbació i la freqüència d'operació del làser sense injecció. El centre d'organització principal és una bifurcació Hopf–sella–node des d'on s'origina una bifurcació secundària d'òrbites periòdiques, i neix un torus a aquella bifurcació. Es veu que la solució làser estable que existeix per a valors d'injecció baixos, també sofreix una bifurcació de Hopf secundària, creant–se un altre torus. Aquests tours tenen resonàncies per alguns dels valors dels paràmetres: poden existir òrbites tancades damunt els torus. L'estructura de resonàncies dels dos torus interacciona, i a més s'obtenen òrbites homoclíniques

a l'estat apagat a dins de cada una de les llengües d'Arnold. Un dels resultats més importants és l'acumulació de totes les resonàncies cap a la singularitat Hopf–sella–node, que indica l'existència d'una bifurcació global altament degenerada en el punt de codimensió–2.

Es pot comparar el conjunt de bifurcacions obtingut pel làser de classe B amb senyal injectat amb el del làser de classe A amb senyal injectat. La diferència principal entre els dos tipus de làsers des del punt de vista dinàmic és el nombre de variables amb què es treballa. Pels làsers de classe A és suficient amb dues variables i es pot descriure el conjunt complet de bifurcacions. Pels làsers de classe B cal considerar tres equations, i és per aquest motiu que una varietat de fenòmens molt més complexa pot aparèixer. Encara que part de l'estructura de bifurcacions dels làsers de classe B ja estava present en els làsers de classe A (esencialment les tres corbes corresponents a les bifurcacions sella–node de punts fixos), la dinàmica completa del làser de classe B és extremadament complicada. Hem vist que la presència del punt Hopf–sella–node és molt important en els làsers de classe B i que distints tipus de comportaments es poden obtenir. En canvi, la intersecció de les bifurcacions Hopf i sella–node de punts fixos en el cas de classe A no pot ser dels tipus Hopf–sella–node sinó que es tracta de singularitats Takens–Bogdanov. No obstant, aquests singularitats ja eren presents (encara que de distinta manera) en els làsers de classe B incloent–hi bifurcacions d'òrbites periòdiques enlloc de punts fixos. Les bifurcacions d'Andronov globals també s'han obtingunt en ambdós tipus de làsers. El conjunt de bifurcacions per als làsers de classe A per $\alpha = 0$ és molt més senzill que el del cas $\alpha \neq 0$, i aquest darrer es pot obtenir a partir del cas $\alpha = 0$ realitzant alguns canvis. Aquesta situació torna a ser reminiscent del cas del làser de classe B.

5) S'han identificat les respostes òptimes pels làsers de semiconductor sotmesos a modulació periòdica externa. S'han obtingut les corbes que donen la resposta màxima per cada tipus de resonància nT en el pla definit per l'amplitud relativa de modulació i la freqüència de modulació. Aquests dominis d'existència de les resonàncies principals s'han obtingut mitjançant l'aplicació de la teoria quasi–conservativa. Les prediccions han estat comparades amb els resultats numèrics obtinguts a partir de la integració directa d'equacions model, així com amb observacions experimentals descrites per altres grups. En ambdós casos s'obté una concordància qualitativa. S'ha considerat un model que conté explícitament els termes de saturació de guany i els termes d'emissió espontània. Els termes d'emissió espontània modifiquen en gran mesura el comportament qualitatitu dels límits de les inestabilitats, mentre que el terme de saturació de guany dóna lloc a un simple corriment dels límits. Els resultats que s'obtenen teòricament reprodueixen aquest comportament qualitatiu. Finalment, s'observa que la modulació en el bombeig i la modulació en les pèrdues produeixen resultats equivalents si les respectives amplituds de modulació es reescalen de manera adequada. Aquesta relació d'equivalència permet calcular límits d'existència per a la modulació al bombeig (o a les pèrdues) a partir dels límits a les pèrdues (o al bombeig). Es recupera el resultat conegut que

la modulació al terme de pèrdues és més eficient que la modulació al bombeig per obtenir bifurcacions i caos.

Algunes posssibles extensions d'aquest treball inclourien:

- Estudiar la dinàmica del làser en presència de renou en el paràmetre de bombeig. En general, degut a la dinàmica lenta dels portadors, el renou no es considerarà blanc, sinó que de manera més realista es modelitzarà com un renou de color. Aquesta font de renou afecta principalment a les característiques espectrals del làsers. Si es pogués obtenir un potencial de Lyapunov, satisfent la relació de fluctuació–dissipació es podria calcular qualsevol valor mig d'interès a l'estat estacionari.

- Obtenir una forma explícita pel potencial de Lyapunov pel làser amb un camp extern injectat. En el cas del làser de classe A en tenim l'expressió en alguns casos particulars, i a partir d'ella, podem inferir la forma qualitativa general. En el cas del làser de classe B es tractaria d'un problema nou.

- Obtenir el potencial de Lyapunov que té en compte la pulsació auto-sostinguda en alguns làsers de semiconductor. En aquests sistemes, el nombre de fotons i les densitats d'electrons no són constants a l'estat estacionari sinó que oscil·len en el temps. Es pot especular que en aquest cas el potencial seria similar a l'obtingut per al làser de classe B però en aquest cas l'estat estacionari no es tractaria d'un punt fix sinó d'un cicle límit, que es podria obtenir a partir d'una dinàmica residual.

- El corriment de freqüència induït per renou en els làsers de classe A també s'ha obtingut numèricament en alguns tipus de làsers de classe B. Per als làsers de classe A és possible obtenir una expressió analítica per al corriment de freqüència estocàstic ja que la descripció mitjançant la funció de Lyapunov de la dinàmica és tal que la relació fluctuació–dissipació es satisfà. No obstant, encara que ha estat possible obtenir una funció de Lyapunov per als làsers de classe B, la relació fluctuació–dissipació no es satisfà per a aquest tipus de làsers i la funció de Lyapunov no pot donar una descripció completa de la distribució estacionària en el cas estocàstic. Per tant, és un problema obert obtenir una descripció teòrica satisfactòria per al corriment de freqüència induït per renou per als làsers de classe B.

- En aquest treball s'ha obtingut part del conjunt de bifurcacions en el cas del làser de classe B amb senyal injectat. Es podria continuar amb aquesta anàlisi i cercar altres bifurcacions en el mateix espai de paràmetres. Seria interessant relacionar les distintes bifurcacions que es troben per als distints tipus de la bifurcació Hopf–sella–node. A més, en el nostre estudi s'ha restringit l'anàlisi a la regió a prop del centre organitzatiu Hopf–sella–node, i es podria realitzar l'estudi en regions allunyades d'aquest punt.

Conclusions and Outlook

In this work we have studied the dynamics of both class A and class B lasers in terms of Lyapunov potentials. In the case of an injected signal or when some laser parameteres are modulated, and more complex behaviour is expected, the bifurcation set is studied. The main results are the following:

1) For class A lasers, the deterministic dynamics has been interpreted as a movement on the potential landscape, and the relaxational and conservative terms in the dynamical equations of motion have been identified. The combined effects of these two terms produce an spiraling trajectory in the plane defined by the real and imaginary parts of the electric field, with an angular velocity proportional to the detuning parameter.

In the stochastic dynamics (when additive noise is included in the equations) we have found a *noise sustained flow* for the phase of the electric field. It arises from the interaction of the conservative terms with the noise terms. This phase flow manifests as an intrinsic frequency shift of the laser light. An analytical expression allows the calculation of the phase evolution. Although it would be interesting to check experimentally the existence of this noise induce phase drift, we have to stress that, according to our results, the noise intensity required for an observable phase drift is much larger than the typical noise intensity in experiments. Nevertheless, this necessary extra noise could be externally induced. Moreover, this phase drift, obtained for class A lasers, is also present in other types of lasers as, e.g., class B lasers, although for the latter an appropriate theory should be developed. We believe that this is an important and new effect that could appear in other laser systems. It would be interesting to develop a mechanical simile of the Lyapunov potential obtained, that could help us to relate the phenomenon predicted here with other cases of noise sustained flow well documented in the literature.

2) For class A lasers with an injected signal, we have been able to describe the whole bifurcation set of this system (by using analytical and numerical tools) and to determine the *locking range*, i.e. the set of amplitudes (ρ) and (detuning) frequencies (η) for which the laser responds adjusting its frequency to that of the external field. This result is summarized in Fig. 6.2 (c) in which we can identify non–locking regions (labelled NL in that figure). Within the locking range one finds a region with a single stable laser response (L), regions of coexistence of a locking

solution with a non–locking solution (C), as well as a region of coexistence of two locking solutions of different light intensity (B). We have described qualitatively the observed features of the deterministic dynamics in terms of a Lyapunov potential function. We have identified the relaxational, conservative and residual terms in the dynamical equations of motion. Although this description is strictly valid only in the case of a zero–detuning injected signal, the qualitative features remain unchanged when the product $\rho\eta$ is small.

In the stochastic dynamics (when the additive noise coming from the spontaneous emission is explicitly considered in the equations) we have used the Lyapunov potential image to explain the presence of a *stochastic frequency shift* of the laser light. The same potential function allows a quantitative calculation of this effect. The results are in good agreement with numerical simulations of the model equations and we hope that they can be a guide for future experiments in observing this effect in laser systems.

3) In the case of class B lasers, we have obtained a Lyapunov potential only valid in the deterministic case, when noise fluctuations are neglected. We have found that the dynamics is non–relaxational with a nonconstant matrix D. Hence, the fixed point corresponding to the laser in the *on* state has been interpreted as a minimum in this potential. Relaxation to this minimum is reached through damped oscillations. The observation that the potential is nearly constant between two consecutive intensity peaks during the transient relaxation process towards the steady state, has allowed us to obtain an approximate expression for the period of these oscillations. Moreover, an expression relating the period of the oscillations to the value of the potential has allowed us to find a semi–empirical relation that fits (with no adjustable parameters and with a high degree of accuracy) the period of the oscillations from the nonlinear regime up to the relaxation oscillations near the steady state.

4) We have performed a study of the partial bifurcation set around the type II regime of the Hopf–saddle–node singularity in a class B laser with injected signal. Such a detailed study around this regime was missing in the previous literature. The bifurcation parameters we have considered are the intensity of the injected signal and the detuning of the perturbation frequency and the unperturbed laser operating frequency. The main organizing center of the system is the Hopf–saddle–node bifurcation from where a secondary Hopf bifurcation of a periodic orbit originates, and a torus is born at this latter bifurcation. We show that the laser's stable cw solution existing for low injections also suffers a secondary Hopf bifurcation and another torus is created. These tori have resonances for some values of the parameters, in the sense that close orbits on the tori can appear. The resonance structure of both tori interact and homoclinic orbits to the off state are found inside each Arnold tongue. A connection between different resonances in the parameter space has also been obtained. One of the main results is the accumulation of all the above resonances towards the Hopf–saddle–node singularity points to the occurrence of a highly degenerate global bifurcation at the codimension–2 point.

We can compare the bifurcation set obtained for a class B laser with injected signal with the one obtained for a class A laser with injected signal. From the dynamical point of view, the main difference between the two kinds of lasers is the number of variables involved. For class A lasers two variables suffice and the full bifurcation set can be described. For class B lasers, a three–equations system, a more complex variety of phenomena can appear and the system can also show chaotic behaviour. Although part of the bifurcation structure of class B lasers is already present in class A lasers (essentially the tree curves of saddle–node bifurcations of fixed points), the overall dynamics of the former becomes extremely complicated. We have seen that the presence of the Hopf–saddle–node point has a crucial importance for class B lasers and different types of flows can be obtained. Note as contrast that the intersection of Hopf and saddle–node bifurcations of fixed points in class A lasers cannot be of Hopf–saddle–node types but are Takens–Bogdanov singularities instead. Such singularities are also present (in a different form) in class B lasers, not involving bifurcations of fixed points but of periodic orbits. Andronov global bifurcations have also been found in both types of lasers. The bifurcation set for a class A laser in the case $\alpha = 0$ is much simpler than the one found for $\alpha \neq 0$ although the former can be obtained by suitable reduction of the latter. This situation is again reminiscent of the class B laser case.

5) We have identified the optimal responses of a semiconductor laser subjected to an external periodic modulation. The lines that give a maximum response for each type of nT resonance (skeleton lines) are obtained in the plane defined by the relative amplitude modulation and frequency modulation. The domains of existence of the main resonances are obtained by application of the quasi–conservative theory. The predictions are compared with numerical results coming from a direct integration of the model equations and with experimental observations reported by other groups. In both cases we find a good qualitative agreement. We have considered a model that contains explicitly the gain saturation and spontaneous emission terms and we have focused mainly on the effect that these terms have in the regime of large amplitude modulation. We find that the spontaneous emission qualitatively modifies the behaviour of the instabilities boundaries, while the gain saturation leads to a simple quantitative shift of boundaries. Our theoretical results reproduce this overall behaviour. We also find that modulation in pump or losses produce equivalent results if the respective modulation amplitudes are conveniently rescaled. This equivalence relation allows to compute the boundary limits for pump (or loss) modulation if the loss (pump) boundaries are know. We have recovered the results that loss modulation is more efficient to get bifurcations and chaos than pump modulation.

Some possible extensions of this work include:

- To study laser dynamics in the presence of noise in the pump parameter. In general, and due to the slower dynamics of the carriers variable, the noise

should not be considered as white but more realistically it should be modelled as a colored noise. This noise source mainly affects the spectral characteristics of the lasers. If a Lyapunov Potential, satisfying the fluctuation–dissipation relation could be obtained then any mean value of interest in the steady state could be calculated.

- To obtain a complete Lyapunov potential for lasers in the presence of an external field. For class A lasers this has been done for some particular cases and it was possible to infer the qualitative form of the potential in the most general case. For class B lasers with injected signal it would be interesting to perform the description of its dynamics in terms of a Lyapunov potential.

- To obtain a Lyapunov potential that accounts for the self–sustained pulsation phenomena that occurs in some semiconductor lasers. In these systems, the photon number and electron densities are not constant in the steady state but oscillate in time. We speculate that in this case, the potential would be quite similar to that obtained for class B lasers, but the steady state will not be a fixed point, but a limit cycle instead, which could be obtained as a residual dynamics.

- The noise frequency shift obtained in class A lasers has also been found numerically in some class B lasers. For class A lasers it is possible to reach a complete understanding of this stochastic frequency shift since the Lyapunov function description of the dynamics is such that the fluctuation–dissipation relation is satisfied. However, although we have been able to find a Lyapunov function for class B lasers, the fluctuation–dissipation relation is not satisfied for this kind of lasers and the Lyapunov function can not give us a complete description of the stationary distribution in the stochastic case. Therefore, it is an open problem to obtain a satisfactory theoretical description of the noise induced frequency shift for class B lasers.

- We have obtained a subset of the bifurcation set in the case of a class B laser with injected signal. It would be interesting to follow the analysis of this bifurcation set and look for other bifurcations. The important point should be to relate the bifurcations encountered for one type of the Hopf–saddle–node bifurcation to another. Moreover, the analysis of the bifurcation set has been restricted to a region in the space of parameters near the Hopf–saddle-node organizing center, it would be interesting to perform an study in a region far of that center.

List of Figures

Bibliografia

Adler, R. [1946]. A study of locking phenomena in oscillators. *Proc. IRE*, **34**, 351–357. Reprinted in *Proc. IEEE* **61**, 1380 [1973].

Agrawal, G.P. [1986]. Effect of gain nonlinearities on period doubling and chaos in directly modulated semiconductor lasers. *Appl. Phys. Lett.*, **49** (16), 1013–1015.

Agrawal, G.P. [1987]. Gain nonlinearities in semiconductor lasers: theory and application to distributed feedback lasers. *IEEE Journal of Quantum Electronics*, **QE-23**, 860–868.

Agrawal, G.P., and Dutta, N.K. [1986]. *Long–Wavelength Semiconductor Lasers.* New York: Van Nostrand Reinhold.

Arecchi, F.T., Lippi, G.L., Puccioni, G.P., and Tredicce, J.R. [1984]. Deterministic chaos in laser with injected signal. *Opt. Comm.*, **51**, 308.

Arnold, V. [1983]. *Geometrical Methods in the Theory of Ordinary Differential Equations.* New-York: Springer–Verlag.

Aronson, D.G., Hall, M.A., Hall, G.R., and McGehee, R.P. [1982]. Bifurcations from an invariant circle for two–parameter families of maps of the plane: A computer–assisted study. *Commun. Math. Phys.*, **83**, 303–354.

Balle, S., Colet, P., and San Miguel, M. [1991]. Statistics for the transient response of single–mode semiconductor laser gain swiching. *Physical Review A*, **43** (11), 498–506.

Bennett, S., Snowden, C.M., and Iezekiel, S. [1997]. Nonlinear dynamics in directly modulates multiple–quantum–well laser diodes. *IEEE Journal of Quantum Electronics*, **33** (11), 2076–2083.

Braza, P.A., and Erneux, T. [1990]. Constant phase, phase drift, and phase entrainment in lases with an injected signal. *Physical Review A*, **41** (11), 6470–6479.

Breuer, D., and Petermann, K. [1997]. Comparison of NRZ- and RZ- Modulation Format for 40–Gb/s TDM Standard–Fiber Systems. *IEEE Photonics Technology Letters*, **9**, 398–400.

Bykov, V.V. [1993]. The bifurcations of separatrix contours and chaos. *Physica D*, **62**, 290–299.

Cahn, J.W., and Hilliard, J.E. [1958]. Free energy of a nonuniform system. I. Interfacial free energy. *J. Chem. Phys.*, **28**, 258–267.

Chizhevsky, V.N. [2000]. Coexisting attractors in a CO_2 laser with modulated losses. *J. Opt. B: Quantum Semiclass. Opt.*, **2**, 711–717.

Chizhevsky, V.N., and Turovets, S.I. [1993]. Small signal amplification and classical squeezing near period doubling bifurcations in a modulated CO_2–laser. *Opt. Commun.*, **102**, 175–182.

Ciuchi, S., de Pasquale, F., San Miguel, M., and Abraham, N. B. [1991]. Phase and amplitude correlations in the transient evolution of a detuned laser after switch-on. *Physical Review A*, **44**, 7657.

Descalzi, O., and Graham, R. [1992]. Gradient expansion of the nonequilibrium potential for the supercritical Ginzburg–Landau equation. *Phys. Lett. A*, **170**, 84.

Descalzi, O., and Graham, R. [1994]. Nonequilibrium potential for the Ginzburg–Landau equation in the phase–turbulent regime. *Z. Phys. B*, **93**, 509–513.

Doedel, E., Fairgrieve, T., Sandstede, B., Champneys, A., Kuznetsov, Y., and Wang, S. [1997]. AUTO97: Continuation and bifurcation software for ordinary differential equations. *http://indy.cs.concordia.ca/auto/main.html.*

Drozdov, Yu.M. [1955]. Forced oscillations in the quasiconservative nonlinear systems with one degree of freedom: Examples (In Russian). *Prikladnaya Matematika i Mekhanika*, **19**, 33–40.

Erneux, T., Baer, S.M., and Mandel, P. [1987]. Subharmonic bifurcation and bistability of periodic solutions in a periodically modulated laser. *Physical Review A*, **35**, 1165–1171.

Fisher, I., Liu, Y., and Davis, P. [2000]. Synchronization of chaotic semiconductor laser dynamics on sub–ns timescales and its potential for chaos communication. *Physical Review A*, **62**, R011801.

Gallagher, D.F.G., White, I.H., Carroll, J.E., and Plumb, R.G. [1985]. Gigabit pulse position bistability in semiconductor lasers. *L. Lightwave Technology*, **LT-5**, 1391–1398.

Gard, T.C. [1987]. *Introduction to Stochastic Differential Equations.* Monographs and Textbooks in Pure and Applied Mathematics, vol. 114. Marcel Dekker.

Gardiner, C.W. [1985]. *Handbook of Stochastic Methods.* Springer–Verlag.

Gavrielides, A., Kovanis, V., and Erneux, T. [1997]. Analytical stability boundaries for a semiconductor laser subject to optical injection. *Optics Communications*, **136**, 253–256.

Glendinning, P., and Sparrow, C. [1986]. T–points: a codimension two heteroclinic bifurcation. *Journal of Statistical Physics*, **43**, 479–488.

Goedgebuer, J.P., Larger, L., and Porte, H. [1998]. Optical cryptosystem based on synchronization of hiperchaos generated by a delayed feedback tunable laser diode. *Phys. Rev. Lett.*, **80**, 2249–2252.

Graham, R. [1987]. Weak noise limit and nonequilibbrium potential of dissipative dynamical systems. *Instabilities and Nonequilibrium Structures.*

Graham, R. [1991]. Nonequilibrium potentials in spatially extended pattern forming systems. *Instabilities and Nonequilibrium Structures III.*

Greiner, A., Strittmatter, W., and Honerkamp, J. [1988]. Numerical integration of stochastic differential equations. *J. Stat. Phys*, **51** (1/2), 95–108.

Guckenheimer, J., and Holmes, P. [1983]. *Nonlinear Oscillations, Dynamical Systems and Bifurcations of Vector Fields.* New York: Springer–Verlag.

Gunton, J.D., San Miguel, M., and Sahni, P. [1983]. The dynamics of first order phase transitions. *Phase Transitions and Critical Phenomena*, **8**.

Haken, H. [1983]. *Synergetics.* Springer–Verlag.

Haken, H. [1984]. *Laser Theory.* Springer–Verlag.

Haken, H. [1985]. *Light.* Laser Light Dynamics, vol. 2. Amsterdam: North–Holland.

Haken, H., and Sauermann, H. [1963]. Nonlineal interactions of laser modes. *Z. Phys.*, **173**, 261.

Haug, H. [1969]. Quantum–mechanical rate equations for semiconductor lasers. *Physical Review*, **184** (2), 338–348.

Hecht, E., and Zajac, A. [1986]. *Óptica.* Addison–Wesley Iberoamericana.

Hemery, E., Chusseau, L., and Lourtioz, J.M. [1990]. Dynamical behaviors of semiconductor lasers under strong sinusoidal current modulation: Modelling and experiment at 1.3μm. *IEEE Journal of Quantum Electronics*, **26**, 633–641.

Henry, C.H. [1982]. Theory of the linewidth of semiconductor lasers. *IEEE Journal of Quantum Electronics*, **QE-18** (2), 259–264.

Henry, C.H. [1983]. *IEEE Journal of Quantum Electronics*, **QE-19**, 1391.

Hernández-García, E., Toral, R., and San Miguel, M. [1990]. Intensity correlation functions for the colored gain–noise model of dye lasers. *Physical Review A*, **42** (11), 6823–6830.

Hilborn, R.C. [1994]. *Chaos and Nonlinear Dynamics.* New York: Oxford University Press.

Hirschberg, P., and Laing, C. [1995]. Succesive homoclinic tangencies to a limit cycle. *Physica D*, **89**, 1–14.

Hohenberg, P.C., and Halperin, B.I. [1977]. Theory of dynamical critical phenomena. *Rev. Mod. Phys.*, **49**, 435–485.

Homar, V.M. 1996. *Semiconductor Laser Dynamics under Feedback and Modulation. Single and Multimode Operation.* Ph.D. thesis, Universitat de les Illes Balears.

Hori, Y., Serizawa, H., and Sato, H. [1988]. Chaos in a directly modulated semiconductor lasers. *J. Opt. Soc. Am. B*, **5** (5), 1128–1132.

Jackson, E.A. [1989]. *Perspectives of Nonlinear Dynamics.* Cambridge: Cambridge University Press.

Kao, Y.H., and Lin, H.T. [1993]. Virtual Hopf precursor of period doubling route in directly modulated semiconductor lasers. *IEEE J. Quantum Electronics*, **29**, 1617–1623.

Katz, A.M. [1955]. Forced oscillations in the quasiconservative nonlinear systems with one degree of freedom (In Russian). *Prikladnaya Matematika i Mekhanika*, **19**, 13–32.

Kawaguchi, H. [1994]. *Bistabilities and Nonlinearities in Laser Diodes.* Boston-London: Artech House.

Kirk, V. [1991]. Breaking of symmetry in the saddle–node Hopf bifurcation. *Physics Letters A*, **154**, 243–248.

Kloeden, P.E., and Platen, E. [1992]. *Numerical Solution of Stochastic Differential Equations.* Berlin: Springer–Verlag.

Krauskpof, B., Wieczork, S., and Lenstra, D. [2000]. Routes to chaos in an optically injected semiconductor laser. *Proceedings of SPIE*, **3944**, 612–619.

Kressel, M.P., and Ippen, E.P. [1987]. *Appl. Phys. Lett.*, **51**, 1765.

Kuznetsov, Y. [1997]. *Elements of Applied Bifurcation Theory.* Series of Applied Mathematical Sciences, vol. 112. Springer.

Lamb, W.E. [1964]. Theory of optical masers. *Phys Rev.*, **134**, 1429–1450.

Lamela, H., Carpintero, G., and Mancebo, F. [1998a]. Period tripling and chaos in the dynamic behavior of directly modulated diode lasers. *IEEE Journal of Quantum Electronics*, **34** (10), 1797–1801.

Lamela, H., Carpintero, G., and Acebo, P. [1998b]. Truncation of the Feigenbaum sequence in directly modulated semiconductor lasers. *IEEE Journal of Quantum Electronics*, **34** (3), 491–496.

Lee, C.-H., and Shin, S.-Y. [1989]. Transformation of rate equations and approximate transient solutions for semiconductor lasers. *IEEE Journal of Quantum Electronics*, **25** (5), 878–884.

Lim, C.G., Iezekiel, S., and Snowden, C.M. [2000]. Is noise a crucial factor in rate equation modeling of nonlinear dynamics in laser diodes? *Applied Physics Letters*, **77**, 3493–3495.

Liu, H.F., and Ngai, W.F. [1993]. Nonlinear dynamics of a directly modulated 1.55 μm InGaAsP distributed feedback semiconductor laser. *IEEE Journal of Quantum Electronics*, **29** (6), 1668–1675.

Lyapunov, A.M. [1992]. *Stability of Motion.* London: Taylor & Francis.

Matsui, Y., Kutsuzawa, S., Arahira, S., Ogawa, Y., and Suzuki, A. [1998]. Bifurcation in 20–Ghz gain–switched 1.55–μm MQW lasers and its control by CW injection seeding. *IEEE Journal of Quantum Electronics*, **34**, 1213–1223.

Milshtein, G.N. [1974]. Approximate integration of stochastic differential equations. *Theory Prob. Appl.*, **19**, 557–562.

Milshtein, G.N. [1978]. A method of second order accuracy integration of stochastic differential equations. *Theory Prob. Appl.*, **23**, 396–401.

Mirasso, C.R., Colet, P., and San Miguel, M. [1993]. Dependence of time jitter on bias level for single–mode semiconductor lasers under high speed modulation. *IEEE Journal of Quantum Electronics*, **29**, 23–31.

Mirasso, C.R., Colet, P., and García-Fernández, P. [1996]. Synchronization of chaotic semiconductor lasers: Application to encoded communications. *Phot. Tech. Lett.*, **8**, 299–301.

Montagne, R., Hernández-García, E., and San Miguel, M. [1996]. Numerical study of a Lyapunov functional for the complex Ginzburg–Landau equation. *Physica D*, **96**, 47–65.

Nizette, M., and Erneux, T. [1999]. Injection locked semiconductor lase dynamics from large to small detunings. *Physics and Simulation of Optoelectronic Devices VII. Eds., Proc. SPIE 3625*, 679–691.

Novikov, E.A. [1964]. *Zh. Eksp. Teor. Fiz.*, **47**, 1919.

Novikov, E.A. [1965]. *Soviet Physics JETP*, **20**, 1290–1294.

Olshansky, R., Su, C.B., Manning, J., and Powazinik, W. [1984]. Measurement of radiative and nonradiative recombination rates in InGaAsP and AlBaAs light sources. *IEEE Journal of Quantum Electronics*, **QE-20**, 838–854.

Oppo, G-L., Politi, A., Lippi, G-L., and Arecchi, F.T. [1986]. Frecuency pushing in lasers with injected signal. *Physical Review A*, **34** (5), 4000–4007.

Oppo, G.L., and Politi, A. [1985]. Toda potential in laser equations. *Zeitschrift für Physik B - Condensed Matter*, **59**, 111–115.

Petermann, K. [1988]. *Laser Diode Modulation and Noise.* Dordrecht: Kluwer Academic Publishers.

Risken, H. [1989]. *The Fokker–Plank Equation.* Springer–Verlag.

Saleh, B.E.A., and Teich, M.C. [1991]. *Fundamentals of Photonics.* New York: Wiley.

Samson, A.M., and Turovets, S.I. [1987]. Hierarchy of bifurcations in a laser with periodic modulation of losses. *Doklady AN BSSR*, **31**, 888–890.

Samson, A.M., Logvin, Yu.A., and Turovets, S.I. [1990]. Therole of potential symmetry and shape of a nonlinear oscillator in the bifurcation hierarchy for harmonic action. *Sov. Radiophysics and Quantum Electronics*, **33**, 40–50.

Samson, A.M., Turovets, S.I., Chizhevsky, V.N., and Churakov, V.V. [1992]. Nonlinear dynamics of a loss–switched CO_2 laser. *Sov. Phys. JETP*, **74** (4), 628–639.

San Miguel, M., and Sagues, F. [1987]. Dynamics of transient pattern formation in nematic liquid crystals. *Physical Review A*, **36**, 1883–1893.

San Miguel, M., and Toral, R. [1997]. *Stochastic effects in physical systems in Instabilities and Nonequilibrium Structures VI.* Kluwer acad. pub. edn. E. Tirapegui and W. Zeller.

San Miguel, M., Montagne, R., Amengual, A., and Hernández-García, E. [1996]. *Instabilities and Nonequilibrium Structures V.* Kluwer acad. pub. edn. E. Tirapegui and W. Zeller.

Sancho, J.M., San Miguel, M., Katz, S.L., and Gunton, J.D. [1982]. Analytical and numerical studies of multiplicative noise. *Physical Review A*, **26**, 1589–1609.

Sargent, M., Scully, M.O., and Lamb, W.E. [1974]. *Laser Physics.* Reading Mass. Addison–Wesley Publ. Comp.

Schecter, S. [1987]. The saddle–node separatrix–loop bifurcation. *SIAM J. Math. anal.*, **18**, 1142–1156.

Schwartz, I.B. [1988]. Infinite primary saddle–node bifurcation in periodically forced systems. *Phys. Lett. A*, **126** (7), 411–418.

Schwartz, I.B., and Erneux, T. [1994]. Subharmonic hysteresis and period doubling bifurcations for a periodically driven laser. *SIAM J. Appl. Math.*, **54** (4), 1083–1100.

Simpson, T., Liu, J.M., Huang, K.F., and Tai, K. [1997]. Nonlinear dynamics induced by external optical injection in semiconductor lasers. *Quantum Semiclass. Opt.*, **9**, 765–784.

Solari, H.G., and Oppo, G-L. [1994]. Laser with injected signal: Perturbation of an invariant circle. *Optics Communications*, **111**, 173–190.

Solari, H.G., Natiello, M.A., and Mindlin, G.B. [1996]. *Nonlinear Dynamics. A two way trip from physics to math.* London: Institute of Physics Publishing.

Sparrow, C., and Swinnerton-Dyer, H.P.F. [1995]. The Falkner–Skan equation I: creation of strange invariant sets. *Journal of Differential Equations*, **199** (2), 336–394.

Statz, H., and deMars, G.A. [1960]. *Quantum Electromics.* New York: C. H. Townes. Colombia University Press.

Strogatz, S.H. [1994]. *Nonlinear Dynamics and Chaos.* Reading: Addison–Wesley Publ. Co.

Svelto, O. [1982]. *Principles of Lasers.* New York: Plenum Press.

Tang, C.L., Statz, H., and deMars, G.A. [1963]. Spectral output and spiking behavior of solid state lasers. *J. Appl. Phys.*, **34**, 2289–2295.

Tang, M., and Wang, S. [1986]. Simulation studies of bifurcation and chaos in semiconductor laser. *Appl. Phys. Lett.*, **48** (14), 900–902.

Tang, M., and Wang, S. [1987]. Simulation studies of dynamical behaviour of semiconductor laser with Auger recombination. *Appl. Phys. Lett.*, **50**, 1861–1863.

Toral, R., and Chakrabarti, A. [1993]. Generation fo Gaussian distributed random numbers by using a numerical version method. *Comp. Phys. Comm.*, **74**, 327.

Tredicce, J.R., Arecchi, F.T., Lippi, G-L., and Puccioni, G.P. [1985a]. Instabilities in lasers with an injected signal. *Journal of the Optical Society of America B*, **2**, 173.

Tredicce, J.R., Abraham, N.B., Puccioni, G.P., and Arecchi, F.T. [1985b]. On chaos in lasers with modulated parameters: a comparative analysis. *Optics Communications*, **55**, 131–134.

Šil'nikov, L.P. [1965]. A case for the existance of a denumerable set of periodic motions. *Sov. Math. Dokl.*, **6**, 163–166.

Šil'nikov, L.P. [1966]. On the generation of a periodic motion from a trajectory which leaves and re–enters a saddle–saddle state of equilibrium. *Sov. Math. Dokl.*, **7**, 155–1158.

van der Graaf, W.A. 1997. *Nonlinear Dynamics of Semiconductor Lasers Driven by External Optical Fields.* Ph.D. thesis, Amsterdam.

van Kampen, N.G. [1981]. *Stochastic Processes in Physics and Chemistry.* North–Holland.

van Tartwijk, G.H.M., and Lenstra, D. [1995]. Semiconductor lasers with optical injection and feedback. *Quantum Semiclass. Opt.*, **7**, 87–143.

Wada, K., Marui, H., Horinaka, H., and Cho, Y. [1998]. Disappearance of chaos on a 0.8 μm AlGaAs Fabry–Perot semiconductor laser modulated near the relaxation oscillation frequency. *Optics Communications*, **155**, 301–305.

Weiss, C.O., and Vilaseca, R. [1991]. *Dynamics of Lasers.* Weinhemim: VCH Publishers.

Wieczorek, S., Krauskopf, B., and Lenstra, D. [2000a]. Global view of complicated dynamics in optically injected semiconductor lasers. *Procedings of SPIE*, **3944**, 602–611.

Wieczorek, S., Krauskopf, B., and Lentra, D. [2000b]. Mechanism for multistability in a semiconductor laser with optical injection. *Optics communications*, **183** (1-4), 215–226.

Wieczorek, S., Krauskopf, B., and Lenstra, D. [2000c]. A unifying view of bifurcations in semiconductor lasers subject to optical injection. *Optics Communications*, **172**, 279–295.

Wiggins, S. [1991]. *Introduction to Applied Nonlinear Dynamical Systems and Chaos.* Vol. 2. Springer–Verlag.

Wilson, J., and Hawkes, J.F.B. [1989]. *Optoelectronics, An Introduction.* 2nd edn. Cambridge: Prentice Hall.

Yang, Y.M., and Liu, H.F. 2001. *Control of period doubling in modulated semiconductor lasers and its application to all–optical clock division.* Tech. rept. Paper 4283-47. Photonic West 2001, San José, USA.

Yeung, M.K.S., and Strogatz, S. [1998]. Nonlinear dynamics of a solid–state laser with injection. *Physical Review E*, **58**, 4421–4435.

Yoon, T.H., Lee, C.H., and Shing, S.Y. [1989]. Perturbation analysis of bistability and period doubling in directly–modulated laser diodes. *IEEE Journal of Quantum Electronics*, **25**, 1993–2000.

Zimmermann, M.G., and Natiello, M.A. [1998]. Homoclinic and heteroclinic bifurcations close to a twisted heteroclinic cycle. *International Journal of Bifurcation and Chaos*, **8**, 359.

Zimmermann, M.G., Natiello, M.A., and Solari, H.G. [1997]. Šil'nikov–saddle–node interaction: laser with injected signal. *Physica D*, **109**, 293–314.

Zimmermann, M.G., Natiello, M.A., and Solari, H.G. [2001]. Global bifurcations in a laser with injected signal: beyond Adlers approximation. *Chaos*, **11**, 500–513.

Currículum

FORMACIÓ ACADÈMICA

- LLICENCIATURA: Ciències Físiques. Universitat de les Illes Balears (UIB). Juny de 1996.
- Memòria d'Investigació. UIB. Març de 2000.
- Suficiència Investigadora. UIB. Juliol de 2000.

ASISTÈNCIA A CURSOS I REUNIONS

- "VI Curso de Introducción a la Investigación en Óptica" al **Instituto de Óptica Daza de Valdés (CSIC)**. Madrid, 11 i 12 d'abril de 1996. Rebut borsa de viatge.
- Curs d'estiu de la **Fundación General de la UCM** : "Iniciación a los Sistemas Dinámicos". San Lorenzo de El Escorial, 7 a 11 de juliol de 1997. Dirigit per Rafael de la Llave Canosa. Modalitat becària.
- Participació en el curs de la **7th Jyväskylä International Summer School**: "Introduction to extended dynamical systems". Jyväskylä, Finlàndia, 11 a 15 d'agost de 1997. Prof. T. Gallay. Rebut beca del programa EU TMR.
- Asistència a la "III Reunión Barcelona–Palma de Física Estadística y No Lineal". Barcelona, 30 i 31 de gener de 1998.
- Asistència al curs: " Optical solitons: theoretical challenges and industrial perspectives" al Centre de Physiques des Houches. Les Houches, França, 28 de setembre a 2 d'octubre de 1998. Rebut beca del programa EU TMR.
- Participació en l'escola internacional: "Space time chaos: characterization, control and synchronization". Instituto de Física, Universidad de Navarra. Pamplona, 19 a 23 de juny de 2000.
- Curs d'estiu de la **Fundación General de la UCM** : "Hitos matemticos de finales del siglo XX". San Lorenzo de El Escorial, 6 al 10 d'agost de 2001. Dirigit per Carlos Andradas. Modalitat becària.

CURSOS DE DOCTORAT

- Sistemes dinàmics (3 c). Curs 1996-97. UIB
- Mecànica estadística: Transicions de fase (3 c). Curs 1996-97. UIB
- Introducció a la dinàmica no lineal de làsers (2 c). Curs 1996-97. UC
- Introducció als làsers de semiconductor (2 c). Curs 1996-97. UC
- Làsers de semiconductor per a comunicaciones òptiques (2 c). Curs 1996-97. UC
- Mètodes de simulació numèrica en física. (3 c). Curs 1997-98. UIB
- Dinàmica d'estructures espaciotemporals (5 c). Curs 1997-98. UIB

ALTRES CURSOS DE DOCTORAT – ESPECIALIZACIÓ

- Solitons en comunicacions òptiques (2 c). Prof. L. Pesquera. 2 i 3 de juny de 1998. UC
- Solitons òptics espacials: propietats i aplicacions a dispositius fotònics (2 c). Prof. Ll. Torner. 4 i 5 de juny de 1998. UC
- Tècniques de supercomputació. Prof. J. Massó. Juliol de 1998. UIB

COMUNICACIONS

- C. Mayol, R. Toral i C. R. Mirasso, "A Lyapunov potential description for laser dynamics" (pòster); *VIII Reunión de Física Estadística, FISES '97.* Getafe, Madrid. 25 a 27 de setembre de 1997.
- C. Mayol, R. Toral i C. R. Mirasso, "A Lyapunov potential description for semiconductor lasers" (pòster); Centre de Physique des Houches, Les Houches, França, 28 de setembre a 2 d'octubre de 1998.
- C. Mayol, S.I. Turovets, R. Toral, C.R. Mirasso i L. Pesquera, "Asymptotic theory of instabilities in directly modulated semiconductor lasers", *Semiconductor and Integrated Optoelectronics 2000 Conference (SIOE '2000)*, Cardiff, UK, 17 a 19 d'abril de 2000.
- C. Mayol, M.A. Natiello i M.G. Zimmermann, "Laser with injected signal (LIS): small detuning" (pòster), Escuela internacional sobre *Space time chaos: characterization, control and synchronization.* Universidad de Navarra, Pamplona, 19 a 23 de juny de 2000.

- C. Mayol, S.I. Turovets, R. Toral, C.R. Mirasso i L. Pesquera, "Asymptotic Theory of Instabilities in Directly Modulated Semiconductor Lasers" (pòster), *International Quantum Electronics Conference (IQEC '00)*, Niza, França, 10 a 15 de setembre de 2000.

- C. Mayol, S.I. Turovets, R. Toral, C.R. Mirasso i L. Pesquera, "Asymptotic Theory of Instabilities in Directly Modulated Semiconductor Lasers" (pòster), *X Reunión de Física Estadística, FISES 2000.* Santiago de Compostela, Espanya. 21 a 23 de setembre de 2000.

PUBLICACIONS DE PRESENTACIONS EN CONGRESSOS

- C. Mayol, R. Toral, and C.R. Mirasso, "A Lyapunov Potential for Laser Dynamics". Proceeding of the *VIII Reunión de Física Estadística, FISES '97*, Anales de Física, Monografías 4 RSEF (1998). pàg. 271-272.

- C. Mayol, S.I. Turovets, R. Toral, C.R. Mirasso, and L. Pesquera, "Asymptotic Theory of Instabilities in Directly Modulated Semiconductor Lasers". Technical Digest of SIOE '2000. Paper Poster 47.

- C. Mayol, S.I. Turovets, R. Toral, C.R. Mirasso, and L. Pesquera, "Asymptotic Theory of Instabilities in Directly Modulated Semiconductor Lasers". Conference Digest of IQEC '00. Paper Poster QTuE4.

- C. Mayol, S.I. Turovets, R.Toral, C.R. Mirasso, and L. Pesquera, "Asymptotic Theory of Instabilities in Directly Modulated Semiconductor Lasers". Llibre del congrés FISES 2000. *X Congreso de Física Estadística.* Setembre 2000. pàg. 128.

PUBLICACIONS EN REVISTES AMB "REFEREE"

- C. Mayol, R. Toral, and C.R. Mirasso, "Lyapunov Potential Description for Laser Dynamics". Physical Review A, **59**, 4690–4698 (1999).

- C. Mayol, S.I. Turovets, R. Toral, C.R. Mirasso, and L. Pesquera, "Main Resonances in Directly Modulated Semiconductor Lasers: Effect of Spontaneous Emission and Gain Saturation". IEE Proc.–Optoelectronics, **148** (1), 41–45 (2001).

- C. Mayol, M.A. Natiello, and M.G. Zimmermann, "Resonance structure in a weakly detuned laser with injected signal", International Journal of Bifurcation and Chaos, **11** (10), 2587–2605 (2001).

- C. Mayol, R. Toral, C.R. Mirasso, S.I. Turovets, and L. Pesquera, "Theory of Main Resonances in Directly Modulated Diode Lasers". Acceptat a IEEE Journal of Quantum Electronics, a publicar–se el març de 2002.

- C. Mayol, R. Toral, C.R. Mirasso, and M. Natiello, "Class *A* lasers with injected signal: bifurcation set and Lyapunov potential function". Enviat a Physical Review E (2002).

ESTADES ALTRES CENTRES

- Estada predoctoral, Programa de Formació de Professorat Universitari. Departament de Matemàtiques, *Lunds Tekniska Hogskola*, Lund, Suècia. 6 d'agost a 29 d'octubre de 1999 (12 setmanes). Prof. responsable: Mario Natiello.
- Departamento de Física Moderna. Universidad de Cantabria, Santander. Estada mitjançant el conveni entre la Universidad de Cantabria i la Universitat de les Illes Balears. 13 a 26 de març de 2000 (2 setmanes). Prof. responsables: Luis Pesquera i Sergei I. Turovets.
- Estada predoctoral, Programa de Formació de Professorat Universitari. Departament de Matemàtiques, *Lunds Tekniska Hogskola*, Lund, Suècia. 27 d'abril a 19 de maig de 2000 (3 setmanes). Prof. responsable: Mario Natiello.